

# Tensor network investigation of frustrated Ising models

Présentée le 20 mai 2022

Faculté des sciences de base  
Chaire de théorie de la matière condensée  
Programme doctoral en physique

pour l'obtention du grade de Docteur ès Sciences

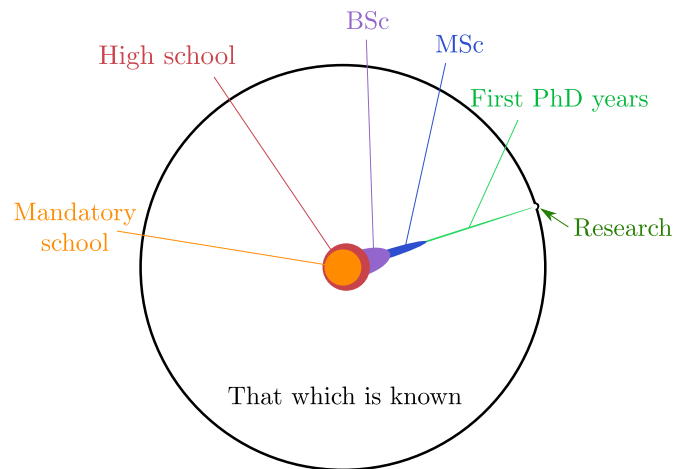
par

**Jeanne COLBOIS**

Acceptée sur proposition du jury

Prof. P. Ricci, président du jury  
Prof. F. Mila, directeur de thèse  
Dr B. Canals, rapporteur  
Prof. T. Nishino, rapporteur  
Prof. A. Läuchli, rapporteur





“On me posait souvent la question: “Mais alors quand vous faites de la recherche, vous êtes où, vous êtes à quel niveau, qu’est-ce-que vous faites, une thèse c’est quoi, etc.” et j’ai trouvé une façon graphique de le représenter que j’ai piquée à quelqu’un. [...] C’est ça la recherche. La recherche fondamentale, elle est là. C’est, soudain, je vais dans le précipice. Soudain, je vais là où personne n’a été avant. Et ça, c’est quand même une aventure de la pensée absolument incroyable. C’est une des grandes aventures humaines. C’est aller, soudain, mesurer un truc que personne n’a mesuré avant vous; essayer de faire un modèle sur un truc que personne n’a fait avant vous. Et parfois, vous n’allez rien trouver. Et parfois, vous allez trouver un petit truc. Et parfois, si vous êtes Einstein, vous allez faire un énorme lobe comme ça. Le truc exaltant, c’est pas ça, c’est pas seulement la découverte, c’est essayer. C’est être au bord du précipice; vous n’avez plus de bouquin qui vous dise ce que vous allez trouver. [...] Et ça, il n’y a pas tant de métiers que ça qui vous permettent d’aller aux frontières de la connaissance et de les repousser un petit peu. Je vous invite à cette aventure de la pensée humaine.”

Julien Bobroff, *Pourquoi fait-on de la recherche* (Transcription d’un extrait de la conférence de Julien Bobroff sur la supraconductivité au lycée Saint-Louis le 17 décembre 2011.)

Image: Matt Might, *The Illustrated Guide to a PhD*.

To my grandparents



# Acknowledgments

First and foremost, I would like to thank my PhD advisor Frédéric Mila, for giving me the opportunity of doing a PhD under his supervision, for his guidance, advice and patience during these years - and for his teaching before that. Frédéric always has a profound respect for his students and provides them with an ideal setting for finding out who they are as researchers. He gives them a lot of freedom, and at the same time he is always available to provide thoughtful advice and guidance. I cannot thank him enough for the insightful questions, for teaching me when to push forward and when to stop and contemplate, and for always looking for improvement. I very much hope to be able to keep learning from him. I would also like to thank the members of the Jury for their careful reading of the manuscript, their questions and the very interesting discussion.

The thesis was a less lonely adventure than I initially expected and I had the pleasure of getting to know and collaborating with a number of great scientists during these four years. For their interest, their countless ideas, the never-ending scientific discussions, a warm welcome in Ghent, and sharing their VUMPS implementation with me, I would like to thank Prof. Frank Verstraete and his group. A particular thank you goes to Bram Vanhecke for our collaborations and our discussions in Benasque, Ghent and especially online during the covid times. I would also like to thank Laurens Vanderstraeten for sharing his knowledge and experience of tensor networks and physics, always providing good ideas. Finally, I would like to thank Frank Verstraete for his never-ending enthusiasm and ideas about our projects, for systematically widening our point of view and for providing us with so many questions that it would probably make for a lifetime of scientific research. A more general thank you also goes to the Ghent team as a whole, especially Laurens, Robijn, Maarten, Benoît, Markus and Ghertian: it has been a lot of fun getting to know you.

For giving me the chance to work on data from their experiments and for teaching me everything I know about creating artificial spin systems, I would like to thank Prof. Laura Heyderman and members of her group. In particular, I would like to thank Kevin Hofhuis for collecting and walking me through the experimental data, for performing micromagnetic computations and for bouncing ideas back and forth in our weekly discussions. Thank you also to Aleš Hrabec, Zhaochu Luo and Xueqiao Wang for performing the experiments as well as for a warm welcome and great visit of the Paul Scherrer Institute. I would also like to thank Laura Heyderman for giving the momentum to the project while at the same time

## Acknowledgments

---

granting Kevin and I a lot of freedom, and also for taking interest in the side aspects of research.

For getting me involved in their project on quantum skyrmions and for the fascinating discussions, I would like to thank Oleg Sotnikov, Mikhail Katsnelson, Evgeny Stepanov and Vladimir Mazurenko.

For conference lunches and blackboard discussions, thank you so much: Natalia Chepiga, Anna Francuz, Gabriela Wójtowicz, Patrick Emonts, Patrick Hümbeli, Juraj Hasik, Stefanie Czischek and Philipp Schmoll, and also the Pedro Pascual conference center in Benasque. For an introduction to mathematical physics, I would like to thank Clément Hongler.

The CTMC group is a great place to be a PhD student, and I would like to thank all former and current members for their friendship and daily physics discussion: Mithilesh Nayak, Fransisco Kim, Samuel Gozel, Samuel Nyckees, Ivo Maceira, Zakaria Jouini, Bimla Danu, Kunio Tokushuku, Danis Badrtdinov and Adrien Bolens. A special thanks goes to Saeed Jaromi, Olivier Gauthé and Loic Herviou for sharing all they know about tensor networks. For teaching me about Monte Carlo, for their mentorship and enthusiasm, I will always be grateful to Jon D’Emidio and Andrew Smerald. I would also like to thank Aubry Jaquier for the IT support, and Anh Eymann and Anna Maria De Domenico for all the administrative work.

The PhD studies also involved supervising students, some of whom I would like to thank here: Samuel Nyckees, for the perfect balance between laid-back attitude and hard work, and Manuel Stathis, Bernhard Lüscher and Afonso Rufino, for making me a better teacher.

I also would like to thank two of my physics teachers in high school, Nicolas Paul and Olivier Caccivio, whose lectures and guidance sparked my interest in condensed matter; and a whole-hearted thank you to Hans Beck for his encouragements and for a three hours discussion which was at once a lesson in superconductivity and in science popularization.

To the friends I made during the PhD and the ones that were already around, Marie, Naomi, Coralie, Elodie, Alexandre, Laetitia, Isis, Adrien, Joao, Siyu, Mohamed and Alex: thank you for all the wonderful moments. To all the musicians of the CBLN and the EPFL Big Band and their respective conductors Jacques-Alain Frank and Samuel Urscheler, and to my successive piano teachers Emile Willemin, Caroline Apotheloz and Marie Salis: thank you for the music.

This thesis would not have happened without the constant support of my family and especially my parents, Bruno and Anne Marie, and my siblings, Laurent and Bérangère, throughout my life and studies. I am, as always, more grateful than words can say for the advice and encouragements, the music and the hikes. Je vous aime. És végül Miklósnak a túrákért, a napsütésért, a nevetésért, a csokiért és a kedvességet: köszönöm. Szeretlek.

*Lausanne, April 9, 2022*

J. C.

# Abstract

In spin systems, geometrical frustration describes the impossibility of minimizing simultaneously all the interactions in a Hamiltonian, often giving rise to macroscopic ground-state degeneracies and emergent low-temperature physics. In this thesis, combining tensor network (TN) methods to Monte Carlo (MC) methods and ground-state energy lower bound approaches, we study two-dimensional frustrated classical Ising models. In particular, we focus on the determination of the residual entropy in the presence of farther-neighbor interactions in kagome lattice Ising antiferromagnets (KIAFM).

In general, using MC to determine the residual entropy is a significant challenge requiring ad-hoc updates, a precise evaluation of the energy at all temperatures to allow for thermodynamic integration, and a good control of the finite-size scaling behavior. As an alternative, we turn to TNs; however, we argue that, in the presence of frustration and macroscopic ground-state degeneracy, standard algorithms fail to converge at low temperatures on the usual TN formulation of partition functions. Inspired by methods for constructing ground-state energy lower bounds, we propose a systematic way to find the ground-state local rule using linear programming. Characterizing the rules as tiles that can be tessellated to form ground states of the model gives rise to a natural contractible TN formulation of the partition function. This method provides a direct access to the ground-state properties of frustrated models and, in particular, allows an extremely precise determination of their residual entropy.

We then study two models inspired by artificial spin systems on the kagome lattice with out-of-plane (OOP) anisotropy. The first model is motivated by experiments on an array of chirally coupled nanomagnets. We argue that the farther-neighbor to nearest-neighbor couplings ratios in this system are much smaller than in the dipolar case,  $J_2/J_1$  being of the order of 2%. A comparison of the experimental correlations with the results of extensive TN and MC simulations shows that (1) the experimental second- and third-neighbor correlations are inverted as compared to those of a pure nearest-neighbor model at equilibrium (even with a magnetic field), and (2) second-neighbor couplings as small as 1% of the nearest-neighbor couplings will affect the spin-spin correlations even at fairly high temperatures.

Motivated by dipolar coupled artificial spin systems, we turn to the progressive lifting of the ground-state degeneracy of the KIAFM. We provide a detailed study of the ground-state phases of this model with up to third neighbor interactions, for arbitrary  $J_2, J_3$  such that  $J_1 \gg |J_2|, |J_3|$ ,

## Abstract

---

obtaining exact results for the ground-state energies. When all couplings are antiferromagnetic, we exhibit three macroscopically degenerate ground-state phases and establish their residual entropy using our TN approach. Furthermore, in the phase corresponding to the dipolar KIAFM truncated to third neighbors, we use the ground-state tiles to establish the existence of a mapping to the ground-state manifold of the triangular Ising antiferromagnet.

Keywords: condensed matter physics, Ising model, antiferromagnetism, kagome lattice, frustration, residual entropy, tensor networks, VUMPS, Monte Carlo, ground-state energy lower bounds

# Résumé

Dans les systèmes de spins, la frustration géométrique désigne l'impossibilité de minimiser simultanément tous les termes du Hamiltonien, ce qui donne souvent lieu à des fondamentaux macroscopiquement dégénérés et à une physique émergente à basse température. Dans cette thèse, en combinant des méthodes de réseaux de tenseurs (TN) à des méthodes de Monte Carlo (MC) et à des approches permettant de déterminer des bornes inférieures de l'énergie du fondamental, nous étudions des modèles d'Ising classiques frustrés à deux dimensions. Nous nous intéressons particulièrement à la détermination de l'entropie résiduelle lorsque des interactions à plus longue portée sont présentes dans des modèles d'Ising antiferromagnétiques sur le réseau kagomé (KIAFM).

En général, l'utilisation de MC pour déterminer l'entropie résiduelle est un défi important nécessitant des mises à jour ad-hoc, une évaluation précise de l'énergie à toutes les températures pour permettre l'intégration thermodynamique, et un bon contrôle des effets de taille finie. Nous explorons le potentiel des TNs comme alternative au MC. Dans un premier temps, nous remarquons qu'en présence de frustration et de dégénérescence macroscopique du fondamental, les algorithmes standards ne convergent pas lorsqu'ils sont appliqués à la formulation usuelle de la fonction de partition en termes de réseaux de tenseurs. Inspirés par des méthodes permettant de construire des bornes inférieures pour l'énergie du fondamental, nous proposons une approche systématique pour trouver la règle qui caractérise le fondamental en utilisant la programmation linéaire. Les fondamentaux du modèle peuvent être construits en pavant le réseau à l'aide de motifs qui correspondent à cette règle. Cela donne lieu à une formulation naturelle de la fonction de partition à l'aide d'un réseau de tenseurs qui peut être contracté. Cette méthode donne un accès direct aux propriétés des fondamentaux de modèles frustrés et, en particulier, permet de déterminer leur entropie résiduelle de manière très précise.

Nous étudions ensuite deux modèles inspirés par des systèmes de spin artificiels sur le réseau kagomé ayant une anisotropie hors du plan (OOP). Le premier modèle est motivé par des expériences menées sur un réseau de nano-aimants couplés par une interaction chirale. Nous fournissons des éléments suggérant que le rapport des couplages à longue portée au couplage entre premiers voisins est bien plus faible que dans le cas dipolaire,  $J_2/J_1$  étant de l'ordre de 2%. En comparant les corrélations expérimentales à des résultats détaillés issus de simulations TN et MC, nous montrons (1) que les corrélations expérimentales aux deuxièmes et

troisièmes voisins sont inversées par rapport à celles d'un modèle purement premiers voisins à l'équilibre (même en prenant en compte un champ magnétique), et (2) que des interactions aux deuxièmes voisins de l'ordre de 1% des interactions aux plus proches voisins affectent les corrélations même à des températures relativement élevées.

Motivés par des systèmes de spins artificiels avec couplages dipolaires, nous nous intéressons ensuite à la levée progressive de la dégénérescence du KIAFM. Nous effectuons une étude détaillée des phases du fondamental de ce modèle avec des couplages jusqu'aux troisièmes voisins, pour des valeurs arbitraires de  $J_2, J_3$  satisfaisant  $J_1 \gg |J_2|, |J_3|$ , et nous obtenons des résultats exacts pour l'énergie des fondamentaux. Lorsque tous les couplages sont antiferromagnétiques, nous décrivons trois phases macroscopiquement dégénérées dont nous déterminons l'entropie résiduelle à l'aide de notre approche de TNs. De plus, dans la phase correspondant au modèle dipolaire tronqué aux troisièmes voisins, nous utilisons les motifs décrivant le fondamental pour démontrer rigoureusement qu'il existe une relation avec l'ensemble des fondamentaux du modèle d'Ising triangulaire antiferromagnétique.

Mots-clés : matière condensée, modèle d'Ising, antiferromagnétisme, réseau kagomé, frustration, entropie résiduelle, réseaux de tenseurs, VUMPS, Monte Carlo, bornes inférieures pour l'énergie du fondamental

# Contents

<b>Acknowledgments</b>	<b>i</b>
<b>Abstract (English/Français)</b>	<b>iii</b>
<b>List of Figures</b>	<b>xi</b>
<b>List of Tables</b>	<b>xv</b>
<b>List of acronyms</b>	<b>xvii</b>
<b>Introduction</b>	<b>1</b>
<b>I Methods</b>	<b>11</b>
<b>1 Algorithms for classical Ising models</b>	<b>13</b>
1.1 Preliminary: dimer configurations . . . . .	13
1.1.1 Dimer mapping . . . . .	13
1.2 Monte Carlo simulations . . . . .	15
1.2.1 The algorithm . . . . .	16
1.2.2 Energy of the generalized dimer configurations . . . . .	19
1.3 Tensor networks for classical Ising models . . . . .	20
1.3.1 Partition functions as tensor network contractions . . . . .	21
1.3.2 Uniform matrix product states . . . . .	27
1.3.3 Tangent space and variational principle . . . . .	30
1.3.4 The VUMPS and multi-site VUMPS algorithms for MPOs . . . . .	34
1.4 Ground-state energy lower bounds . . . . .	39
1.4.1 Kaburagi and Kanamori’s method of inequalities . . . . .	39
1.4.2 MAX-MIN approach for ground state energy lower bounds . . . . .	45
1.4.3 Alternative approaches . . . . .	47
1.5 Summary . . . . .	48
<b>2 Contractible tensor networks for classical frustrated Ising models</b>	<b>49</b>
2.1 “Standard” construction . . . . .	51
2.1.1 Issue with the zero temperature limit . . . . .	51
2.2 Nearest-neighbor Ising antiferromagnet on the kagome lattice . . . . .	52

## Contents

---

2.2.1	Ground state . . . . .	52
2.3	Nearest-neighbor Ising antiferromagnet on the triangular lattice . . . . .	54
2.3.1	Ground state . . . . .	54
2.3.2	Hamiltonian tessellation . . . . .	55
2.4	Generic implementation . . . . .	58
2.4.1	Maximal lower bound . . . . .	58
2.4.2	Getting the most out of knowing the ground state energy . . . . .	59
2.4.3	Generic tensor network . . . . .	60
2.4.4	Testing for the saturation of the maximal lower bound . . . . .	61
2.4.5	Convergence at finite temperature . . . . .	61
2.5	Using symmetries . . . . .	62
2.5.1	Invariance under the cluster symmetry group . . . . .	62
2.5.2	An example . . . . .	64
2.6	Farther-neighbor Ising model on the kagome lattice . . . . .	65
2.6.1	Results . . . . .	66
2.6.2	Analysis of the ground-state tiles . . . . .	68
2.7	Summary and outlook . . . . .	70
	Statement of contribution . . . . .	72
 <b>II The role of farther-neighbor couplings</b>		<b>73</b>
 <b>3 Effect of very small farther-neighbor couplings in an artificial spin system</b>		<b>75</b>
3.1	Experiment: a kagome lattice of chirally coupled nanomagnets . . . . .	76
3.1.1	Experimental setup . . . . .	76
3.1.2	Micromagnetic simulations and effective model . . . . .	77
3.1.3	Experimental results . . . . .	83
3.2	Nearest-neighbor model . . . . .	84
3.2.1	Nearest-neighbor Ising antiferromagnet in zero field . . . . .	84
3.2.2	Nearest-neighbor Ising antiferromagnet in a field . . . . .	89
3.3	Next-nearest-neighbor Ising antiferromagnet . . . . .	93
3.4	Results in the $J_1 - J_2 - J_{3  }$ model . . . . .	97
3.4.1	Ground state of the $J_1 - J_2 - J_{3  }$ model with and without a field . . . . .	99
3.4.2	Effect of the temperature and spin-spin correlations . . . . .	103
3.5	Discussion . . . . .	109
3.6	Summary and outlook . . . . .	112
	Statement of contribution . . . . .	114
 <b>4 Progressive lifting of the KIAFM ground-state degeneracy</b>		<b>115</b>
4.1	Known results and special points . . . . .	117
4.1.1	$J_1 - J_2$ model . . . . .	117
4.1.2	Dipolar point in the $J_1 - J_2 - J_3$ model . . . . .	119
4.1.3	$J_1 - J_2 - J_{3  }$ model . . . . .	120



4.1.4	Dipolar ground state and low energy configurations . . . . .	121
4.2	Ground-state phase diagram . . . . .	123
4.2.1	Applying Kanamori's method . . . . .	123
4.2.2	Overview of the ground-state phase diagram for $J_1 \gg J_2, J_3$ . . . . .	125
4.3	Ferromagnetic farther-neighbor couplings and benchmark . . . . .	129
4.4	Chevrons phase . . . . .	132
4.4.1	$J_1 - J_2$ model . . . . .	132
4.4.2	Introducing a small $J_3$ coupling . . . . .	133
4.5	Pinwheels phase : a mapping to the triangular lattice Ising antiferromagnet . . . . .	136
4.5.1	Numerical results . . . . .	137
4.5.2	Mapping to the ground state of the TIAFM . . . . .	139
4.5.3	Consequences for the ground-state correlations in the pinwheels phase . . . . .	143
4.6	Strings phase and relation to the triangular lattice Ising antiferromagnet . . . . .	147
4.6.1	$J_2 = 0$ . . . . .	147
4.6.2	Overview of the strings phase . . . . .	149
4.6.3	TIAFM and strings on the honeycomb lattice . . . . .	151
4.6.4	Any string configuration on the honeycomb lattice maps to at least one ground state of the strings phase . . . . .	152
4.6.5	Any ground-state configuration of the strings phase maps to a string configuration on the honeycomb lattice . . . . .	155
4.7	Discussion and outlook . . . . .	156
<b>5</b>	<b>Summary and outlook</b>	<b>161</b>
	<b>Appendices</b>	<b>165</b>
<b>A</b>	<b>Complement on Monte Carlo</b>	<b>167</b>
A.1	A short introduction to Monte Carlo . . . . .	167
A.1.1	Markov Chain Monte Carlo methods . . . . .	167
A.1.2	Metropolis-Hastings algorithm . . . . .	168
A.1.3	Applications of the Metropolis-Hastings algorithm . . . . .	169
A.1.4	Computing the residual entropy via thermodynamic integration . . . . .	170
A.2	Probability table, zero-bounce and one-bounce solutions . . . . .	171
A.3	Proof of detailed balance for Alg. 1 and dealing with periodic boundary conditions . . . . .	173
A.4	Monte Carlo parameters . . . . .	175
A.4.1	Monte Carlo simulations parameters and remarks for Chapter 2 . . . . .	175
A.4.2	Monte Carlo simulations parameters for Chapter 3 . . . . .	178
<b>B</b>	<b>Complement on tensor networks</b>	<b>181</b>
B.1	Introduction to uniform MPSs . . . . .	181
B.2	Derivation of the tangent space projector . . . . .	184
<b>C</b>	<b>Complement on the Kanamori method of inequalities</b>	<b>187</b>
C.1	List of references . . . . .	187

## Contents

---

C.2	Relation between the MAX-MIN approach and Kanamori's polytope . . . . .	189
<b>D</b>	<b>Pseudocode for the linear program to find ground state tiles</b>	<b>193</b>
<b>E</b>	<b>Details related to the chirally coupled artificial spin systems</b>	<b>195</b>
E.1	Experiments . . . . .	195
E.2	Micromagnetic simulations . . . . .	196
E.3	More about the $J_1 - J_2 - J_{3  }$ model in zero field . . . . .	198
E.4	Detail of the $J_1 - J_2 - J_{3  } - h$ ground states . . . . .	199
<b>F</b>	<b>Ground-state phase diagrams</b>	<b>203</b>
E.1	Kanamori inequalities . . . . .	203
E.1.1	$J_1 - J_2 - J_{3  }$ models . . . . .	203
E.1.2	$J_1 - J_2 - J_{3  } - J_{3\star}$ models . . . . .	205
E.2	Ground-state phase diagrams . . . . .	206
E.2.1	$J_1 - J_2 - J_{3  }$ . . . . .	206
E.2.2	$J_1 - J_2 - J_3$ . . . . .	210
E.2.3	Comparison of the phase diagrams . . . . .	218
<b>G</b>	<b>Complementary plots for the <math>J_1 \gg J_2, J_3</math> model</b>	<b>221</b>
G.1	Residual entropy and phase boundaries . . . . .	221
G.2	State not belonging to the chevrons phase . . . . .	222
G.3	TIAFM spin-spin correlations . . . . .	222
	<b>Bibliography</b>	<b>227</b>
	<b>Curriculum Vitae</b>	<b>249</b>

# List of Figures

1	Macroscopic ground-state degeneracy on the triangular and kagome lattices. . . . .	3
2	Water ice and spin ice. . . . .	4
3	Definition of the couplings. . . . .	8
1.1	Mapping from an Ising model on the kagome lattice to a dimer model on the dice lattice. . . . .	14
1.2	Definition of the couplings. . . . .	15
1.3	The steps of the myopic dual worm algorithm. . . . .	18
1.4	Interaction paths in the dimer model. . . . .	20
1.5	1D Ising model partition function and tensor network. . . . .	21
1.6	2D Ising model partition function and tensor network: vertex model . . . . .	23
1.7	2D Ising model partition function and tensor network: face and dual. . . . .	26
1.8	Kaburagi and Kanamori's method on the $J_1 - J_2$ model. . . . .	42
1.9	Ground-state phase diagram of the $J_1 - J_2$ model. . . . .	43
1.10	Tiling on the kagome lattice. . . . .	46
2.1	Partition function for one site in CTMRG. . . . .	50
2.2	Standard tensor network construction for the Ising partition function on the triangular and kagome lattices. . . . .	51
2.3	Two similar tensor network constructions for the ground state of the kagome lattice Ising antiferromagnet. . . . .	53
2.4	Tensor network constructions for the ground state of the TIAFM. . . . .	55
2.5	Failure and success of the convergence of the VUMPS algorithm for the TIAFM. . . . .	56
2.6	Tensor network constructions for the ground state of the TIAFM, with weights. . . . .	57
2.7	Tessellation of spins on the kagome lattice. . . . .	58
2.8	Solving the $J_1 - J_2$ ground-state energy using symmetries. . . . .	65
2.9	Definition of the Hamiltonian for a $J_1 - J_2 - J_3$ model on the kagome lattice. . . . .	65
2.10	Residual entropy per site in a frustrated model converging to a third of the TIAFM entropy. . . . .	66
2.11	An example of a spin configuration in the ground state. . . . .	67
2.12	Monte Carlo results for the residual entropy as a function of the inverse linear system size. . . . .	67
2.13	The two types of tiles in the ground state of the $J_1 - J_2 - J_3$ model with ferromagnetic $J_1$ and antiferromagnetic $J_2$ and $J_3$ . . . . .	68

## List of Figures

---

2.14	Type II tiles and domain walls. . . . .	69
2.15	Tensor network construction to probe the rules for tiling type-II tiles. . . . .	70
3.1	Kagome lattice samples of chirally coupled nanomagnets. . . . .	77
3.2	Couplings and configurations for an effective model on a five-sites cluster. . . . .	78
3.3	Configurations of the regions with OOP and IP anisotropy on a triangle. . . . .	79
3.4	The value of the couplings obtained from the micromagnetic simulations. . . . .	81
3.5	Experimental short-range spin-spin correlations of 20 kagome samples. . . . .	82
3.6	Tensor network formulations for the partition function of the nearest-neighbor model on the kagome lattice. . . . .	85
3.7	Correlation length in the KIAFM ground-state manifold. . . . .	87
3.8	First few correlations in the KIAFM and comparison to the experiments. . . . .	88
3.9	Example of ground-state configurations of the KIAFM in a magnetic field $0 < h < 4J_1$ . . . . .	90
3.10	Correlation length of the KIAFM in a critical magnetic field. . . . .	91
3.11	Tensor network results for the magnetization of the KIAFM in a field. . . . .	92
3.12	Tensor network results for the correlations of the KIAFM in a field. . . . .	93
3.13	Tensor network results for the proportion of triangles of a given magnetization at $h = 1.6J_1$ . . . . .	94
3.14	Overview of the first few correlations for selected magnetic field in the KIAFM. . . . .	94
3.15	Overview of the behavior of the specific heat and entropy as a function of the temperature and $J_2$ . . . . .	96
3.16	Overview of the behavior of the first spin-spin correlations as a function of the temperature and $J_2$ . . . . .	97
3.17	Map of the descending order of the correlations as a function of $T/J_1$ and $J_2/J_1$ . . . . .	98
3.18	Candidate ground-state phase diagram for the farther-neighbor model in a magnetic field for $J_2 < \frac{1}{3}J_1$ . . . . .	101
3.19	Two ground-state configurations for the $J_1 - J_2 - J_{3  }$ model in the $m = 1/9$ plateau. . . . .	102
3.20	Qualitative behavior of the magnetization as a function of the field and temperature in the $J_1 - J_2 - J_{3  } - h$ model. . . . .	104
3.21	Overview of the behavior of the first few correlations as a function of the temperature for the values of $J_2$ and $J_{3  }$ from micromagnetic simulations. . . . .	104
3.22	Specific heat and residual entropy in the $m = 1/3$ plateau. . . . .	105
3.23	Spin-spin correlations in the $m = 1/3$ plateau. . . . .	105
3.24	Map of the descending order of the correlations as a function of $T/J_1$ and $h/J_1$ in the $J_1 - J_2 - J_{3  } - h$ model. . . . .	106
3.25	Behavior of the first few correlations in Region <b>B</b> . . . . .	108
3.26	Behavior of the first few correlations and the ratios of triangles in Region <b>C</b> . . . . .	108
4.1	Definition of the couplings. . . . .	117
4.2	Ground state of the dipolar Ising antiferromagnet on the kagome lattice. . . . .	118
4.3	Polytope from Kanamori's method of inequalities reduced for $J_{3  } = J_{3\star}$ . . . . .	124
4.4	Polytope from Kanamori's method of inequalities reduced for $J_1 \gg J_2, J_3$ . . . . .	126

4.5	Ground-state phase diagram of the $J_1$ - $J_2$ - $J_3$ model for $J_1$ antiferromagnetic and $ J_2 ,  J_3  < J_1/2$ . . . . .	127
4.6	Ground-state tiles in the two ordered phases. . . . .	130
4.7	Reminder: idea behind the tensor network construction . . . . .	130
4.8	Additional ground-state tiles at the phase boundary between the ordered phases when $J_3$ is zero across the hexagons. . . . .	130
4.9	Benchmark: residual entropy when $J_3 = 0$ across the hexagon. . . . .	131
4.10	Ground-state tiles for the $J_1$ - $J_2$ model. . . . .	132
4.11	$J_1$ - $J_2$ ground-state manifold: fluxes . . . . .	133
4.12	A ground state of the $J_1$ - $J_2$ model, different from the DKIAFM ground state. . .	134
4.13	Ground-state tiles in the chevrons phase. . . . .	135
4.14	Two ground states in the chevrons phase, different from the DKIAFM ground state. . . . .	135
4.15	Residual entropy per site of the chevrons phase from tensor network contractions. .	136
4.16	Monte Carlo snapshot in the pinwheels phase. . . . .	137
4.17	Residual entropy in the pinwheels phase. . . . .	138
4.18	The four types of ground-state tiles in the pinwheels phase. . . . .	139
4.19	Graphical proof that two empty hexagons cannot be next-nearest neighbors in the pinwheels phase. . . . .	141
4.20	Rhombi in the pinwheels phase. . . . .	142
4.21	Convention for labeling the sites of kagome to discuss the correlations in the pinwheels phase. . . . .	143
4.22	Spin-spin correlations in the pinwheels phase. . . . .	146
4.23	Additional tiles at $J_2 = 0$ . . . . .	148
4.24	The ground-state tiles in the strings phase . . . . .	149
4.25	Maximally flippable ground state of the strings phase. . . . .	150
4.26	A snapshot of a ground state in the strings phase. . . . .	151
4.27	Residual entropy per site of the $J_1$ - $J_3$ model. . . . .	152
4.28	String configurations and TIAFM . . . . .	153
4.29	Creating and moving strings in the strings phase . . . . .	154
4.30	Support to prove that the strings are well constructed in the strings phase. . . .	157
A.1	Periodic boundary conditions and reference for winding numbers. . . . .	174
A.2	High temperature expansion and specific heat. . . . .	176
A.3	Specific heat for independent runs. . . . .	176
A.4	Bootstrap analysis . . . . .	177
E.1	Optimization of the demagnetization protocol. . . . .	196
E.2	Micromagnetic simulations results for five-site clusters. . . . .	197
E.3	Overview of the behavior of the specific heat and entropy as a function of the temperature in the $J_1 - J_2 - J_{3  }$ model. . . . .	198
E.4	An example of a ground-state configuration for the $J_1 - J_2 - J_{3  }$ model. . . . .	199

## List of Figures

---

E.5	Magnetization as a function of the temperature for the $J_1 - J_2 - J_{3\parallel}$ model at $h = 6J_{3\parallel}$ .	200
E.6	Magnetization as a function of the temperature for the $J_1 - J_2 - J_{3\parallel}$ model at $h = 4(J_1 + J_2) - 6J_{3\parallel}$ .	200
E.7	Two ground-state configurations for the $J_1 - J_2 - J_{3\parallel}$ model in the $m = 5/9$ plateau.	200
E.8	Two ground-state configurations for the $J_1 - J_2 - J_{3\parallel}$ model in the $m = 17/27$ plateau.	201
E.1	Ground-state phases snapshots	205
E.2	Ground-state phases snapshots, for the $J_1 - J_2 - J_{3\parallel} - J_{3\star}$ model.	206
E.3	Extended ground-state phase diagram: $J_1 - J_2 - J_{3\parallel}$ .	209
E.4	Candidate ground-state phase diagram for the $J_1 - J_2 - J_3$ model.	210
E.5	Long-range ordered state for $J_1/2 > J_3 > J_1/4$ .	212
E.6	Macroscopically degenerate phase	213
E.7	Updated inequalities polytope.	214
E.8	Sub-extensive degeneracy for $J_1$ ferromagnetic and $J_3 > 3J_1/5$ .	216
E.9	Long-range ordered state giving an energy upper bound for phase 10B.	216
E.10	Updated candidate ground-state phase diagram for the $J_1 - J_2 - J_3$ models.	217
G.1	Residual entropy per site of the $J_1 - J_2$ model.	222
G.2	MC Snapshot in the $J_1 - J_2 - J_3$ model from tensor networks at the $J_2 = 2J_3$ point.	223
G.3	Residual entropy of the $J_1 - J_2 - J_3$ model from tensor networks at the $J_2 = 2J_3$ point.	223
G.4	Residual entropy of the $J_1 - J_2 - J_3$ model from tensor networks at the $J_2 = J_3$ point.	224
G.5	Residual entropy per site of the $J_1 - J_3$ model.	224
G.6	Example of configuration that does not belong to the chevrons phase.	225
G.7	Spin-spin correlations in the TIAFM ground-state manifold.	225

# List of Tables

2.1	Tensor network results obtained using VUMPS on the row-to-row transfer matrix	52
3.1	Experimental values for the first few spin-spin correlations.	83
3.2	Experimental values for the proportion of triangles with a given net magnetization.	83
3.3	First spin-spin correlations in the ground state of the KIAFM in zero field.	86
3.4	First spin-spin correlations in the ground state of the KIAFM in a field $0 < h/J_1 < 4$ .	89
3.5	First spin-spin correlations in the ground state of the KIAFM in a field $h = 4J_1$ .	90
3.6	First spin-spin correlations in the ground state of the $J_1 - J_2$ model on the kagome lattice.	95
3.7	Residual entropy in the ground state for $J_2 = J_{3  } \lesssim 0.2$ as a function of the magnetic field.	100
4.1	Summary of known results in the $J_1 - J_2 - J_3$ models.	118
4.2	Overview of the results	128
C.1	Compilation of ground-state determinations (Reproduced and completed).	189
E.1	Results of the micromagnetic simulations for five-site clusters.	197
E.1	Coefficients of the 10 relevant inequalities for $J_1 - J_2 - J_{3  }$ models on the kagome lattice.	204
E.2	The 9 Kaburagi and Kanamori corners for $J_1 - J_2 - J_{3  }$ models on the kagome lattice.	204
E.3	The 17 Kaburagi and Kanamori inequalities for $J_1 - J_2 - J_{3  } - J_{3\star}$ models on the kagome lattice.	207
E.4	The 21 Kaburagi and Kanamori corners for $J_1 - J_2 - J_{3  } - J_{3\star}$ models on the kagome lattice.	208
E.5	The 11 Kaburagi and Kanamori corners for $J_1 - J_2 - J_3$ models on the kagome lattice.	211





# List of acronyms

Throughout this thesis, we will use the following acronyms:

CTMRG	Corner transfer matrix renormalization group
DKIAFM	Dipolar kagome lattice Ising antiferromagnet
DMI	Dzyaloshinskii-Moriya interactions
HOTRG	Higher-order tensor renormalization group
(i)DMRG	(Infinite) density matrix renormalization group
IP	In-plane
(i)TEBD	(Infinite) time-evolving block decimation
KIAFM	(Nearest-neighbor) kagome lattice Ising antiferromagnet
KSI	Kagome spin ice
LP	Linear program
LRO	Long-range order
MC	Monte Carlo
MFM	Magnetic force microscopy
MPO	Matrix product operator
MPS	Matrix product state
OOP	Out-of-plane
PEPS	Projected entangled pair states
SVD	Singular-value decomposition
TIAFM	(Nearest-neighbor) triangular lattice Ising antiferromagnet
TN	Tensor network
TNR	Tensor network renormalization
TRG	Tensor renormalization group
VUMPS	Variational uniform matrix product state
XPEEM	X-ray photoemission electron microscopy



# Introduction

In 1920, the statistical mechanics book of Gibbs is only twenty years old, and quantum mechanics is in its infancy. Wilhelm Lenz, a physics theory professor at Hamburg University and former student of Sommerfeld, proposes to explain the Curie-Weiss law using a model in which magnetic moments are not able to rotate freely but are constrained to a certain axis, and can only take values plus or minus one [1]. In the hope of explaining ferromagnetism starting from microscopic interactions and motivated by this first success, Lenz and his student Ernst Ising introduce the following model<sup>1</sup>:

$$H = -J \sum_{\langle i, j \rangle} \sigma_i \sigma_j, \quad (1)$$

where the interactions  $J > 0$  between the local magnetic moments  $\sigma_i = \pm 1$  are only of nearest-neighbor range,  $\langle i, j \rangle$  describing nearest-neighbor pairs on the lattice. They hope that this simple microscopic law can explain the macroscopic properties of magnets; but Ising solves the linear chain exactly and shows that there is no spontaneous magnetization [3–5]. This is the origin of the now celebrated Ising model.

Part of the importance of the Ising model comes from the fact that it can be seen as a semiclassical approximation of Heisenberg’s model for quantum spins [6]

$$H = -J \sum_{\langle i, j \rangle} \hat{\mathbf{S}}_i \cdot \hat{\mathbf{S}}_j, \quad (2)$$

where the nearest-neighbor interaction arises from the overlap of the electronic wavefunctions on neighboring atoms and the Pauli exclusion principle<sup>2</sup>. Moreover, it is exactly solvable in a range of cases. Perhaps the most notable case is the development of Kramers and Wannier’s transfer matrix formalism<sup>3</sup> [9, 10] by Lars Onsager to solve the 2D square lattice Ising model. As we will see, the transfer matrix approach can be seen as one of the origins of tensor

---

<sup>1</sup>This modern expression of the model is actually due to Pauli [2].

<sup>2</sup>It seems that Lenz asked Ising two questions for his thesis: justify using interactions of nearest-neighbor range, and study analytically the three-dimensional Ising model [7]. With his model, Heisenberg answered the first question in 1928, four years after Ising finished his PhD. Physicists are still developing tools to answer the second question. (See also [8] for a history of the Ising model.)

<sup>3</sup>In the one dimensional case, they state “The task of finding the state sum can be reduced to finding the largest eigenvalue of some matrix.”

networks [11]. A number of other planar Ising models have been solved exactly [12–18] in the few years following Onsager’s and Kaufman’s solution to the model on the square lattice [19, 20], but it was understood only later why all planar translation invariant Ising models are exactly solvable [21]. The true importance of the Ising model comes from its behavior at the critical temperature, where the free energy of the model has a non-analytic behavior and the macroscopic behavior changes drastically from paramagnetism to ferromagnetism. In many ways, it is the archetypal model for the study of collective phenomena and phase transitions. Although the ideas of scale invariance, universality and renormalization group originate elsewhere, thanks to its apparent simplicity, the Ising model is the textbook example of these concepts. The three-dimensional version of the model still is of importance to this day, for instance as a challenging application of the conformal bootstrap [22]. In its generalized expression,

$$H = \sum_{(i,j)} J_{i,j} \sigma_i \sigma_j \quad (3)$$

and due to its simplicity, the Ising model also has applications in countless fields in and outside of physics. A non-exhaustive list includes the study of spin glasses [23, 24], of alloy thermodynamics [25], of solid-on-solid phase transitions [26], but also in the modeling of social dynamics [27] and economics [28].

In this thesis, we are interested in the properties of a particular family of Ising models, namely frustrated Ising models. The archetypal example is that of the triangular lattice Ising antiferromagnet (TIAFM), first studied by Wannier [14]. In this case, the interactions are assumed to be of nearest-neighbor range and antiferromagnetic ( $J > 0$ ). As Wannier underlines in his work, from the point of view of the partition function, ferromagnetism is not very different from antiferromagnetism on bipartite lattices in the absence of a field, and the ground state just has Néel long-range order (LRO). However, the triangular lattice is not bipartite, which results in a singular property of the ground state. Because of the impossibility to minimize the energy on each bond of a single triangle (Fig. 1a), the antiferromagnetic Ising Hamiltonian has six different ground states on this triangle. It is easy to see from Fig. 1b that the ground state of the model on a triangular lattice has a macroscopic ground-state degeneracy, characterized by a non-zero residual entropy per site:

$$S_{\text{TIAFM}} = \lim_{N \rightarrow \infty} \frac{1}{N} \ln \left( W_{\text{TIAFM}}^{(N)} \right) \geq \frac{1}{3} \ln(2), \quad (4)$$

where  $N$  is the number of triangular lattice sites, and  $W_{\text{TIAFM}}^{(N)}$  is the number of ground states of the model for a certain lattice size (growing exponentially with the size of the lattice). Using the transfer matrix formalism, Wannier and independently Houtappel [14–16] computed exactly the TIAFM residual entropy as

$$S_{\text{TIAFM}} = 0.323066... \quad (5)$$

Another lattice on which the Ising antiferromagnet has a macroscopic ground-state degeneracy

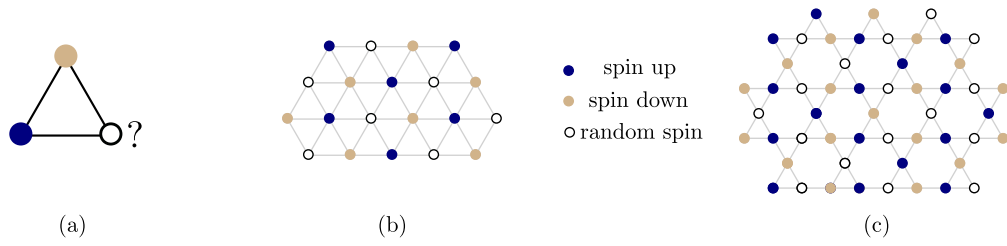


Figure 1 – Geometrical frustration. (a) The nearest-neighbor Ising antiferromagnet on a triangle has geometrical frustration: all three spin pairs cannot be antiferromagnetically aligned. This results in a macroscopic ground-state degeneracy of the model on (b) the triangular lattice and (c) the kagome lattice. The black circles correspond to sites on which the spin can be either up or down without changing the energy.

is the kagome lattice (Fig. 1c). It was first introduced in 1951 by Syozi [17], who found it as the star-triangle transformation of a decorated honeycomb lattice with one additional spin in the middle. It is of particular interest for the ferromagnetic Ising model because each site has the same number of nearest neighbors as in the square lattice, and Syozi used it to disprove the natural conjecture that the Curie point is solely determined by the coordination number [17]. It is Husimi who suggested the name kagome, which describes a pattern for traditional Japanese woven bamboo baskets. Syozi showed that there is no phase transition in the kagome lattice Ising antiferromagnet (KIAFM), and Kano and Naya computed its residual entropy [18]:

$$S_{\text{KIAFM}} = 0.501833... \quad (6)$$

The antiferromagnets on non-bipartite lattices such as the triangular and kagome lattices are often referred to as frustrated. More precisely, the term “frustration” was coined by Toulouse (inspired by a lecture from Anderson) in the context of spin glasses to describe the impossibility of satisfying simultaneously all exchange interactions in disordered systems [29]. He made the remark that frustration can also occur on perfectly regular lattices, referring to the TIAFM. The type of frustration arising in these systems is now described as *geometrical* frustration, referring to the inability to propagate to the whole lattice the favored local order [31–33]. As we just saw, the frustration leads to an accidental (not symmetry-induced) and typically macroscopic ground-state degeneracy. Interestingly, the presence of a macroscopic ground-state degeneracy does not imply any results for the decay of the spin-spin correlations in the ground state [34]. In fact, the TIAFM has algebraically decaying spin-spin correlations [35], while the KIAFM has a very short correlation length [36, 37]. The ground state can even have LRO, as is the case of the AF Potts model on the dice lattice [38].

The TIAFM and KIAFM are not the first historical instances of a macroscopic ground-state degeneracy. Indeed, ice, the solid phase of water, also possesses a residual entropy corresponding to a macroscopic ground-state degeneracy [39]. Pauling [40] very successfully explained the phenomenon. His result relies on the fact that in ice, the water molecules essentially keep their integrity and are arranged in such a way that each oxygen atom has four other

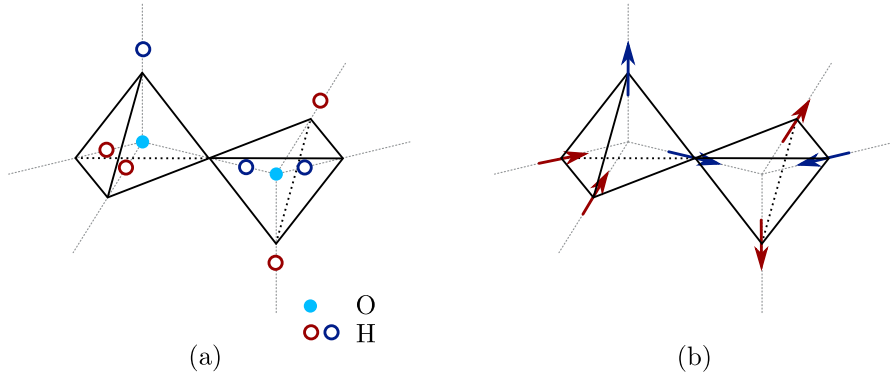


Figure 2 – Water ice and spin ice. (a) The arrangement of water molecules in ice, with the oxygen located at the center of the tetrahedron and the two hydrogen atoms in the direction of the tetrahedra symmetry axes. This results in a "two-close, two-far" ice rule. (b) Spin ice : the spins are aligned with the symmetry axis of the tetrahedra and are either pointing in or out of each given tetrahedron. The stabilized states respect a "two-in two-out" rule, an "ice-rule" by analogy with water ice.

nearest-neighbor oxygen atoms. Along a bond between two oxygen atoms there are two equilibrium positions for the hydrogen atom. This results in the Bernal and Fowler "ice rules" for the arrangements of the  $H^+$  ions in ice [41]: there should be only one proton per bond, and for each oxygen, there should be two protons near it, and two protons away from it (Fig. 2a). Pauling suggests a simple approximation: among the sixteen local configurations associated with each oxygen, only six respect the ice rules. Neglecting constraints on these configurations, the residual entropy of ice can be estimated as

$$S_{\text{Water}} = \frac{1}{N_O} k_B \ln \left( 2^{2N_O} \left( \frac{6}{16} \right)^{N_O} \right) \quad (7)$$

in very good agreement with the experimental result.

Water ice gave its name (by historical analogy) to a set of pyrochlore oxides which can be effectively described by Ising degrees-of-freedom on a lattice of corner-sharing tetrahedra, constrained to pointing along the direction connecting two tetrahedra centers, and coupled effectively by ferromagnetic dipolar interactions [42–44]. In these *spin ice* systems (typical instances being  $\text{Dy}_2\text{Ti}_2\text{O}_7$  and  $\text{Ho}_2\text{Ti}_2\text{O}_7$ ), the interactions lead to frustration and a two-in two-out rule for the Ising spins, i.e., an *ice rule* (Fig. 2). A number of compounds exhibit magnetic properties intrinsically related to an underlying kagome lattice structure, the most notable examples being spin glasses in jarosites [45, 46], quantum spin liquids<sup>4</sup> in pyrochlores

<sup>4</sup>In the rest of this work we often mention the notions of spin liquids, spin glasses and spin ice. It is important to realize that, because these terms are of historical origin and have often been introduced by analogy with one or the other feature of water, ice and glasses, they are not necessarily mutually exclusive. The term spin ice typically is connected to the existence of a rule analogous to the Bernal and Fowler rules in water ice; the term spin liquid often refers to the absence of symmetry breaking at zero temperature, and the spin glasses are often called so by analogy between the magnetic disorder in the spin glass and the positional disorder of conventional glass. All three notions require a more detailed definition than we can provide here and we refer the interested reader to

[46], and more recently in herbertsmithite [46, 49, 50] and kapellasite [51]. The important difference between these compounds and the spin ice is that the quantum fluctuations do not play a significant role in the latter.

This semi-classical aspect does not prevent spin-ice compounds from exhibiting fascinating emergent physics [52]. First, the long-range dipolar couplings stabilize an ice phase (a cooperative paramagnet), which survives down to very low temperature ([53] and references therein). Second, the spin ice materials are very sensitive to external magnetic fields [52], resulting in various collective behaviors depending on the field orientation, of which we will only mention the  $\langle 111 \rangle$  magnetization plateau [43, 54]. In this second case, the result relates to the fact that the pyrochlore lattice can be obtained by stacking kagome-lattice planes and decorating each kagome lattice triangle with an additional spin placed in alternance on one or the other side of the kagome plane. When the temperature and the field are low enough, the moments of these external spins are aligned with the field, but the moments in the kagome planes can keep respecting an ice rule of their own. Reducing the analysis to the kagome planes, in the presence of the field the problem is analogous to the KIAFM in a longitudinal field, which exhibits a magnetization plateau in the ground state. At values of the field corresponding to this plateau, the ground state of the model can in turn be mapped onto a model of hardcore dimers on the honeycomb lattice, yielding a residual entropy related to that of the TIAFM, and algebraic spin-spin correlations [52, 54–56]. It is common to refer to classical spin systems exhibiting a macroscopic ground-state degeneracy together with spin-spin correlations decaying to zero at long distances as *classical spin liquids* [48, 57, 58]. This term comes from the *quantum* spin liquids introduced by Anderson [59] for describing alternatives to magnetic long-range order in frustrated quantum antiferromagnets. The ice phase of spin ice, or the ground state of the TIAFM, despite their macroscopic degeneracy and being smoothly connected to the behavior of the model at high temperature, exhibit an algebraic decay of the spin-spin correlations; for the sake of precision one can then talk about *algebraic spin liquids*. An alternative name for these phases is *cooperative paramagnet*, a term introduced by Villain [60] to underline the distinction with a usual paramagnet where the correlations decay exponentially. A number of cooperative paramagnetic phases are also known as *Coulomb phases*, when the local constraint (for instance the ice rule) can be expressed as a conservation law for a flux that can be coarse-grained to an analogue of a divergence-free magnetic field [53, 61]. The notion of Coulomb phase or Coulomb gases is very general and such phases can be realized in a number of systems, see Refs. [61, 62]. Although in most systems the term Coulomb phase refers to the fact that defects on configurations that would otherwise belong to the ground-state manifold (local breakings of the gauge constraint) have effective Coulomb interactions of entropic origin [61], in the dipolar, pyrochlore spin ice, introducing charges via a “dumbbell” description of the spins shows that the dipolar spin-spin interaction results (approximately) in Coulomb interactions between the charges. In that case, the effective Coulomb interactions are of *energetic* origin [53, 63]. We thus see that in spin ice compounds the long-range interactions play a crucial role.

---

Refs. [47, 48] for in-depth discussions.

This leads us to a different kind of spin ice: artificial spin ice. These artificial systems are arrays of mesoscopic single-domain nanomagnets, with the great advantage that the local magnetic moments can be probed individually using magnetic microscopy techniques, such as magnetic force microscopy (MFM) or X-ray photoemission electron microscopy (XPEEM). The nanomagnets interact either via their magnetostatic fields or, in the case of connected nanomagnets, via exchange interactions. First introduced as an artificial analogue of spin ice in two dimensions [64, 65], the versatility of the designs and the relative ease of observation have made the study of artificial spin systems a field in its own right, with a domain of applications now far exceeding spin ice and even statistical spin systems (see for instance the recent reviews Refs. 57, 66).

The first artificial spin ice devices were athermal systems which required a demagnetization protocol to reach low energy states [67–70]; they nonetheless enabled the *direct* observation of an ice rule in kagome spin ice [71]. In the hope of studying at equilibrium statistical physics problems, one direction of pursuit for artificial spin systems has been the development of thermally active artificial spin systems [72–78], with developments still ongoing to allow one to probe very low energy states, for instance the long-range ordered ground states of kagome spin ice [79]<sup>5</sup>. There is a wide range of artificial spin systems geometries, involving periodic frustrated systems of elongated magnets with in-plane or out-of-plane anisotropy [80–82], periodic systems of x-y magnets, quasicrystals and even 3D structures, as summarized in Box 2 of Ref. 66. The flexibility in the design of these arrays makes them extremely useful for the study of frustration and emergent Coulomb phases in two dimensional systems [64, 69, 83].

If one is interested in studying at-equilibrium statistical mechanics of frustrated systems, artificial spin systems might not seem at first as a promising approach. Indeed, if the goal is to explore collective phenomena and exotic emergent models, it might seem that it will be a great challenge for the single spin flip dynamics which is available either through demagnetization protocols or thermalization procedure [57]. In fact, it was shown that in thermally active systems, the single-spin-flip dynamics does give access to states that correspond locally to low-temperature configurations but have clear signatures of out-of-equilibrium physics on a larger scale (see e.g. [84]). Moreover, one could expect the modelization with Ising Hamiltonians to be limited by structural disorder in the arrays or the large size of the nanomagnets in regards to the lattice spacing. Yet, great success has been achieved with simple descriptions ignoring the effect of disorder: in a great majority of the artificial spin systems, a modeling with the interactions of dipolar nature and corrections to the nearest-neighbor interactions is sufficient. It has even been suggested that the disorder in the switching fields of the arrays actually helps athermal systems to explore a variety of low-energy states [85–87]. The presence of the long-range couplings has been shown to play an essential role in the selection of the spin-spin correlations, even at fairly large effective temperatures, for instance in the case of the kagome ice (KSI) [71, 88] and the dipolar kagome Ising antiferromagnet (DKIAFM)

---

<sup>5</sup>Note that the question of whether these thermally active systems actually allow to reach better equilibrium than athermal systems with a demagnetization protocol is subtle, since both techniques only give access to single-spin-flip dynamics; see next paragraph.



[80, 81]. The in-plane kagome artificial spin ice is a particularly striking example of the essential effect of the long-range, dipolar interactions: indeed, while the model truncated to second-neighbor interactions and the full dipolar model have the same long-range ordered ground states, the nature of the phases at finite temperature and the transitions to these phases are fundamentally different due to the long-range interactions. This is well characterized again by introducing charges based on a dumbbell picture of the spins: the spin ice II phase is a spin liquid (it has a residual entropy) but there is an underlying charge order. Another manifestation of the presence of long-range dipolar couplings is the example of square ice, where a charge picture yields a background of charge zero vertices. Depending on the magnetic properties of the background (ordered or disordered) and on whether the pairs of charge defects are free to move, the defects can be identified to classical analogues of magnetic monopoles (as in spin ice) [57, 89]. By contrast, in the in-plane *kagome* ice, the background is charged; again, when one observes defects on this background they may be called “monopoles” when the charge background is disordered, and one can study the interactions between the charge defects on an ordered or disordered background [72, 89–92], yet, importantly, one should note that the underlying phase is not a Coulomb phase [57].

The case of the KSI and the DKIAFM is particularly interesting, because at the nearest-neighbor level the models are strongly related. Indeed, the nearest-neighbor version of the KSI is described by Ising spins  $\vec{s}_i = \sigma_i \vec{e}_i$  on the sites of the kagome lattice, with the unit vectors  $\{\vec{e}_i\}_{i=1,2,3}$  pointing in the directions connecting two triangle centers. By convention we can take  $\vec{e}_i$  to point always to the center of up triangles. Then

$$H_{\text{NN-KSI}} = -J_1 \sum_{\langle i,j \rangle} \vec{s}_i \cdot \vec{s}_j = \frac{J_1}{2} \sum_{\langle i,j \rangle} \sigma_i \sigma_j = \frac{1}{2} H_{\text{KIAFM}}. \quad (8)$$

The ferromagnetic nearest-neighbor KSI is therefore directly related to the antiferromagnetic nearest-neighbor Ising model with out-of-plane anisotropy, and in the absence of farther-neighbor interactions, they exhibit the same physics [80, 93, 94]. Yet, the farther-neighbor interactions differ and create two very different behaviors. In the KSI, Monte Carlo simulations predict a series of magnetic phase transitions and two very different spin ice phases [95–98]. In contrast, in the DKIAFM [81, 82], a first-order phase transition to a long-range ordered ground state has been established [82, 99, 100].

The fact that farther-neighbor interactions induce such a strong difference can be expected already by looking at the model with next-nearest-neighbor interactions. Indeed,

$$H_{J_1-J_2:\text{KSI}} = -J_1 \sum_{\langle i,j \rangle} \vec{s}_i \cdot \vec{s}_j - J_2 \sum_{\langle i,j \rangle_2} \vec{s}_i \cdot \vec{s}_j = \frac{J_1}{2} \sum_{\langle i,j \rangle} \sigma_i \sigma_j + \frac{J_2}{2} \sum_{\langle i,j \rangle_2} \sigma_i \sigma_j. \quad (9)$$

The next-nearest-neighbor interactions in KSI are antiferromagnetic ( $J_2 < 0$ ), resulting in effective *ferromagnetic* interactions in the corresponding Ising model, whereas the DKIAFM has all pair interactions antiferromagnetic. As a result, in the case of KSI, the next-nearest-neighbors interaction immediately lifts the macroscopic ground-state degeneracy to a long-

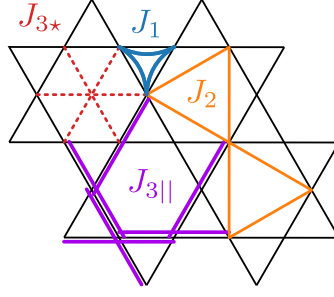


Figure 3 – Definition of the couplings in Eq. 10. There are two types of third-neighbor couplings based on the distance; we call them  $3*$  if they cross the hexagon and  $3||$  if they correspond to two nearest-neighbor bonds.

range ordered  $\sqrt{3} \times \sqrt{3}$  order [94, 101–103]. However, it is easy to see that it is not the case in the DKIAFM, where the ground-state degeneracy is only partially lifted, resulting in a finite residual entropy [93, 99, 102]. Therefore, part of this thesis is motivated by the question of how the macroscopic ground-state degeneracy of the nearest-neighbor model gets lifted in the DKIAFM. We will study the model with third-nearest-neighbor interactions, and show that even then the macroscopic ground-state degeneracy does not get completely lifted.

In artificial spin systems, the possibility of tuning the interactions has been explored since the very first work [64]. The historical approach has been to simply change the lattice spacing between nanomagnetic islands (a non-exhaustive list includes Refs. 64, 80, 104). In connected spin ice, the effective interactions can be tuned by varying the thickness and width of the nanomagnets, for instance in square ice [105, 106] or kagome ice [106], or yet by controlling the micromagnetic interactions via the creation of a hole at the interaction vertex [107]. Other approaches include the introduction of a soft ferromagnetic underlayer below the moments [108], magnetic bridges between the nanomagnets [109], or separating two sublattices of a square ice system (six-vertex model) by a small vertical distance [89, 110–112], allowing for the observation of the macroscopic degeneracy of square ice and of magnetic monopoles. Part of the work presented in this thesis is motivated by a particular approach to reinforcing the nearest-neighbor interactions in artificial spin systems with out-of-plane anisotropy: chirally coupled systems [113]. Conceptually, these systems rely on using interfacial Dzyaloshinskii-Moriya interactions (DMI) to create regions with out-of-plane anisotropy (OOP regions) connected by chiral domain walls to regions with in-plane anisotropy (IP regions). A strong nearest-neighbor antiferromagnetic coupling between OOP regions can be mediated by connecting them with IP regions. Motivated by these results, we will see that the short-range farther-neighbor to nearest-neighbor interaction ratios are significantly reduced in a kagome lattice chirally coupled system. However, we will show numerically that for at-equilibrium Ising models, even very small short-range interaction still affect the spin-spin correlations up to fairly high effective temperatures.

In the context of both works, we will be interested in studying models of the form:

$$H(\vec{\sigma}) = J_1 \sum_{\langle i,j \rangle_1} \sigma_i \sigma_j + J_2 \sum_{\langle i,j \rangle_2} \sigma_i \sigma_j + J_{3||} \sum_{\langle i,j \rangle_{3||}} \sigma_i \sigma_j + J_{3\star} \sum_{\langle i,j \rangle_{3\star}} \sigma_i \sigma_j - h \sum_i \sigma_i, \quad (10)$$

on the kagome lattice, where  $\langle i, j \rangle_k$  stand for the  $k^{\text{th}}$  nearest-neighbor couplings, as indicated in Fig. 3. Such Ising models with farther-neighbor interactions are often studied efficiently using Monte-Carlo simulations, and we will discuss a particular algorithm introduced in Ref. 114 that we will apply to some special cases of Eq. 10. Determining the ground-state phase diagram of classical frustrated spin systems with farther-neighbor interactions can be challenging and typically requires constructing ground-state energy lower-bounds as a complement to the Monte-Carlo results. In order to prove that the Monte Carlo simulations reach the ground state, we will discuss techniques to obtain such lower bounds. Additionally, another numerical technique has been established over the last twenty years as a tool for the study of statistical mechanics of lattice models : tensor network renormalization group techniques. Although tensor networks are perhaps best known as support for a modern formulation of White’s Density Matrix Renormalization Group (DMRG) [115–118], producing outstanding results in the study of 1D quantum systems ([119, 120] and references therein), and, in the form of projected-entangled pair states (PEPS) as a natural support for quantum spin liquid states in 2D quantum systems [121–124], their origin can in fact be traced back to Kramer and Wannier’s transfer matrix, introduced for the study of the classical Ising models [9, 10, 125]. It is therefore not surprising that tensor networks have also had a lot of success in the study of classical statistical mechanics in two-dimensional (2D) and three-dimensional (3D) spin systems (selected examples are [126–133] for the 2D case and [134–140] for the 3D case). As we will see, the essential idea relies on writing the partition function as a tensor network that can then be contracted (approximately) using standard contraction algorithms (TRG [141–143], TNR [144, 145], CTMRG [146, 147], VUMPS [148–151] or (i)TEBD [152–154]). However, we will see that the stability of these algorithms can depend on the precise formulation of the tensor network. We will discuss a challenge faced by the “standard” approach to the tensor network formulation of the partition function of frustrated Ising models, and suggest a solution that we will then apply to some of the models with farther-neighbor interactions that we motivated above.

The rest of this thesis is organized as follows. Chapter 1 is dedicated to an introduction to three existing methods for studying Ising models, including a Monte Carlo algorithm designed for short-range geometrically frustrated Ising models [114], a description of the VUMPS algorithm [148, 149, 151] and a discussion of methods to build ground-state energy lower bounds [25, 155–158]. In Chapter 2, relying extensively on Ref. 159, we describe the convergence issue associated with the contraction of the standard tensor network associated with classical spin systems. We use well-known approaches for ground-state energy lower bounds to propose an alternative formulation of the partition function of classical frustrated Ising models as contractible tensor networks. We apply this method to the study of ground state properties, and describe an extension to finite temperature.

Part II of this thesis focuses on the effect of short-range farther-neighbor couplings in frustrated Ising models on the kagome lattice, applying the methods of Part I. Chapter 3 is motivated by experimental results obtained for the spin-spin correlations in a kagome lattice of chirally coupled nanomagnets [113]. In this Chapter, following closely Ref. 160, we discuss how spin-spin correlations of the kagome lattice nearest-neighbor antiferromagnetic Ising model in a field are affected by the presence of extremely small farther-neighbor couplings. In Chapter 4, we study the partial lifting of the macroscopic ground-state degeneracy induced by farther-neighbor couplings on the nearest-neighbor Ising antiferromagnet on the kagome lattice, making connections with the ground state of the TIAFM and the DKIAFM. Finally, in Chapter 5 we summarize the main results of this thesis and give an outlook.

## Methods **Part I**



# 1 Algorithms for classical Ising models

The purpose of this chapter is to introduce a common background relevant to all the other chapters of this thesis. We start by introducing a very useful alternative description of the spin configurations on the kagome lattice as dimer configurations on the dice lattice. Then, we present a Monte Carlo algorithm designed specifically for short-range frustrated models on the kagome and triangular lattices [114]. We proceed with an introduction to tensor networks for classical spin systems and a presentation of the variational uniform matrix product state algorithm (VUMPS) which will be used throughout this thesis [148, 149, 151]. Finally, we discuss established methods for computing lower bounds for the ground-state energy of classical spin systems [25, 155–158, 161].

## 1.1 Preliminary: dimer configurations

### 1.1.1 Dimer mapping

We first introduce a mapping from configurations of Ising spins on a planar lattice (e.g. the kagome or triangular lattice)  $\mathcal{L}$  to configurations of dimers on its dual lattice (e.g. the dice lattice or the honeycomb lattice)  $\mathcal{L}^*$ , which is obtained by associating a vertex to each face of  $\mathcal{L}$  and an edge to each edge of  $\mathcal{L}$ . The dimer mapping is defined by

$$d_{b_{i,j}} = \sigma_i \sigma_j = \begin{cases} 1 & \text{if } \sigma_i = \sigma_j (\rightarrow \text{“there is a dimer”}) \\ -1 & \text{if } \sigma_i = -\sigma_j (\rightarrow \text{“there is no dimer”}) \end{cases} \quad (1.1)$$

where  $b_{i,j}$  is the bond of the dual graph lying between the nearest-neighbor sites  $i$  and  $j$  of the original graph, as shown in Fig. 1.1. If the bond variable  $d_{b_{i,j}}$  is positive, we say that there “is” a dimer on the bond. On the triangular lattice, this mapping goes back to a remark by Kasteleyn relating the behavior of dimers on the honeycomb lattice to the models of spins on the triangular lattice [162] and the work of Nienhuis, Hilhorst and Blöte [26, 62]. It is a two-to-one mapping, corresponding to a global spin flip which does not change the dimer configuration. To be able to map back from dimer configurations to spin configurations,

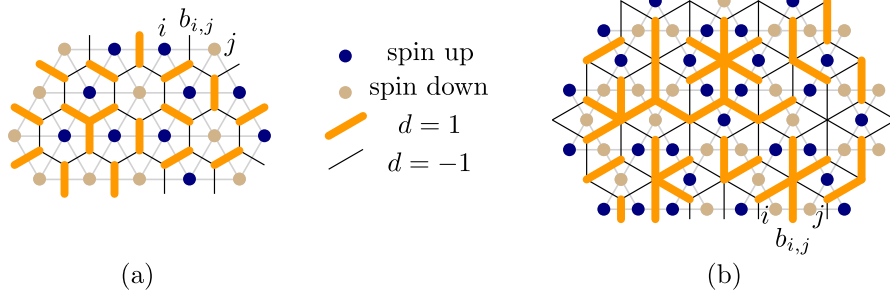


Figure 1.1 – Definition of the dimer configuration from the spin configuration. For a spin configuration defined on the direct lattice (in grey), the dimer configuration on the dual lattice (in black) is defined as in Eq. 1.1. We place an orange segment on the dual lattice when the dimer variable is positive. (a) Spin configuration on the triangular lattice and corresponding dimer configuration on the dual honeycomb lattice. (b) Spin configuration on the kagome lattice and corresponding dimer configuration on the dual dice lattice. For a dimer configuration to correspond to a spin configuration, it has to satisfy the constraints that the number of dimers touching a dual-lattice vertex with odd-coordination has to be odd, while for even-coordinated vertices, the number of dimers has to be even.

some constraints have to be added on the dimer configurations. These constraints come from considering closed loops defined on the direct lattice. If we consider a vertex  $v$  of the dual lattice, corresponding to a face of the original lattice, and we label with  $\{b(v)\}$  the dual bonds connected to this site, we must have

$$\prod_{b \in \{b(v)\}} d_b = 1. \quad (1.2)$$

to enforce that the spin configuration is consistent on an elementary loop on the direct lattice circling around the (dual) vertex  $v$ . This imposes that odd-coordinated vertices of the dual lattice (e.g. corresponding to triangles in the kagome lattice) have to be occupied by an odd number of dimers while even-coordinated vertices (corresponding to hexagons in the kagome lattice) have to be occupied by an even number of dimers. In the case of open boundary conditions, this condition is sufficient to enforce the consistency of the spin configuration on larger loops, since these can be seen as a combination of the elementary loops. If the boundary conditions are periodic, additional non-local constraints must be enforced: since an empty dual bond separates two spins of opposite signs, a loop defined on the direct lattice and winding the torus must cross an even number of empty dual bonds.

This mapping is especially useful in the case of the TIAFM because, in that case, any spin configuration belonging to the ground state maps to a *hardcore* dimer model on the honeycomb lattice; that is, each site on the honeycomb lattice has to be occupied exactly once, corresponding to the fact that in the ground state, no triangle can have all three spins pointing in the same direction. From this, one can recover the residual entropy of the TIAFM by using Kasteleyn's theorem relating the number of hardcore dimer configurations to the determinant of a matrix [162]. In the ground state of the KIAFM, this dimer mapping is not hardcore: the



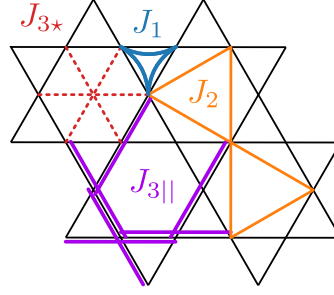


Figure 1.2 – Definition of the couplings in Eq. 1.3. There are two types of third-neighbor couplings based on the distance; we call them  $3\star$  if they cross the hexagon and  $3||$  if they correspond to two nearest-neighbor bonds.

six-coordinated vertices can be shared among dimers.

## 1.2 Monte Carlo simulations

In this section, we describe in detail the dual worm algorithm of Rakala and Damle [114], which will be used throughout this thesis.

As mentioned in the introduction, in most of this thesis we will be interested in studying models of the form:

$$H(\vec{\sigma}) = J_1 \sum_{\langle i,j \rangle_1} \sigma_i \sigma_j + J_2 \sum_{\langle i,j \rangle_2} \sigma_i \sigma_j + J_{3||} \sum_{\langle i,j \rangle_{3||}} \sigma_i \sigma_j + J_{3\star} \sum_{\langle i,j \rangle_{3\star}} \sigma_i \sigma_j, \quad (1.3)$$

on the kagome lattice, where  $\langle i,j \rangle_k$  stand for the  $k^{\text{th}}$  nearest-neighbor couplings, as indicated in Fig. 1.2.

In Ref. 114, two rejection-free dual worm algorithms are introduced. They are designed for simulating frustrated two-dimensional Ising antiferromagnets. The focus is on the triangular lattice Ising antiferromagnet with farther-neighbor, finite-range interactions; however, it is mentioned that one of the two algorithm, the *myopic dual worm algorithm* is easily generalizable to the kagome lattice Ising antiferromagnet with up to third-nearest-neighbor couplings ( $J_{3||}$  in Fig. 1.2). This is the algorithm we present here, with a very slight generalization to include both types of third-nearest-neighbor couplings on the kagome lattice ( $J_{3||}$  and  $J_{3\star}$  in Fig. 1.2).

The dual worm algorithm of Ref. 114 is directly inspired from a similar algorithm [163, 164] introduced as an alternative to the Wolff [165] and the Swendsen-Wang [166] algorithms for non-frustrated Ising models.

The key point of the myopic dual worm algorithm is the result that two dimer configurations  $\mathcal{C}_1$  and  $\mathcal{C}_2$  that differ only by the configurations of the dimers on a single, closed loop on the

dual lattice correspond to two spin configurations  $\mathcal{S}_1$  and  $\mathcal{S}_2$  that differ by flipping the cluster of spins encircled by the loop. Thus, if one can use the mapping from spin configurations to dimer configurations to rewrite the Hamiltonian in Eq. 1.3 as a Hamiltonian for dimer configurations, and then efficiently propose loop updates in the dimer configuration space, then one effectively has a way of proposing cluster updates in the original spin problem on kagome. What Ref. 164 proposes is to build loops as worm updates, i.e. growing a string of flipped dimer variables constructed by respecting a *local* version of the detailed balance condition such that when the head of the worm meets its tail, creating a loop, the update can immediately be accepted. In a general importance sampling Monte Carlo algorithm we can decompose the transition matrix  $\mathcal{P}$  describing the Markov Chain update process into a *generation probability* and an *acceptance probability* according to

$$\mathcal{P}(\vec{\sigma}'|\vec{\sigma}) = \begin{cases} g(\vec{\sigma}'|\vec{\sigma}) A(\vec{\sigma}'|\vec{\sigma}) & \text{if } \vec{\sigma}' \neq \vec{\sigma} \\ 1 - \sum_{\vec{\sigma}'' \neq \vec{\sigma}} \mathcal{P}(\vec{\sigma}''|\vec{\sigma}) & \text{if } \vec{\sigma}' = \vec{\sigma} \end{cases} \quad (1.4)$$

where  $g(\vec{\sigma}'|\vec{\sigma})$  is the probability that the spin configuration  $\vec{\sigma}'$  is generated from the configuration  $\vec{\sigma}$ , and where  $A(\vec{\sigma}'|\vec{\sigma})$  is the probability that  $\vec{\sigma}'$  is accepted knowing that  $\vec{\sigma}$  is the previous configuration of the Markov Chain. The dual worm algorithm relies on imposing the detailed balance condition only through  $g(\vec{\sigma}'|\vec{\sigma})$ , such that  $A(\vec{\sigma}'|\vec{\sigma}) = 1$  if  $g(\vec{\sigma}'|\vec{\sigma}) \neq 0$ .

The algorithm uses *directed* worm updates, in the sense that at each step, the probability that the head of the worm comes back on its tracks and erases the last segment of the worm is minimized (often referred to as the bounce probability) [164, 167–171]. In this sense, it is also inspired from the directed loop updates in Quantum Monte Carlo (QMC) [172–174]<sup>1</sup>.

### 1.2.1 The algorithm

Let us start with describing the algorithm for the worm construction.

In order to satisfy detailed balance in a local way, the worm is constructed by alternating two types of steps: the *probabilistic* step, where the direction in which the worm's head is moved is chosen with probabilities depending on the local dimer configuration, and the *myopic* step, where the direction where the worm's head is moved is chosen with uniform probabilities (only forbidding backtracking). This makes use of the fact that both in the triangular and kagome lattice cases, the dual lattice is bipartite. We can thus split each dual lattice into two subsets of vertices, which we will name the *entry/exit* sites and the *vertex* sites. In the honeycomb lattice case, the two subsets are equivalent and can be chosen arbitrarily, whereas in the dice lattice case, we select the six-coordinated sites as entry/exit sites and the three-coordinated sites as vertex sites, as illustrated in Fig. 1.3.

---

<sup>1</sup>In the earlier papers, worm updates in the spirit of the algorithm we present here are referred to as *geometrical* worm updates [167], by contrast with the worm updates approach based on the high-temperature expansion of the partition function [163] where worm updates are created on the original lattice.

**Algorithm 1** Myopic dual worm algorithm.

---

```

1: function WORM UPDATE( $\vec{d}$ )
2:   Randomly select an entry site  $e^{(1)}$  on the dual lattice.
3:    $n \leftarrow e^{(1)}$ 
4:   Among the  $n_d$  dual bonds sharing  $e^{(1)}$ , randomly select one with uniform probability
      $1/n_d$ .
5:   Name this dual bond  $b^{(1)}$ , and  $v^{(1)}$  the other dual site it is connected to.
6:    $v^{(1)}$  is now the head of the worm.
7:   while head on a vertex site  $v^{(k)}$  or head on an entry site  $e^{(k)} \neq n$  do
8:     if head on a vertex site then  $\triangleright$  probabilistic step
9:       The head is on  $v^{(k)}$  and it arrived there from  $e^{(k)}$  through the dual bond  $b^{(k)}$ .
10:      Considering the local dimer configuration, check the probability table  $T^{v^{(k)}}$ .
11:       $b_1, b_2, b_3 \leftarrow$  the three dual bonds connected to  $v^{(k)}$ 
12:      With probability  $T_{b^{(k)}, b_i}^{v^{(k)}}$ :  $b^{(k+1)} \leftarrow b_i$ .
13:       $d_{b^{(k)}} \leftarrow -d_{b^{(k)}}$ .  $\triangleright$  Flip the dimer variable on  $b^{(k)}$ .
14:       $d_{b^{(k+1)}} \leftarrow -d_{b^{(k+1)}}$ .  $\triangleright$  Flip the dimer variable on  $b^{(k+1)}$ .
15:       $e^{(k+1)} \leftarrow$  other site connected to  $b^{(k+1)}$ .
16:     else  $\triangleright$  myopic step
17:       The head is on  $e^{(k)}$  and it arrived there from  $v^{(k-1)}$ .
18:        $e^{(k)}$  is connected to  $n_d - 1$  other vertices.
19:       Randomly select one among the  $n_d - 1$  other sites, it will be  $v^{(k)}$ .  $\triangleright$  uniform prob.
20:        $b^{(k)} \leftarrow (e^{(k)}, v^{(k)})$ 
21:    $W_1, W_2 \leftarrow$  winding numbers of the worm update.
22:   return  $\vec{d}, W_1, W_2$ 
23: function MAIN( $\vec{\sigma}_m$ )
24:    $\vec{d} \leftarrow$  SPIN TO DIMER MAPPING( $\vec{\sigma}_m$ )
25:    $(\vec{d}, W_1, W_2) \leftarrow$  WORM UPDATE( $\vec{d}$ )
26:   if OBC then
27:      $\vec{\sigma}_{m+1} \leftarrow$  DIMER TO SPIN MAPPING( $\vec{d}$ )
28:   else
29:     while  $\text{mod}(W_1, 2) \neq 0 \parallel \text{mod}(W_2, 2) \neq 0$  do
30:        $(\vec{d}, W_1^{\text{new}}, W_2^{\text{new}}) \leftarrow$  WORM UPDATE( $\vec{d}$ )
31:        $W_1 += W_1^{\text{new}}, W_2 += W_2^{\text{new}}$ 
32:    $\vec{\sigma}_{m+1} \leftarrow$  DIMER TO SPIN MAPPING( $\vec{d}$ )
return  $\vec{\sigma}_{m+1}$ 

```

---

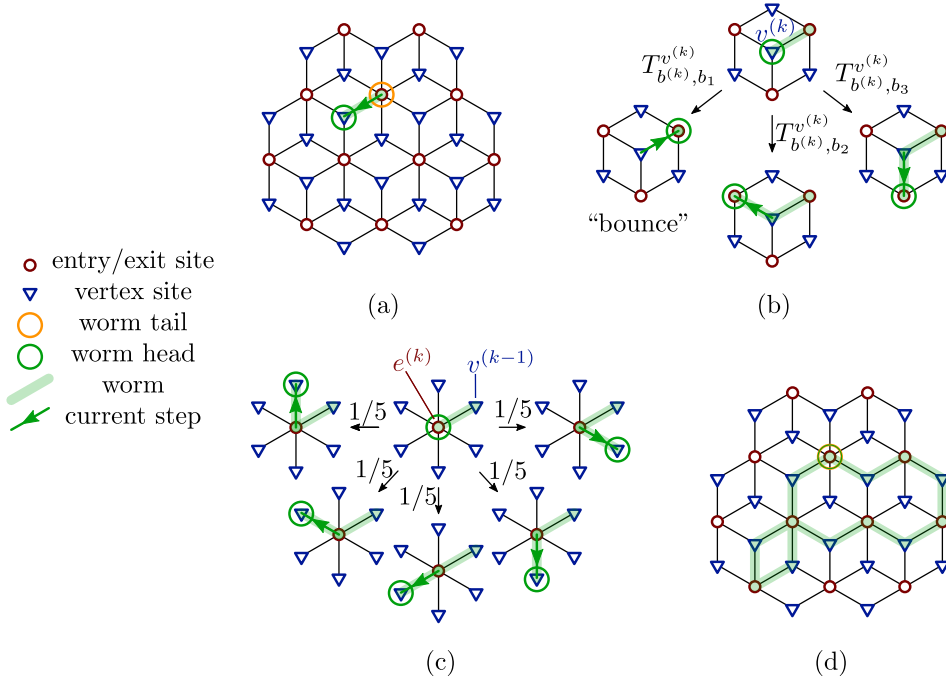


Figure 1.3 – The steps of the myopic dual worm algorithm on the dice lattice. (see also the pseudocode in Alg. 1). (a) Randomly selecting an entry site and one of the neighboring vertex sites. (b) Probabilistic step: the head of the worm is moved with weighted probabilities contained in the probability table  $T^{v^{(k)}}$ . (c) Myopic step : the head of the worm is moved without taking into account the local configuration. (d) When the worm's head arrives on the starting site, the worm closes.

The steps of the myopic dual worm algorithm are described in Fig. 1.3, and the pseudocode is given in Alg. 1. The probabilistic step of the algorithm occurs when the head of the worm is on a vertex site, and the myopic step when the head is on an entry/exit site. In Fig. 1.3a, an entry site is chosen randomly with uniform probabilities. It will be the worm's tail. The worm's head is moved with uniform probability to one of the six neighboring vertex sites. In Fig. 1.3b, we show the probabilistic step. At a vertex site, the head of the worm is moved to one of the three neighboring exit sites with the weights given by the probability table  $T^{v^{(k)}}$ , which depends on the local configuration of the dimers. There is some freedom in selecting the probability table, and it is constructed in such a way that the bounce probability (backtracking) is minimized. The myopic step is shown in Fig. 1.3c: at an entry site, the head of the worm is moved to one of the neighboring vertex sites with uniform probability but without backtracking. Finally, when the worm closes (Fig. 1.3d), the update is accepted provided that the periodic boundary conditions of the spin model are respected.

### 1.2.2 Energy of the generalized dimer configurations

During the process of the dual worm construction, the dimer configuration violates the dimer rules (Eq. 1.2) at the tail of the worm as well as at the head of the worm. To build the worm by respecting a local detailed balance condition, the energy of the dimer configuration must be defined without mapping back to a spin configuration, and ignoring the “infinite cost” of breaking the generalized dimer rules. Therefore, we want to define a Hamiltonian for the generalized dimer model, which reduces to the spin model Hamiltonian when the dimer configuration respects the dimer rules. Considering two (direct) lattice sites  $i_0$  and  $i_l$  connected by a path of nearest-neighbor bonds

$$\Gamma = \{(i_0, i_1), (i_1, i_2), \dots, (i_{l-1}, i_l)\} \quad (1.5)$$

on the direct lattice, it is trivial that

$$\sigma_{i_0} \sigma_{i_l} = \prod_{k=0}^{l-1} d_{b_{i_k, i_{k+1}}} = \prod_{\alpha \in \Gamma} d_{b_\alpha}. \quad (1.6)$$

This allows one to rewrite Eq. 1.3 as

$$H(\vec{d}) = J_1 \sum_{\Gamma_1} d_{b_{\Gamma_1}} + J_2 \sum_{\Gamma_2} \prod_{\alpha \in \Gamma_2} d_{b_\alpha} + J_{3||} \sum_{\Gamma_{3||}} \prod_{\alpha \in \Gamma_{3||}} d_{b_\alpha} + \frac{J_{3\star}}{2} \sum_{\Gamma_{3\star}} \prod_{\alpha \in \Gamma_{3\star}} d_{b_\alpha}, \quad (1.7)$$

where the interaction paths  $\Gamma_1$  to  $\Gamma_{3\star}$  are defined in Fig. 1.4, where  $\alpha$  goes through the (direct lattice) site pairs of the path, and where  $d_{b_\alpha}$  is the value of the dimer variable on the bond  $b_\alpha$  of the dual lattice, as in Eq. 1.1. The nearest-neighbor interaction results in paths  $\Gamma_1$  that are just one pair of nearest-neighbor sites, and therefore  $d_{b_{\Gamma_1}}$  is the value of the dimer variable separating those two sites.  $\Gamma_2$  ( $\Gamma_{3||}$ ) are paths made of two pairs of sites and correspond to nearest-neighbor (next-nearest-neighbor) dimer-dimer interactions, while the  $\Gamma_{3\star}$  interaction paths correspond to three-dimer interactions. For this last term, the coupling is divided by two, because, as shown in Fig. 1.4, we separate the interaction across the hexagons into two paths passing on either side of the hexagon center. Formulated this way, it is transparent that the definition of the Hamiltonian for the dimer model can be in principle generalized to Ising models with finite-range pair interactions.

In general, the weight of a given dimer configuration  $\vec{d}$  will be given by

$$\begin{aligned} \mathcal{W}(\vec{d}) &= \frac{1}{\mathcal{Z}} e^{-\beta H(\vec{d})} \\ &= \frac{1}{\mathcal{Z}} \prod_{\Gamma_1} \left( e^{-\beta J_1 d_{b_{\Gamma_1}}} \right) \prod_{\Gamma_2} \left( e^{-\beta J_2 (\prod_{\alpha \in \Gamma_2} d_{b_\alpha})} \right) \prod_{\Gamma_{3||}} \left( e^{-\beta J_{3||} (\prod_{\alpha \in \Gamma_{3||}} d_{b_\alpha})} \right) \prod_{\Gamma_{3\star}} \left( e^{-\beta \frac{J_{3\star}}{2} (\prod_{\alpha \in \Gamma_{3\star}} d_{b_\alpha})} \right). \end{aligned} \quad (1.8)$$

With this definition, all the necessary elements are in place for implementing the dual worm algorithm. In Appendix A.2, we give more detail about the implementation of the probability table to minimize the bounce probability. In Appendix A.3 we give a proof of detailed balance

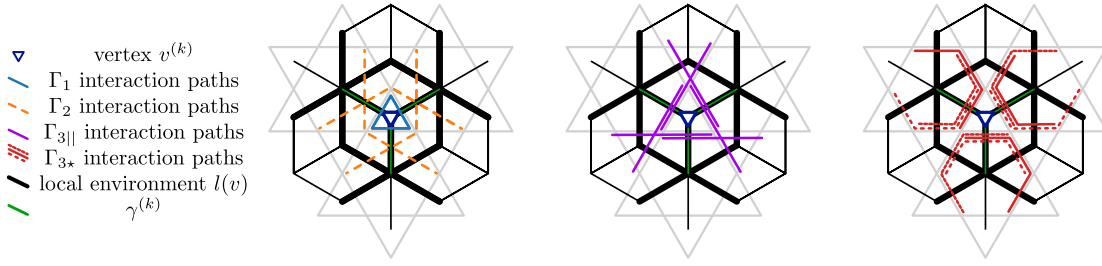


Figure 1.4 – Interaction paths in the dimer model, used in Eq. 1.7. Here, we illustrate some of the nearest, next-nearest and 3<sup>rd</sup> nearest neighbor interaction paths playing a role when computing the probability table at vertex  $v^{(k)}$ . The probability table for the propagation of the worm from a vertex  $v^{(k)}$  gives the probabilities to proceed on the three bonds connected to  $v^{(k)}$  (denoted by  $\gamma^{(k)}$ ). As discussed in Appendix A.2, to build it, one has to take into account the dimer configuration in the local environment  $l(v)$  (in bold black), corresponding to all the dual bonds which share an interaction path with one of the bonds in  $\gamma^{(k)}$ .

for Algorithm 1 and discuss how the periodic boundary conditions have to be managed. As a final remark, one might wonder whether this algorithm applies to any Ising model on a non-bipartite lattice whose dual lattice is bipartite; indeed, it clearly applies to an Ising model on the triangular lattice, whose dual lattice is honeycomb [114]. One instance of such an application is a recent work on the cubic lattice [175]. In general the required ingredients in this method besides the dual lattice being bipartite is the possibility of doing a step with minimal bounce on one of the two (dual) sublattices.

### 1.3 Tensor networks for classical Ising models

To introduce tensor networks for classical spin systems and the associated notation, one natural path to follow starts with the 1D and 2D classical Ising models and their formulation in terms of transfer matrices. This is also how tensor networks for classical spin systems have arisen historically, with the first transfer matrix approaches introduced to study the Ising model in the 1940s and 1950s [9, 10, 14, 15, 17–20]<sup>2</sup>.

In the following we essentially follow the notes by Nishino [183, 185] as well as the recent review on tensor networks by Okunishi, Nishino and Ueda [125] to introduce tensor networks for statistical mechanics. The discussion of the tangent space and the VUMPS algorithm is based on the lecture notes by Vanderstraeten, Haegeman and Verstraete [150]. More general introductions to tensor networks can be found in Refs. 119, 186 for historical reviews of

<sup>2</sup>This was followed by the introduction of the corner transfer matrix (CTM) and the first steps towards tensor network approaches in statistical mechanics, pioneered by Baxter in the 1970s-1980s ([11, 176, 177], [178] and references therein); the famous AKLT result [179]; the development of DMRG by White [115, 116]; the notion of matrix product state [180]; and finally the connection between CTM and DMRG made by Nishino and Okunishi [146, 181, 182]. In the 2000s, the introduction of a wide variety of tensor product constructions and of contraction algorithms gave rise to the field of tensor networks. See Refs. 125, 183, 184 for a detailed discussion of the history of tensor networks.

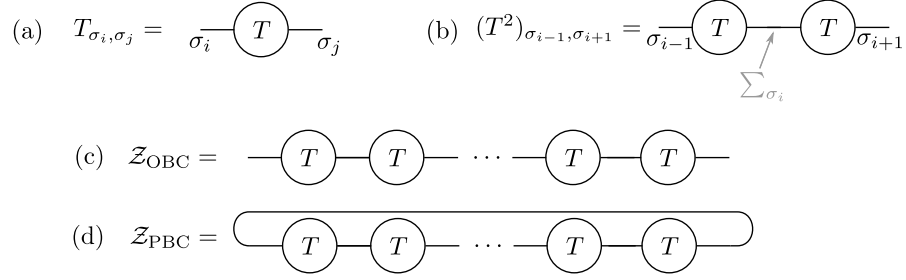


Figure 1.5 – Transfer matrix and tensor notation for the partition function of the 1D Ising model. (a) A matrix (or rank-2 tensor)  $T$  (Eq. 1.10) is represented with two legs, each leg corresponding to an index. Here,  $T$  corresponds to the Boltzmann weight of a nearest-neighbor bond in the Ising model. (b) The product of two matrices along a shared index (Eq. 1.12) is represented by connecting the legs which are summed over: the resulting object still has two open legs and is therefore still a matrix. (c) The 1D Ising model partition function with open boundary conditions. There are two free indices. (d) These indices can be contracted over to obtain the partition function for periodic boundary conditions.

DMRG and Ref. 117 for a review of DMRG in the MPS formulation, Refs. 187 for a review on diagonalization methods for transfer matrices and MPOs, and Refs. 120, 125, 184 for broader reviews of the topic of tensor networks and of the mathematical foundations of the field.

### 1.3.1 Partition functions as tensor network contractions

Consider the partition function of the nearest-neighbor Ising model

$$\mathcal{Z} = \sum_{\vec{\sigma}} e^{-\beta H} = \sum_{\vec{\sigma}} e^{K \sum_{\langle i, j \rangle} \sigma_i \sigma_j} \quad (1.9)$$

where we defined  $K = \beta J$  with  $\beta$  the inverse temperature, where  $\langle i, j \rangle$  stands for nearest-neighbor bonds, and where the Hamiltonian is characterized by a nearest-neighbor coupling  $J$  with  $J > 0$  for ferromagnetic interactions.

In the 1D Ising model, it is a standard exercise to write it as the trace of a transfer matrix. Defining the rank-2 tensor

$$T_{\sigma_i, \sigma_j} := \exp(K \sigma_i \sigma_j), \quad (1.10)$$

one finds that

$$\mathcal{Z} = \sum_{\vec{\sigma}} \prod_{\langle i, j \rangle} \exp(K \sigma_i \sigma_j) = \sum_{\vec{\sigma}} T_{\sigma_1, \sigma_2} T_{\sigma_2, \sigma_3} \cdots T_{\sigma_{N-1}, \sigma_N} = \sum_{\sigma_1 \sigma_N} (T^{N-1})_{\sigma_1, \sigma_N}, \quad (1.11)$$

where we use the fact that there are only two tensors involving  $\sigma_i$  ( $T_{\sigma_{i-1}, \sigma_i}$  and  $T_{\sigma_i, \sigma_{i+1}}$ ) and therefore one can isolate the sum over  $\sigma_i$  of these two tensors. In tensor network notation, the rank-2 tensor  $T$  is represented with two legs corresponding to each of the indices (Fig. 1.5a),

the product

$$\sum_{\sigma_i} T_{\sigma_{i-1}, \sigma_i} T_{\sigma_i, \sigma_{i+1}} \quad (1.12)$$

is represented with a connection between the two legs corresponding to the summed index (Fig. 1.5b), and the partition function is represented as a string of tensors, a tensor network<sup>3</sup> (Fig. 1.5c and d). We use the term contraction to describe the process of performing all the multiplications to compute the tensor network result. In the case of periodic boundary conditions (Fig. 1.5c) and a system of  $N$  sites this gives the well-known result that

$$\mathcal{Z}_{\text{PBC}} = \text{Tr}(T^N) = \lambda_+^N \left( 1 + \left[ \frac{\lambda_-}{\lambda_+} \right]^N \right) \quad (1.13)$$

where  $\lambda_+, \lambda_-$  are the eigenvalues of the “site-to-site transfer matrix”  $T$ , i.e. (Fig. 1.5b)

$$\lambda_{+,-} = e^{\beta J} \pm \sqrt{2 \cosh(2\beta J)}. \quad (1.14)$$

This corresponds to the fact that we can write

$$T^N = \lambda_+^N \sum_{i=+,-} \left( \frac{\lambda_i}{\lambda_+} \right)^N |r_i\rangle \langle l_i| \quad (1.15)$$

where  $|l_i\rangle$  and  $|r_i\rangle$  correspond to the left- and right-eigenvectors of the transfer matrix, and where  $\langle l_i | r_j \rangle = \delta_{i,j}$ . Provided that the leading eigenvalue is non-degenerate (which is the case in the 1D Ising model that we are discussing here), we have

$$T^N \rightarrow \lambda_+^N |r_+\rangle \langle l_+| \quad (1.16)$$

Fig. 1.5c illustrates the case with open boundary conditions (Eq. 1.11), which can be changed to fixed boundary conditions by contracting with a one-legged tensor on each end selecting the value of the spin.

There are several ways to extend the spirit of this construction to the square lattice Ising model. The most straightforward way is to keep the idea of associating a Boltzmann weight to each bond of the lattice:

$$\mathcal{Z} = \sum_{\vec{\sigma}} \prod_{\langle i,j \rangle} T_{\sigma_i, \sigma_j}. \quad (1.17)$$

In this case, four tensors involve the spin at site  $i$ :  $T_{\sigma_{i-x}, \sigma_i}$ ,  $T_{\sigma_i, \sigma_{i+x}}$ ,  $T_{\sigma_{i-y}, \sigma_i}$  and  $T_{\sigma_i, \sigma_{i+y}}$  (where  $\pm x$  and  $\pm y$  indicate moves to nearest neighbors in the two directions of the square lattice). Since we want to write tensor products and for that we need to sum on variables which only belong to two tensors (and not four like here), we will add at each site  $i$  a dummy tensor which will allow us to sum over four different instances of  $\sigma_i$  ( $\sigma_{i,1}$ ,  $\sigma_{i,2}$ ,  $\sigma_{i,3}$ ,  $\sigma_{i,4}$ , numbered clockwise from the top) and will make sure that all these instances actually map back to the

---

<sup>3</sup>Or “tensor train” in applied mathematics [188].



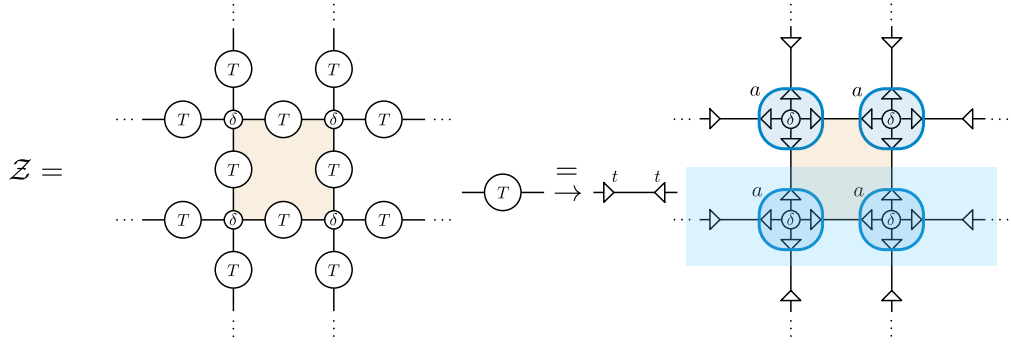


Figure 1.6 – Transfer matrix and tensor notation for the partition function of the 2D Ising model (see e.g. [147]). In this construction we associate a Boltzmann weight tensor  $T$  to each bond in the lattice (Eq. 1.10). A  $\delta$ -tensor (Eq. 1.18) is associated to each lattice site. We can take the square root  $t = \sqrt{T}$  (Eqs. 1.20, 1.21) and group the tensors on each site, resulting in a tensor  $a$  (Eq. 1.22, shown in blue). The 1D row-to-row transfer matrix in this case is highlighted in blue.

same spin<sup>4</sup>. This is achieved by defining a  $\delta$ -tensor

$$\delta_{\sigma_{i,1},\sigma_{i,2},\sigma_{i,3},\sigma_{i,4}} = \begin{cases} 1 & \text{if } \sigma_{i,1} = \sigma_{i,2} = \sigma_{i,3} = \sigma_{i,4} \\ 0 & \text{otherwise} \end{cases}. \quad (1.18)$$

Thus, we can rewrite

$$\mathcal{Z} = \sum_{\vec{\sigma}_1, \vec{\sigma}_2, \vec{\sigma}_3, \vec{\sigma}_4} \prod_i \delta_{\sigma_{i,1},\sigma_{i,2},\sigma_{i,3},\sigma_{i,4}} T_{\sigma_{i-1},\sigma_{i,1}} T_{\sigma_{i,2},\sigma_{i+1}} \quad (1.19)$$

where  $i$  spans the square lattice sites. Indicating sites  $i$  by row index  $r$  and column index  $c$ , it is natural to introduce the square-root  $t$  of the tensor  $T$  by writing:

$$\sum_{v_{r,c}} t_{\sigma_i, v_{r,c}} t_{v_{r,c}, \sigma_{i-y}} = T_{\sigma_i, \sigma_{i-y}}, \quad (1.20)$$

and

$$\sum_{h_{r,c}} t_{\sigma_i, h_{r,c}} t_{h_{r,c}, \sigma_{i+x}} = T_{\sigma_i, \sigma_{i+x}}, \quad (1.21)$$

where  $v_{r,c}$  ( $h_{r,c}$ ) stand for new variables taking two possible values and living on the vertical (horizontal) bonds between sites  $i$  and site  $i-y$  (site  $i$  and site  $i+x$ ). Contracting the  $t$  tensors around one site with the  $\delta$  tensor on this site (Fig. 1.6), we get a rank-4  $a$  tensor

$$a_{v_{r-1,c}, h_{r,c}, v_{r,c}, h_{r,c-1}} := \sum_{\sigma_{i,1}, \sigma_{i,2}, \sigma_{i,3}, \sigma_{i,4}} \delta_{\sigma_{i,1}, \sigma_{i,2}, \sigma_{i,3}, \sigma_{i,4}} t_{v_{r-1,c}, \sigma_{i,1}} t_{\sigma_{i,2}, h_{r,c}} t_{\sigma_{i,3}, v_{r,c}} t_{h_{r,c-1}, \sigma_{i,4}}, \quad (1.22)$$

<sup>4</sup>One can check easily that this would work as well in the 1D case, except there it is not required.

## Chapter 1. Algorithms for classical Ising models

where  $i$  is the site corresponding to row  $r$  and column  $c$ . Contracting the tensor network of  $a$  tensors on the vertices of the square lattice sites (indexed by row and columns) gives the partition function

$$\mathcal{Z} = \sum_{\vec{v}, \vec{h}} \prod_{r,c}^{N,M} a_{v_{r-1,c}, h_{r,c}, v_{r,c}, h_{r,c-1}}, \quad (1.23)$$

where for now we are not setting the boundary conditions and we have assumed a  $M \times N$  lattice.

We can rewrite this partition function as a product

$$\mathcal{Z} = \sum_{\vec{v}} \prod_{r=1}^N (\mathcal{T}^{(r)})_{v_{(r,1)}, \dots, v_{(r,N)}}^{v_{(r-1,1)}, \dots, v_{(r-1,N)}} \quad (1.24)$$

of row-to-row transfer matrices

$$(\mathcal{T}^{(r)})_{v_{(r,1)}, \dots, v_{(r,M)}}^{v_{(r-1,1)}, \dots, v_{(r-1,M)}} = \sum_{h_{(r,1)}, \dots, h_{(r,M)}} \prod_c a_{v_{(r-1,c)}, h_{(r,c)}, v_{(r,c)}, h_{(r,c-1)}}, \quad (1.25)$$

highlighted in blue in Fig. 1.6. Just as in the 1D case, we can alternatively use open boundary conditions, fixed boundary conditions (set by selecting the appropriate three-legged tensors at the boundary) or periodic boundary conditions. For instance, if  $h_{(r,0)} = h_{(r,M)}$  for each row, we obtain the Ising model on a cylinder, and if furthermore  $v_{(0,c)} = h_{(N,c)}$  for each column, then the partition function is given by the trace of  $\mathcal{T}$  to the power of the number of rows.

Another natural way of constructing the 2D square lattice Ising partition function is to define the Boltzmann weights  $W$  on the faces of the square lattice (“interactions round a face” models, see e.g. [176, 181]; see Fig. 1.7a):

$$W_{\sigma_{(r,c)}, \sigma_{(r,c+1)}, \sigma_{(r+1,c)}, \sigma_{(r+1,c+1)}} = e^{\frac{1}{2}\beta J(\sigma_{(r,c)}\sigma_{(r,c+1)} + \sigma_{(r,c+1)}\sigma_{(r+1,c+1)} + \sigma_{(r+1,c+1)}\sigma_{(r+1,c)} + \sigma_{(r+1,c)}\sigma_{(r,c)})} \quad (1.26)$$

where a one-half factor is introduced in the exponent to avoid double-counting. Again, the partition function constructed from  $W$  is not directly a tensor network, but can easily be formulated as one by introducing  $\delta$ -tensors on each site (Fig. 1.7b). Writing each  $\delta$ -tensor as a product of four three-legged delta tensors gives rise to a tensor network of plaquette weights. This is similar to what we will obtain in Chapter 2.

An alternative is to use the dimer variables that are already appearing naturally in Eq. 1.26 to define a tensor network on the dual lattice (Fig. 1.7c):

$$W_{d_{(r-1,c)}^v, d_{(r,c)}^h, d_{(r,c)}^v, d_{(r,c-1)}^h} = e^{\frac{1}{2}\beta J(d_{(r-1,c)}^v + d_{(r,c)}^h + d_{(r,c)}^v + d_{(r,c-1)}^h)}, \quad (1.27)$$

where we have indicated by  $h$  or  $v$  whether the dimer variable lives on a horizontal or vertical dual bond. We will use such a “dual” approach in Chapter 3. To the best of our knowledge, in the context of tensor networks, such a dual representation was first used on the triangular

lattice in the original work by Levin and Nave on TRG [141]<sup>5</sup>.

Finally, splitting each bond interaction equally between the two neighboring plaquettes is not necessarily the best option. We can also associate all the Boltzmann weight with one of the two plaquettes. Defining the tensors

$$\tilde{W}_{\sigma_{(r,c)},\sigma_{(r,c+1)},\sigma_{(r+1,c)},\sigma_{(r+1,c+1)}} = e^{\beta J(\sigma_{(r,c)}\sigma_{(r,c+1)} + \sigma_{(r,c+1)}\sigma_{(r+1,c+1)} + \sigma_{(r+1,c+1)}\sigma_{(r+1,c)} + \sigma_{(r+1,c)}\sigma_{(r,c)})}, \quad (1.28)$$

we can obtain the 2D Ising model partition function by arranging these in a checkerboard pattern (Fig. 1.7d, see also Ref. 125).

We therefore have a range of options to write partition functions of Ising models. We will see in Chapter 2 that the precise choice of implementation of the partition function as a tensor network can affect the convergence of standard approximate contraction algorithms in the case of frustrated spin systems.

In all these cases, we obtain the partition function as a contraction of the appropriate tensor network, as depicted in Figs. 1.6 and 1.7. One way to contract it is to follow Baxter's work [11] and to distinguish between the two spatial directions by considering the row-to-row transfer matrix  $\mathcal{T}$  which transfers the bond variable values vertically from one row to the next. Consider the leading (largest in magnitude) eigenvalue  $\Lambda_0$  of the row-to-row transfer matrix  $\mathcal{T}$  and the corresponding leading eigenvector  $|L_0\rangle$  (from the top). Just as in the 1D case, if we put periodic boundary conditions in the horizontal direction, we can write

$$\mathcal{T}^N = \Lambda_0^N \sum_i \left( \frac{\Lambda_i}{\Lambda_0} \right)^N |R_i\rangle \langle L_i| \quad (1.29)$$

where  $|L_i\rangle$  and  $|R_i\rangle$  correspond to the left- and right-eigenvectors of the transfer matrix, and where  $\langle L_i | R_j \rangle = \delta_{i,j}$ . If the leading eigenvector is non-degenerate, then in the limit of large systems, we have

$$\mathcal{T}^N \rightarrow \Lambda_0^N |R_0\rangle \langle L_0|, \quad (1.30)$$

where  $\Lambda_0$  is itself growing exponentially with the horizontal system size  $M$ . This type of relations will be the backbone for evaluating partition functions using tensor networks. In the thermodynamic limit we then have

$$\mathcal{Z} \rightarrow \Lambda_0^N. \quad (1.31)$$

To evaluate partition functions of classical models, we are therefore interested in computing the leading eigenvalue and eigenvectors of the row-to-row transfer matrix.

---

<sup>5</sup>See also [189] for a nice overview of the possible constructions, [21] for an overview of dimer models for planar Ising models. In the triangular lattice, interesting alternatives in the transfer matrix formulation can be found in Refs. 190, 191 and references therein.

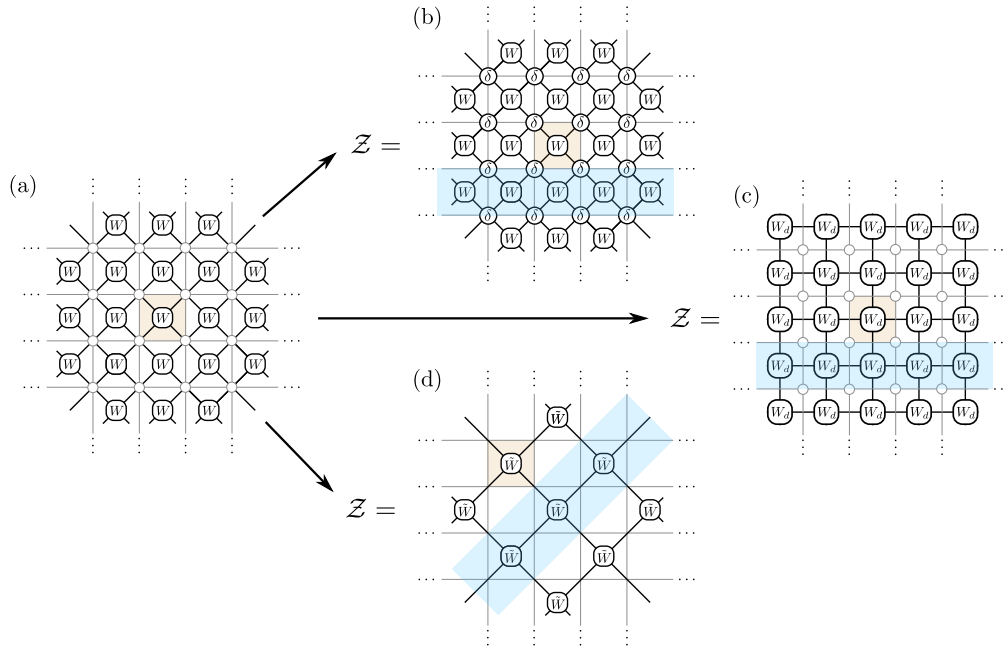


Figure 1.7 – Transfer matrix and tensor notation for the partition function of the 2D Ising model. The square lattice is shown in light gray. The row-to-row transfer matrix is highlighted in blue in each case. The “interactions round a face” construction (a) can give rise to three tensor network formulations. The most direct (b) replaces each site with a  $\delta$ -tensor. When building the row-to-row transfer matrix this tensor is trivially split into two. Alternatively (not shown here), we can use a diagonal row-to-row transfer matrix (similar to (d)). (c) Another possibility is to associate dual (dimer) variables to each bond. (d) We can also avoid double counting by defining a tensor on only half of the plaquettes in a checkerboard pattern.

#### 1.3.2 Uniform matrix product states

##### Motivation

In the previous section, we have seen that the row-to-row transfer matrix for classical Ising models can be obtained as a product of four-legged tensors determined by the appropriate Boltzmann weight. In the field of tensor networks, such an object is known as a matrix product operator (MPO). We should note that this is already a very efficient encoding of the transfer matrix, since we describe a  $2^M \times 2^M$  operator using only a  $2 \times 2 \times 2 \times 2$  tensor.

The row-to-row transfer matrix being efficiently encoded, we still face the challenge that the leading eigenvector that we are looking for is in principle a very high-dimensional object, with  $2^M$  degrees of freedom. The question is therefore if we can approximate this eigenvector using an Ansatz that is efficiently encoded. Having distinguished between the two spatial directions, we essentially want to find the leading eigenvector of a 1D operator. Facing this problem, Baxter [11] justified an Ansatz which is in spirit very close to what is now used in the tensor network methods that have been extremely successful in the context of 1D quantum systems.

These methods rely on the matrix product state (MPS) Ansatz to encode the eigenvectors. This essentially corresponds to describing a  $d^M$  dimensional object using a product of  $\chi \times d \times \chi$  tensors ( $d$  being 2 for Ising models). In the case of translation-invariant eigenvectors, the translation-invariant version of this Ansatz, a uniform MPS, is particularly efficient because it allows to encode the eigenvector using a single  $\chi \times d \times \chi$  tensor. There are a few important features of the MPS Ansatz. First, MPSs with a finite bond dimension  $\chi$  can approximate the ground state of gapped local 1D Hamiltonians with arbitrary accuracy [115]. Second, the MPS Ansatz satisfies the area-law of entanglement, that is, partitioning the system between one central section of size  $L$  and the rest of the 1D lattice, one observes that for  $L$  sufficiently large the entanglement entropy becomes constant (in general dimension, it would grow proportionally to the size of the boundary). This explains precisely why it is good at approximating ground states of gapped local Hamiltonians in 1D, which are known to have this property. Finally, MPSs are dense, in the sense that any state in the many-body Hilbert space can be represented if  $\chi$  is sufficiently large<sup>6</sup> ([120] and references therein).

We now give a short practical introduction to the uniform MPSs, namely the MPSs where translation invariance is assumed. A slightly more detailed introduction to uniform matrix product states can be found in Appendix B. A large part of these ideas were lying under the surface of Baxter's work [11], but for a thorough introduction in a more standard framework, we refer the reader to the 2019 lecture notes by Vanderstraeten et al. [150] and references therein, and to the reviews mentioned at the beginning of this section.

---

<sup>6</sup>In the case of critical states, the bond dimension would have to be taken to infinity in principle. We therefore exchange the problem of finite-size scaling with the problem of finite-bond dimension scaling.

### Single site unit cell

In the following, we are thinking of finite-size systems of size  $M$ , and taking mentally the thermodynamic limit where appropriate. Uniform MPSs provide an Ansatz to approximate states  $|\phi\rangle \in \otimes_{j=1}^M \mathbb{C}^d$ , where  $j$  indexes the sites of the one-dimensional lattice, and  $d$  is the dimension of the (Hilbert) space on each site. The Ansatz comes in the form of a *state*  $|\psi(A)\rangle$  defined as a *uniform product* of a single three-legged tensor  $A_{\alpha_j, \alpha_{j+1}}^{s_j}$  repeated on every site in the lattice (hence the name “uniform MPS”):

$$|\psi(A)\rangle = \sum_{\vec{s}} \cdots A^{s_{j-1}} A^{s_j} A^{s_{j+1}} \cdots |\dots, s_{j-1}, s_j, s_{j+1}, \dots\rangle \quad (1.32)$$

where

$$|\dots, s_{j-1}, s_j, s_{j+1}, \dots\rangle = \otimes_{j \in \mathbb{Z}} |s_j\rangle \quad (1.33)$$

are the states in the local (one site) Hilbert space. Pictorially, we represent this Ansatz as

$$|\psi(A)\rangle := \cdots \text{---} \boxed{A} \text{---} \boxed{A} \xrightarrow{\alpha_j} \boxed{A} \xrightarrow{\alpha_{j+1}} \boxed{A} \text{---} \cdots \quad (1.34)$$

$\downarrow \quad \downarrow \quad \downarrow \quad \downarrow \quad \downarrow$   
 $s_j$

In this construction, the tensor  $A_{\alpha_j, \alpha_{j+1}}^{s_j}$  can be thought of as a map  $A: \mathbb{C}^\chi \otimes \mathbb{C}^\chi \rightarrow \mathbb{C}^d$  from the virtual space labeled by  $\alpha_j, \alpha_{j+1}$  to the physical space labeled by  $s_j$ . The dimension  $\chi$  of the virtual space is called the *bond dimension* and will be the parameter for refining the Ansatz.

$A$  defines  $|\psi(A)\rangle$  uniquely, but the converse is not true, since the transformation

$$\text{---} \boxed{A_L} \text{---} = \text{---} \bigcirc L \text{---} \boxed{A} \text{---} \bigcirc L^{-1} \text{---} , \quad (1.35)$$

does not change the state in Eq. 1.34. In particular, we can make the practical choice of selecting  $L$  such that:

$$\begin{array}{c} \boxed{A_L} \\ \downarrow \\ \boxed{A_L^*} \end{array} = \left( \begin{array}{c} \text{---} \bigcirc L \text{---} \bigcirc L^{-1} \text{---} \end{array} \right) . \quad (1.36)$$

An MPS in this form is said to be left-orthonormal, or to be in the left gauge. Similarly, we can construct the equivalent MPS in the right gauge. Importantly, when doing this we are always assuming (unless otherwise stated) that the MPS is injective, namely the leading eigenvalue of the transfer matrix Eq. 1.36 is non-degenerate (see also Appendix B). The left and right gauges are most useful when they are combined appropriately to write an MPS in the mixed gauge:

$$|\psi(A)\rangle = \cdots \text{---} \boxed{A_L} \text{---} \boxed{A_L} \text{---} \bigcirc L \text{---} \boxed{A} \text{---} \bigcirc R \text{---} \boxed{A_R} \text{---} \boxed{A_R} \text{---} \cdots , \quad (1.37)$$

$$= \cdots \text{---} \boxed{A_L} \text{---} \boxed{A_L} \text{---} \boxed{A_L} \text{---} \bigcirc L \text{---} \bigcirc R \text{---} \boxed{A_R} \text{---} \boxed{A_R} \text{---} \cdots . \quad (1.38)$$

This allows us to define the center-site tensor  $A_C$  and the gauge tensor  $C$  as

$$\text{---} \bigcirc_C \text{---} = \text{---} \bigcirc_L \text{---} \bigcirc_R \text{---} , \quad \text{---} \boxed{A_C} \text{---} = \text{---} \bigcirc_L \text{---} \boxed{A} \text{---} \bigcirc_R \text{---} . \quad (1.39)$$

$C$  implements the map from the left-gauge tensor  $A_L$  to the right-gauge tensor  $A_R$ , and can be brought into a diagonal form by an additional unitary transformation that can be absorbed in  $A_L$  and  $A_R$ .  $C$  directly encodes the entanglement spectrum of the state and the Schmidt decomposition of the state can immediately be read in Eq. 1.38 (see Appendix B).

Given a tensor  $A$  finding the associated mixed gauge  $(A_L, A_R, A_C, C)$  is straightforward. However, we will also encounter the situation where we only have  $A_C$  and  $C$  and we want to find  $A_L$  and  $A_R$  defining a consistent mixed gauge MPS, i.e. satisfying

$$\text{---} \boxed{A_C} \text{---} = \text{---} \triangleleft_{A_L} \text{---} \bigcirc_C \text{---} = \text{---} \bigcirc_C \text{---} \triangleleft_{A_R} \text{---} . \quad (1.40)$$

It has been shown [148] that one way of solving for  $A_L$  and  $A_R$  is to perform the polar decompositions

$$\text{---} \boxed{A_C} \text{---} = \text{---} \bigcirc_{U^l} \text{---} \bigcirc_{P^l} \text{---} , \quad \text{---} \boxed{A_C} \text{---} = \text{---} \bigcirc_{P^r} \text{---} \bigcirc_{U^r} \text{---} , \quad (1.41)$$

$$\text{---} \bigcirc_C \text{---} = \text{---} \bigcirc_{V^l} \text{---} \bigcirc_{Q^l} \text{---} , \quad \text{---} \bigcirc_C \text{---} = \text{---} \bigcirc_{Q^r} \text{---} \bigcirc_{V^r} \text{---} , \quad (1.42)$$

where  $P^{l,r}, Q^{l,r}$  are hermitian and positive matrices, and where  $U^{l,r}$  and  $V^{l,r}$  are unitary. When  $A_C, C, A_L$  and  $A_R$  are all consistent, the unicity of the solution to the polar decomposition ensures that  $P^{l,r} \sim Q^{l,r}$  and that

$$\text{---} \triangleleft_{A_L} \text{---} := \text{---} \bigcirc_{U^l} \text{---} \bigcirc_{V^{l\dagger}} \text{---} , \quad \text{---} \triangleleft_{A_R} \text{---} := \text{---} \bigcirc_{V^{r\dagger}} \text{---} \bigcirc_{U^r} \text{---} . \quad (1.43)$$

#### Multi-site unit cell

Before moving on to the variational principle based on the uniform MPS Ansatz, we must introduce the version of the uniform MPS Ansatz where the translation invariance is not on one site as in the above, but on multiple sites. Indeed, the invariance of the row-to-row transfer matrix under translations by one site does not necessarily imply the translation invariance of its fixed point which might only be invariant under a translation of  $n_x$  sites. Furthermore, in some cases it makes sense to look for an eigenvector of the squared row-to-row transfer matrix. A useful example to have in mind is the square lattice Ising antiferromagnet: the leading eigenvector of the one-row transfer matrix corresponds to a superposition of an antiferromagnetic chain with the same chain shifted by one site to the left. There are two non-desirable effects of this. The first is numerical: such a superposition corresponds to a non-injective MPS and therefore breaks the unicity of the leading left and right eigenvectors

of the MPS overlap. The second is physical and corresponds to the fact that we typically are interested in the physical behavior within symmetry-broken sectors (e.g., we want to compute the magnetization of the 2D ferromagnetic Ising model and find a non-zero result). Therefore, both from the numerical point of view and from the point of view of physics, it is often more practical to allow for the spontaneous symmetry breaking and have access to the leading eigenvector corresponding to one of the symmetry-broken states. One might also encounter cases where the transfer matrix itself does not have one-site translation invariance. In all these cases, we want an Ansatz with a unit cell involving multiple sites.

A simple approach is to group sites together to be able to use the one-site Ansatz and related algorithms. However, it is more efficient to introduce a multi-site Ansatz and adjust the algorithms appropriately. This Ansatz will be defined by  $n_x$  tensors  $\{A^{(1,c)}\}_{c=1,\dots,n_x}$  of dimensions  $\chi \times d \times \chi$ . In Ref. 151 these tensors are seen as elements of a single four-legged tensor  $A$ , with the fourth leg labeling the site in the unit. Here we chose to keep this label explicit. The corresponding Ansatz for a three-sites unit cell would be:

$$|\psi(\{A\})\rangle := \cdots - \boxed{A^{(1,3)}} - \boxed{A^{(1,1)}} - \boxed{A^{(1,2)}} - \boxed{A^{(1,3)}} - \boxed{A^{(1,1)}} - \cdots \quad (1.44)$$

We can still write the left- and right-orthonormal forms, with

$$\begin{array}{c} \text{Left leg} \\ \text{Right leg} \end{array} \begin{array}{c} \text{Top leg} \\ \text{Bottom leg} \end{array} \begin{array}{c} \text{Left leg} \\ \text{Right leg} \end{array} = \left( \begin{array}{c} \text{Left leg} \\ \text{Right leg} \end{array} \begin{array}{c} \text{Top leg} \\ \text{Bottom leg} \end{array} \begin{array}{c} \text{Left leg} \\ \text{Right leg} \end{array} \right) = \left( \begin{array}{c} \text{Left leg} \\ \text{Right leg} \end{array} \begin{array}{c} \text{Top leg} \\ \text{Bottom leg} \end{array} \begin{array}{c} \text{Left leg} \\ \text{Right leg} \end{array} \right) \quad \forall c. \quad (1.45)$$

The main difference is that the tensors  $A_C$  and  $C$  now satisfy:

$$\boxed{A_C^{(1,c)}} = \boxed{A_L^{(1,c)}} \diamond \boxed{C^{(1,c+1)}} = \boxed{C^{(1,c)}} \diamond \boxed{A_R^{(1,c)}}, \quad (1.46)$$

where it is understood that  $c$  and  $c + 1$  are given modulo  $n_x$  (with the appropriate shift).

Finally, when there is translation symmetry breaking also in the vertical direction, in the sense that the row-to-row transfer matrix should be applied  $n_y$  times to get back to the original state, it is useful to take into account the state at the intermediate steps of the application of the transfer matrix. In this case, the tensors for the Ansatz corresponding to the state at step  $r$  will be labeled  $\{A^{(r,c)}\}_{c=1,\dots,n_x}$ , with  $r = 1, \dots, n_y$ .

### 1.3.3 Tangent space and variational principle

In the following we introduce the main support for the VUMPS algorithm, which is used throughout this thesis. This is far from being the only option to contract two-dimensional tensor networks; in fact, in the context of PEPS, the most widely used technique is the CTMRG of Nishino and Okunishi [146, 154, 192, 193]. Another method is the fixed-point corner method



(FPCM) [149], which is a variation on CTMRG where the corner tensor equations are solved using an eigenvalue solver. The VUMPS approach is perhaps closest in spirit to the less used infinite time-evolving block decimation (iTEBD) approach, where the top (and bottom) MPS are evaluated in the spirit of a power method [147].<sup>7</sup>

#### Variational principle

We want to use MPS as a variational Ansatz. In the quantum case, we have an operator  $H$  describing the Hamiltonian and we want to optimize, for a given bond dimension  $\chi$ ,

$$\min_A \frac{\langle \psi(A^*) | H | \psi(A) \rangle}{\langle \psi(A^*) | \psi(A) \rangle}. \quad (1.47)$$

In the classical case, which we will be focusing on from now on, we instead have a row-to-row transfer matrix  $\mathcal{T}(T)$  in the form of an MPO:

$$\mathcal{T}(T) = \cdots \begin{array}{c} | \\ \boxed{T} \\ | \end{array} \begin{array}{c} | \\ \boxed{T} \\ | \end{array} \begin{array}{c} | \\ \boxed{T} \\ | \end{array} \begin{array}{c} | \\ \boxed{T} \\ | \end{array} \begin{array}{c} | \\ \boxed{T} \\ | \end{array} \cdots, \quad (1.48)$$

We are looking for the leading eigenvector of this transfer matrix in the form of a normalized MPS, which will formally have to satisfy

$$\begin{array}{c} \cdots \begin{array}{c} | \\ \boxed{A} \\ | \end{array} \begin{array}{c} | \\ \boxed{A} \\ | \end{array} \begin{array}{c} | \\ \boxed{A} \\ | \end{array} \begin{array}{c} | \\ \boxed{A} \\ | \end{array} \begin{array}{c} | \\ \boxed{A} \\ | \end{array} \cdots \\ | \\ \begin{array}{c} | \\ \boxed{T} \\ | \end{array} \begin{array}{c} | \\ \boxed{T} \\ | \end{array} \begin{array}{c} | \\ \boxed{T} \\ | \end{array} \begin{array}{c} | \\ \boxed{T} \\ | \end{array} \begin{array}{c} | \\ \boxed{T} \\ | \end{array} \cdots \end{array} \quad (1.49)$$

$$\approx \Lambda \cdots \begin{array}{c} | \\ \boxed{A} \\ | \end{array} \begin{array}{c} | \\ \boxed{A} \\ | \end{array} \begin{array}{c} | \\ \boxed{A} \\ | \end{array} \begin{array}{c} | \\ \boxed{A} \\ | \end{array} \begin{array}{c} | \\ \boxed{A} \\ | \end{array} \cdots$$

$\Lambda = \langle \psi(A^*) | \mathcal{T}(T) | \psi(A) \rangle$  is actually ill-defined in the thermodynamic limit, since it should grow exponentially with the longitudinal system size. Indeed, we can formally write this overlap as

$$\Lambda = \cdots \begin{array}{c} \begin{array}{c} \triangleleft \boxed{A_L} \end{array} \begin{array}{c} \triangleleft \boxed{A_L} \end{array} \begin{array}{c} \boxed{A_C} \end{array} \begin{array}{c} \triangleright \boxed{A_R} \end{array} \begin{array}{c} \triangleright \boxed{A_R} \end{array} \\ | \\ \begin{array}{c} | \\ \boxed{T} \\ | \end{array} \begin{array}{c} | \\ \boxed{T} \\ | \end{array} \begin{array}{c} | \\ \boxed{T} \\ | \end{array} \begin{array}{c} | \\ \boxed{T} \\ | \end{array} \begin{array}{c} | \\ \boxed{T} \\ | \end{array} \cdots \\ \begin{array}{c} \triangleleft \boxed{A_L^*} \end{array} \begin{array}{c} \triangleleft \boxed{A_L^*} \end{array} \begin{array}{c} \boxed{A_C^*} \end{array} \begin{array}{c} \triangleright \boxed{A_R^*} \end{array} \begin{array}{c} \triangleright \boxed{A_R^*} \end{array} \end{array} \quad (1.50)$$

<sup>7</sup>In most of this thesis, the results have been obtained with the VUMPS approach in order to contract two-dimensional tensor networks. There is no deep reason behind this choice and in principle one could have used CTMRG/FPCM. There are however two practical reasons: first, it does seem that CTMRG would struggle on some of the gapless ground-state phases that we obtain, but in principle the speed of convergence could be improved by using FPCM; second, multi-site unit cells are particularly easy to deal with in VUMPS, at least when one is only interested in the leading eigenvalue. We did not investigate TRG/TNR, though they do show the same convergence problems on frustrated systems as we observe in Chapter 2 [194]. Because of the step of splitting the tensors, it is unclear whether the solution that we provide to this problem would also work with these contraction techniques.

Introducing the left and right fixed points  $G_L$  and  $G_R$  satisfying the equations

$$G_L \begin{array}{c} \triangle A_L \\ \square T \\ \triangle A_L^* \end{array} = \lambda_L G_L, \quad G_R \begin{array}{c} \triangle A_R \\ \square T \\ \triangle A_R^* \end{array} = \lambda_R G_R, \quad G_L \begin{array}{c} \diamond C \\ \square T \\ \diamond C^* \end{array} G_R = 1, \quad (1.51)$$

with  $\lambda_R$  and  $\lambda_L$  being the left and right eigenvalues of largest magnitude, we find that

$$\lambda_L = \lambda_R = G_L \begin{array}{c} \triangle A_L \\ \square T \\ \triangle A_L^* \end{array} G_R = G_L \begin{array}{c} \triangle A_C \\ \square T \\ \triangle A_C^* \end{array} G_R. \quad (1.52)$$

Note that in Eq. 1.51 the normalization corresponds to the general relation between left and right (or top and bottom) eigenvectors that we need when we want to write equations of the form of Eq. 1.30.

Therefore,  $\Lambda = \lim_{N \rightarrow \infty} \lambda_R^N = \lim_{N \rightarrow \infty} \lambda_L^N$  where  $N$  is the number of sites in the horizontal direction. What we are really interested in is the partition function for one site  $\lambda = \Lambda^{1/N}$ . We want to maximize  $\lambda$  or, equivalently, we want to minimize the free energy per site  $\beta f = -\ln(\lambda)$ .

### Tangent space

There are several ways of reaching the VUMPS equations that allow to optimize  $|\psi(A)\rangle$ . The approach we present here (Ref. 150) is based on the fact that uniform MPS give a mapping between  $\chi \times d \times \chi$  tensors  $A$  and a set of states in the Hilbert space which forms a smooth manifold ([195] and references therein). This approach also gives us a way of growing the bond dimension of the Ansatz, providing a good initial state to run the fixed-point algorithm at a larger bond dimension once the fixed-point has converged at a lower bond dimension [196].

It can be easily seen that the MPS manifold is not a linear subspace<sup>8</sup>, and it is therefore tempting to do the following: to each  $A$  a point  $|\psi(A)\rangle$  in the MPS manifold is associated, and we want to look at the tangent space to the MPS manifold at  $|\psi(A)\rangle$ . In Appendix B we follow Ref. 150 in deriving the projector  $\mathcal{P}_A$  that projects a state in the Hilbert space on the part of the tangent manifold which is orthogonal to  $|\psi(A)\rangle$ . In the mixed gauge, this projector is given

<sup>8</sup> $|\psi(A+B)\rangle \neq |\psi(A)\rangle + |\psi(B)\rangle$

by:

$$\mathcal{P}_A = \sum_n \left( \begin{array}{c} \cdots \quad A_L^* \quad \cdots \\ \cdots \quad A_L \quad \cdots \\ s_{n-1} \quad s_n \quad s_{n+1} \end{array} \right) - \sum_n \left( \begin{array}{c} \cdots \quad A_L^* \quad A_L^* \quad \cdots \\ \cdots \quad A_L \quad A_L \quad \cdots \\ s_{n-1} \quad s_n \quad s_{n+1} \end{array} \right). \quad (1.53)$$

### Example: truncating a uniform MPS

As a useful example, we consider the case of a uniform MPS  $|\psi(A')\rangle$  with a certain bond dimension  $\chi'$  that we want to approximate by another uniform MPS  $|\psi(A)\rangle$  with a bond dimension  $\chi$ , a procedure known as truncation. The standard approach is to use the Schmidt decomposition Eq. B.16 and to truncate the singular values and accordingly the  $U$  and  $V$  tensors in  $A_L$  and  $A_R$  (Eqs. B.13, B.14). Another possible approach is the maximization of the logarithm of the fidelity [196]:

$$\max_A \lim_{N \rightarrow \infty} \frac{1}{N} \ln \left( \frac{\langle \psi(A^*) | \psi(A') \rangle_N \langle \psi(A') | \psi(A) \rangle_N}{\langle \psi(A^*) | \psi(A) \rangle_N} \right) \quad (1.54)$$

where we denote by  $\langle . | . \rangle_N$  the overlap two  $N$ -site MPSs (with PBC), such that the quantities are well defined. Working with uniform MPS the zero gradient condition is

$$\langle \partial_{A^*} \psi(A^*) | \left( |\psi(A')\rangle - \frac{\langle \psi(A^*) | \psi(A') \rangle}{\langle \psi(A^*) | \psi(A) \rangle} |\psi(A)\rangle \right) = 0 \quad (1.55)$$

which shows why we typically want to reduce the parametrization of the tangent space vectors  $|\partial_A \psi(A)\rangle$  only to those which are orthogonal to  $|\psi(A)\rangle$ . Indeed, here,  $|\psi(A)\rangle$  is always a trivial solution. We can use the tangent space projector that we just introduced to formulate the condition for the optimum as

$$\mathcal{P}_A |\psi(A')\rangle = 0. \quad (1.56)$$

In the mixed gauge this condition together with the translation invariance of  $|\psi(A)\rangle$  and  $|\psi(A')\rangle$  becomes

$$\sum_n \left( \begin{array}{c} \cdots \quad A' \quad A' \quad A' \quad \cdots \\ \cdots \quad A_L^* \quad \cdots \\ \cdots \quad A_L \quad \cdots \\ s_{n-1} \quad s_n \quad s_{n+1} \end{array} \right) = \sum_n \left( \begin{array}{c} \cdots \quad A' \quad A' \quad A' \quad \cdots \\ \cdots \quad A_L^* \quad A_L^* \quad \cdots \\ \cdots \quad A_L \quad A_L \quad \cdots \\ s_{n-1} \quad s_n \quad s_{n+1} \end{array} \right). \quad (1.57)$$

Introducing the left- and right fixed points  $G_L$  and  $G_R$  satisfying

$$\begin{array}{c} \text{---} G_L \text{---} A' \text{---} \\ | \\ \text{---} A_L^* \text{---} \end{array} = \lambda \begin{array}{c} \text{---} G_L \text{---} \end{array}, \quad \begin{array}{c} \text{---} A' \text{---} G_R \text{---} \\ | \\ \text{---} A_R^* \text{---} \end{array} = \lambda \begin{array}{c} \text{---} G_R \text{---} \end{array}, \quad (1.58)$$

we can contract the top left and right channels in Eq. 1.57 yielding

$$\begin{array}{c} \frac{1}{\lambda} \begin{array}{c} \text{---} G_L \text{---} A' \text{---} G_R \text{---} \\ | \\ \text{---} A_L^* \text{---} \end{array} \end{array} = \begin{array}{c} \text{---} G_L \text{---} G_R \text{---} \\ | \\ \text{---} A_L^* \text{---} \end{array} = \begin{array}{c} \text{---} G_L \text{---} G_R \text{---} \\ | \\ \text{---} A_L^* \text{---} \end{array} \begin{array}{c} \text{---} C \text{---} \end{array}. \quad (1.59)$$

We are thus looking for a solution to such self-consistent equations. The algorithm then goes as follows: starting from a random tensor  $A^{(0)}$  we evaluate the corresponding  $A_L^{(0)}$  and  $A_R^{(0)}$ . We then evaluate  $A_C^{(1)}$  and  $C^{(1)}$  using Eq. 1.59, then evaluate the corresponding new  $A_L^{(1)}$  and  $A_R^{(1)}$  based on the polar decomposition as in Eqs. 1.41, 1.42 and 1.43. We iterate this procedure until convergence of the error measures

$$\epsilon_L = \left\| \begin{array}{c} \text{---} A_C^{(k)} \text{---} \\ | \\ \text{---} A_L^{(k)} \text{---} \end{array} - \begin{array}{c} \text{---} A_L^{(k)} \text{---} C^{(k)} \text{---} \end{array} \right\|_2, \quad \epsilon_R = \left\| \begin{array}{c} \text{---} A_C^{(k)} \text{---} \\ | \\ \text{---} C^{(k)} \text{---} A_R^{(k)} \text{---} \end{array} \right\|_2, \quad (1.60)$$

which are essentially equal close to convergence (note that here  $k$  labels the iteration, and we are working with a single unit cell). There is no fundamental guarantee that this procedure should converge, but in practice this iterative way of solving the fixed point equations works well.

### 1.3.4 The VUMPS and multi-site VUMPS algorithms for MPOs

#### VUMPS

With this, we have everything in hands to introduce the VUMPS algorithm for transfer matrices (VUMPS stands for variational uniform matrix product states). The approach is very similar to what we just described for the variational truncation of a uniform MPS. Inspired by that result and the discussion leading up to Eq. 1.52, we note that the optimality condition corresponding to Eq. 1.49 can be written as

$$\mathcal{P}_A(\mathcal{T}|\psi(A)\rangle - \Lambda|\psi(A)\rangle) = 0. \quad (1.61)$$

Using the same approach as for the truncation of the MPS, we get the condition

$$\frac{1}{\lambda} \begin{array}{c} \text{---} A_C \text{---} \\ | \\ G_L \text{---} T \text{---} G_R \\ | \\ \text{---} A_L \text{---} \end{array} = \begin{array}{c} \text{---} C \text{---} \\ | \\ G_L \text{---} G_R \\ | \\ \text{---} A_L \text{---} \end{array} = \begin{array}{c} \text{---} C \text{---} \\ | \\ G_L \text{---} G_R \\ | \\ \text{---} A_R \text{---} \end{array}, \quad (1.62)$$

where  $G_L$  and  $G_R$  are the left- and right fixed point as in Eq. 1.51. We have fixed the gauge and therefore the gauge tensor  $C$  transforming  $A_L$  into  $A_R$  is defined up to a factor. The fixed point should therefore satisfy the Eq. 1.62 with the conditions

$$\begin{array}{c} \text{---} A_C \text{---} \\ | \end{array} \propto \begin{array}{c} \text{---} V_{G,T}(A_C) \text{---} \\ | \end{array} \quad \text{with} \quad \begin{array}{c} \text{---} V_{G,T}(X) \text{---} \\ | \end{array} = \begin{array}{c} \text{---} X \text{---} \\ | \\ G_L \text{---} T \text{---} G_R \\ | \\ \text{---} \end{array}, \quad (1.63)$$

$$\begin{array}{c} \text{---} C \text{---} \\ | \end{array} \propto \begin{array}{c} \text{---} V_G(C) \text{---} \\ | \end{array} \quad \text{with} \quad \begin{array}{c} \text{---} V_G(X) \text{---} \\ | \end{array} = \begin{array}{c} \text{---} C \text{---} \\ | \\ G_L \text{---} G_R \\ | \\ \text{---} \end{array}. \quad (1.64)$$

These eigenvalue equations can be solved using an Arnoldi method, yielding the VUMPS algorithm (Algorithm 2).

#### Multi-site VUMPS

We now sketch the multi-site VUMPS algorithm. A thorough description can be found in Refs. 149, 151, 197. Here, we only want to mention how Eqs. 1.62, 1.63 and 1.64 have to be adjusted to allow for translation symmetry breaking in the horizontal and/or vertical directions. In this case we use  $n_y$  Ansätze  $\{|\psi(\mathbb{A}^{(r)})\rangle\}_{r=1}^{n_y}$  where  $\mathbb{A}^{(r)} = \{A^{(r,c)}\}_{c=1}^{n_x}$  is the set of

## Chapter 1. Algorithms for classical Ising models

**Algorithm 2** VUMPS algorithm: find the optimal MPS approximation of the fixed point of the row-to-row transfer matrix  $\mathcal{T}(T)$

---

```

1: function VUMPS( $T, A, \delta$ )                                 $\triangleright A$ : initial guess;  $\delta$ : tolerance.
2:    $(A_L, A_R, A_C, C) \leftarrow \text{MIXED CANONICAL FORM}(A, \delta)$ 
3:   Initialize  $\epsilon > \delta$ .
4:   repeat
5:     Compute the left fixed-point  $G_L$  and  $\lambda_L$                  $\triangleright$  Eq. 1.51, Using  $T$  and  $A_L$ 
6:     Compute the right fixed-point  $G_R$  and  $\lambda_R$                  $\triangleright$  Eq. 1.51, Using  $T$  and  $A_R$ 
7:     Check that  $\lambda_L \cong \lambda_R = \lambda$ 
8:     Normalize  $G_L$  by  $\text{OVERLAP}(G_L, G_R, C)$ 
9:      $(\lambda, \tilde{A}_C) \leftarrow \text{ARNOLDI}(X \rightarrow V_{G,T}(X), \text{tol. } \epsilon/10, \text{initial guess } A_C)$   $\triangleright A_C$  from Eq. 1.63
10:     $\tilde{C} \leftarrow \text{ARNOLDI}(X \rightarrow V_G(X), \text{tol. } \epsilon/10, \text{initial guess } C)$   $\triangleright C$  from Eq. 1.64
11:     $(A_L, A_R, A_C, C) \leftarrow \text{OPTIMIZEALAR}(\tilde{A}_C, \tilde{C})$   $\triangleright A_L$  and  $A_R$  from  $A_C$  and  $C$ 
12:     $\epsilon \leftarrow \|V_{G,T}(A_C)/\lambda - A_L V_G(C)\|_2$   $\triangleright$  Error on Eq. 1.62
13:  until  $\epsilon < \delta$ 
  return  $\tilde{\sigma}_{m+1}$ 

```

---

tensor describing the Ansatz at row  $r$ . The essential idea is that we want to solve

$$\begin{array}{c}
 \overbrace{\dots - A^{(r,1)} - \dots - A^{(r,n_x)} - A^{(r,1)} - \dots}^{n_x} \\
 \vdots \\
 \dots - T - \dots - T - T - \dots \\
 \vdots \\
 \dots - T - \dots - T - T - \dots
 \end{array}
 \left. \vphantom{\begin{array}{c} \dots \\ \vdots \\ \dots \end{array}} \right\} n_y
 \quad (1.65)$$

$$\approx \Lambda \dots - A^{(r,1)} - \dots - A^{(r,n_x)} - A^{(r,1)} - \dots$$

which we rewrite as a set of equations for each  $r = 1, \dots, n_y$

$$\begin{array}{c}
 \dots - A^{(r,1)} - \dots - A^{(r,n_x)} - A^{(r,1)} - \dots \\
 \vdots \\
 \dots - T - \dots - T - T - \dots
 \end{array}
 , \quad (1.66)$$

$$\approx \lambda_r \dots - A^{(r+1,1)} - \dots - A^{(r+1,n_x)} - A^{(r+1,1)} - \dots$$

where the  $\lambda_r$  are such that  $\Lambda = \lambda_1 \cdots \lambda_{n_y}$ . The fixed-point equations become

$$\begin{array}{c} \text{Diagram: } G_L^{(r,c)} \text{ and } G_R^{(r,c+1)} \text{ connected by } A_C^{(r,c)} \text{ and } T \\ \text{Diagram: } G_L^{(r,c)} \text{ and } G_R^{(r,c+1)} \text{ connected by } T \end{array} = \lambda_{A_C} \text{Diagram: } A_C^{(r+1,c)} \quad (1.67)$$

and

$$\begin{array}{c} \text{Diagram: } G_L^{(r,c)} \text{ and } G_R^{(r,c)} \text{ connected by } C^{(r,c)} \\ \text{Diagram: } G_L^{(r,c)} \text{ and } G_R^{(r,c)} \text{ connected by } C^{(r,c)} \end{array} = \lambda_C \text{Diagram: } C^{(r+1,c)} \quad (1.68)$$

The fixed point tensors  $G_L^{(r,c)}$  and  $G_R^{(r,c)}$  obey

$$\begin{array}{c} \text{Diagram: } G_L^{(r,c)} \text{ connected to a chain of } T \text{ and } A_C \text{ tensors} \\ \text{Diagram: } G_L^{(r,c)} \text{ connected to a chain of } T \text{ and } A_C \text{ tensors} \end{array} = \lambda_L^{(r,c)} \text{Diagram: } G_L^{(r,c)} \quad (1.69)$$

and

$$\begin{array}{c} \text{Diagram: } A_C \text{ and } T \text{ tensors connected to } G_R^{(r,c)} \\ \text{Diagram: } A_C \text{ and } T \text{ tensors connected to } G_R^{(r,c)} \end{array} = \lambda_R^{(r,c)} \text{Diagram: } G_R^{(r,c)} \quad (1.70)$$

respectively. In these equations, we only indicate the indices of  $A_L$  and  $A_R$ , the fact that the tensor corresponds to  $A_L$  or  $A_R$  being understood from the shape of the tensor, and the conjugation being taken appropriately for the tensors in the bottom row.

In the case of one- or two-row Hermitian transfer matrices, we can solve these equations either in parallel or sequentially in the  $x$  and  $y$  direction, yielding the same results [151, 197]. As in the original VUMPS algorithm, we can solve for  $\{A_C\}$  and  $\{C\}$  using an Arnoldi solver, applied to the vertical transfer matrix constituted of the appropriate strings of  $G_L$  and  $G_R$  tensors on the left and on the right (and with  $T$  when solving for  $A_C$ ). In that case we are looking directly for  $\lambda^{n_y} = \lim_{N \rightarrow \infty} \Lambda^{1/N}$  similar to the single-site case.

Note that occasionally we might encounter transfer matrices which are not Hermitian. In this case and as suggested in Ref. 149 the top and bottom uniform MPSs can be computed independently, just as in the iTEBD approach. To the best of our knowledge, the possibility of optimizing simultaneously the top and bottom fixed point together using VUMPS, as is done for instance in iDMRG, has not been explored yet. In the case of translation symmetry breaking (or other symmetry breaking) one then has to make sure that the top and bottom fixed point belong to the same symmetry-broken sectors. If the transfer matrix is not Hermitian or if it has three or more rows, the algorithm is not justified by a variational principle anymore but is still valid from the point of view of the tangent space projection. If one encounters issues it can be modified and turned into a sequential optimization of the normalized fidelity between  $\mathcal{T}|\psi(\mathbb{A}^{(r)})\rangle$  and  $|\psi(\mathbb{A}^{(r+1)})\rangle$  as we described for truncating a uniform MPS (see Refs. 150, 196, 197).

Once the boundary MPSs are evaluated using the VUMPS algorithm, single-site observables can be computed straightforwardly as

$$\langle O \rangle = \frac{1}{\lambda} \text{Tr} \left( G_L^{(r,c)} \begin{array}{c} A_C^{(r,c)} \\ O \\ A_C^{(r+1,c)} \end{array} G_R^{(r,c+1)} \right), \quad (1.71)$$

where we used that  $G_L, G_R$  are normalized such that  $\lambda_C = 1$  with  $\text{Tr}((C^{(r,c)})^\dagger C^{(r,c)}) = 1$ , and where  $\lambda$  is the approximation of the partition function for one site. Correlations between single-site observables can (for instance) be obtained as

$$\langle O_{(r,c)} O_{(r,c+n)} \rangle = \frac{\text{Tr} \left( G_L^{(r,c)} \begin{array}{c} A_C^{(r,c)} \\ O \\ A_C^{(r+1,c)} \end{array} \begin{array}{c} \text{---} (r,c+1) \text{---} \dots \text{---} (r,c+n) \text{---} \\ T \\ \text{---} (r+1,c+1) \text{---} \dots \text{---} (r+1,c+n) \text{---} \end{array} G_R^{(r,c+n+1)} \right)}{\text{Tr} \left( G_L^{(r,c)} \begin{array}{c} A_C^{(r,c)} \\ T \\ A_C^{(r+1,c)} \end{array} \begin{array}{c} \text{---} (r,c+1) \text{---} \dots \text{---} (r,c+n) \text{---} \\ T \\ \text{---} (r+1,c+1) \text{---} \dots \text{---} (r+1,c+n) \text{---} \end{array} G_R^{(r,c+n+1)} \right)}, \quad (1.72)$$

It is easy to see that, at long-range, the connected correlations  $\langle O_{(r,c)} O_{(r,c+n)} \rangle - \langle O_{(r,c)} \rangle \langle O_{(r,c+n)} \rangle$  will decay exponentially [120]. This is a feature of MPS and this is one of the reasons why finite bond dimension scaling is needed when the states that we are trying to approximate are critical. It implies that, when studying models such as the TIAFM whose ground state has



critical correlations, very large bond dimensions will be required (see for instance the contrast between the KIAFM and TIAFM residual entropy results in Ref. 140).

With this, we have everything in hands to study classical Ising models using tensor networks.

### 1.4 Ground-state energy lower bounds

When studying frustrated spin systems with Monte Carlo simulations, we generally encounter the problem of proving rigorously that the Monte Carlo simulations reach the ground state energy. Furthermore, as we will see in Chapter 2, for studying macroscopically degenerate ground states of frustrated systems with tensor networks, we will find it useful to be able to build lower bounds for the energy.

In this section we discuss two elegant approaches for computing ground-state energy lower bounds for models of the type of Eq. 1.3. The first is a method introduced in 1966 by Kanamori, and known as Kanamori's method of inequalities, or the configurational polytope [25, 155–157, 161] (see Appendix C.1 for a detailed list of references). The second is similar to the Anderson bounds [198] but was developed systematically in the context of generalized classical Ising models [158]. Both methods boil down to solving a linear program (LP), and the main challenge in both cases is to limit the exponential number of inequalities that have to be included to build the LP. In Appendix C.2, following Ref. 158, we show that both methods are dual to one another in the LP sense. Since going into an introduction on linear programming would take us too far out of our path, we refer the interested reader to the very useful book by Grötschel *et al.* [199].

#### 1.4.1 Kaburagi and Kanamori's method of inequalities

The configurational polytope method was introduced in Ref. 155 and later re-explored by several authors [25, 101, 156, 157, 161, 200–202]. (In Ref. 25pp.109–110, F. Ducastelle provides a detailed list of applications to Ising models until 1990, which we reproduce in Appendix C.1). We start by discussing the idea in a general setting, showing that finding the ground-state energy lower bound can be formulated as a LP, and that the main difficulty lies with writing the inequalities defining it. We then specialize to a simple example to illustrate one way of constructing the inequalities.

##### Generic formulation

In general, we will be interested in solving Hamiltonians of the form:

$$H = \sum_{k=1}^n \left( J_k \sum_{(i,j)_k} \sigma_i \sigma_j \right) + J_0 \sum_i \sigma_i \quad (1.73)$$

## Chapter 1. Algorithms for classical Ising models

---

where  $J_k$  can take any value,  $n$  is finite (and preferably small), and  $J_0$  acts as a magnetic field. Introducing  $N_k$  as the number of pairs of range  $k$ , we can define the correlations:

$$c_k := \frac{1}{N_k} \sum_{(i,j)_k} \sigma_i \sigma_j \quad \forall k = 1, \dots, n \quad (1.74)$$

and

$$c_0 := m = \frac{1}{N} \sum_i \sigma_i, \quad (1.75)$$

the energy per site can be rewritten

$$\frac{H}{N} = \sum_{k=0}^n J_k z_k c_k, \quad (1.76)$$

where  $z_k = N_k/N$ , with  $N$  the number of sites. By construction, the correlations  $c_0, \dots, c_n$  are bounded between  $-1$  and  $1$ . Finding the ground state energy per site amounts to finding the set of correlations minimizing  $H/N$  for fixed  $J_k$ , which seems trivial as we have a linear function and a finite number of correlations. However, not every set of correlations in  $[-1, 1]^{n+1}$  can be realized in practice. Defining  $P \subset [-1, 1]^{n+1}$  the set of possible correlations, two important remarks have to be made:

1.  $P$  is convex (in the thermodynamic limit). This is the case because the components of  $N\vec{c}$  for any point  $\vec{c} \in P$  are extensive quantities, and therefore for  $\vec{c}_1, \vec{c}_2 \in P$ , any point on the line connecting  $\vec{c}_1$  to  $\vec{c}_2$  can be realized as the correlations of a mixture of two configurations corresponding respectively to  $\vec{c}_1$  and  $\vec{c}_2$ . The contribution from the boundary between the two phases vanishes in the thermodynamic limit.
2. The linear function in Eq. 1.76 reaches its extremum on the boundary of  $P$ .

Therefore, if one has access to the set  $P$  of possible correlations and it is a polytope, the ground-state problem can be solved as a LP. The main challenge then lies in finding  $P$ . Kaburagi and Kanamori [155, 203, 204] suggest an algorithm to find constraints on the possible correlations in the form of inequalities arising from geometrical constraints (i.e. constraints related to the lattice topology). In general, these inequalities are valid for all  $\vec{c} \in P$  but also for some additional correlations. We call  $I \subset [-1, 1]^{n+1}$  the polytope corresponding to the set of correlations satisfying the inequalities of Kanamori. Because  $I \supset P$ , these inequalities directly imply a lower bound on the ground state energy for any values of the  $J_k$ :

$$\min_{\vec{c}} \sum_{k=0}^n J_k z_k c_k, \quad \text{under } A\vec{c} \geq \vec{b}, \quad (1.77)$$

where  $A\vec{c} \geq \vec{b}$  are the Kanamori inequalities. Given the corners of the polytope  $I$ , if one can show that each corner is *constructible*, in the sense that there exists a configuration which realizes the corresponding correlations, then this implies  $I = P$ .

Phrased like this, the two challenges posed by this approach are

1. Find  $A$  and  $\vec{b}$  (or alternatively, find  $I$ ).
2. Show that  $P = I$ , which turns the lower bounds into exact results for the ground state energy.

Below, on a simple example, we present the main ideas for constructing a set of inequalities constraining the correlations, as suggested by Kaburagi and Kanamori [203]. We also sketch an approach for constructing the set of inequalities slightly more systematically [101, 200].

### $J_1 - J_2$ model on the kagome lattice

As a simple example, we consider a family of  $J_1 - J_2$  models on the kagome lattice, with Hamiltonians:

$$H = J_1 \sum_{\langle i,j \rangle_1} \sigma_i \sigma_j + J_2 \sum_{\langle i,j \rangle_2} \sigma_i \sigma_j \quad (1.78)$$

$$\Rightarrow \frac{1}{2} \frac{H}{N} = J_1 c_1 + J_2 c_2 = \vec{J} \cdot \vec{c}, \quad (1.79)$$

where the couplings  $J_1$  and  $J_2$  can take arbitrary real values, and where we have introduced the (disconnected) correlations:

$$c_1 := \frac{1}{2N} \sum_{\langle i,j \rangle} \sigma_i \sigma_j \quad c_2 := \frac{1}{2N} \sum_{\langle i,j \rangle_2} \sigma_i \sigma_j, \quad (1.80)$$

with  $N$  the number of sites in the system. We used the fact that there are  $2N$  nearest- and next-nearest-neighbor bonds per site on the kagome lattice.

As illustrated in Fig. 1.8a, for a fixed energy per site and fixed values of  $J_1$  and  $J_2$ , Eq. 1.79 defines a line in the  $c_1 - c_2$  space (correlation space). The idea behind Kaburagi and Kanamori's method is to build constraints on the possible values of  $c_1$  and  $c_2$ , using clusters like the ones shown in Fig. 1.8b. These constraints are a consequence of the type of on-site degrees of freedom (here, Ising), the number of couplings involved in the Hamiltonian as well as the geometry of the lattice, but do *not* depend on the values of the couplings. Once these constraints are found, they define the set  $I_{J_1 - J_2}$  of possible values for the spin-spin correlations, highlighted in orange in Fig. 1.8c, and no correlation outside of this set can be realized. From this, it is straightforward to obtain lower bounds for the ground-state energy. Indeed, changing the energy per site just moves the line defined by Eq. 1.79 along  $\vec{J}$ ; when the line reaches the boundary of the set of allowed correlations, the energy cannot be lowered anymore.

The construction of the constraints on the correlations starts with simple inequalities such as

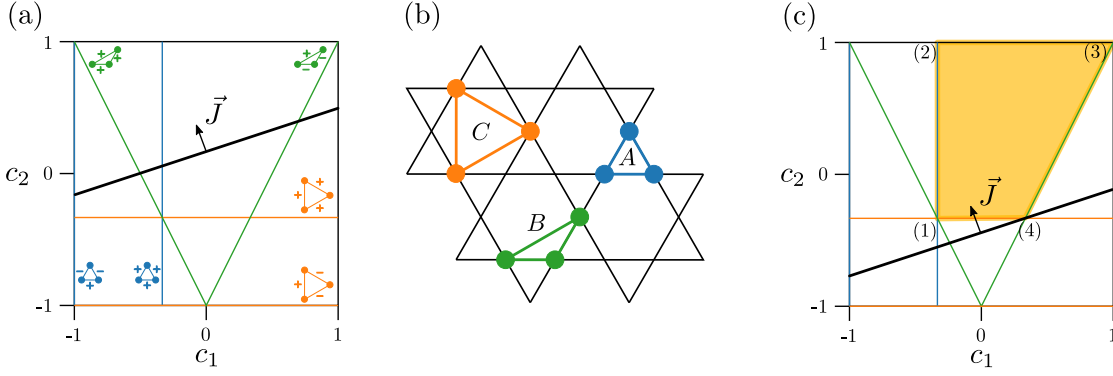


Figure 1.8 – Kaburagi and Kanamori's method on the  $J_1 - J_2$  model. (a) A fixed energy and a set of couplings correspond to a line in the correlation space. All the correlations cannot be realized by a classical Ising model; they are constrained by the possible correlations that can be reached on a three-site cluster (b). The constraints obtained from the clusters and the inequalities in Eq. 1.82 are illustrated in (a), with labels indicating the signs and the clusters used to build the inequalities. (c) The constraints finally define a polygon in the correlation space. The energy is extremal at the boundary of the polygon. The corners (1)-(4) correspond to ground state phases while the edges of the polygon correspond to first order ground state phase transitions.

the fact that for any cluster of three spins:

$$(\sigma_1 + s_2\sigma_2 + s_3\sigma_3)^2 \geq 1, \quad (1.81)$$

which implies

$$s_2\sigma_1\sigma_2 + s_3\sigma_1\sigma_3 + s_2s_3\sigma_2\sigma_3 \geq -1, \quad (1.82)$$

where  $s_2, s_3$  are arbitrary signs. These inequalities are valid for any of the clusters in Fig. 1.8b. Considering a cluster and one of the corresponding inequalities, the local constraint can be turned into a global constraint on the correlations. Indeed, the cluster is selecting a few nearest- and/or next-nearest-neighbor bonds. By applying all the lattice symmetries to the cluster, all the nearest- and/or next-nearest-neighbor bonds of the lattice can be selected. Summing the local inequality over all these copies of the cluster, one gets an inequality involving  $c_1$  and  $c_2$ .

In our case, we get the following results (by selecting some specific inequalities in Eq. 1.82):

$$\text{Cluster A : } \sigma_1\sigma_2 + \sigma_2\sigma_3 + \sigma_1\sigma_3 \geq -1 \Rightarrow 3 \sum_{\langle i,j \rangle_1} \sigma_i\sigma_j \geq -2N \Rightarrow c_1 \geq -\frac{1}{3}, \quad (1.83)$$

$$\begin{aligned} \text{Cluster B : } \sigma_1\sigma_2 \pm (\sigma_2\sigma_3 + \sigma_1\sigma_3) \geq -1 &\Rightarrow \sum_{\langle i,j \rangle_2} \sigma_i\sigma_j \pm 2 \sum_{\langle i,j \rangle_1} \sigma_i\sigma_j \geq -N \\ &\Rightarrow c_2 \pm 2c_1 \geq -1, \end{aligned} \quad (1.84)$$

$$\text{Cluster C : } \sigma_1\sigma_2 + \sigma_2\sigma_3 + \sigma_1\sigma_3 \geq -1 \Rightarrow 3 \sum_{\langle i,j \rangle_2} \sigma_i\sigma_j \geq -2N \Rightarrow c_2 \geq -\frac{1}{3}. \quad (1.85)$$

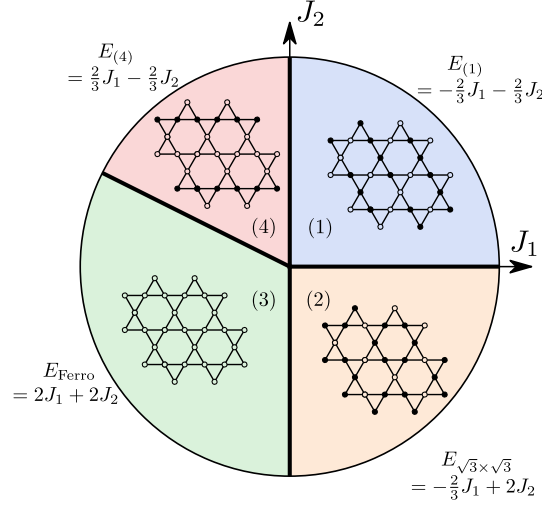


Figure 1.9 – Ground-state energies of the  $J_1 - J_2$  model on the kagome lattice from Kaburagi and Kanamori’s method. We note that while phases (2) and (3) correspond to long-range ordered states, it is easy to see phases (1) and (4) have a macroscopic ground-state degeneracy. The labels (1)-(4) correspond to the corners in Fig. 1.8.

Clearly, there could be other inequalities; here, we selected only the most restrictive ones. The set of all possible inequalities defines the convex set  $I_{J_1 - J_2}$  in the correlation space (indicated in orange in Fig. 1.8c). The set  $P_{J_1 - J_2}$  of correlations that can be realized is contained in but not necessarily equal to the inequalities set. To obtain exactly the ground state energy, one still has to prove that  $P_{J_1 - J_2} = I_{J_1 - J_2}$ . When the inequalities set is a polygon (or a polytope when generalized to a larger number of correlations), this can be done by finding an instance of a configuration realizing the correlations for each of the corners of the polygon. The fact that the correlations are known is often helpful. In the  $J_1 - J_2$  model, this is easily done, and one obtains the ground state phase diagram shown in Fig. 1.9, where for each ground-state phase we have indicated an instance of a ground-state structure which produces the correlations corresponding to the associated corner of the polytope.

### Finding the inequalities

Extending on the simple example above, the brute-force approach to finding the inequalities when we are only interested in pair interactions is essentially [101, 200]:

1. Find all possible clusters involving pairs of sites up to  $n$ th neighbors which appear in the Hamiltonian.

2. For each cluster, write all possible inequalities, i.e. for  $k$  sites:

$$\text{mod}(k, 2) \leq \left( \sum_{i=1}^k s_i \sigma_i \right)^2 \leq k^2 \quad (1.86)$$

3. For each couple (inequality, cluster), apply all lattice symmetries and extract the inequality for  $c_0, c_1, \dots, c_n$
4. From the set of all inequalities, extract the inequalities polyhedron.

Notice that for a finite  $n$ , there is a finite number of inequalities generated that way. We also note that this approach works very well in the case of the  $J_1 - J_2 - J_{3\parallel}$  model on the kagome lattice [101], as detailed in Appendix F.1.1.

When the corners of the polytope  $I$  defined by the inequalities are all constructible, then  $P = I$  and we have that each corner of the polytope corresponds to a ground state phase of the original model; additionally, as highlighted in Ref. 200, a  $k$ -dimensional region in the boundary of the polytope corresponds to a  $n + 1 - k$  dimensional region in the  $(J_0, J_1, \dots, J_n)$  ground state phase diagram. Indeed, a fixed  $\vec{J}$  together with an energy per site  $E$  corresponds to a  $n$ -dimensional hyper-surface  $\mathcal{S}_{\vec{J}}^E$  in the  $(n + 1)$ -dimensional correlation space. The energy per site reaches an extremum when  $\mathcal{S}_{\vec{J}}^E$  intersects the polytope  $P$  only at its boundary, i.e.

$$\mathcal{S}_{\vec{J}}^E \cap P \subset \partial P, \quad (1.87)$$

where we have denoted  $\partial P$  the boundary of the polytope. The corners of the polytope thus correspond to the correlations in the ground state of the model for a family of values of the couplings. Considering a corner  $\vec{c}$  of the polytope, it is easy to see that the family of models admitting this corner as ground-state correlations corresponds to an  $n + 1$  dimensional region in the ground-state phase diagram. Indeed, if  $\vec{J}_{\vec{c}}$  defines a hyper-surface that intersect the polytope *only* at this corner, there are  $n + 1$  degrees of freedom in  $\vec{J}_{\vec{c}}$ . Similarly, if  $\vec{J}_{\mathcal{B}}$  defines a hyper-surface whose intersection with the polytope is exactly the  $k$ -dimensional boundary region  $\mathcal{B}$ , there are  $n + 1 - k$  degrees of freedom in  $\vec{J}_{\mathcal{B}}$ . Thus, one-dimensional edges of the polytope correspond to phase boundaries in the ground state phase diagram, two-dimensional faces correspond to a point at the intersection of multiple phases, and so on.

When the corners of the polytope  $I$  are not obviously constructible, the problem becomes challenging. By an additional insight into the specific problem, or by computing upper bounds on the energy using small-scale Monte Carlo simulations [201], one can often convince oneself that there are missing inequalities (see e.g. Appendix F.1.2). One way to construct better inequalities is to include weights in the initial inequalities [201, 202]. Perhaps the most general approach to either deciding whether a given corner of the polytope is constructible or finding an inequality that eliminate it can be found in Refs. 25 and 157.

Another very important challenge related to this method is that in some cases it can occur that

the number of corners of the inequalities polytope becomes infinite even for a finite range of the couplings [205, 206].

### 1.4.2 MAX-MIN approach for ground state energy lower bounds

We now move on to a different method for computing ground-state energy lower bounds, akin to Anderson bounds [198]. This method was discussed in 2016 by Huang et. al. [158]<sup>9,10</sup>. It is the direct inspiration for the work presented in Chapter 2.

We are considering a generic system of Ising spins  $\vec{\sigma}_i$  on a lattice, with a translation invariant Hamiltonian  $H$  containing only local interaction terms  $h_k$  of strictly bounded range (e.g., finite range further neighbor pair interactions):

$$H(\vec{\sigma}) = \sum_{k \in \mathbf{C}} \sum_{\Gamma_k} h_{\Gamma_k}(\vec{\sigma}|_{\Gamma_k}) \quad (1.88)$$

where  $\mathbf{C}$  is a list of interaction clusters,  $\Gamma_k$  are the translations and rotations of the interaction cluster  $k$  over the lattice, and where  $\vec{\sigma}|_{\Gamma_k}$  denotes the configuration of the few spins on the translated cluster  $\Gamma_k$ . For instance, in the TIAFM Hamiltonian

$$H(\vec{\sigma}) = \sum_{\langle i,j \rangle} J \sigma_i \sigma_j, \quad (1.89)$$

there is only one interaction cluster which is the pair interaction,  $\Gamma_1$  would index the nearest-neighbor bonds and  $h_{\Gamma_1}(\vec{\sigma}|_{\Gamma_1})$  would be the term  $J \sigma_i \sigma_j$  for  $\Gamma_1 = \langle i, j \rangle$ . The essential idea for building a ground-state energy lower bound can be understood easily when thinking of this archetypal example. Indeed, in that case, the Hamiltonian can be rewritten as a sum of local Hamiltonians on the triangles tiling the lattice:

$$H(\vec{\sigma}) = \sum_{\Delta_{i,j,k}} \alpha_{\Delta} J(\sigma_i \sigma_j + \sigma_j \sigma_k + \sigma_k \sigma_i) + \sum_{\nabla_{i,j,k}} (1 - \alpha_{\Delta}) J(\sigma_i \sigma_j + \sigma_j \sigma_k + \sigma_k \sigma_i), \quad (1.90)$$

where the weight  $\alpha_{\Delta}$  describe how each bond is split between up and down triangles.

The splitting of the Hamiltonian according to equation 1.89 directly provides a lower bound for the ground-state energy per site:

$$\frac{H}{N} \geq -3J \quad (1.91)$$

which is obtained by assuming that the energy of each nearest-neighbor bond is minimized. Of course, frustration means this cannot be the case, and this lower bound is not in practice realized. A tighter lower bound is obtained by considering the different splitting of the

<sup>9</sup>They additionally propose a systematic way to compute *upper bounds* for the ground state energy which does not resort to a Monte Carlo approach but rather to existing MAX-SAT solvers.

<sup>10</sup>Although at first read it might seem like Richards, Allen and Cahn [156, 161] are proposing this same method, it can be seen that they are actually formulating the configurational polytope method in a way which is essentially the dual formulation of Huang et al.'s MAX-MIN approach, see Eq. C.5.

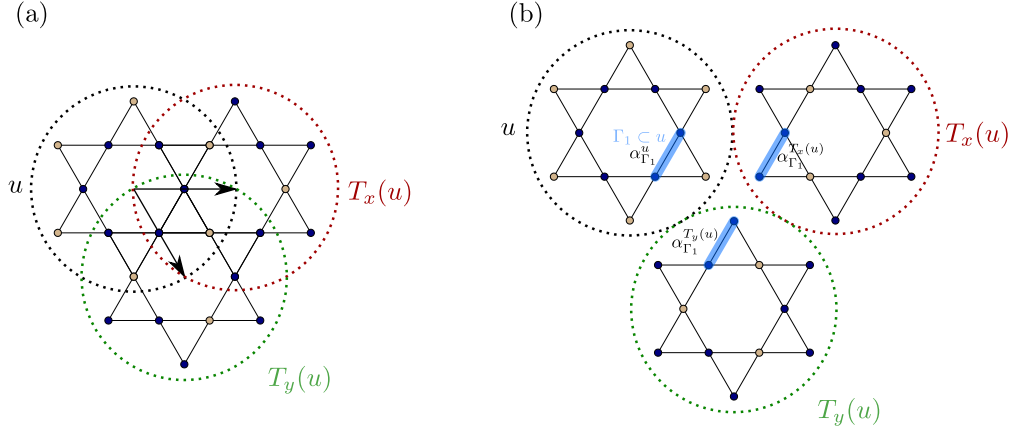


Figure 1.10 – Tiling on the kagome lattice. (a) The cluster  $u$  consists of twelve spins, and it shares five spins with each of the translated clusters  $T_x(u)$  and  $T_y(u)$ . (b) For a nearest-neighbor interaction cluster  $\Gamma_1$  shared between three translations of  $u$ , we can associate three weights that must sum to one and that state how much of the energy is accounted for in each cluster.

Hamiltonian given by Eq. 1.90:

$$\frac{H}{N} \geq -J, \quad (1.92)$$

which is obtained by assuming that the energy of each triangular Hamiltonian is minimized. Because there exists a state which minimizes all the triangular Hamiltonians simultaneously, this lower bound actually gives the ground-state energy of the nearest-neighbor antiferromagnetic Ising model.

The method we now discuss is essentially a generalization of this idea [158]. We start with a reference cluster of spins  $u$  (our triangles in the case of the TIAFM), selected such that we can cover the lattice with the set  $\mathcal{T}_u$  of overlapping translated  $u$ 's (see for instance Fig. 1.10). If there are  $N_{\mathcal{T}_u}$  such translated clusters, then the number of sites  $n_u$  associated with one cluster is  $n_u = N/N_{\mathcal{T}_u}$ . This reference cluster provides us with a way of splitting the Hamiltonian, which can be rewritten as a sum of strictly local terms acting within a single cluster provided that the range of the interactions is short enough:  $u$  must be such that for all the interaction clusters  $k \in \mathbf{C}$ , we can find  $\Gamma_k \subset u$ . We can associate to each Hamiltonian term  $h_{\Gamma_k}$  some weights  $\alpha_{\Gamma_k}^v$  describing how it is shared between various translations  $v$  of the cluster  $u$ . This results in a splitting of the Hamiltonian according to:

$$H(\vec{\sigma}) = \sum_{v \in \mathcal{T}_u} \sum_{k \in \mathbf{C}} \sum_{\Gamma_k \subseteq v} \alpha_{\Gamma_k}^v h_{\Gamma_k}(\vec{\sigma}|_{\Gamma_k}) = \sum_{v \in \mathcal{T}_u} H_v^{\vec{\alpha}}(\vec{\sigma}|_v) \quad (1.93)$$

$$\sum_{v \in \mathcal{T}_u | \Gamma_k \subseteq v} \alpha_{\Gamma_k}^v = 1, \quad \forall k, \forall \Gamma_k. \quad (1.94)$$

Since, in this form, the Hamiltonian contains only terms that act within a cluster, the minimum of  $H_u^{\vec{\alpha}}$  with respect to the spin configurations on  $u$  implies a lower bound on the global ground-



state energy per site. This bound can be optimized by maximizing over  $\vec{\alpha}$  under the constraints in Eq. 1.94:

$$E_{\text{LB}} = \frac{1}{n_u} \max_{\vec{\alpha}} \min_{\vec{\sigma}|_u} H_u^{\vec{\alpha}}(\vec{\sigma}|_u). \quad (1.95)$$

This optimization can be expressed as a LP [199]<sup>11</sup> :

$$E_{\text{LB}} \leftarrow \max_{\vec{\alpha}} E, \quad \text{with} \quad \begin{cases} H_u^{\vec{\alpha}}(\vec{\sigma}|_u) \geq n_u E \quad \forall \vec{\sigma}|_u \\ \sum_{v \in \mathcal{T}_u | \Gamma_k \subseteq v} \alpha_{\Gamma_k}^v = 1 \quad \forall k, \forall \Gamma_k \end{cases}, \quad (1.98)$$

where the result of the maximization,  $E_{\text{LB}}$ , is a lower bound for the ground state energy per site. This lower bound corresponds to the actual ground state energy if and only if it is possible to tile the plane with the local ground state configurations  $\vec{\sigma}_u$  s. t.  $H_u^{\{\alpha\}}(\vec{\sigma}|_u) = n_u E$  in a consistent way.

### 1.4.3 Alternative approaches

Finding ground-states of short-range translation invariant Ising models has applications in a wide variety of domains, and the approach we discussed here are only two of the many approaches.

An important discussion is given in Ref. 33: by constructing lower bounds for the ground state energy in a manner which is reminiscent of the two approaches discussed above, remarks can be made on the definition of frustration. They are motivated by the fact that in the TIAFM, for instance, the frustration seems to be relieved when considering triangular clusters, in the sense that all the Hamiltonians on these triangles can be minimized simultaneously. This makes it seem as though the notion of frustration is dependent on the form in which the Hamiltonian is given, and suggests having two definitions of frustration: a “soft” frustration, which can be relaxed by selecting large enough clusters, and a “strong” frustration, for which no cluster would exist which would relax the frustration (see also Chapter 2).

Another direction that we did not explore in detail is the relation of the ground-state energy lower bounds for classical Ising models to Bell inequalities [207–209]. In particular, Ref. 209 proposes a scheme which in our terms would allow one to find the configurational polytope from the inside: if the correlations can be evaluated correctly (for instance via Monte Carlo sampling), their algorithm either confirms that a candidate vertex belongs to the configurational polytope or, if not, delivers an inequality that removes this corner.

<sup>11</sup>We can introduce a matrix  $A$  and a vector  $\vec{b}$  expressing the constraints in Eq. 1.98 as

$$A\vec{\alpha} - n_u E \geq \vec{b}, \quad (1.96)$$

and, introducing  $\vec{c}^T = (0, 0, \dots, 1)$ , we can easily formulate  $A'$  such that the problem takes a more standard LP form:

$$\max_{[\vec{\alpha}, E]} \vec{c}^T [\vec{\alpha}, E], \quad A'[\vec{\alpha}, E] \geq \vec{b}. \quad (1.97)$$

In this way, it is clear that any feasible solution of the LP is also an optimal solution.

### 1.5 Summary

In this Chapter we have introduced three methods which will be used throughout the thesis: a Monte Carlo myopic dual-worm algorithm specifically designed for frustrated Ising models on the triangular and the kagome lattices, tensor networks and the VUMPS algorithm for the study of classical spin systems, and finally some approaches for constructing ground-state energy lower bounds for generalized Ising models.

## 2 Contractible tensor networks for classical frustrated Ising models

In this Chapter, we discuss the expression of the partition function of classical frustrated spin systems such that the associated tensor network can be contracted using standard techniques. The initial motivation stems from the fact that tensor networks are extremely powerful for solving counting problems [187, 210], while computing the residual entropy of a frustrated spin system with Monte Carlo can prove challenging at times, if only because it typically calls for the thermodynamic integration of the specific heat over the whole temperature range, often requires ad-hoc Monte Carlo updates to fight critical slowing-down and/or frustration effects, and implies a good control of the finite-size scaling behavior of the residual entropy [211, 212].

In the case of approximate tensor network contractions, the leading eigenvalue  $\lambda$  of the transfer matrix is directly related to the partition function for one site (see Chapter 1). In particular, when considering the partition function up to a factor related to the ground state energy per site  $E_0$  and the number of sites  $N$ , the residual entropy can be obtained as

$$\mathcal{Z}_0 := e^{\beta E_0 N} \mathcal{Z} \quad S = \lim_{\beta \rightarrow \infty} \frac{1}{N} \ln(\mathcal{Z}_0), \quad (2.1)$$

which is related to the leading eigenvalue as

$$\lambda = \mathcal{Z}_0^{1/N}, \quad (2.2)$$

if  $\mathcal{Z}_0$  corresponds to the partition function that we are trying to compute.

As we discussed in the introduction to tensor networks for classical spin systems, this leading eigenvalue can be obtained straightforwardly from the tensor network contraction algorithm. In the case of VUMPS, it is actually the direct output of the code. In CTMRG, it can be evaluated easily as depicted in Fig. 2.1.

Because of the above reasons, it seems that obtaining the residual entropy of arbitrary classical frustrated spin systems with finite-range interactions should be an easy task, only requiring to contract the appropriate tensor network. Indeed, tensor networks have been applied suc-

$$\lambda = \frac{\text{Diagram 1}}{\text{Diagram 2}}$$

Figure 2.1 – Computing the partition function for one site in CTMRG (see Refs. 125, 176).

cessfully to study phase transitions in 2D [129–132, 213] and 3D [139] frustrated classical spin systems. Moreover, very precise results have been obtained with variational optimization for two-dimensional and three-dimensional classical systems featuring a macroscopic degeneracy [126, 140]. However, with the notable exception of Refs. 126, 140, and to the best of our knowledge, a constant in these works is either the absence of macroscopic ground-state degeneracy, or, occasionally, an impossibility to converge or a convergence to a negative partition function when such macroscopic degeneracy is expected [132, 213]. There is a reason for this absence: in the case of TRG [141] and its improvements [143, 144], the problem of contracting the tensor network associated with ground states of spin glasses in the low temperature (large  $\beta$ ) limit is a well-established issue [213–215], due to the imperfect cancellation of tensor elements which scale exponentially to zero or infinity at low temperatures [214]<sup>1</sup>. In Ref. 214, it was shown that the problem can be solved by increasing drastically the numerical precision, but because of the increase in computational resources, this is not in general a viable strategy. We note that the numerical instability is also present in a TNR-based Metropolis-Hastings algorithm study of Villain’s odd model [194, 216]. These issues seem thus mostly related to the simultaneous presence of frustration and macroscopic ground-state degeneracy, and only seem to arise at low temperatures.

In this Chapter, we tackle this problem in the case of frustrated, translation invariant Hamiltonians with a finite-range of the couplings. The core idea relies on the fact that Ref. 140 uses the knowledge of the ground-state local rules to build the tensor networks. To understand why it matters, we first introduce the “standard” construction for tensor networks of classical spin systems. We then argue empirically that the failure of the contraction for this construction is at its core related to frustration, and can be managed by writing a different construction for the tensor network, relieving the frustration. We make this argument based on very simple examples, the TIAFM and the KIAFM, and suggest an approach to the solution inspired by the construction of ground-state energy lower bounds [158], before moving on to a more subtle example as an application. Further examples will be discussed in Chapter 4.

<sup>1</sup>Note that the result in Ref. 214 can be obtained with an exact contraction, and does not necessarily require using TRG. It is actually a nice Mathematica exercise to implement the exact contraction and check how the validity of the contraction depends on a set precision.

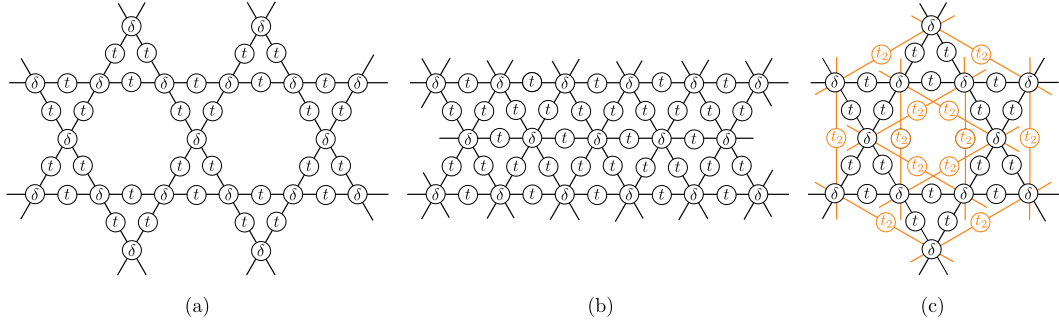


Figure 2.2 – Standard tensor network construction for the partition function of (a) the KIAFM, (b) the TIAFM, (c) the kagome lattice Ising antiferromagnet with next-nearest-neighbor interactions. The matrices  $t$  and  $t_2$  carry the Boltzmann weights, while the  $\delta$  tensors enforce that neighboring  $t$ 's ( $t_2$ 's) share the same spin.

## 2.1 “Standard” construction

Partition functions for classical spin systems can be expressed as contractions of tensor networks in the spirit of the transfer matrix formalism, a representation which is not unique. As we saw in Chapter 1, the standard construction consists in associating to each interaction a matrix  $t$  accounting for its Boltzmann weight, and to each on-site variable a  $\delta$  tensor, i.e. a tensor whose rank corresponds to the number of interactions involving that site and which is 1 only when all its indices take the same value. In the particular case of the kagome and triangular lattice Ising (anti)ferromagnets, this standard formulation leads to the tensor networks of Fig. 2.2, where the Boltzmann weights are given by

$$t^{\sigma_i, \sigma_j} = e^{-\beta J \sigma_i \sigma_j}, \quad (2.3)$$

so that the matrix  $t$  reads

$$t = \begin{pmatrix} e^{-\beta J} & e^{+\beta J} \\ e^{+\beta J} & e^{-\beta J} \end{pmatrix}, \quad (2.4)$$

with  $J > 0$  for the antiferromagnet. Contracting the tensor network amounts to finding the leading eigenvalue and leading eigenvector of the row-to-row transfer matrices (see Chapter 1). When the algorithm converges, the logarithm of the leading eigenvalue, directly related to the free energy per site at the given inverse temperature  $\beta$ , is obtained with an extremely high accuracy.

### 2.1.1 Issue with the zero temperature limit

However, it is obvious that low temperature properties cannot be directly probed from the standard construction since the zero temperature limit of Eq. (2.3) cannot be taken. Similarly, the partition function is ill-defined in that limit. In simple cases, this problem can be solved by considering the regularized partition function  $\mathcal{Z}_0$  whose zero temperature limit is always

## Chapter 2. Contractible tensor networks for classical frustrated Ising models

	KIAFM	TIAFM
MPS	0.5018331646 ( $\chi = 10$ )	0.3230659407 ( $\chi = 250$ )
Exact	0.5018331646 [18]	0.3230659669 [15]

Table 2.1 – Tensor network results obtained using VUMPS on the row-to-row transfer matrix ( $\chi$  is the MPS bond dimension). Reproduced from Ref. 140.

well defined and is directly related to the residual entropy:

$$\mathcal{Z}_0 := e^{\beta E_0 N} \mathcal{Z} \quad S = \lim_{\beta \rightarrow \infty} \frac{1}{N} \ln(\mathcal{Z}_0) \quad (2.5)$$

where we have introduced the ground state energy per site  $E_0$  and the number of sites  $N$ .

Indeed, to compute  $\mathcal{Z}_0$  instead of  $\mathcal{Z}$ , one has to contract the tensor network based on  $t_0^{\sigma_i, \sigma_j} = e^{\beta \frac{E_0}{z}} t^{\sigma_i, \sigma_j}$  where  $z$  is the number of bonds per site. In a non-frustrated system, all the pair interactions are minimized simultaneously, removing all exponentially diverging matrix elements, hence ensuring that the zero temperature limit can be taken both in  $t_0$  and  $\mathcal{Z}_0$ . However, in a frustrated system, the pair interactions cannot be minimized simultaneously and  $t_0$  still contains exponentially diverging factors. For instance, compare the tensors for the ferromagnetic and antiferromagnetic Ising models on the kagome lattice<sup>2</sup>:

$$t_0^F = \begin{pmatrix} 1 & e^{-2\beta|J|} \\ e^{-2\beta|J|} & 1 \end{pmatrix} \quad t_0^{AF} = \begin{pmatrix} e^{-\frac{4}{3}\beta J} & e^{\frac{2}{3}\beta J} \\ e^{\frac{2}{3}\beta J} & e^{-\frac{4}{3}\beta J} \end{pmatrix}. \quad (2.6)$$

## 2.2 Nearest-neighbor Ising antiferromagnet on the kagome lattice

### 2.2.1 Ground state

To build up to a generic construction, we start by re-exploring the simple frustrated models where a solution is known. The simplest is the KIAFM. In this model, the ground-state configurations have to satisfy a “2-up 1-down, 2-down 1-up” rule (no ferromagnetic triangles). This is easily seen by writing the Hamiltonian as a sum of triangular Hamiltonians

$$H = \sum_{\langle i, j \rangle} J \sigma_i \sigma_j = \sum_{\substack{\Delta_{i,j,k} \\ \nabla_{i,j,k}}} J(\sigma_i \sigma_j + \sigma_j \sigma_k + \sigma_k \sigma_i) \quad (2.7)$$

$$:= \sum_{\Delta_{i,j,k}} H_{\Delta_{i,j,k}} + \sum_{\nabla_{i,j,k}} H_{\nabla_{i,j,k}}. \quad (2.8)$$

One triangular Hamiltonian is minimized by non-ferromagnetic spin configurations on the triangle. Since the triangular Hamiltonians can be simultaneously minimized, *all* the ground

<sup>2</sup>The tensors are the same for the TIAFM.

## 2.2. Nearest-neighbor Ising antiferromagnet on the kagome lattice

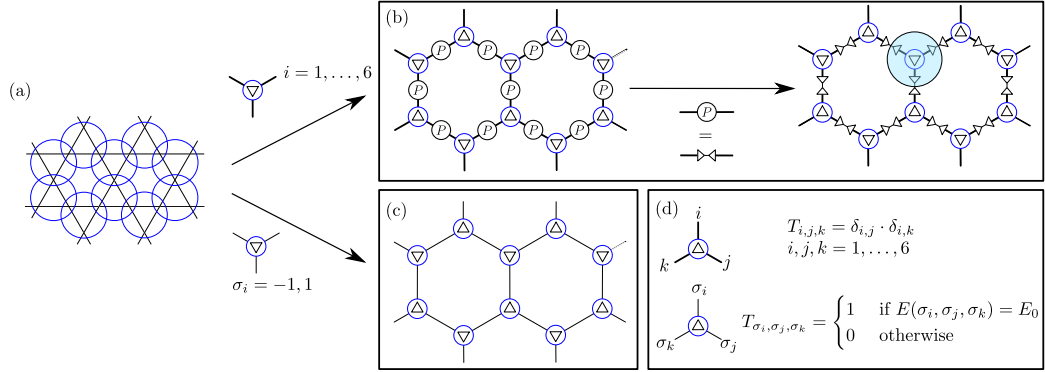


Figure 2.3 – Two similar tensor network constructions for the ground state of the kagome lattice Ising antiferromagnet. (a) The Hamiltonian can be split up into triangular terms. The configurations which minimize the triangular Hamiltonian can be tiled to create ground states. We can build a tensor network to count the tilings and study the ground state manifold by associating a tensor to each triangle. (b) One way is to label each ground-state configuration of the triangle ( $i = 1, \dots, 6$ ) and to introduce bond matrices  $P$  enforcing that spins must match. The bond dimension is significantly reduced by performing an SVD on  $P$  and re-grouping the tensors around a triangular tensor. At finite temperature, the construction is the same, only the tensors are promoted to consider more configurations and provide them with a Boltzmann weight. (c) Another way is to let the tensor network bonds bear the spin degrees of freedom and to set the triangular tensor values to one when the energy corresponds to the local ground state energy (d). The fact that shared spins must match is automatically enforced. At finite temperature, Boltzmann weights are readily included.

states of the model can be described as tilings of 2-up 1-down, 2-down 1-up triangles on kagome, where the triangular tiles fit if the shared spin is the same (Fig. 2.3a).

This is easily translated into a tensor network (slightly different from the one in Ref. 140; see also Ref. 126) on the (dual) honeycomb lattice. The prescription is as follows (Fig. 2.3b):

1. On each site of the dual lattice (center of the kagome triangles), place a  $\delta$  tensor with rank 3 and bond dimension 6 describing the 6 ground state configurations of this triangle,
2. On each bond of the dual lattice (sites of the kagome lattice), place a bond matrix  $P$  with bond dimension 6 which is 1 if the two connected tensor assign the same value to their shared spin, and 0 otherwise,
3. Reduce the bond dimension of the tensor network to 2 by performing a singular value decomposition (SVD) on the  $P$  tensors and grouping the resulting tensors with the  $\delta$  tensors on the triangles.

This tensor network is well defined and provides the ground state entropy of the kagome lattice with a precision of  $10^{-10}$  (Table 2.1). This example demonstrates that it can be very useful to

use clusters (here triangles) to build a tensor network. However, the choice of clusters, which is rather natural in the case of kagome, is in general a subtle issue, as we now show on the example of the triangular lattice.

## 2.3 Nearest-neighbor Ising antiferromagnet on the triangular lattice

### 2.3.1 Ground state

We proceed with the archetype of frustration: the triangular lattice Ising antiferromagnet. Inspired by the kagome construction, we look for *tiles* that can be used to build all the ground states. We want to find them as local ground state configurations of *local* Hamiltonians (the equivalent of the triangular Hamiltonian in the previous section) which can be *simultaneously minimized*. This last criterion is essential to ensure that each ground state can be described using these tiles.

For this, we notice that the Hamiltonian can be written as a sum of terms acting only on one type of triangles, for instance  $\triangle$  triangles:

$$H = \sum_{\langle i,j \rangle} J \sigma_i \sigma_j = \sum_{\triangle_{i,j,k}} J (\sigma_i \sigma_j + \sigma_j \sigma_k + \sigma_k \sigma_i). \quad (2.9)$$

The triangular Hamiltonian is minimized by non-ferromagnetic triangles. Since there exists a state which minimizes all the triangular Hamiltonians, the set of all ground states can be obtained by tiling non-ferromagnetic down triangles, which fit if the spins in the overlap of three triangles have the same orientation<sup>3</sup>. The corresponding tensor network has  $\delta$  tensors at the centers of up triangles and rank-3  $P$  tensors enforcing the consistency on the spin shared by three  $\delta$  tensors (Fig. 2.4a).

Another valid splitting of the Hamiltonian is to share bonds between up and down triangles:

$$H = \sum_{\langle i,j \rangle} J \sigma_i \sigma_j = \sum_{\substack{\triangle_{i,j,k} \\ \nabla_{i,j,k}}} \frac{J}{2} (\sigma_i \sigma_j + \sigma_j \sigma_k + \sigma_k \sigma_i). \quad (2.10)$$

This splitting amounts to tiling non-ferromagnetic up *and* down triangles with the condition that on a shared bond, the two spins must match; the corresponding tensor network is defined on the honeycomb lattice and has  $\delta$  tensors on up *and* on down triangles, with bond matrices  $P$  now taking care of two spins (Fig. 2.4b). Note that we have chosen to give the tensor network minimal connectivity: not all triangles that share a spin are connected, some shared spins are implicitly enforced to be the same via multiple bonds.

---

<sup>3</sup>Indeed, there cannot be a ground state containing a ferromagnetic down triangle: this would mean that one of the triangular Hamiltonians is not minimized.



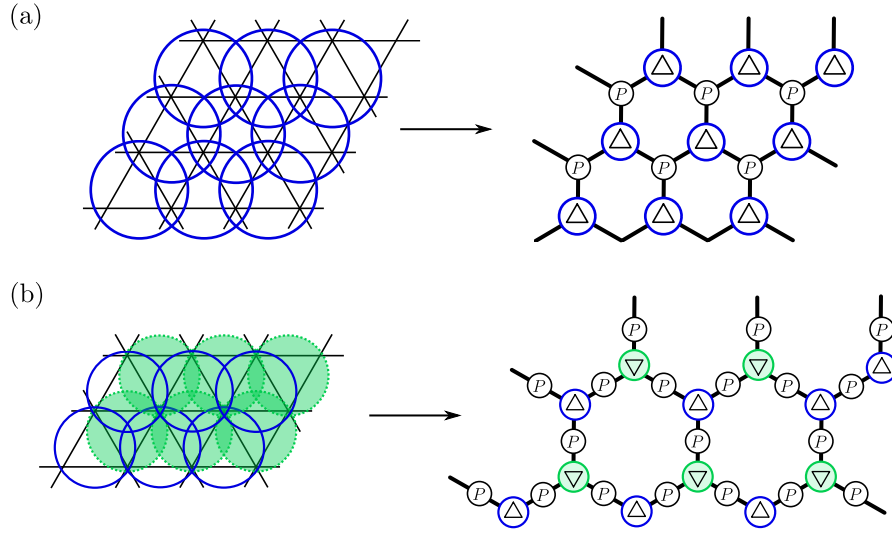


Figure 2.4 – Tensor network constructions for the ground state of the TIAFM: the Hamiltonian can be split up into triangular terms in various ways. The configurations which minimize the triangular Hamiltonian can be tiled to create ground states. (a) Construction corresponding to Eq. (2.9). (b) Construction corresponding to Eq. (2.10).

These two splittings are equally valid (in the thermodynamic limit or with periodic boundary conditions), and both solve the regularization problem by working directly in the ground state. However, standard contraction algorithms fail to converge for the first construction, while they converge and lead to the correct answer for the second one (Fig. 2.5, Table 2.1).

The main difference between the two cases is that, while in the second construction the constraint forbidding down triangles to be ferromagnetic is imposed at the level of the tensors, in the first construction it is imposed non-locally. Indeed, since the Hamiltonians in Eqs. (2.9) and (2.10) are the same, they must have the same energy for all global states, implying that if a state contains a down triangle which is ferromagnetic, it must also contain a ferromagnetic up triangle. The key point is that these two triangles can be arbitrarily far apart. Accordingly, approximate algorithms, which are based on large but finite bond dimensions, fail to converge.

#### 2.3.2 Hamiltonian tessellation

In general, we don't have such an insight on the ground state of frustrated models. To generalize tensor network constructions, the question thus boils down to being able to select *a priori* among all possible splittings of the Hamiltonian of interest, the equivalent of Eq. (2.10) and not Eq. (2.9).

On the triangular lattice, these two splittings can be seen as instances of the following *Hamiltonian tessellation* (we will use this term to describe a set of ways of splitting the Hamiltonian), which is a light version of Eqs. 1.93 and 1.94 introduced in Chapter 1 to compute ground-state

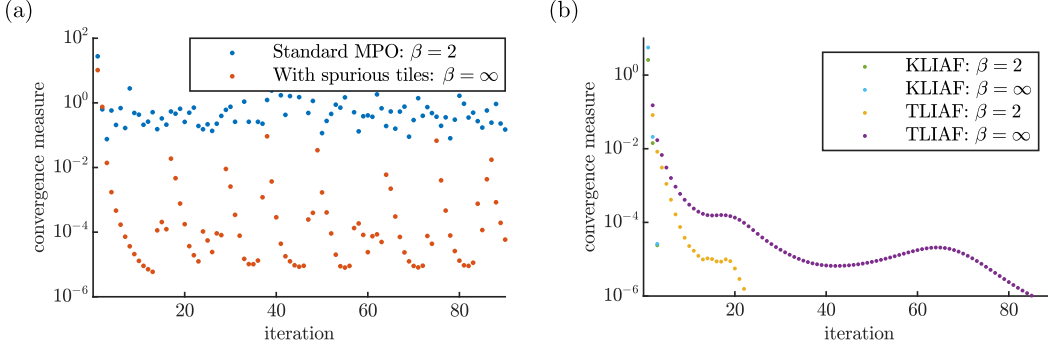


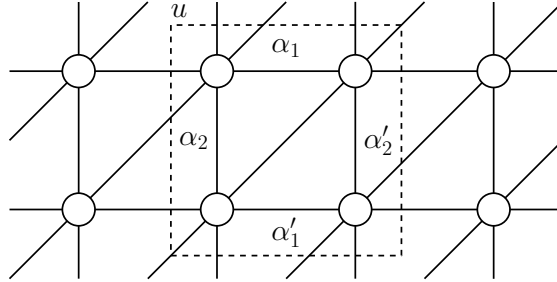
Figure 2.5 – (a) Failure of the VUMPS algorithm to converge [148–150] for the antiferromagnetic triangular lattice Ising model at  $\beta = 2$  using the standard tensor network from Fig. 2.2 and at  $\beta = \infty$  using the construction based on Eq. (2.9). (b) VUMPS convergence for the antiferromagnetic Kagome lattice Ising model at  $\beta = 2$  and  $\beta = \infty$ , and the same for the antiferromagnetic triangular Ising model using the construction of Eq. (2.11). We use MPS with a bond dimension of  $\chi = 80$  and a variational convergence measure, see Ref. 150. We observed similar behavior using CTMRG [146, 154], and a similar issue was observed for real-space renormalization techniques in Refs. 132, 213, 214.

energy lower bounds :

$$H = \sum_{v \in \mathcal{T}_u} \sum_{n \in v} \alpha_n^v h_n = \sum_{v \in \mathcal{T}_u} H_v^{\tilde{\alpha}} \quad (2.11)$$

$$\sum_{v \in \mathcal{T}_u \text{ s.t. } n \in v} \alpha_n^v = 1, \quad \forall n \quad (2.12)$$

where for later convenience we have considered a cluster  $u$  regrouping two triangles:



$\mathcal{T}_u$  is the set of clusters obtained from translating  $u$  on the lattice (with overlaps). Each cluster is seen as a collection of bonds (indexed by  $n$ ) and to each bond Hamiltonian  $h_n$  ( $h_{\langle i,j \rangle} = J\sigma_i\sigma_j$ ) we associate weights  $\alpha_n^v$  specifying how much of it is accounted for in each cluster (Eq. 2.12 imposes that terms appearing in a single cluster have weight 1). In the following, to ensure translation invariance, we always choose the  $\alpha_n^v$  to be the same for each  $v \in \mathcal{T}_u$ <sup>4</sup>. In our triangular case, each cluster has five interaction terms, four of which are

<sup>4</sup>In programmatic terms, the Hamiltonian tessellation can be thought of as a class of Hamiltonian splittings described by the choice of the cluster  $u$ , and where choosing the values for the weights  $\{\alpha_n^v\}$  defines an instance of

### 2.3. Nearest-neighbor Ising antiferromagnet on the triangular lattice

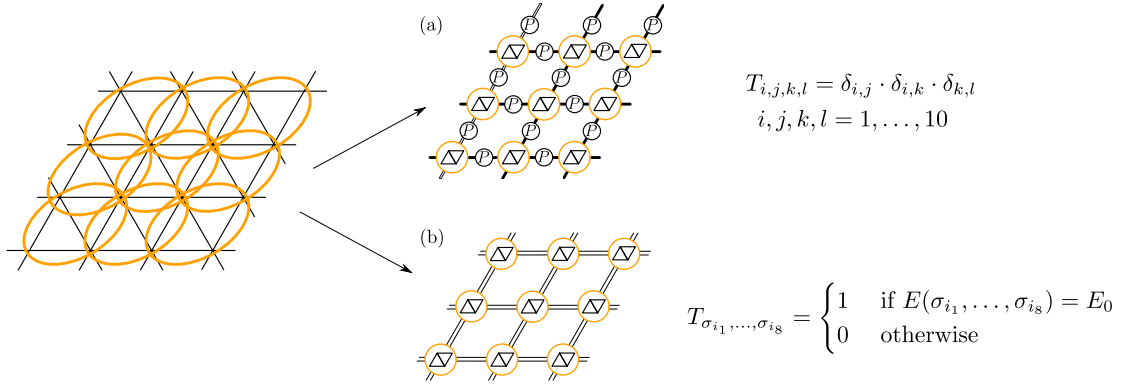


Figure 2.6 – Two tensor network constructions based on the Hamiltonian tessellation Eq. (2.11). (a) Labeling the local ground-state configurations, associating a delta tensor with each pair of triangles, and introducing  $P$  matrices enforcing that shared spins must match. The bond dimension is significantly reduced by performing an SVD on the bond matrices  $P$ . (C.f. Fig. 2.3a). (b) Alternative construction: the bond variables are the spin degrees of freedom. The local tensor selects configurations that are in the ground state. (C.f. Fig. 2.3b)

shared with neighboring clusters, and the associated weights must satisfy the constraints

$$\alpha'_{1,2} = 1 - \alpha_{1,2} \quad (2.13)$$

by translation invariance and Eq. (2.12).

We find the tiles – which will allow us to build ground states – as local ground-state configurations  $\{\vec{\sigma}|_u^{\vec{\alpha}}\}$  on  $u$  minimizing the local Hamiltonian  $H_u^{\vec{\alpha}}$ . Depending on the weights, we get different ground-state configurations  $\{\vec{\sigma}|_u^{\vec{\alpha}}\}$ ; only the weights for which all the local Hamiltonians can be simultaneously minimized provide tiles which can be used to describe the whole ground-state manifold. In our case, this further restricts the weights to

$$\alpha_1 = \alpha_2 \in [0, 1]. \quad (2.14)$$

This is the (convex) set of weights which satisfy

$$H^{\vec{\alpha}}(\vec{\sigma}|_u) \geq -J \forall \vec{\sigma}|_u \text{ on } u \quad (2.15)$$

where  $-J$  is the ground state energy per cluster. The boundaries of the convex set are defined by some of these inequalities becoming equalities.

In this formulation, we can see in a new light what happens on the triangular lattice. By construction, for any weights in the convex set defined by Eqs. (2.13) and (2.14), all the ground states can be constructed as tilings of the local ground-state configurations. On the one hand, Eq. (2.10) corresponds to Eq. (2.11) with  $\alpha_1 = \alpha_2 = 1/2$ . There are 10 local ground

the class.

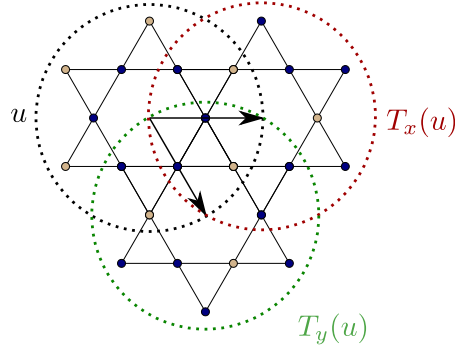


Figure 2.7 – A tessellation of spins on the kagome lattice: the cluster  $u$  consists of twelve spins, and it shares five spins with each of the translated clusters  $T_x(u)$  and  $T_y(u)$ .

state configurations of the unit  $u$ , hence 10 tiles. These are the configurations containing no ferromagnetic triangles. On the other hand, Eq. (2.9) corresponds to Eq. (2.11) with  $\alpha_1 = \alpha_2 = 0$ . At this point (which lies on the boundary of the convex set), an additional accidental ground-state degeneracy occurs: configurations for which the up triangle is ferromagnetic now have the ground-state energy as well. These two additional tiles cannot play a role in the ground-state manifold, since there are weights for which they are not ground-state tiles; so, they cannot fit into any global ground state. We call such tiles *spurious* because they do not really belong to the ensemble of ground-state tiles. Thus, according to our observation that contraction is possible for the tessellation of Eq. (2.10) but not for that of Eq. (2.9), it sounds like a good idea to get rid of such tiles to ensure the convergence of the tensor network.

## 2.4 Generic implementation

All of the above can be quite straightforwardly adapted for a generic system of  $d$ -level spins  $\sigma_i$  on a lattice, with a translation invariant Hamiltonian containing only local interaction terms  $h_n$  of strictly bounded range (e.g., finite range farther neighbor pair interactions):

$$H(\vec{\sigma}) = \sum_{n \in \mathbf{C}} \sum_{\Gamma_n} h_n(\vec{\sigma}|_{\Gamma_n}) \quad (2.16)$$

where  $\mathbf{C}$  is a list of interaction clusters,  $\Gamma_n$  are the translations and rotations of the interaction cluster  $n$  over the lattice, and where  $\vec{\sigma}|_{\Gamma_n}$  denotes the configuration of the few spins on the translated cluster  $\Gamma_n$ .

### 2.4.1 Maximal lower bound

The first part of the approach is exactly what we did in Chapter 1, Sec. 1.4.2 when we presented the MAX-MIN approach to compute ground-state energy lower bounds. Given a reference cluster of spins  $u$ , we cover the lattice with the set  $\mathcal{T}_u$  of overlapping translated  $u$ 's such that

the Hamiltonian can be rewritten as a sum of strictly local terms acting within a single cluster (see for instance Fig. 2.7).

Just like in the triangular case, we associate to each Hamiltonian term  $h_n$  weights  $\alpha_n^v$  describing how they are shared between clusters, recovering exactly the expression that we gave for the triangular lattice in Eqs. (2.11) and (2.12). Since, in this form, the Hamiltonian contains only terms that act within a cluster, we retrieve our LP from Eq. 1.98 by maximizing over  $\alpha_n^u$  the minimum of the local Hamiltonian:

$$E_u \leftarrow \max_{\vec{\alpha}} E, \quad \text{with} \quad \left\{ \begin{array}{l} H_u^{\vec{\alpha}}(\vec{\sigma}|_u) \geq E \quad \forall \vec{\sigma}|_u \\ \sum_{v \in \mathcal{T}_u \text{ s.t. } \Gamma_n \subseteq v} \alpha_{\Gamma_n}^v = 1 \quad \forall n, \forall \Gamma_n \end{array} \right. , \quad (2.17)$$

where the result of the maximization,  $E_u$ , is the candidate ground state energy per cluster, and where  $\vec{\sigma}|_u$  goes through the configurations of  $u$ .

### 2.4.2 Getting the most out of knowing the ground state energy

The point that we want to make is that if the maximal lower bound is saturated (i.e. if  $u$  is such that there exists a global state which has  $E_u$  as energy per cluster, or equivalently when this lower bound matches an upper bound), one gets more than just the ground-state energy. Indeed, for the weights  $\vec{\alpha}$  which realize this maximal lower bound, by construction the local cluster Hamiltonians  $H_u^{\vec{\alpha}}$  can be simultaneously minimized if and only if the maximal lower bound is saturated. We will say that such a Hamiltonian has *minimal frustration*. In this case, all the ground states are characterized as tilings of the configurations of the cluster  $u$  belonging to the set

$$G^{\vec{\alpha}} := \left\{ \vec{\sigma}|_u \text{ s.t. } H_u^{\vec{\alpha}}(\vec{\sigma}|_u) = E_u \right\}. \quad (2.18)$$

In this sense, the set of tiles  $G^{\vec{\alpha}}$  is a local rule.

There are however many solutions of (2.17), namely all sets of weights  $\vec{\alpha}$  satisfying

$$H_u^{\vec{\alpha}}(\vec{\sigma}|_u) \geq E_u, \quad \text{for all configurations } \vec{\sigma}|_u \text{ of } u. \quad (2.19)$$

As we have seen in the triangular lattice case, not all such solutions  $\vec{\alpha}$  will do. In the space of the weights, the set of  $\vec{\alpha}$  for which all these inequalities are satisfied takes the form of a convex set, which we will refer to as  $A^u$ , corresponding to the generalization of Eqs. (2.14). The set of ground-state tiles  $G_u^{\vec{\alpha}}$  does not depend on the weights in the *interior* of  $A^u$ . However, just like in the triangular lattice case, the boundary is defined by some of the inequalities becoming equalities, and accidental degeneracies will occur:

$$G_u^{\vec{\alpha} \in \text{Int}(A^u)} \subset G_u^{\vec{\alpha} \in \text{Boundary}(A^u)}. \quad (2.20)$$

The associated additional configurations must be spurious tiles, which could spoil the contractibility of the tensor network as well as hinder the understanding of the ground-state

manifold.

Thus, for a generic problem, we need to

1. find a cluster  $u$  such that the maximal lower bound for the ground state energy,  $E_u$ , is saturated,
2. find weights  $\tilde{\alpha}$  in the interior of  $A^u$ .

Note that the second step allows one to get rid of avoidable spurious tiles, but there could as well be some tiles in  $G_u^{\tilde{\alpha} \in \text{Int}(A^u)}$  which do not belong to any ground state. Getting rid of the avoidable tiles might help, but in general, because of the lack of insight into the problem, several clusters might need to be tested. Additionally, to find a point in the interior of  $A^u$ , splitting the weights evenly among clusters does not always work. The fact that the problem can be phrased as a linear program is thus very helpful: first, it allows one to rapidly test for various candidate clusters  $u$ ; second, with a bit of additional work as mentioned below, it allows one to enforce the selection of weights in the interior of  $A^u$ , thus getting rid of avoidable spurious tiles.

As a technical note, linear program solvers only output extreme points of the convex set, so simply solving (2.17) will systematically give  $\tilde{\alpha}$  corresponding to avoidable spurious tiles. We show in Appendix D how to overcome this by finding boundary points that form a simplex of the same effective dimension as  $A^u$ , ensuring that any point in the interior of this simplex will also lie in the interior of  $A^u$ <sup>5</sup>. Another technical challenge is that the number of constraints scales exponentially in the number of spins per cluster. In Appendix D, we also show how to work around this problem by systematically and progressively incorporating inequalities as we build the corners of the interior simplex, such that only a very limited number of inequalities is needed.

### 2.4.3 Generic tensor network

Finally, the procedure to write a contractible tensor network is easily generalized. For the ground state, the tiles  $G_u^{\tilde{\alpha} \in \text{Int}(A^u)}$  are described by  $\delta$  tensors, placed on each dual vertex, coinciding with the clusters of  $\mathcal{T}_u$ . The overlapping spins matching condition is enforced by bond matrices  $P$ . Performing an SVD on the rank-deficient bond matrices keeps the tensor network bond dimension reasonably small. This is the generalization of the construction in Fig. 2.6a<sup>6</sup>. The generalization of the construction in Fig. 2.6b is obtained by labeling the tensors with the surrounding spin variables, and setting the weight to one when the configuration belongs to  $G_u^{\tilde{\alpha} \in \text{Int}(A^u)}$ <sup>7</sup>.

---

<sup>5</sup>A simplex is the generalization to high dimension of triangles and tetrahedrons.

<sup>6</sup>In a sense, we have obtained a vertex model.

<sup>7</sup>This construction is somewhat reminiscent of Baxter's "interactions round a face" models (IRF models), where the local weight takes into account the spins around a face of the square lattice.

#### 2.4.4 Testing for the saturation of the maximal lower bound

Provided that the maximal ground-state lower bound is saturated, all of the above is given. Rigorously proving that it is the case is equivalent to finding one ground state, or proving that the tiles  $G_u^{\tilde{\alpha}}$  corresponding to the maximal lower bound can tile the plane. In general, this is an undecidable problem [208, 217–219].

However, in practice, there is a whole range of models where it remains manageable, for instance by constructing an upper bound with linear programming [158]. Moreover, the tensor network formulation typically helps to deal with this question. Indeed, if the tiles  $G_u^{\tilde{\alpha}}$  cannot tile the plane, then the associated partition function is zero in the thermodynamic limit. Thus, reciprocally, if the (exact) leading eigenvalue associated with the transfer matrix is larger than or equal to one, this implies that the plane can be tiled using  $G_u^{\tilde{\alpha}}$  and that the lower bound is saturated. In practice, we are using tensor network algorithms which compute the contraction of the partition function and the leading eigenvalue approximately. The convergence parameter is the bond dimension of the candidate leading eigenvector in the form of a MPS. We deduce from the above that if, for increasing MPS bond dimensions, the approximate contractions converge consistently to a leading eigenvalue which is larger than or equal to one, we have numerical evidence that the maximal lower bound is saturated, implying in turn that we found the ground-state manifold and its degeneracy. Conversely, if the contraction does not converge, we cannot conclude: this could either mean that the lower bound is not saturated, or that it is saturated but unavoidable spurious tiles spoil the convergence. In this case, one should try a different cluster.

#### 2.4.5 Convergence at finite temperature

We note additionally that the above construction can in principle readily be generalized to a finite-temperature tensor network. Here, we just give the idea for the construction and show that it converges at finite temperatures for the triangular lattice Ising antiferromagnet.

The ground-state tensor network that we built can be seen as the zero-temperature limit of a slightly more general construction, where the  $\delta$  tensor is promoted to a tensor  $D_0$  (with a larger bond dimension) describing each configuration and its Boltzmann weight relative to the ground state. In the triangular lattice case, the finite-temperature tensor network formulation of the regularized partition function  $\mathcal{Z}_0$  associated with a Hamiltonian tessellation using  $u$  and weights  $\alpha_1 = \alpha_2 =: \alpha \in ]0, 1[$  on the TIAFM is thus given by bond matrices  $P$  of bond dimension 16, and by  $D_0$  tensors of the same bond dimension defined on each couple of triangles as

$$\begin{aligned} D_0^{\{\sigma\},\{\sigma'\},\{\sigma''\},\{\sigma'''\}}(\alpha, \beta) \\ = \delta^{\{\sigma\},\{\sigma'\},\{\sigma''\},\{\sigma'''\}} B(\{\sigma\}, \alpha, \beta) \end{aligned} \tag{2.21}$$

where the Boltzmann weight is given by

$$B(\{\sigma\}, \alpha, \beta) = e^{-\beta J[\alpha(\sigma_1\sigma_2 + \sigma_1\sigma_4) + (1-\alpha)(\sigma_2\sigma_3 + \sigma_3\sigma_4) + 2]} \quad (2.22)$$

and where, for short, we denoted by  $\{\sigma\}$  the configuration of the four spins. After SVD and grouping, the bond dimension of the network is reduced to 4. Importantly, in the standard construction, tensor network algorithms fail to converge even at modest inverse temperatures, when  $\beta$  is still small enough that the values in  $t_0$  are well defined, and no “NaN” arise; the criterion for convergence is simply never met. In contrast, our tensor network can be contracted without issues at any inverse temperature (Fig. 2.5). The zero-temperature limit of  $D_0$  is well-defined by construction, and in that limit it reduces to a  $\delta$  tensor corresponding to the 10 ground state tiles on  $u$ .

## 2.5 Using symmetries

Before moving on to the full example, let us describe how to take advantage of the cluster symmetries, something we have not discussed in the above. Here, we give a few ideas to simplify the search for optimal solutions by using the cluster symmetry group  $G_u$ , i.e. the group of local transformations that leave  $u$  invariant. They are essentially an application of existing approaches in semi-definite programming, see for instance Ref. 220, and are very similar to the ideas used in exact diagonalization (see e.g. Ref. [221]).

### 2.5.1 Invariance under the cluster symmetry group

We want to show that the LP in Eq. 2.17 is invariant under the cluster symmetry group  $G_u$ , under the assumption that the original Hamiltonian is also invariant under this group. We first motivate this by showing that if this linear program is invariant, then we can look for an optimal solution in the subspace of weights which are invariant under  $G_u$ .

**Invariance of a LP under a symmetry group.** Just as in semi-definite programming, considering a LP

$$\max_{\vec{y}} \vec{c}^T \vec{y} \text{ subject to } A\vec{y} \leq \vec{b}, \vec{y} \geq \vec{0}, \quad (2.23)$$

we say that it is invariant under the group  $G$  if for any feasible solution  $\vec{y}$  (that is,  $\vec{y}$  satisfies the constraints, but is not necessarily optimal) and for any  $g \in G$

$$g\vec{y} \text{ is feasible (i.e., also satisfies the constraints)}, \quad (2.24)$$

$$\text{and } \vec{c}^T g\vec{y} = \vec{c}^T \vec{y}. \quad (2.25)$$

**If the LP is  $G$ -invariant, we can look for an optimal solution in the set of symmetric  $\vec{y}$ .**



It is easy to see that if the program in Eq. 2.23 is  $G$ -invariant, it implies that if  $\vec{y}^*$  is an optimal solution, its group average

$$\vec{y}_G^* := \frac{1}{|G|} \sum_{g \in G} g \vec{y}^* \quad (2.26)$$

is also an optimal solution. Indeed, by definition of the invariance of Eq. 2.23 under  $G$ ,  $g \vec{y}^*$  is feasible, and thus

$$\frac{1}{|G|} A \sum_{g \in G} g \vec{y}^* \leq \frac{1}{|G|} \sum_{g \in G} \vec{b} = \vec{b} \quad (2.27)$$

which implies that  $\vec{y}_G^*$  is feasible. Furthermore,

$$\vec{c}^T \vec{y}_G^* = \vec{c}^T \left( \frac{1}{|G|} \sum_{g \in G} g \vec{y}^* \right) = \frac{1}{|G|} \sum_{g \in G} (\vec{c}^T g \vec{y}^*) \quad (2.28)$$

$$= \frac{1}{|G|} \sum_{g \in G} (\vec{c}^T \vec{y}^*) = \vec{c}^T \vec{y}^* \geq \vec{c}^T \vec{y} \quad \forall \vec{y}, \quad (2.29)$$

which shows that  $\vec{y}_G^*$  is also optimal. This implies in turn that we can look for solutions in the subspace of invariant  $\vec{y}$ 's.

**The LP from the MAX-MIN approach is invariant under the cluster symmetry group  $G_u$ .**

As mentioned in Sec. 1.4.2, the LP in Eqs. 2.17 can be rewritten as

$$\max_{[\vec{\alpha}, E]} \vec{c}^T [\vec{\alpha}, E], \quad A' [\vec{\alpha}, E] \geq \vec{b}. \quad (2.30)$$

where  $\vec{c}^T = (0, 0, \dots, 1)$  and where we have introduced  $A'$  and  $\vec{b}$  such that

$$A' [\vec{\alpha}, E] \geq \vec{b} \iff H_u^{\vec{\alpha}}(\vec{\sigma}|_u) \geq E_u, \quad \text{for all configurations } \vec{\sigma}|_u \text{ of } u. \quad (2.31)$$

We introduce  $\mathcal{D}$  the representation of the cluster symmetry group on the space of weights  $\vec{\alpha}$ , and  $\Gamma$  the representation of this same group on the cluster configurations  $\vec{\sigma}|_u$ . Eq. 2.25 is trivially satisfied since  $\vec{c}^T = (0, 0, \dots, 1)$ . The fact that Eq. 2.24 is satisfied can be seen by applying an element  $g$  of the group to a given cluster configuration:

$$H_u^{\vec{\alpha}}(\vec{\sigma}|_u) \geq E \quad \forall \vec{\sigma}|_u \quad (2.32)$$

$$\Rightarrow H_u^{\vec{\alpha}}(\Gamma(g)\vec{\sigma}|_u) \geq E \quad \forall \vec{\sigma}|_u \quad \forall g \in G \quad (2.33)$$

$$\Rightarrow H_u^{\mathcal{D}(g)^{-1}\vec{\alpha}}(\vec{\sigma}|_u) \geq E \quad \forall \vec{\sigma}|_u \quad \forall g \in G \quad (2.34)$$

To go from the first to the second line, we used that if a configuration belongs to the local ground state tiles, then its transformations under the cluster symmetry group must also belong to the ground state tiles; and to go from the second to the third, we simply applied the group element inverse to the weights instead of applying the group element to the tile.

This might seem counter-intuitive when thinking of a Hamiltonian with a long-range-ordered ground state that spontaneously breaks some or all of these symmetries. However, if a LRO ground state breaks these symmetries, then there must be some finite ground-state degeneracy relating the various symmetry-broken ground states. These must all be described by the same set of tiles, and therefore if one tile belongs to the local ground state configurations, so do its transformation under  $G_u$ . The spontaneous symmetry breaking does not happen at the level of the tiles, but at the level of the tiling: in a symmetry broken ground state, tiles belonging to one symmetry-broken sector can only be tessellated with tiles of the same sector, just as the Type-I tiles above.

**Reducing the number of configurations.** This shows that we can look for the solutions  $\vec{\alpha}$  in the subspace of weights that are invariant under the cluster symmetry group. Since we now optimize in the set  $S_{G_u}$  defined as:

$$S_{G_u} := \{\vec{\alpha} | \forall g \in G_u, D(g)\vec{\alpha} = \vec{\alpha}\} \quad (2.35)$$

we trivially have that for any configuration  $\vec{\sigma}|_u$ ,

$$H_u^{\vec{\alpha}}(\Gamma(g)\vec{\sigma}|_u) = H_u^{D(g)^{-1}\vec{\alpha}}(\vec{\sigma}|_u) = H_u^{\vec{\alpha}}(\vec{\sigma}|_u). \quad (2.36)$$

We can reduce the number of configurations to one per orbit, where we say that  $\vec{\sigma}|_u$  and  $\vec{\sigma}'|_u$  are in the same orbit if and only if there exists  $g \in G_u$  s.t.  $\vec{\sigma}|_u = \Gamma(g)\vec{\sigma}'|_u$

### 2.5.2 An example

As a simple example, we consider the  $J_1$ - $J_2$  model of Sec. 1.4.1, on the kagome lattice:

$$H = J_1 \sum_{\langle i,j \rangle} \sigma_i \sigma_j + J_2 \sum_{\langle i,j \rangle_2} \sigma_i \sigma_j. \quad (2.37)$$

We use the cluster shown in Fig. 2.8a. We assume cluster symmetries as well as translation invariance. First, because they are not shared between neighboring clusters, the weights associated with the  $J_2$  couplings have to be all set to one, and so do the weights of the two  $J_1$  interactions that are lying inside the cluster. Then, by applying the cluster symmetries, we can reduce the space of weights to a single parameter  $\alpha$ . Applying the cluster symmetries and the  $\mathbb{Z}_2$  symmetry, we only have to consider a smaller number of configurations.

For  $J_1 = 1$  and  $J_2 = 0.2$ , the results are shown in Fig. 2.8b. This example is important for two reasons: first, it shows that we cannot always select the weights to be evenly shared between bonds, depending on the cluster that is used. Indeed, here,  $\alpha = 1/2$  would not produce the correct ground-state tiles. Second, it shows that a solution that is invariant under the cluster symmetry group is not necessarily in the interior of the convex set  $A^u$ . Indeed, at  $\alpha = 0$  and  $\alpha = 0.4$ , there are accidental degeneracies.

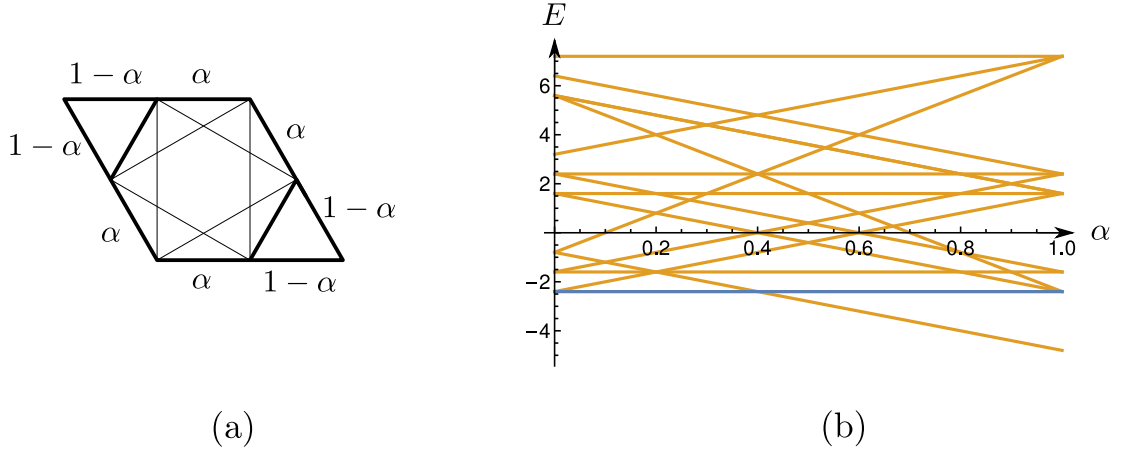


Figure 2.8 – (a) The cluster used to look for the ground-state energy of the  $J_1$ - $J_2$  model. The thin lines correspond to  $J_2$  interactions. (b) The energies of the cluster configurations for the  $J_1$ - $J_2$  Hamiltonian on kagome (Eq. 2.37), as a function of the free weight  $\alpha$ . The ground state energy is shown in blue.

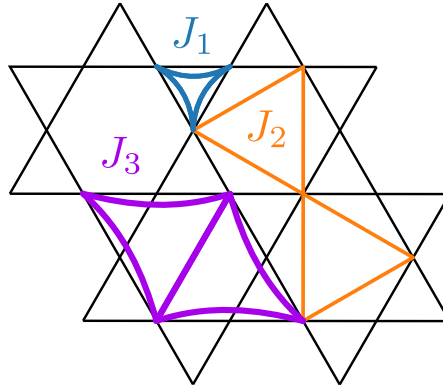


Figure 2.9 – The two-body Ising interactions present in the test model 2.38.

## 2.6 Farther-neighbor Ising model on the kagome lattice

As a challenging test case and motivated by our interest in models with farther-neighbor couplings on the kagome lattice, we consider a frustrated Ising model inspired by Refs. 82, 99, 101, 102, 222:

$$H = J_1 \sum_{\langle ij \rangle} \sigma_i \sigma_j + J_2 \sum_{\langle\langle ij \rangle\rangle} \sigma_i \sigma_j + J_3 \sum_{\langle\langle\langle ij \rangle\rangle\rangle} \sigma_i \sigma_j, \quad (2.38)$$

where the sums run over (distance-based) first, second, and third nearest neighbors respectively, as is illustrated in Fig. 2.9. We take  $J_1 = -1$  (ferromagnetic), and  $J_2 = J_3 = 10$  (antiferromagnetic).

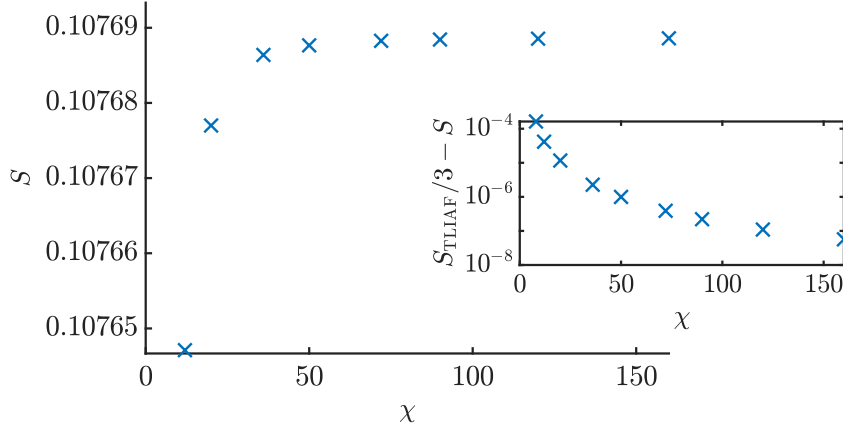


Figure 2.10 – The residual entropy per site of the minimally frustrated tensor network for the model in Eq. (2.38), obtained with the VUMPS algorithm with different bond dimensions  $\chi$ . In the inset we show that the value converges to a third of the value for the Ising antiferromagnet on the triangular lattice [15].

### 2.6.1 Results

As our reference cluster  $u$  for the tessellation, we use a full kagome star (12 spins, Fig. 2.7), for which 18 weights need to be determined. From the linear program, we find a ground state energy lower bound  $E = \frac{2}{3}J_1 - \frac{2}{3}J_2 - J_3$  and 132 candidate ground state tiles. The tensor network we construct for the ground state ensemble, assuming those candidate tiles, has bond dimension 18 (very small compared to the total number of tiles of the cluster,  $2^{12} = 4096$ ). The VUMPS algorithm [148–150] converges nicely for this MPO for all bond dimensions of the MPS and finds a leading eigenvalue that is both real and larger than one. We thus obtain with a good level of confidence that the ground-state tiles can tile the plane, which implies minimal frustration. The contraction readily provides the ground-state entropy to a very high precision (Fig. 2.10).

Note that this method did not rely on constructing a periodic ground state, or any insight from the Monte Carlo results which are presented below; the mere existence of the state in Fig. 2.11 however *proves* this result.

For comparison, we calculated the residual entropy using Monte Carlo methods (the technical details can be found in Appendix A.4.1). Though one can easily generate some ground-state configurations of the model (Fig. 2.11), the evaluation of the residual entropy via thermodynamic integration is a challenge which required a thousand CPU hours for a significantly less accurate result (compare Fig. 2.12 to Fig. 2.10).

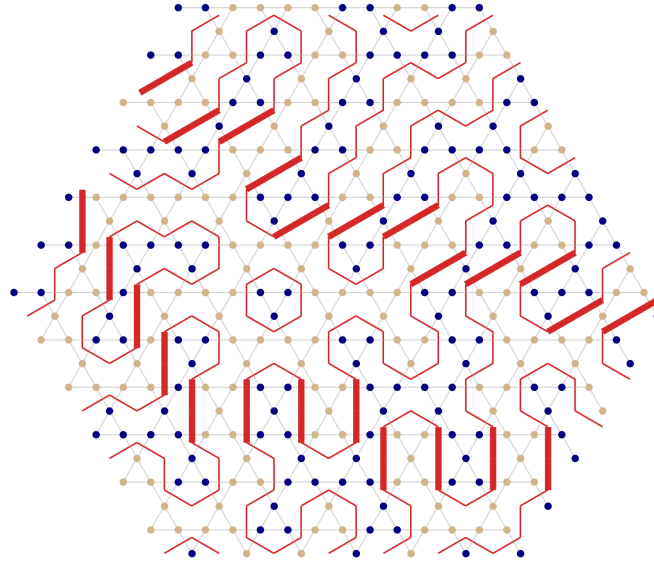


Figure 2.11 – An example of a spin configuration in the ground state. The red lines separate up and down spins, and the red lines that cross a hexagon in a straight line have been accentuated. The tiles with a thick line separate symmetry-broken sectors where all up (resp. down) triangles are ferromagnetic. This configuration was generated during our Monte Carlo sampling and illustrates the results obtained from the tensor network.

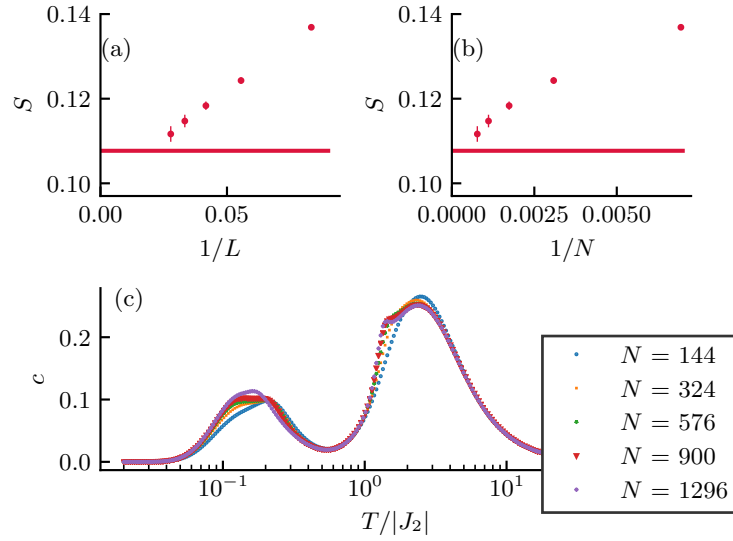


Figure 2.12 – Monte Carlo results for the residual entropy as a function of the inverse linear system size (a) and of the inverse system size (b). For each size, the entropy is obtained by integrating the heat capacity (c) over the temperature on the whole temperature range. The heat capacity is measured on 216 temperatures thermalized with 16'384 Monte Carlo steps (MCS, consisting of 2 full updates of the state with single spin flip, 2 with the dual worm and one parallel tempering step) and measured over 1'048'576 MCS.

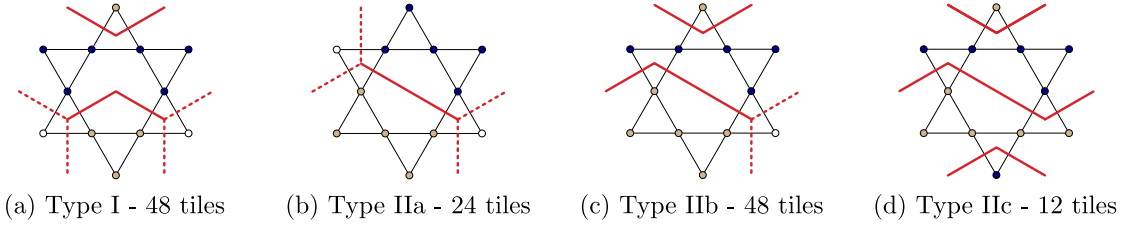


Figure 2.13 – The two types of tiles in the ground state of the model with ferromagnetic  $J_1$  and antiferromagnetic  $J_2$  and  $J_3$  interactions. There are 132 tiles in total. The blue, respectively yellow dots correspond to up, respectively down spins. The red segments represent the lines on the dual dice lattice separating up from down spins. The dotted segments stand for the fact that the line can go in either directions (but not both).

### 2.6.2 Analysis of the ground-state tiles

The residual entropy obtained by contracting the tensor network is within  $10^{-7}$  of one third of the TIAFM entropy, suggesting some kind of correspondence between the dominant part of the ground-state manifolds of both models. This correspondence can be partially understood thanks to exact statements based on the tiles and the tensor network construction. The 132 tiles can be split up into two types: type-I tiles for which all up (respectively down) triangles are ferromagnetic (Fig. 2.13a), and type-II tiles which have one up and one down antiferromagnetic triangle (Fig. 2.13b, c, and d). We proceed to understand the ground-state ensemble of this model by first characterizing the type-I ensemble, and then describing how type-II tiles modify this picture.

#### Type-I ensemble

The type-I tiles are exactly all the configurations of  $u$  for which the three ferromagnetic triangles are never all pointing in the same direction. Each ferromagnetic triangle can be seen as an Ising degree of freedom; the type-I tiles are thus all the configurations for which these three degrees of freedom are never aligned. The tiles can be separated into two sub-types by reflection symmetry: the tiles where the new Ising degrees of freedom live on up triangles, and those where they live on down triangles. A global state made of tiling uniquely type-I tiles can only be made of one of these sub-types, because the tiles in one sub-type cannot be overlapping with the tiles in the other sub-type. Therefore, the type I ensemble features reflection symmetry breaking.

The up (down) triangles are arranged as triangular lattice, and we have seen that the type-I tiles are *all* the configurations for which the three effective Ising degrees of freedom are not all aligned. So, there are no other constraints for tiling these type-I tiles. It straightforwardly follows that the effective Ising degrees of freedom must act like the spins of an Ising antiferromagnet on the triangular lattice, a model whose residual entropy is known exactly [15]. The residual entropy of the type-I ensemble is thus given by  $S = \frac{1}{3} S_{\text{TIAFM}}$ .

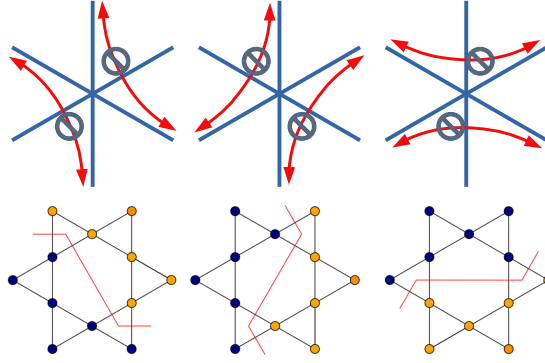


Figure 2.14 – The red arrows indicate which angles can not be made by the different types of domain wall. These restrictions make it such that domain walls can not make U-turns.

### Type-II ensemble

First, let us distinguish the type-II tiles from the type-I tiles. All the type-II tiles have a line (indicating an interface between up and down spins) running *straight* across the hexagon. Conversely, all the configurations of the kagome star satisfying this description are type-II tiles. In type-I tiles on the other hand, the lines separating up from down spins must only live on up, respectively down triangles. An immediate consequence of this is that type-II tiles can connect type-I tiles in different reflection symmetry sectors – if there are states containing the two types of tiles.

A key characteristic of a type-II tile is the orientation of the line crossing the hexagon. We use this to identify three subtypes of type-II tiles, illustrated in Fig. 2.14.

Making exact statements about how the tiles of the various subtypes can be matched together is not as easy as in the case of the type-I tiles. To see which subtypes can neighbor one another and how, we are going to use a small tensor network construction, and exact contractions. Imagine a patch of  $5 \times 5$  clusters where we restrict the center tile to one subtype of the type-II tiles, and ask what types the surrounding clusters may be, while satisfying the usual tiling rules. The tensor network for this is shown in Fig. 2.15. To each tensor neighboring the central cluster, we add a leg, allowing one to probe the local configuration. After contraction, the indices of the resulting tensor thus correspond to labels of the tiles of the six nearest-neighbor clusters. If the value of the tensor at a certain set of indices is zero, it means that this configuration of neighboring clusters is not allowed. Some non-zero elements may become zero if we consider a larger patch, or even only if we consider the entire infinite plane - namely, the configuration might be allowed locally but create some tiling issues at larger scales or at infinity.

The first result that we obtain is that a type-II tile must have *exactly two* type-II tiles of the same subtype as nearest neighbors. The type-II tiles must thus make unending strings that conserve subtype, and these strings cannot cross or fuse. Additionally, we obtain from the forbidden local cluster configurations that these strings must either go straight or make  $120^\circ$  angles, but

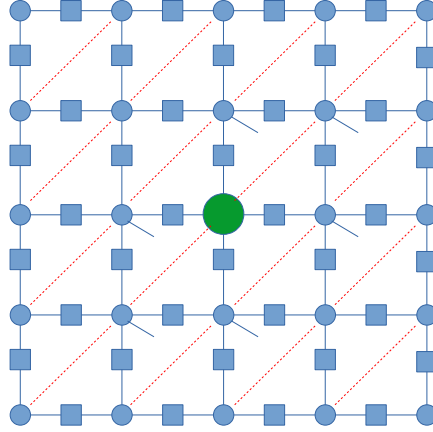


Figure 2.15 – The vertex tensors are  $\delta$  tensors representing the cluster configurations that make up the ground states, on the bonds are the usual  $P$  matrices enforcing tiling rules. Of course, in practice, we perform an SVD and exact truncation of these rank-deficient matrices to be able to perform computations more efficiently. The green vertex tensor in the middle is a  $\delta$  tensor that has been restricted to a single subtype of type-II tiles. The tensor network has a square lattice shape, but in reality the clusters form a triangular lattice, the red dotted lines have therefore been added to indicate nearest neighbors. To the six delta tensors describing the nearest neighbors of the central cluster we give an extra open index, allowing one to probe the local configuration.

cannot make sharp angles. Moreover, of those  $120^\circ$  angles, two of the six are forbidden (which two angles depends on the subtype), making it impossible for a string of type-II tiles to close in on itself (in open boundary conditions). The forbidden angles with corresponding subtype are shown in Fig. 2.14

We thus find that the type-II tiles must form domain walls that extend the entire size of the system, separating different reflection-symmetry broken sectors made up of type-I tiles. A given domain wall can only have one specific symmetry broken sector on either side, so two neighboring domain walls cannot be of the same type, but instead the types must alternate.

Finally, note that based on this analysis it is not clear whether the type-II tiles are actually tessellable, and we only found an upper bound to their freedom. We do however have a number of ground states from the Monte Carlo simulations, and so we can observe that this picture of domain walls is indeed correct.

## 2.7 Summary and outlook

In this Chapter, we have introduced a general approach to build contractible tensor networks for frustrated translation-invariant Ising models with finite-ranged interactions. It relies on the identification of clusters on which the energy can be minimized independently, and on a formulation of the partition function in terms of effective degrees of freedom that correspond



to all the relevant ground states on each cluster. The construction is actually possible for any model with a discrete degree of freedom, for instance Potts or clock models, and in any dimension, the main limitation being the size of the linear program that has to be implemented and solved.

To put this result in perspective, let us come back to the core of the problem faced by tensor networks for frustrated systems, namely the difficulty in numerically contracting tensors with simultaneously very large and very small elements at low temperature because of their exponential dependence on the inverse temperature  $\beta$  with both positive and negative energies. This difficulty is somewhat reminiscent of the sign problem in Quantum Monte Carlo, which excludes the investigation of the low-temperature properties of a quantum system if the off-diagonal matrix elements of the Hamiltonian are not all non-positive, but which at the same time is basis dependent and can in principle be eliminated by a change of basis. What we have proposed here is a reformulation of the partition function in a basis where all elements are of the form  $e^{-\beta E}$ ,  $E \geq 0$ , leading to a tensor of relatively modest dimension with only elements equal to 0 or 1 at zero-temperature, and to a contractible tensor with elements only in the interval  $[0, 1]$  at any positive temperature. As for the sign problem in Quantum Monte Carlo, the identification of the basis does not have in general a polynomial solution. Yet, we have shown that this is in practice possible.

There is another work with a very different approach to solving this problem in the case of spin glasses, when the interactions are set randomly. In Ref. 223, Liu et al. tackle the problem directly at its numerical root, by using the tropical algebra (corresponding to the logarithmic number system) to avoid the numerical issue related to the exponentially large numbers. To date, this approach is however limited to finite size systems (albeit large ones), because it relies on an exact contraction of the tensor network; our approach, on the other hand, is limited to translation invariant problems with finite interaction range.

Closer to our approach, the idea of encoding ground-state local rules was seen to be both necessary and sufficient in a recent preprint on the fully-frustrated XY model [224]. We should also note that although this approach seems to solve the problem when using CTMRG or VUMPS, it is unclear whether additional care should be taken when applying it in the context of TRG, where SVD of the local tensors are performed.

A natural question arising from the approach to find the ground-state local rule relates to the existence and properties of the cluster relaxing the frustration. A first aspect of this question is whether the cluster relaxing the frustration has to be as large as the long-range order unit cell, in the case where such a unit cell exists. We show in Appendix E.2.2 that this needs not be the case, and that the cluster can be smaller than the unit cell for the long-range order. More interestingly, in the absence of long-range order, one can wonder whether there is always a cluster relieving the frustration. Namely, does frustration always have a finite range if the couplings are of finite range? This question has been articulated in Ref. 33, where a distinction is made between systems which have a finite-range frustration (i.e. in our framework, systems

where there exists a cluster size at which frustration can be relaxed), and hypothetical systems which would have an infinite-range geometrical frustration<sup>8</sup>.

### Statement of contribution

The majority of the work detailed in this Chapter has been published in *B. Vanhecke, J. Colbois, L. Vanderstraeten, F. Verstraete, and F. Mila, “Solving frustrated Ising models using tensor networks”, Phys. Rev. Research 3, 013041 (2021) [159]* and is reproduced with permission from all co-authors.

For this paper, B.V. and J.C. have come up with the formulation of the problem and of its solution in close collaboration, under the supervision of L.V., F. V. and F. M. . The VUMPS simulations and the writing and execution of the linear program have been performed by B.V. . The Monte Carlo code has been written and executed by J.C.. The original manuscript has been written by B.V., J.C. and L.V. with contributions from all authors. The additional considerations not published in that paper are the work of J. C., with acknowledgments to B.V. for discussions.

---

<sup>8</sup>Although this exceeds the scope of this thesis by a wide margin, let us mention Ref. 225, where the notions of finite range and long-range frustration are related to the notions of soft and hard frustration in the context of self-assembly in biological systems. It seems that in this context, there might be examples of long-range frustration.

# **The role of farther-neighbor couplings**

**Part II**



### 3 Effect of very small farther-neighbor couplings in an artificial spin system

We gave a general introduction to artificial spin ice and more generically artificial spin systems at the beginning of this thesis. In this chapter, we are interested in a particular kind of artificial spin systems with out-of-plane Ising anisotropy: chirally coupled nanomagnets. Introduced in Ref. 113, these system exhibit a very strong nearest-neighbor coupling interaction. The main idea is to rely on interfacial Dzyaloshinskii-Moriya interactions (DMI) to create regions with out-of-plane anisotropy (OOP regions) connected by chiral domain walls to regions with in-plane anisotropy (IP regions). Arranging the OOP regions on a kagome lattice and separating them with IP regions, one can then use the IP regions to create a very strong nearest-neighbor antiferromagnetic coupling between OOP regions. At first sight one could expect the system to behave simply as a nearest-neighbor Ising antiferromagnet on the kagome lattice.

However, as we mentioned in the general introduction, it has been seen in several artificial spin systems that the long-range dipolar interactions play a role in selecting the correlations [71, 81, 88], even in (modified) artificial square ice [226] which is known for reproducing the extensive degeneracy of the ice manifold [89, 110–112]. In this context, three natural questions arise. The first is to find an effective model for the OOP regions in chirally coupled systems. Indeed, it is not clear how to integrate out the degrees-of-freedom associated with the IP regions. The second, if the nearest-neighbor coupling is shown to be significantly stronger than the farther-neighbor couplings, is to determine whether the latter are small enough to be neglected at the effective temperatures reached by the demagnetization protocol in the artificial spin system. The third is to determine whether this effective model fully accounts for the experimental results.

In Sec. 3.1, we describe this experiment in detail, and report on micromagnetic simulations aimed at finding an effective finite-range model for the OOP regions. The resulting antiferromagnetic Ising models has very strong nearest-neighbor couplings and, relatively, weak next and next-next nearest-neighbor couplings - much smaller than in the dipolar case. In the remainder of the Chapter, we progressively build towards this farther-neighbor model, providing tensor network and Monte Carlo data for the spin-spin correlations of a series of short range Ising models on the kagome lattice, and comparing these correlations to the

experimental results. We start in Sec. 3.2 by a comparison with the nearest-neighbor Ising antiferromagnet on the kagome lattice. We find that even when considering a magnetic field, and despite the strong nearest-neighbor couplings in the experiment, this model does not qualitatively explain the experimental observations. In Sec. 3.3, we show that even weak second nearest-neighbor couplings can partially solve the issue, by changing the order of magnitude of the next nearest-neighbor correlations as compared to the next-next nearest-neighbor correlations. We consider the effective farther-neighbor model in a field in Sec. 3.4, and finally give an overall discussion of the results in Sec. 3.5.

## 3.1 Experiment: a kagome lattice of chirally coupled nanomagnets

We begin with a discussion of the experiments. They rely on the interfacial DMI [227–230],

$$H_{\text{DMI}} = \mathbf{D}_{i,j} \cdot (\mathbf{S}_i \times \mathbf{S}_j), \quad (3.1)$$

which is allowed in environments with a lack of inversion symmetry and is induced by spin-orbit coupling. As discussed in Ref. 113, this interaction can be leveraged to induce an effective antiferromagnetic coupling between two OOP regions with well-defined magnetic anisotropy, which take on the role of Ising spins.

### 3.1.1 Experimental setup

In order to create these effective antiferromagnetic couplings, one deposits a magnetic trilayer of Pt, Co and Al. These trilayers have a large DMI at the Pt/Co interface and their magnetic anisotropy can be tuned by oxidation of the Co/Al interface. Through this oxidation, one can thus create regions of in-plane (IP) anisotropy and regions of out-of-plane (OOP) anisotropy and control the location of the domain walls between them with left-handed chirality. The details of the sample fabrication and the demagnetization protocol are given in Appendix E.1.

Consider a simple system where two regions with OOP anisotropy, which we model as Ising spins, are connected by a region with IP anisotropy. Because of the DMI, it is energetically favorable to have the Ising spins in an antiferromagnetic arrangement. In Ref. 113, it was shown that this antiferromagnetic alignment can be realized in Ising chains and on the square lattice after applying an external magnetic field and provided that the IP regions are small enough. A small kagome sample was also brought to a ground state of the antiferromagnetic nearest-neighbor Ising model - namely, an ice-rule obeying state. Here, we apply this procedure to larger kagome systems (Fig. 3.1).

### Magnetic force microscopy

Magnetic force microscopy (MFM) measurements are performed after the demagnetization protocol to extract the OOP spin configurations (see Appendix E.1 for details about the MFM

### 3.1. Experiment: a kagome lattice of chirally coupled nanomagnets

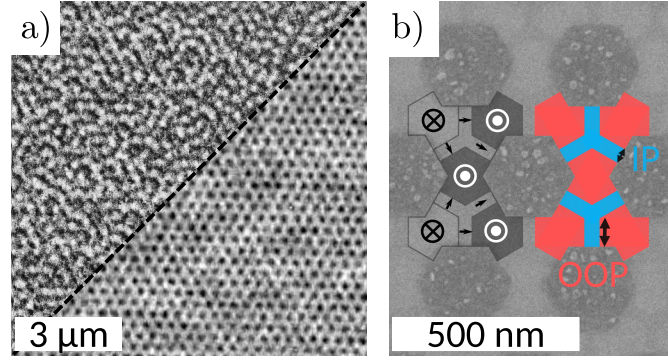


Figure 3.1 – The samples are extended kagome lattices etched from Pt(6 nm)/Co(1.6 nm)/Al(2 nm) films. (a) Top left: magnetic force microscopy (MFM) image of a sample. The black/white contrast shows the up/down magnetization of the regions with OOP anisotropy. Bottom right: AFM image of the sample structure. (b) Scanning electron microscopy image. Local Al oxidation can be seen as a grey contrast difference. A schematic of the out-of-plane (OOP) and in-plane (IP) regions is shown. The OOP (red) and IP (blue) anisotropy regions are defined by an OOP edge length of 100 nm an IP region width of 50 nm. The OOP center to center distance is then geometrically set and is  $\sqrt{3}\text{OOP edge length} + \text{IP width}$ . An example op OOP and IP configuration is illustrated.

scan protocol). An example of the resulting phase contrast is given in Fig. 3.1. The contrast gives information about the OOP magnetization, with white (black) for down (up) magnetized OOP regions. The low thickness of magnetic material makes the highly sensitive MFM tip a good candidate for imaging the stray fields of the samples.

#### 3.1.2 Micromagnetic simulations and effective model

As we will discuss in Sections 3.2 and 3.3, the results of tensor networks and Monte Carlo simulations strongly suggest that farther-neighbor couplings are relevant in this experiment. We see two possible sources of such couplings: the simple magnetostatic (dipolar) interaction between the regions with out-of-plane (OOP) anisotropy, and a possible interaction (of magnetostatic nature or some more subtle origin) between the regions with in-plane (IP) anisotropy. Here, we determine the likelihood of these scenarios by performing micromagnetic simulations [88, 231–234].

Our aim is to find an effective Hamiltonian for the OOP regions, which are modeled with Ising variables. Indeed, it is *a priori* unclear how to combine the IP region and the DMI interactions with the dipolar interactions to give an effective model for the Ising spins. We therefore perform micromagnetic simulations for islands (OOP and IP regions) with three and five sites to determine these effective interactions. For this, we consider the most generic spin model for five sites, including three-, four- and five-site interactions, respecting the cluster symmetries. In the micromagnetic computations, we did not find any evidence suggesting  $\mathbb{Z}_2$  symmetry breaking. The effective Hamiltonian thus reduces to the following expression,

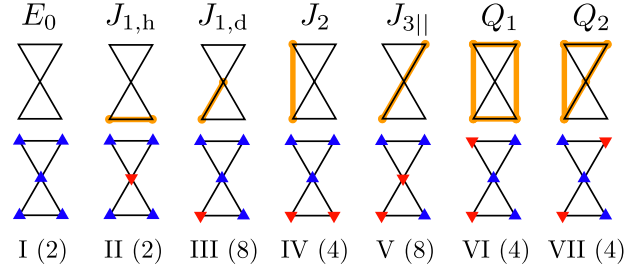


Figure 3.2 – The first row indicates the couplings for the generic model with five sites of Eq. 3.2 (the symmetries of the system and the  $\mathbb{Z}_2$  symmetry being imposed). The orange lines indicate the group of spins involved in the interaction corresponding to a given coupling. If the symmetries are imposed, some configurations will have the same energy; we can therefore group configurations by their energy. The second row shows one configuration (blue triangles for up spins, and red triangles for down spins) for each of these seven different groups. Each group is indexed by a Roman number and the Arabic numbers indicate how many configurations are in each group.

where this symmetry is explicitly imposed by removing terms with an odd number of spins:

$$\begin{aligned}
 H = E_0 &+ J_{1,h} \sum_{\langle i,j \rangle_{1,h}} \sigma_i \sigma_j + J_{1,d} \sum_{\langle i,j \rangle_{1,d}} \sigma_i \sigma_j \\
 &+ J_2 \sum_{\langle i,j \rangle_2} \sigma_i \sigma_j + J_{3||} \sum_{\langle i,j \rangle_{3||}} \sigma_i \sigma_j \\
 &+ Q_1 \sum_{\langle i,j,k,l \rangle_1} \sigma_i \sigma_j \sigma_k \sigma_l + Q_2 \sum_{\langle i,j,k,l \rangle_2} \sigma_i \sigma_j \sigma_k \sigma_l
 \end{aligned} \quad , \quad (3.2)$$

and where the groups of spins to which the couplings apply are defined in Fig. 3.2. The  $J$  couplings correspond to the usual pair interactions while the  $Q$  couplings correspond to four-site interactions.

We performed micromagnetic simulations using MuMax<sup>3</sup> (v3.10) [233, 234] to determine the (relative) coupling constants of the chirally coupled nanomagnet geometry. The cell sizes are chosen such that the angled edges are accurately simulated. Interfacial DMI is introduced by setting  $D_{\text{ind}} = 0.9 \pm 0.1 \text{ mJ/m}^2$  [113]. The detail of the simulation parameters are given in Appendix E.2.

We first simulate the system in the absence of regions with IP anisotropy, where the interactions are of dipolar nature, similar to Ref. 82. The detail of the results for each configuration of



### 3.1. Experiment: a kagome lattice of chirally coupled nanomagnets

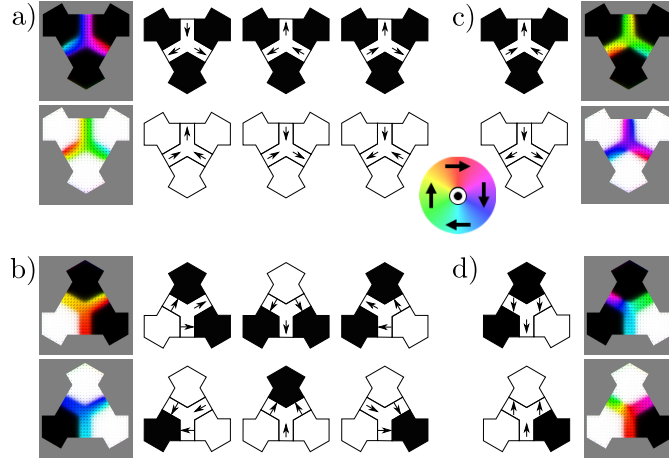


Figure 3.3 – Configurations of the regions with OOP anisotropy and IP anisotropy on a triangle. Black and white OOP regions correspond to up and down Ising spins, respectively. (a) and (b) In the grey squares, the results of the micromagnetic simulations are given; these results are also schematically represented for readability. The colors in the IP region refer to the orientation of the local magnetization in the plane, as labeled by the colored disk. (a) Optimal configuration of the IP regions when all the Ising spins are aligned: 1-in 2-out for all up spins, 2-in 1-out for all down spins. These configurations have energy  $E = -7.5588 \cdot 10^{-18} \pm 10^{-22}$  J. (b) Optimal configurations of the IP regions when one or two spins are up: the IP region points towards the up spins. These configurations have energy  $E = -8.209 \cdot 10^{-18} \pm 5 \cdot 10^{-21}$  J. (c) and (d) Examples of IP configurations which give a higher energy for the OOP configurations corresponding to (a) and (b). Here, the schematic representation shows how the IP region was initialized. (c) A two-in one-out configuration for all up spins, or a one-in two-out configuration for all down spin, is not energetically favorable. (d) If, initially, the IP magnetization does not point towards the up spin(s), the system tries to relax to the IP configurations shown in (b).

Fig. 3.2 can be found in Appendix E.2. We find that

$$\begin{aligned}
 J_1^{\text{dip}} &= (1.87 \pm 0.01) \cdot 10^{-20} \text{ J} \\
 \frac{J_2^{\text{dip}}}{J_1^{\text{dip}}} &= 0.1188 \pm 0.0006 \\
 \frac{J_{3||}^{\text{dip}}}{J_1^{\text{dip}}} &= 0.0769 \pm 0.0003
 \end{aligned} \tag{3.3}$$

where the errors are dominated by the error on  $J_1$  – we find two slightly different values for  $J_{1,d}$  and  $J_{1,h}$ <sup>1</sup>.  $Q_1$  and  $Q_2$  are zero within the error bars. In this case, we indeed recover the dipolar couplings, with a factor of 1.6 correction to the nearest-neighbor coupling as compared to the point-dipole approximation, coming from the finite size of the elements and their proximity [81, 82].

<sup>1</sup>  $J_{1,h} = 1.868 \cdot 10^{-20}$  J while  $J_{1,d} = 1.884 \cdot 10^{-20}$  J. We use the average of these values for  $J_1$ , and the difference of these values to the average as an estimate of the error on  $J_1$ .

### Chapter 3. Effect of very small farther-neighbor couplings in an artificial spin system

---

We then consider the effect of the IP regions. A small subtlety has to be addressed in this case: *a priori*, for a given OOP configuration (labeled by roman numbers in Fig. 3.2), there can be several IP configurations. We proceed in two steps

1. For each configuration of three Ising spins on a triangle, we find the IP configuration that minimizes the energy (see Fig. 3.3). From this, we can already extract the nearest-neighbor coupling

$$J_1 = (1.63 \pm 0.01) \cdot 10^{-19} \text{J}, \quad (3.4)$$

(for an IP width of 50 nm) that is almost one order of magnitude larger than in Eq. 3.3. The main source of the error is that the micromagnetic results are not completely rotation-invariant, a difficulty probably related to the use of a square grid for discretization in MuMax<sup>3</sup>.

2. For each configuration of five Ising spins on a pair of triangles, we look for the combined configuration of the two IP regions minimizing the energy. The optimal configurations and their respective energies can be found in Appendix E.2. The effective model for the OOP region (Ising spins) is based on these energies.

It is important to note that we assume here that the IP region will take the configuration that locally minimizes the energy. Because of the limited MFM resolution and the small width of the IP regions, we have not been able to determine from the experimental scans whether this is actually the case.

We give the results for various IP widths and for various values of the DMI in Fig. 3.4. In particular, for an IP width of 50 nm and for  $D = 0.9 \text{ mJ/m}^2$ , corresponding to our experiment, we find for the full  $J_1$  coupling involving dipolar and IP-mediated interactions:

$$J_1 = (1.6 \pm 0.03) \cdot 10^{-19} \text{J}. \quad (3.5)$$

This result, computed by minimizing the energy of pairs of triangles, is in agreement (within the error bars) with the result of the equality in Eq. 3.4 which was obtained by minimizing the energy of single triangles. For the farther-neighbor couplings, we find:

$$\frac{J_2}{J_1} \cong 0.0235 \pm 0.0004 \quad (3.6)$$

and

$$\frac{J_{3||}}{J_1} \cong 0.0103 \pm 0.0001. \quad (3.7)$$

We see that, as compared to the pure OOP model, when the IP region of width 50 nm is taken into account, the nearest-neighbor coupling is increased by almost a factor of 10, but that the

### 3.1. Experiment: a kagome lattice of chirally coupled nanomagnets

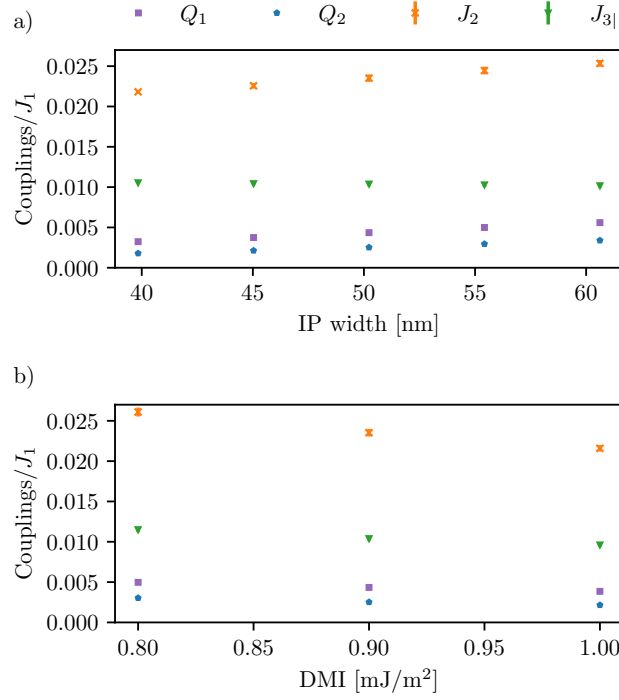


Figure 3.4 – The value of the couplings from Fig. 3.2, relative to  $J_1$ , as obtained from the micromagnetic configurations. Error bars for  $J_2/J_1$  and  $J_{3||}/J_1$  are computed from the error bars on  $J_1$  and from the change in the value of  $J_2$  and  $J_{3||}$  when  $Q_1$  and  $Q_2$  are taken into account versus when they are not. a) Variation of the couplings as a function of the width of the IP domain, with  $D = 0.9$  mJ/m<sup>2</sup>. b) Variation of the couplings as a function of the DMI, with an IP width of 50 nm.

farther-neighbor couplings are affected as well by a factor

$$\frac{J_2}{J_2^{\text{dip}}} \cong 1.67 \pm 0.01 \quad (3.8)$$

and

$$\frac{J_{3||}}{J_{3||}^{\text{dip}}} \cong 1.12 \pm 0.01, \quad (3.9)$$

respectively.

If the IP region had only contributed to the nearest-neighbor coupling (and not to farther-neighbor couplings), the  $J_2^{\text{dip}}$  and  $J_{3||}^{\text{dip}}$  couplings would have had to be compared not to  $J_1^{\text{dip}}$  but to the full  $J_1$ . In this case, instead of the couplings in Fig. 3.4, for an IP width of 50 nm, we

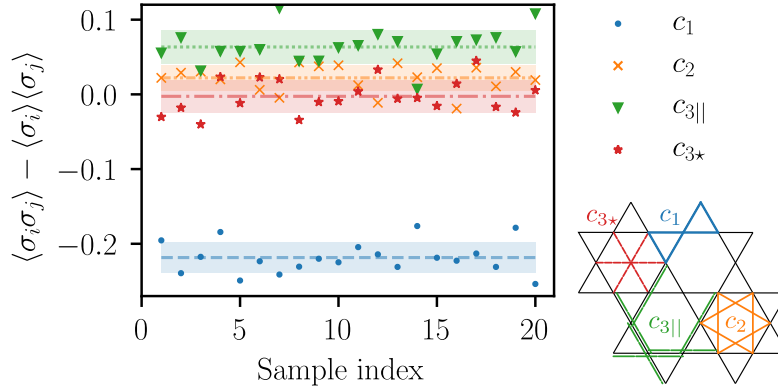


Figure 3.5 – Short range spin-spin correlations of the 20 kagome samples. The considered spin pairs are defined in the inset.  $c_1$  and  $c_2$  correspond to nearest and next nearest-neighbor correlations,  $c_{3||}$  and  $c_{3*}$  to 3rd neighbors. The dashed lines show the mean value and the highlighted areas correspond to one standard deviation around the average.

would have found that

$$\begin{aligned} \frac{J_2^{\text{dip}}}{J_1} &= 0.0139 \pm 0.0002 \\ \frac{J_{3||}^{\text{dip}}}{J_1} &= 0.0090 \pm 0.0001. \end{aligned} \quad (3.10)$$

Thus, when the DMI and dipolar interactions are considered for a cluster of five sites, we find that the nearest-neighbor couplings are increased by a much larger factor than the second and third neighbor couplings, resulting in an effective model with very small farther-neighbor interactions as compared to the nearest-neighbor couplings. These results vary only slightly with the change in IP width or in DMI, as shown in Fig. 3.4.

### Sources of a magnetic field

On top of the effective model discussed above, we have to consider the possible effect of a magnetic field. Indeed, there are two possible sources of a longitudinal field (i.e., a magnetic field parallel to the Ising spin axis) in the experiment: the offset of the demagnetization field, and the stray field of the MFM measurement tip<sup>2</sup>. The saturation field of the samples (of the order of  $4J_1$ ) is estimated to be of the order of 2 kOe. The offset in the demagnetization field is of the order of 10 Oe, and the stray fields from the MFM tip are of order 500 Oe. This means that if there is a field, we expect it to be of the order of  $h \sim J_2$  to  $h \sim J_1$ .

<sup>2</sup>A careful look at the MFM results showed some islands changing contrast during the tip scanning process, which suggest a tip-sample interaction

### 3.1. Experiment: a kagome lattice of chirally coupled nanomagnets

$c_1$	$c_2$	$c_{3  }$	$c_{3\star}$
$-0.218 \pm 0.02$	$0.022 \pm 0.02$	$0.063 \pm 0.02$	$-0.003 \pm 0.02$

Table 3.1 – Experimental values for the first spin-spin correlations (See Fig. 3.5).

$r_{m_\Delta=+3}$	$r_{m_\Delta=+1}$	$r_{m_\Delta=-1}$	$r_{m_\Delta=-3}$
$0.10 \pm 0.024$	$0.60 \pm 0.03$	$0.28 \pm 0.04$	$0.015 \pm 0.008$

Table 3.2 – Experimental values for the proportion of triangles with a given net magnetization.

#### 3.1.3 Experimental results

To characterize the experimental results, we proceed as in Ref. 81 and we extract the experimental spin-spin correlations in order to compare them against the models under consideration. More precisely, for the four types of spin pairs illustrated in Fig. 3.5, we estimate the connected correlation functions

$$\langle \sigma_i \sigma_j \rangle - \langle \sigma_i \rangle \langle \sigma_j \rangle \quad (3.11)$$

using, for spin pairs of type  $k$ , the unbiased estimator

$$c_k = \frac{M}{M-1} \left( \frac{1}{M} \sum_{(i,j)_k} \sigma_i \sigma_j - \frac{1}{M^2} \sum_{i:(i,j)_k} \sigma_i \sum_{j:(i,j)_k} \sigma_j \right) \quad (3.12)$$

where  $M$  is the number of spin pairs of type  $k$  in the lattice and where  $\sum_{(i,j)_k}$  denotes the sum over all spin pairs of type  $k$ . Note that we use the statistical field theory expressions: “connected” correlations means  $\langle \sigma_i \sigma_j \rangle - \langle \sigma_i \rangle \langle \sigma_j \rangle$  and “disconnected” correlations means  $\langle \sigma_i \sigma_j \rangle$ . The results for each sample are shown in Fig. 3.5. In this figure, the shaded areas correspond to the values of the respective correlations that are within one standard deviation of the mean over the samples. These means are given in Table 3.1. As shown in Fig. 3.5, the results vary significantly from one sample to the next. Yet, we note that the descending order of the correlations is almost systematically  $|c_1| > c_{3||} > c_2$ , often with  $c_2 \gtrsim c_{3\star}$ . This qualitative result will drive our analysis.

Additionally, we consider two other observables which are characteristic of the experimental results. First, for the net magnetization of the samples, we get a result significantly different from zero:  $m = 0.19 \pm 0.05$ ; all the samples are magnetized in the same direction. Second, in each sample there are 10% to 20% of ferromagnetic triangles (“frustrated” triangles, which do not respect the two-up one-down, two-down one-up ice rules); we therefore compute the proportion of triangles with a given magnetization (analogous to the often used charge definition, but without introducing a sign). The results are given in Table 3.2; overall, the proportion of ice-rule-breaking triangles is  $r_{fr} = r_{m_\Delta=+3} + r_{m_\Delta=-3} = 0.12 \pm 0.03$ .

## 3.2 Nearest-neighbor model

Given the very strong nearest-neighbor couplings predicted by the micromagnetic simulations, we start by checking whether the experimental results from Sec. 3.1 can be understood using a purely nearest-neighbor model,

$$H_{\text{NN}} = J_1 \sum_{\langle i,j \rangle} \sigma_i \sigma_j - h \sum_i \sigma_i. \quad (3.13)$$

### 3.2.1 Nearest-neighbor Ising antiferromagnet in zero field

As we discussed in the general introduction, the kagome lattice is a natural playground for frustrated models. In particular, the nearest-neighbor Ising antiferromagnet on this lattice is known to have no order at any temperature, and it was shown by A. Sütö that the spin-spin correlations decay exponentially [36], with

$$|\langle S_i S_j \rangle| \leq 4 \times 0.74^{|i-j|} \quad (3.14)$$

which implies an upper bound for the correlation length<sup>3</sup>:

$$\xi \leq \xi_{\text{Sütö}} - 1/\ln 0.74 = 3.32109. \quad (3.15)$$

An exact result was obtained more recently for the correlation length between “middle spins” from transfer matrix computations using Toeplitz determinants [37]:

$$\xi = -\frac{2}{\ln(10 - \sqrt{96})} \cong 1.250559... \quad (3.16)$$

It is well known that the correlation length can be computed from the two leading eigenvalues of the transfer matrix  $\lambda_1, \lambda_2$  (see for instance [178]) as

$$\frac{1}{\xi} = -\ln \frac{\lambda_2}{\lambda_1}. \quad (3.17)$$

We write the partition function of the nearest-neighbor model on the kagome lattice as a tensor network as depicted in Fig. 3.6. We contract these networks using the VUMPS algorithm [148, 149], which finds the leading eigenvector of the (infinite) 1D transfer matrix using as a variational Ansatz a translation invariant MPS (see Chapter 1).

---

<sup>3</sup>Note that the magnetization is zero in the ground state of the model, hence the connected or disconnected correlations have the same value

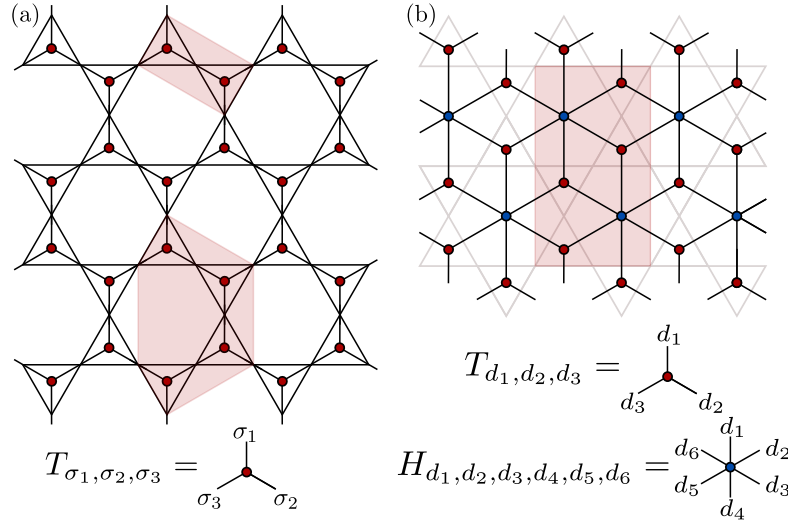


Figure 3.6 – Tensor network formulations for the partition function of the nearest-neighbor model on the kagome lattice. In highlight, we indicate the regions that can be grouped in a single tensor such that the tensor network on the honeycomb or dice lattice is reduced to a square lattice tensor network which can then be contracted using VUMPS. (a) “Direct” construction on the honeycomb lattice, with the tensor on the triangle given by Eq. 3.18, and which is easily extended to the nearest-neighbor model in a field. (b) “Dual” construction on the dice lattice, with the tensors given in Eqs. 3.20, 3.21. This construction is easily extended to the next nearest-neighbor model in zero field.

In the “direct” construction, the tensor

$$T_{\sigma_i, \sigma_j, \sigma_k} = e^{-\beta J_1 (\sigma_i \sigma_j + \sigma_j \sigma_k + \sigma_k \sigma_i + 1)} \quad (3.18)$$

describes all the Boltzmann weights on a triangle, with a shift corresponding to the ground state energy on a triangle. In the “dual” construction, we use a classical dimer variable defined on each nearest-neighbor bond  $\langle i, j \rangle$

$$d_{i,j} := \sigma_i \sigma_j. \quad (3.19)$$

The tensor on each triangle is

$$T_{d_{i,j}, d_{j,k}, d_{k,i}} = \begin{cases} e^{-\beta J_1 (d_{i,j} + d_{j,k} + d_{k,i} + 1)} & d_{i,j} d_{j,k} d_{k,i} = 1 \\ 0 & \text{otherwise} \end{cases}, \quad (3.20)$$

and the tensor on each hexagon  $H_{d_1, d_2, d_3, d_4, d_5, d_6}$  only imposes that the number of dimers is even, such that the dimer configuration maps to a spin configuration (see Chapter 1):

$$H_{d_1, d_2, d_3, d_4, d_5, d_6} = \begin{cases} 1 & \text{if } d_1 d_2 d_3 d_4 d_5 d_6 = 1 \\ 0 & \text{otherwise} \end{cases}. \quad (3.21)$$

### Chapter 3. Effect of very small farther-neighbor couplings in an artificial spin system

	$c_1$	$c_2$	$c_{3  }$	$c_{3\star}$
Exact [235]	$-1/3$	0.1234...	0.1014 ...	-0.0743...
Direct TN	$-1/3$	0.12343725	0.10144577	-0.07480837
Dual TN	$-1/3$	0.12343725	0.10144577	-0.07480837

Table 3.3 – First spin-spin correlations in the ground state of the nearest-neighbor model (See Fig. 3.8).

In both constructions, we recover the exact ground state entropy of the kagome Ising antiferromagnet [18] to the 14th decimal place. For the first few correlations in the ground state, the two tensor constructions agree to the 3rd decimal place with the exact results [235, 236] (Table 3.3).

To extract the correlation length from the direct tensor network, we follow Ref. 237 and compute the first eigenvalues of the transfer matrix

$$\lambda_j = e^{-(\epsilon_j + i\phi_j)P} \quad (3.22)$$

with  $|\lambda_1| > |\lambda_2| > |\lambda_3| \geq |\lambda_4| \geq \dots$ , where  $\epsilon_j$  and  $\phi_j$  correspond respectively to the log of the absolute value and to the phase, and where  $P$  stands for the periodicity of the MPS in units of the number of lattice sites. The correlation length is thus given by

$$\frac{1}{\xi} = \epsilon_2 - \epsilon_1. \quad (3.23)$$

To extract the correlation length in the dual tensor network formulation, one can use the fact that the product of two spins is given by the product along a path of all the dimer variables separating them. We thus define a correlation tensor  $C$  as the contraction along  $d_c$  of the two tensors

$$T_{d_{\text{top},2},d_r,d_c}^c = d_{\text{top},2} T_{d_{\text{top},2},d_r,d_c}, \quad (3.24)$$

$$H_{d_{\text{top},1},d_c,d_3,d_4,d_5,d_6}^c = d_{\text{top},1} H_{d_{\text{top},1},d_c,d_3,d_4,d_5,d_6}. \quad (3.25)$$

The correlation length is then given by

$$\frac{1}{\xi} = \epsilon - \epsilon_1 \quad (3.26)$$

with  $\lambda = e^{-(\epsilon + i\phi)P}$  corresponding to the leading eigenvalue of the transfer matrix based on  $C$  (note that here, the periodicity of the MPS compared to the lattice is  $P = 2$ ). In both the direct and the dual cases, we define

$$\delta_{i,j} = \epsilon_j - \epsilon_i \quad (3.27)$$



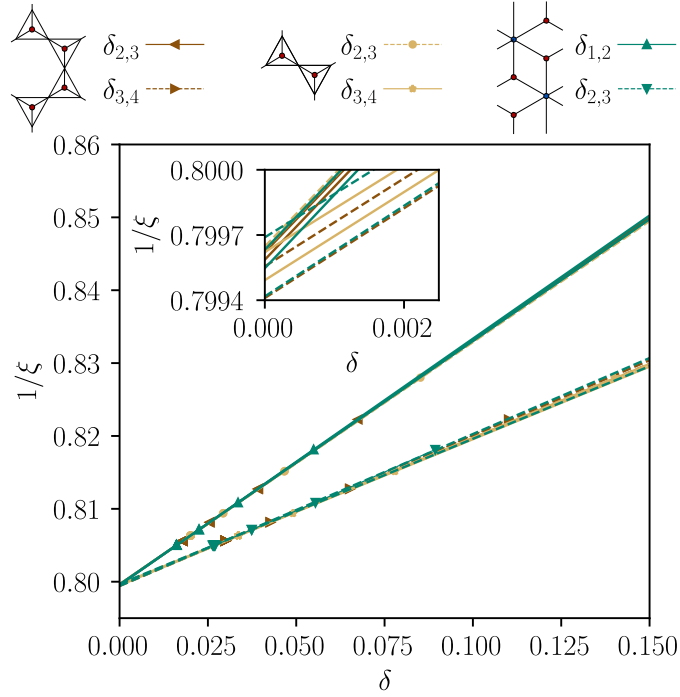


Figure 3.7 – For two slightly different tensor network constructions, we plot one over the correlation length (Eq. 3.23) as a function of the logarithm of another “gap” in the transfer matrix spectrum (Eq. 3.27). The legend indicates, for each set of points, to which unit cell it is associated and which gap  $\delta$  in the transfer matrix spectrum is selected. The correlation length corresponds to the correlations along a line of kagome lattice nearest neighbors. For each set of points we do two fits, one with all the points and one without the largest  $\delta$ . The inset shows the crossing of each of these fit with the axis  $\delta = 0$ , giving an estimate for the actual correlation length in the limit of an infinite bond dimension.

the other gaps in the transfer matrix spectrum, which must go to zero in the limit of infinite bond dimensions to produce algebraic corrections to the form of the correlations [237]. In Fig. 3.7, the value of the correlation length as a function of such gaps for different bond dimensions is illustrated; in the direct construction this is shown for two different orientations for the contractions displayed in Fig. 3.6. We are limited to a maximal bond dimension of  $\chi = 14$ , after which the Schmidt values fall below numerical precision. From using the various constructions, selecting various gaps, and making the fits with all the points and all the points but one, we can finally extract the correlation length along the nearest-neighbor chains and the errors on its estimation as

$$\xi = 1.2507 \pm 0.0003 \quad (3.28)$$

in units of the lattice spacing. This is extremely short, consistent with the upper bound from A. Sütő’s computation, and matches within the error bars the exact solution given in Eq. 3.16.

As a function of the temperature, the comparison between the tensor networks and the exact solution for the first few correlations is given in Fig. 3.8. We also use it as a benchmark for the

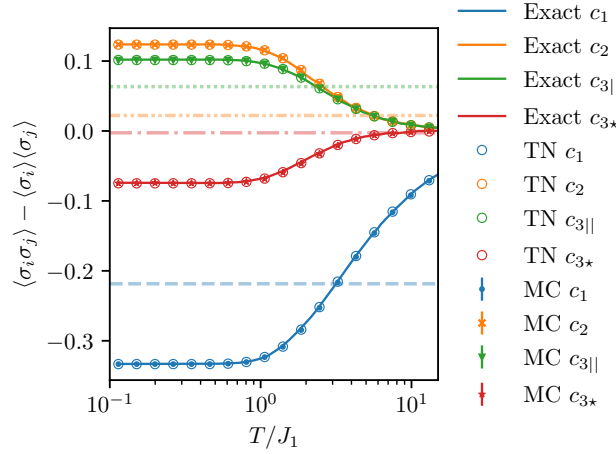


Figure 3.8 – First few correlations in the nearest-neighbor Ising antiferromagnet: comparison between the exact results (Ref. 235, extracted from Ref. 236), and the experimental results. We also show the results of the two numerical methods (TN: tensor networks, with (final) MPS bond dimension  $\chi = 13$ , MC: Monte Carlo with number of sites  $N = 576$ ) as a benchmark. The dashed lines correspond to the four experimental correlations results from Fig. 3.5. The results for the nearest-neighbor correlations are compatible with the experiment at relatively large effective temperatures ( $T \sim 3J_1$ ), but the order of  $c_2$  and  $c_{3||}$  in the experiment is inverted as compared to the theoretical values in the nearest-neighbor model.

Monte Carlo simulations, performed with a dual worm algorithm [114] (Chapter 1).

In Fig. 3.8, we also compare the experimental results for the correlations to the nearest-neighbor Ising antiferromagnet at all temperatures. At this stage, we should recall that the samples are not at all expected to be thermally active. Here, the temperature is introduced as a Lagrange parameter for the energy, in an attempt to account for the non-zero percentage of ice-rule-breaking triangles in a non-biased way<sup>4</sup>. Accordingly, corresponding to the non-zero proportion of frustrated triangles, one can see that the experimental value for the nearest-neighbor correlations correspond to a finite effective temperature.

The description with the nearest-neighbor model fails in two ways. First, because there is no  $\mathbb{Z}_2$  symmetry breaking, the proportions of triangles of given magnetization (Table 3.2) and the finite magnetization cannot be recovered. Second, the relative order of  $c_2$  and  $c_{3||}$  in the experiment is inverted as compared to the nearest-neighbor model: despite the strong value of the nearest-neighbor couplings as compared to the farther-neighbor couplings from Fig. 3.4, considering only nearest-neighbor couplings does not allow for a valid qualitative description of the experiment from the point of view of the descending order of the spin-spin correlations.

<sup>4</sup>As discussed in Ref. 57, the notion of effective temperature mostly describes whether a given snapshot of a configuration of the nanomagnets is characteristic of some state at equilibrium, or conversely, whether an out-of-equilibrium description is required. In the same spirit, it is now quite standard in artificial spin ices to consider an energy-based effective temperature corresponding to the canonical distribution describing effectively the vertex population [70]. This is the approach that we followed here.

### 3.2. Nearest-neighbor model

	$c_1$	$c_2$	$c_{3  }$	$c_{3\star}$
Ref. 54	-4/9	0.36756	0.07688	-0.30396
Direct TN ( $\chi = 80$ )	-4/9	0.36755	0.07689	-0.30396

Table 3.4 – First spin-spin correlations in the critical ground state of the KIAFM in a field.

#### 3.2.2 Nearest-neighbor Ising antiferromagnet in a field

The experiments exhibit a finite magnetization and an imbalance of the number of triangles with a given magnetization. A simple way to account for this in the model is to introduce the corresponding Lagrange parameter, that is, the magnetic field. It is thus natural, as a next step, to test whether a longitudinal magnetic field lifting (partially) the ground-state degeneracy of the nearest-neighbor ground state could be enough to explain not only the magnetization and the proportion of triangles with a given magnetization but also the result that  $c_{3||} \gtrsim 2c_2$ .

We use a tensor network contraction to compute the correlations systematically as a function of field and temperature. Before doing so, we take advantage of this construction to study the ground state phase diagram of this kagome Ising antiferromagnet in a field.

#### Ground-state phase diagram

The ground state of the nearest-neighbor model in a field (Eq. 3.13) is known to exhibit a magnetization plateau  $m = \frac{1}{3}$  for fields  $0 < \frac{h}{J_1} < 4$ , where each triangle bears two spins up and one spin down. Therefore, this magnetization plateau corresponds to a long-range order of the underlying charges, as can be seen in the Monte-Carlo snapshot illustration in Fig. 3.9. The configurations in this plateau can be exactly mapped to a hardcore dimer model on the honeycomb lattice (placing a dimer on each down spin), leading to a macroscopic ground-state degeneracy with a residual entropy corresponding to one third of that of the TIAFM [14, 15, 54, 55, 238, 239]. The *connected* correlations are critical, decaying as  $1/r^2$  ([54, 239] and references therein). In the ground state, the correlations have been tabulated (Fig. 3 of Ref. 54).

The model can be studied using the tensor network expression for the partition function from Fig. 3.6(a), with the slight modification that

$$T_{\sigma_1, \sigma_2, \sigma_3} = \begin{cases} e^{-\beta J_1 (\sum_{\langle i, j \rangle} \sigma_i \sigma_j + 1) + \beta h (\sum_i \sigma_i - 1)/2} & h \leq 4J_1 \\ e^{-\beta J_1 (\sum_{\langle i, j \rangle} \sigma_i \sigma_j - 3) + \beta h (\sum_i \sigma_i - 3)/2} & h \geq 4J_1 \end{cases} \quad (3.29)$$

(see as well Ref. 126 for a similar construction and a contraction with TRG). In the magnetization plateau, with bond dimension  $\chi = 80$ , we find indeed

$$S_{h < 4J_1} = 0.1076886 \pm 10^{-7} \quad (3.30)$$

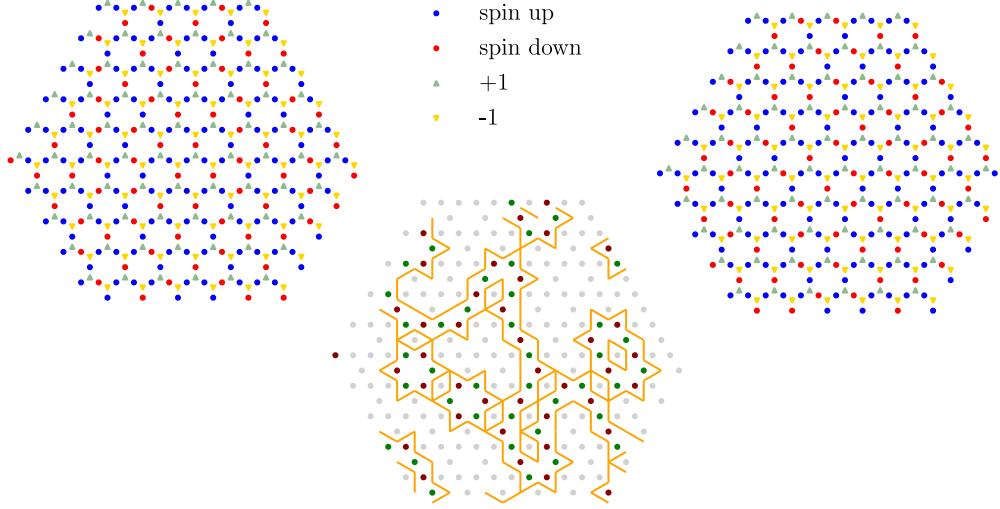


Figure 3.9 – Example of two ground-state configurations in the nearest-neighbor model in a magnetic field  $0 < h < 4J_1$  (leftmost and rightmost panels), and the difference between the two configurations (central panel). The orange lines delimit the regions where spins are flipped. They correspond to updates in the classical dimer configuration on the (dual) dice lattice. The green dots correspond to spins that are flipped from up to down, and the dark red dots to spins that a flipped from down to up. Comparing the two ground states, it can be seen that the underlying charge configuration is long-range ordered, while the spin configuration is not.

which corresponds to one third of the triangular Ising antiferromagnet entropy. We compare the correlations to the result of Ref. 54 in Table 3.4.

Similar to what happens on the square and triangular lattices [240, 241], at the critical field  $h/J_1 = 4$ , a number of additional configurations contribute to the ground state. It has been noted before that at low temperature, this leads to a special value of the magnetization  $m \cong 3/5$  [242]. We find a slightly different value which is consistent between our tensor network computations in the ground state and our MC simulations at  $T/J_1 = 7 \cdot 10^{-3}$ :

$$m_{h=4J_1}^{\text{TN}} = 0.599660907836 \pm 10^{-12} \quad (3.31)$$

$$m_{h=4J_1}^{\text{MC}} = 0.59968 \pm 8 \cdot 10^{-5} \quad (3.32)$$

	$c_1$	$c_2$	$c_{3  }$	$c_{3\star}$
Direct				
TN	-0.1602714	0.04322263	0.0382691	-0.019949696
MC	-0.16025(6)	0.04322(8)	0.03819(8)	-0.0198(3)

Table 3.5 – First spin-spin correlations in the ground state in the nearest-neighbor model in a longitudinal field  $h = 4J_1$ . For the tensor network, the Schmidt values decay extremely fast and fall below numerical precision for  $\chi > 10$ . For the Monte Carlo, we show results with a number of sites  $N = 2304$ , at temperature  $T/J = 7 \cdot 10^{-3}$ .

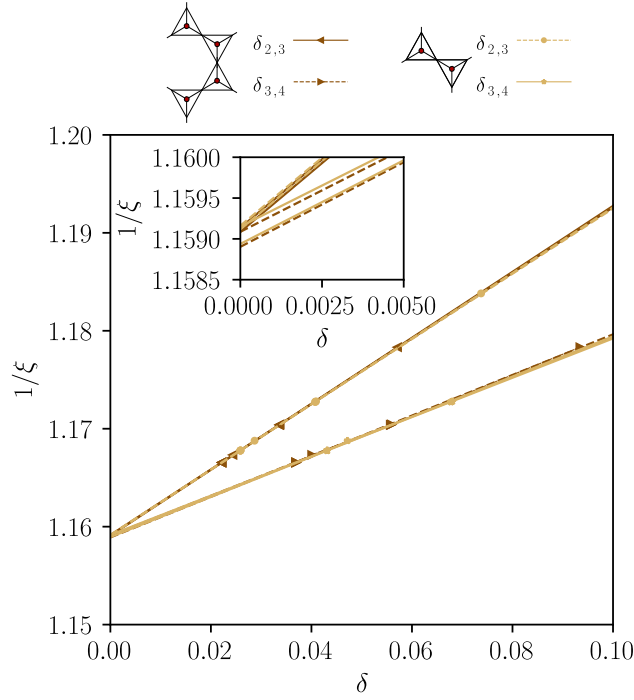


Figure 3.10 – Determining the correlation length Eq. 3.34 (for the connected correlations) at  $h = 4J_1$ . See the caption of Fig. 3.7 for the detail.

For the residual entropy, we find

$$S_{h=4J_1} = 0.387800244253 \pm 10^{-12}. \quad (3.33)$$

The value of the residual entropy is consistent with Ref. 242, although with a significant improvement in the precision owing to the small bond dimension required in the MPS Ansatz<sup>5</sup>. The values of the first few correlations at small but non-zero temperature for  $h/J_1 = 4$  are given in Table 3.5, where it can be seen that the Monte Carlo and tensor network computations agree. A similar analysis as the one performed in zero field (Fig. 3.10) yields a finite correlation length

$$\xi_{h=4J_1} = 0.8627 \pm 0.0001 \quad (3.34)$$

in units of the lattice spacing. This small correlation length is the reason why the tensor network results are obtained with such high precision even with extremely small bond dimension (here, the largest bond dimension is  $\chi = 10$  as for larger bond dimensions, the Schmidt values decay below numerical precision). For  $\frac{h}{J_1} > 4$ , the ground state is the fully ferromagnetic state.

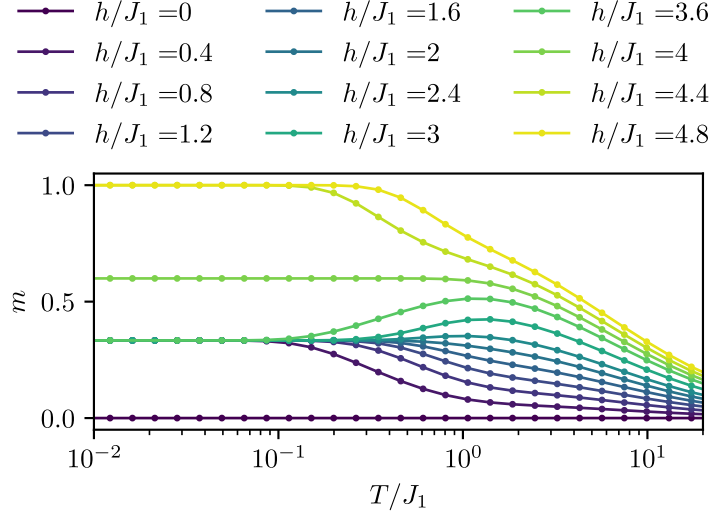


Figure 3.11 – Tensor network results for the magnetization as a function of the field and the temperature for the nearest neighbor Ising antiferromagnet in a magnetic field.

### Temperature

In Fig. 3.11, we give an overview of the magnetization as a function of the field and the temperature for the KIAFM. For each field and temperature we computed as well the first spin-spin correlations and found that  $c_2 \geq c_{3\parallel}$  everywhere. The behavior of the magnetization at intermediate temperatures can be understood on an intuitive level by the comparison of the temperature, the  $J_1$  coupling and the magnetic field  $h$  or its difference with the critical field  $h = 4J_1$ . At small but non-zero  $h$ , the effect of the field can only occur at temperatures of order of  $h$ . Having a look at the first few correlations and comparing them to the values in zero field and at the critical field (Fig. 3.12), we can see that this is indeed what happens. On the other hand, at large fields but small  $4J_1 - h$ , the combined effect of the field and  $J_1$  means that the system first behaves as if the field was critical, with the magnetization increasing to almost  $m = 0.55$  (see also the panel for  $h = 3.8$  in Fig. 3.12), before going back to the ground-state correlations of the critical  $m = 1/3$  plateau.

### Comparison to the experiments

We first check that by introducing a field, we can account for the number of triangles with a given magnetization. For this, we compute the proportions  $r_{m_\Delta=+3}$ ,  $r_{m_\Delta=+1}$ ,  $r_{m_\Delta=-1}$  and  $r_{m_\Delta=-3}$  for regularly spaced fields (every  $0.2J_1$ ). As shown in Fig. 3.13, we find that we obtain the best fit at  $h = (1.6 \pm 0.2)J_1$  for a temperature  $T = (2.8 \pm 0.2)J_1$ . As a direct consequence, in this region, the magnetization and the nearest-neighbor correlations match the experimental

<sup>5</sup>We also confirmed our results by using a slightly different tensor network formulation based on ground state local rules in the spirit of Chapter 2.

### 3.3. Next-nearest-neighbor Ising antiferromagnet

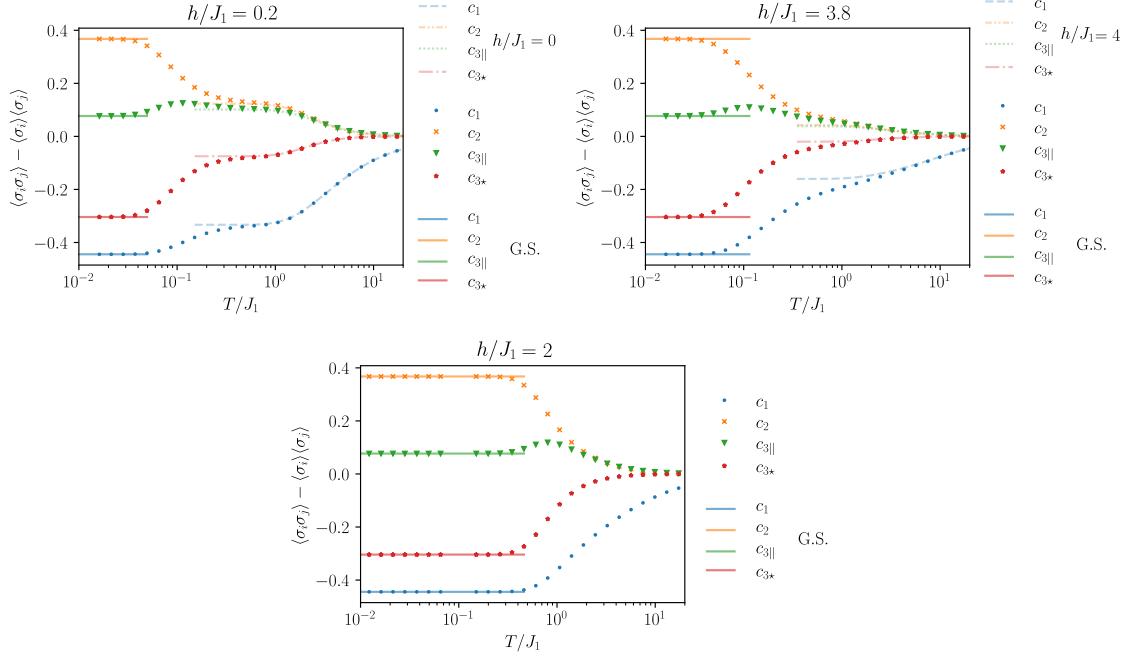


Figure 3.12 – Tensor network results for the correlations as a function of the field and the temperature for the nearest neighbor Ising antiferromagnet in a magnetic field.

results.

From the systematic computation of the spin-spin correlations, we find that at all fields the  $c_2$  correlations remain larger or equal to the  $c_{3||}$  correlations, as suggested by Figs. 3.12 and 3.14. In particular, at large temperatures,  $c_{3||}$  is essentially equal to  $c_2$ . Thus, even though combining the magnetic field and the temperature allows us to account for the proportion of triangles of given magnetization, and therefore account for both the magnetization and the percentages of frustrated triangles, the nearest-neighbor model is not sufficient to fully account for the experimental results. This is possible because the proportion of each type of triangles is mostly related to the nearest-neighbor correlations as well as the magnetization, which are controlled respectively by  $J_1/T$  and  $h/T$ , but the farther-neighbor spin-spin correlations are related to correlations between the triangles.

### 3.3 Next-nearest-neighbor Ising antiferromagnet

Since the nearest-neighbor model does not fully describe the experimental correlations, and since the micromagnetic simulations predict a small but non-zero value for the next-nearest-neighbor couplings, we now consider whether such small couplings are sufficient to explain the inversion of the relative order of the  $c_2$  and  $c_{3||}$  correlations. Farther-neighbor couplings in the  $J_1 - J_2$  model are known to lift the degeneracy either partially [94, 102, 222] or

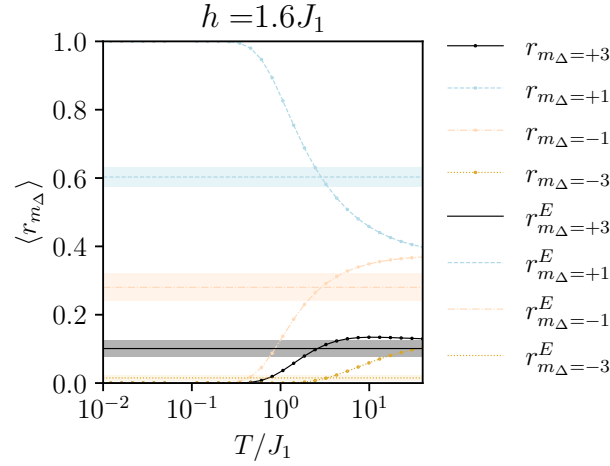


Figure 3.13 – Tensor network results (maximal bond dimension  $\chi = 80$ ) for the proportion of triangles of given magnetization at a field of  $h = 1.6J_1$ . For different fields spaced regularly every  $0.2J_1$ , this is the one at which the prediction from the tensor networks simulations are closest to the experimental results. The optimal temperature is  $T = (2.8 \pm 0.2)J_1$ . The data for the proportion of triangles of each type at regularly spaced fields can be found at [243].

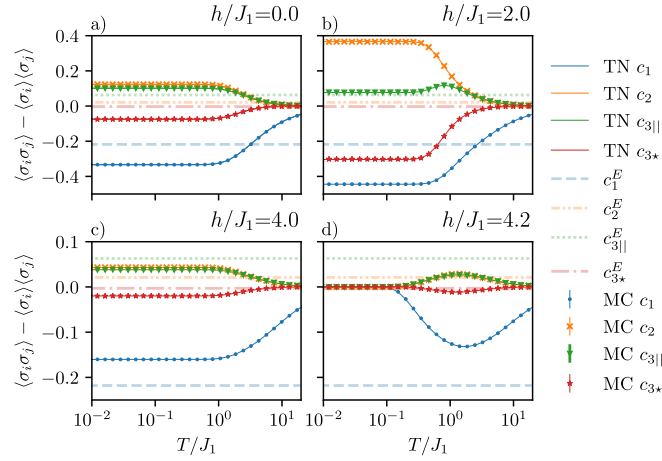


Figure 3.14 – Tensor networks (maximal bond dimension  $\chi = 80$ ) and Monte Carlo ( $N = 2304$  sites) results for the first few correlations at specific magnetic fields. Note the difference in the vertical axis for subplots (a)  $h = 0$  and (b)  $h = 2J_1$  versus (c) critical field  $h = 4J_1$  and (d)  $h = 4.2J_1$ . See as well Tables 3.4 and 3.5 for the values in the ground state. Notice that in the second row, we have zoomed in on the values of the correlations. The data for the correlations at regularly spaced fields can be found at [243].



### 3.3. Next-nearest-neighbor Ising antiferromagnet

	$c_1$	$c_2$	$c_{3  }$	$c_{3\star}$
Dual TN	-1/3	-1/3	0.5726	0.5933
MC	-1/3	-1/3	$0.567 \pm 0.005$	$0.586 \pm 0.005$

Table 3.6 – First spin-spin correlations in the ground state of the next-nearest-neighbor model. The tensor network results are for  $\chi = 144$ . For the Monte Carlo simulations, we show results with the number of sites  $N = 1296$  and at a temperature  $T/J = 7 \cdot 10^{-3}$ .

completely [101, 102] (depending on whether they are ferro- or antiferromagnetic)<sup>6</sup>.

For now, we ignore the problem of the magnetization and consider the Hamiltonian [102]<sup>7</sup>

$$H_{NNN} = J_1 \sum_{\langle i,j \rangle} \sigma_i \sigma_j + J_2 \sum_{\langle i,j \rangle_2} \sigma_i \sigma_j \quad (3.35)$$

where  $\langle i, j \rangle_2$  stands for next nearest-neighbor spin pairs as illustrated by  $c_2$  in the inset of Fig. 3.5. The key question is then how large the next-nearest-neighbor coupling has to be to change the descending order of the farther-neighbor correlations and explain the experimental observation that  $c_{3||} \gtrsim 2c_2$ .

Here, we focus on the case with antiferromagnetic next-nearest-neighbor couplings for the Ising model. It should be noted that, upon changing the sign of the couplings and multiplying them by 2, the model maps onto the in-plane “spin-ice” model on the kagome lattice with *ferromagnetic* next-nearest-neighbor couplings (unlike [93, 94]). We study the model with an ad-hoc Monte Carlo algorithm [114] and our dual tensor network construction from Fig. 3.6(b). The expression of the tensor on the triangle Eq. 3.20 remains unchanged, while Eq. 3.21 becomes

$$H_{d_1, d_2, d_3, d_4, d_5, d_6} = \begin{cases} e^{-\beta J_2 (\sum_{i=1}^6 d_i d_{i+1} + 2)} & \prod_i d_i = 1 \\ 0 & \text{otherwise} \end{cases} \quad (3.36)$$

where  $d_7 = d_1$ .

The  $J_2$  couplings form a set of three interpenetrating kagome sublattices. The “two-up one-down, two-down one-up” ice rule can be satisfied simultaneously on each triangle on the initial kagome lattice as well as on each triangle on these three kagome lattices. The ground-state energy per site is thus [99, 102]

$$E_{\text{G.S.}} = -\frac{2}{3}J_1 - \frac{2}{3}J_2. \quad (3.37)$$

Imposing these rules only leads to a partial lifting of the ground-state degeneracy, and from Pauling estimates one gets a residual entropy per site [99]  $S_{J_1, J_2} \cong \ln \left( 2 \left( \frac{3}{4} \right)^{(4N/3)} \right) = 0.3096$ .

<sup>6</sup>Remember the ground-state phase diagram in Fig. 1.9.

<sup>7</sup>Notice the opposite sign convention and factor two between our convention and that of Ref. 102.

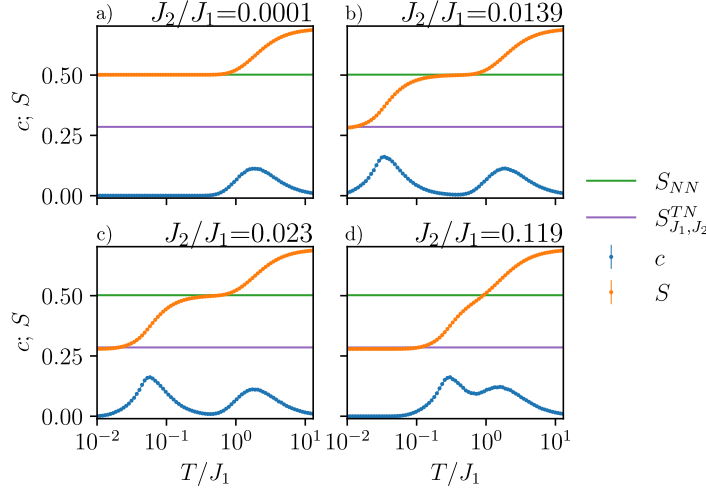


Figure 3.15 – Overview of the behavior of the specific heat and entropy as a function of the temperature for various values of  $J_2$ , with Monte Carlo simulations for two system sizes ( $N = 576, 1296$ ). The smaller system size is shown with a line while the larger system size is shown with symbols.

From the contraction of the tensor network, we get

$$S_{J_1, J_2} = 0.285299 \pm 1.4 \cdot 10^{-6}, \quad (3.38)$$

where the error is estimated from the difference between the value at maximal MPS bond dimension ( $\chi = 144$ ) and the result of the fit in the infinite bond dimension limit. The result matches what we obtain with the method of Ref. 159, and our Monte Carlo thermodynamic integration result  $S_{J_1, J_2} \cong 0.285 \pm 0.001$  (see also Chapter 4). In Table 3.6, we also give the first spin-spin correlations in the ground state, as obtained with both methods.

Takagi and Mekata [102] predicted a KT transition to this critical ground-state phase at temperatures of order of  $J_2$ . Correspondingly, for small values of  $J_2$ , the specific heat exhibits two broad peaks corresponding to the two stages of the loss of entropy (first for imposing the ice rule on nearest-neighbor triangles and then for imposing it on farther-neighbor triangles), while for larger values of  $J_2$ , the two features merge into one [93, 102] (Fig. 3.15).

The behavior of the spin-spin correlations corresponds to this picture (Fig. 3.16), since we find that for small values of  $J_2$  the correlations take their nearest-neighbor model value for a range of temperatures before going to their ground-state values, while for larger values of  $J_2$  the competition between  $J_2$  and  $J_1$  significantly affects the correlations even at large temperatures. Note that Fig. 3.16 shows the values of the correlations with the Monte Carlo simulations for those ratios of  $J_2$  to  $J_1$  corresponding to the three scenarios discussed in Sec. 3.1.2 ( $J_2^{\text{dip}}/J_1$ ,  $J_2/J_1$ ,  $J_2^{\text{dip}}/J_1^{\text{dip}}$ ).

Simulating the model systematically for a range of values of  $J_2$ , we can map out the values of the

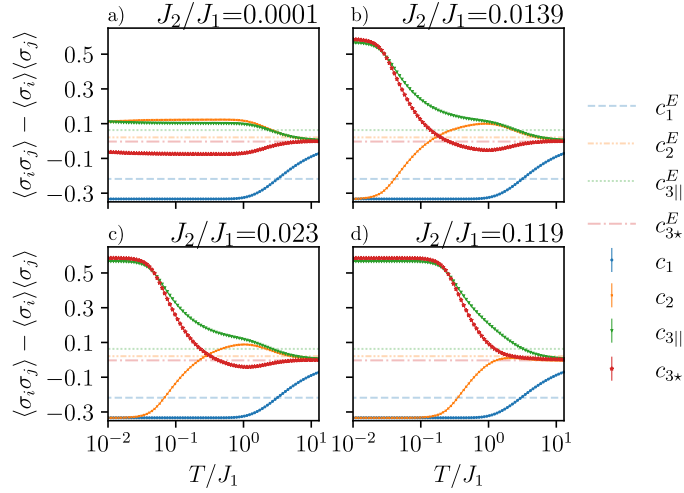


Figure 3.16 – Overview of the behavior of the first spin-spin correlations as a function of the temperature for various values of  $J_2$ , with Monte Carlo simulations for two system sizes ( $N = 576$  and  $1296$ ); the smaller system size is shown with a line while the larger one is shown with symbols. The dashed lines show the experimental values for comparison. (a) For small  $J_2$ , we recover the nearest-neighbor model correlations at intermediate temperatures. (b) and (c) Upon increasing  $J_2$ , the region of temperature where  $c_2 > c_{3||}$  is pushed towards high temperatures, and (d) eventually disappears. When  $J_2$  is large, the  $c_2$  correlations remain negative at any temperature. An overview is shown in Fig. 3.17.

next-nearest-neighbor coupling and of the temperature where the spin-spin correlations are in a certain descending order. This is shown in Fig. 3.17, where one can see that – in agreement with the above discussion – for very small  $J_2/J_1 \lesssim 0.01$ , there is a range of temperatures where the descending order of the correlations is compatible with the nearest-neighbor model. For  $J_2/J_1 \gtrsim 0.01$ , one can see a broad region of temperatures and couplings where the spin-spin correlations are in the same relative order as in the experiment ( $|c_1| > c_{3||} > c_2 \gtrsim c_{3*}$ ), and within this region, a non-negligible region where  $c_{3||} > 2c_2$ . In particular, for the micromagnetic value  $J_2 = 0.023J_1$ , the temperature range where  $c_{3||} > 2c_2$  is  $0.3 \lesssim T/J_1 \lesssim 0.6$ . If  $J_2 \gtrsim 0.06J_1$ , the region where  $c_{3||} > 2c_2$  extends all the way to  $T = 5J_1$ .

Although this model does not involve a magnetic field, it provides evidence that, in order to recover qualitatively the descending order of the spin-spin correlations, farther-neighbor couplings have to play a role. Additionally, it provides an idea of how sensitive the correlations are to these farther-neighbor couplings.

### 3.4 Results in the $J_1 - J_2 - J_{3||}$ model

The micromagnetic simulations predict third-neighbor couplings that are almost half of the second neighbor couplings. Since there is a competition between these couplings, we have to check that, in their presence, the predicted descending order of the correlations is still

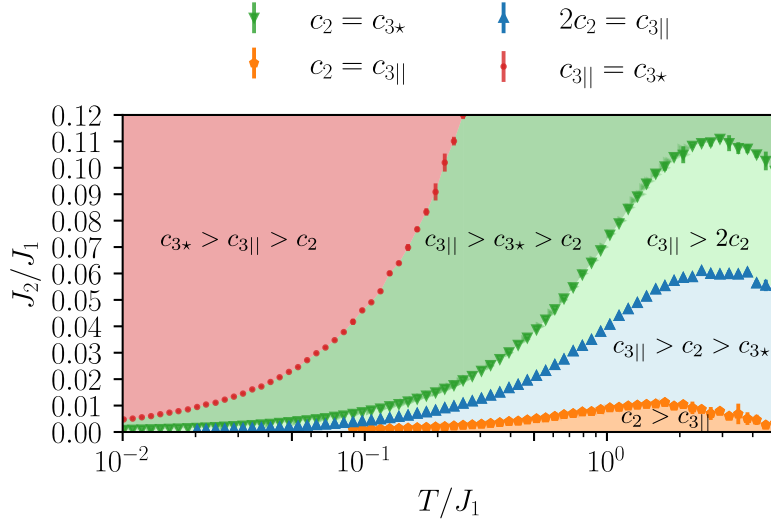


Figure 3.17 – Map of the descending order of the correlations as a function of the temperature  $T/J_1$  and the next nearest-neighbor coupling  $J_2/J_1$  (obtained with MC simulations with  $N = 576$  sites). In the experiment, the correlations satisfy  $c_{3||} > c_2 > c_{3*}$ , with  $c_{3||} \gtrsim 2c_2$  (light green region). For small enough  $J_2$ , there is a temperature region with  $c_2 > c_{3||}$  (orange region), compatible with the nearest-neighbor physics in terms of the descending order of the correlations. Importantly, the smallest value of  $J_2/J_1$  in this graph is  $J_2/J_1 = 0.001$ : for arbitrarily small  $J_2$  the crossing  $c_2 = c_{3||}$  happens at arbitrarily small temperatures (Fig. 3.16). Note as well that at large temperatures, all the correlations are close to zero.

$c_{3||} > c_2 > c_{3\star}$ . Additionally, we have seen in Sec. 3.2 that the proportion of triangles with a given magnetization can be accounted for by introducing a longitudinal magnetic field.

Therefore, we want to consider the following Hamiltonian:

$$H = J_1 \sum_{\langle i,j \rangle_1} \sigma_i \sigma_j + J_2 \sum_{\langle i,j \rangle_2} \sigma_i \sigma_j + J_{3||} \sum_{\langle i,j \rangle_{3||}} \sigma_i \sigma_j - h \sum_i \sigma_i. \quad (3.39)$$

Because of the combination of farther-neighbor frustration and the presence of the field, this model is challenging to study using Monte Carlo simulations. At the same time, writing a converging tensor network formulation for such frustrated systems is non-trivial, because of the challenge of finding the appropriate ground-state local rule in some of the phases. Here, we present a study based on an understanding of the ground state using both methods, and results for the correlations as a function of the temperature using Monte Carlo simulations for small system sizes.

### 3.4.1 Ground state of the $J_1 - J_2 - J_{3||}$ model with and without a field

In zero field, the location of the phase boundaries and the value of the ground-state energy for the ground-state phase diagram has already been established [101], using exact ground-state lower bounds computed with Kanamori's method of inequalities (see Chapter 1 and Appendix F.1.1). For antiferromagnetic couplings  $J_2, J_{3||} > 0$ , there are four different ground-state phases. Our micromagnetic values for the couplings lie well within one of these phases, where

$$E_{\text{G.S.}} = -\frac{2}{3}J_1 - \frac{2}{3}J_2 + \frac{2}{3}J_{3||}. \quad (3.40)$$

As we will show, this phase exhibits a macroscopic ground-state degeneracy.

In this farther-neighbor model, there is a special line for  $J := J_2 = J_{3||}$  where the problem can be elegantly studied using a charge representation [222]. For positive  $J$ , this line coincides with two successive phase boundaries in the ground state of the  $J_1 - J_2 - J_{3||}$  model (see Appendix F.2.1). For  $0 < J < J_1/3$ , a classical spin liquid with an unusual residual entropy  $S \cong 0.32$  (the “hexamer” classical spin liquid) was found in Ref. 222. The effect of a longitudinal magnetic field on this phase has been recently studied in a follow-up work and was shown to give rise, in the ground state, to a number of magnetization plateaus with finite residual entropy [244]. We use these phases to check our tensor network construction in the presence of a magnetic field, and find that the entropies we obtain for the various ground-state phases are in agreement with the existing results (Table 3.7).

As a first step in the tensor network construction, linear programming is used to build ground-state energy lower bounds based on splitting the Hamiltonian into terms defined on clusters [158, 159]. We can thus determine the ground-state energy in the various phases by comparing the lower bound from this method and the upper bound from the Monte Carlo simulations; if they match we have a proof for the value of the ground-state energy, and we

	TN ( $\chi_{\max} = 120$ )	Refs. 222, 244
$h = 0$	$0.322273784 \pm 10^{-9}$	0.32
$m = 1/9$	$0.125616 \pm 10^{-6}$	0.12(6)
$h = 6J_{3  }$	$0.313746908 \pm 10^{-9}$	-
$m = 1/3$	$0.107688 \pm 10^{-6}$	$S_{\text{TIAFM}}/3$
$h = 4(J_1 + J_2) - 6J_{3  }$	$0.26718206 \pm 10^{-8}$	-

Table 3.7 – Residual entropy in the ground state for  $J_2 = J_{3||} \lesssim 0.2$  for the various ground state phases. When indicated by the value of the field, we are looking at a phase boundary, and when indicated by the value of the magnetization plateau, we are looking at the phase between these boundaries.

know that the tensor network will describe the complete ground-state manifold.

Our results for the ground-state phase diagram for  $J_{3||} < J_2$  are summarized in Fig. 3.18. In zero field, we recover the ground-state energy of Eq. 3.40, and from the tensor network construction, we find a residual entropy

$$S_{J_1 - J_2 - J_{3||}} = 0.143949 \pm 6 \cdot 10^{-6} \quad (3.41)$$

which shows that some sort of classical spin liquid is available even when  $J_{3||} \neq J_2$ .

When introducing a finite magnetic field, the system enters an  $m = 1/9$  plateau which survives as long as  $h < 6J_{3||}$ . In this plateau, the ground-state energy is given by

$$E_{1/9} = -\frac{2}{3}J_1 - \frac{2}{3}J_2 + \frac{2}{3}J_{3||} - \frac{1}{9}h. \quad (3.42)$$

We find a zero residual entropy in the thermodynamic limit by contracting the tensor network, but from the Monte Carlo simulations, we find that the ground states differ by non-local updates. In simulations with periodic boundary conditions, these updates correspond to strings of spins that cross the sample and close in on themselves through the periodic boundary conditions (Fig. 3.19.). If one looks at periodic boundary conditions by placing the lattice on a torus, then these updates are winding around the torus. Together with the tensor network result, this suggests that the ground-state degeneracy is macroscopic, but with a sub-extensive residual entropy, growing with the linear system size.

The  $m = 1/3$  plateau corresponds to long-ranged ordered strings of nearest-neighbor up spins separated by down spins, with a ground-state energy

$$E_{1/3} = -\frac{2}{3}J_1 - \frac{2}{3}J_2 + 2J_{3||} - \frac{1}{3}h. \quad (3.43)$$

The phase boundary between the  $m = 1/9$  and  $m = 1/3$  plateau is thus found at  $h = 6J_{3||}$ . At this boundary, the ground states can have various magnetizations, corresponding to mixtures of states of both plateaus. Different sizes in the Monte Carlo simulations select different average magnetizations (Appendix E.4); we therefore refrain from stating a value for the magnetization

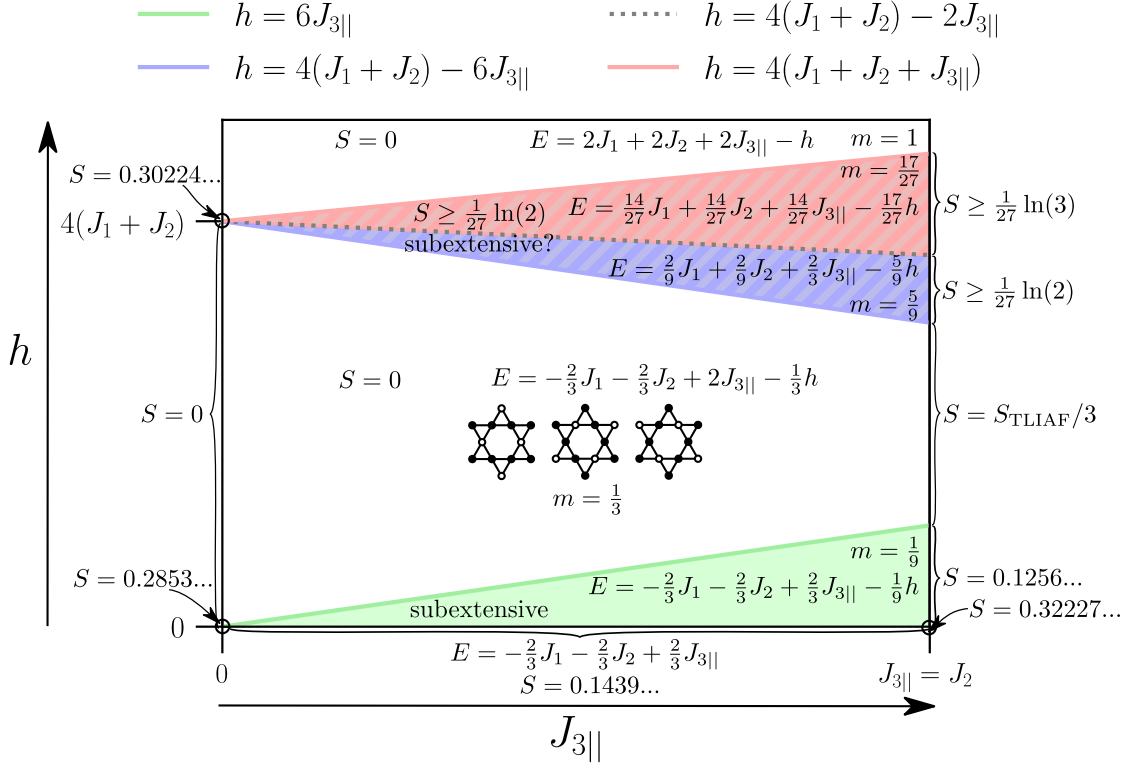


Figure 3.18 – Candidate ground-state phase diagram for the farther-neighbor model in a magnetic field, at a fixed value of  $J_2 < \frac{1}{3}J_1$ . The two hatched regions could only be studied with Monte Carlo computations, whereas the rest of the phase diagram was determined both with Monte Carlo simulations and with tensor networks. When the values are indicated next to arrows, they correspond to a specific point (for instance, we give the result for  $J_{3||} = J_2$  and  $h = 0$ ) and when they are indicated next to brackets they correspond to a specific line (for instance, we give the results for  $J_{3||} = J_2$  and various ranges of the field, which are different from the results for  $J_{3||} < J_2$ ). The ground-state entropies are computed from tensor networks contractions, except for the two inequalities on the  $J_2 = J_{3||}$  line, studied in Ref. 244, and the lower bound in the  $m = 17/27$  plateau, estimated from the Monte Carlo results. The bottom left corner corresponds to the  $J_1 - J_2$  model. A magnetic field in this model immediately lifts the degeneracy to the long range ordered stripe phase. For finite  $J_{3||}$ , there is a macroscopic ground-state degeneracy in zero field. With increasing field, there is first a magnetization plateau at  $m = 1/9$ . Then, the long range ordered stripe phase is selected, followed by a plateau at  $m = 5/9$  and another one at  $m = 17/27$  before saturation. For each phase we give the ground-state energy, which is rigorously proved everywhere except in the two hatched regions.

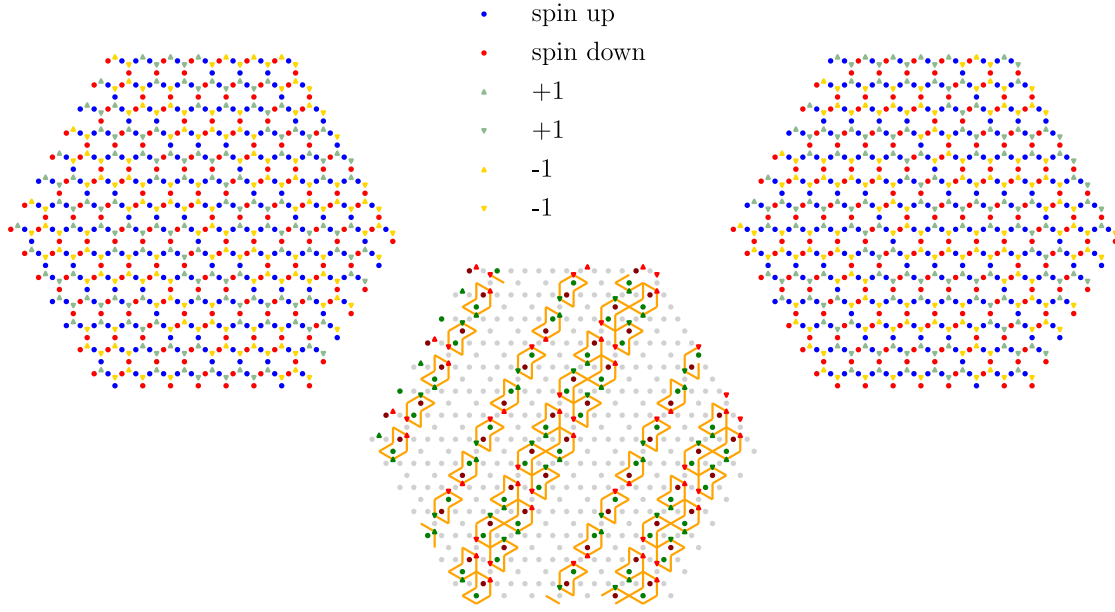


Figure 3.19 – Two examples of ground-state configurations for the  $J_1 - J_2 - J_{3||}$  model, including the corresponding charge configuration, for a magnetic field  $0 < h < 6J_{3||}$  ( $m = 1/9$ ). The central panel shows the difference between the two configurations, with the following convention: the orange lines delimit the regions where spins are flipped, the green (dark red) dots correspond to spins that are flipped from up to down (down to up), and the red (green) triangles correspond to charges that are changed by +2 (-2).



here.

The  $m = 1/3$  plateau extends until  $h = 4(J_1 + J_2) - 6J_{3||}$  where we find a phase boundary. Above this field, the largest clusters that we used to split the Hamiltonian give an energy lower bound which does not match the exact ground-state energy<sup>8</sup>. However, we have evidence from Monte Carlo simulations (Fig. 3.20) that suggests the presence of  $m = 5/9$  and  $m = 17/27$  plateaus corresponding to the ones found at  $J_2 = J_{3||}$  in Ref. 244. The corresponding phase boundaries are at  $h = 4(J_1 + J_2) - 2J_{3||}$  and  $h = 4(J_1 + J_2 + J_{3||})$ , which means that this region is extremely reduced for our micromagnetic values of  $J_1, J_2$  and  $J_{3||}$ . In the  $m = 5/9$  plateau, with periodic boundary conditions in the Monte Carlo, we find again that ground states differ by strings of spins winding the torus, suggesting a sub-extensive residual entropy, whereas some local moves can be seen in the  $m = 17/27$  plateau, providing a lower bound for the residual entropy  $S \geq \frac{1}{27} \ln(2)$  (Appendix E.4).

### 3.4.2 Effect of the temperature and spin-spin correlations

We finally give a qualitative discussion of the effects of temperature on the spin-spin correlation in this farther-neighbor model in a field, and compare our predictions to the experimental results. In the rest of this section we consider  $J_2 = 0.023J_1$  and  $J_{3||} = 0.0103J_1$ , corresponding to the micromagnetic simulations results.

Fig. 3.20 gives a qualitative picture of the magnetization as a function of field and temperature. Because the problem is a challenge for our Monte Carlo simulations (where we use the single-spin-flip algorithm combined with replicas in magnetic field and temperature), we only focus on small system sizes where needed. In Fig. 3.20, the selection of the various magnetization plateaus of the ground state with increasing fields is shown. With increasing temperatures, we find around the  $m = 1/3$  and  $m = 1/9$  plateau a behavior similar to the one in the  $J_1 - h$  model around the  $m = 1/3$  plateau (Sec. 3.2.2): if the field is large, intermediate temperatures will give a larger average magnetization than the plateau value, whereas if the field is small, the magnetization immediately decreases with increasing temperatures.

In analyzing the spin-spin correlations, we first consider Fig. 3.21, presenting the results in zero field. Although, in the ground state, the results are quite different from the  $J_1 - J_2$  model (Fig. 3.16), the qualitative result that there is a temperature range where  $c_{3||} \gtrsim 2c_2$  remains correct. This has to be contrasted to the nearest-neighbor model results, and shows that the experimental results can only be understood by taking into account farther-neighbor couplings, and that  $J_2$  plays the important role, while  $J_{3||}$  is simply not large enough to suppress the effect of  $J_2$ . It can also be seen in this figure that these results would be valid for a wide range of values of the couplings, including the dipolar case truncated to  $3||$  neighbors.

<sup>8</sup>Meaning the corresponding ground-state tiles fail to tile the lattice, and the tensor network contraction fail. Larger clusters would be required, probably made of 6 to 12 stars from what we see of the Monte Carlo simulations; this requires some adaptation of the code to implement symmetries systematically along the lines of Sec. 2.5, which we did not yet tackle.

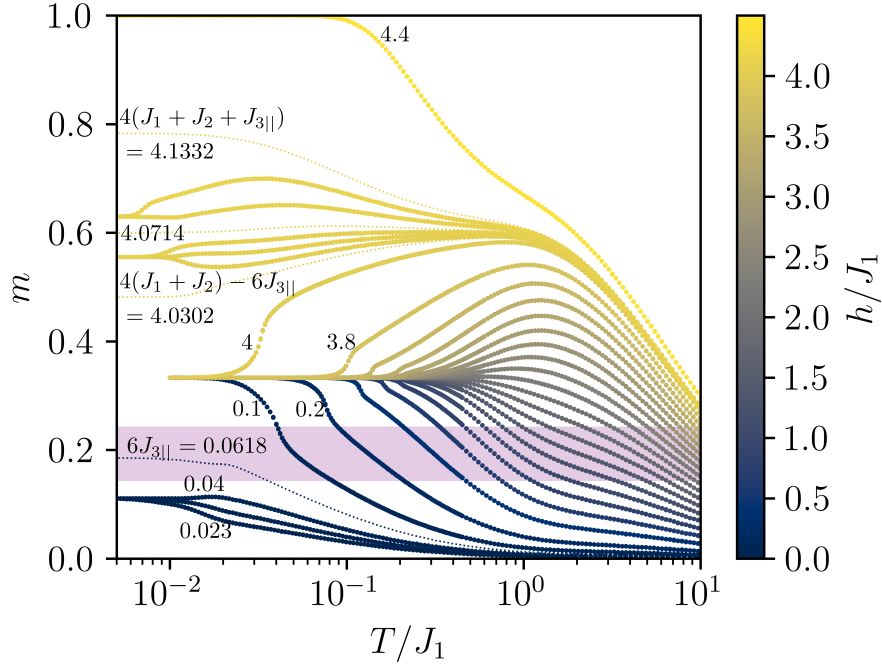


Figure 3.20 – Qualitative behavior of the magnetization as a function of the field and temperature in the  $J_1 - J_2 - J_{3||} - h$  model. The points come from Monte Carlo simulations with  $N = 900$  in the  $m = 1/3$  plateau, with  $N = 144$  in the  $m = 5/9$  plateau and with  $N = 376$  in the other regions. The dotted lines are also from Monte Carlo simulations but correspond to the magnetization at the transition between plateaus; they are only given as a guide to the eye as the results strongly depend on the system size (Appendix E.4). The highlighted region corresponds to the region within one standard deviation of the experimental magnetization. The annotations indicate the value of the magnetic field for various curves.

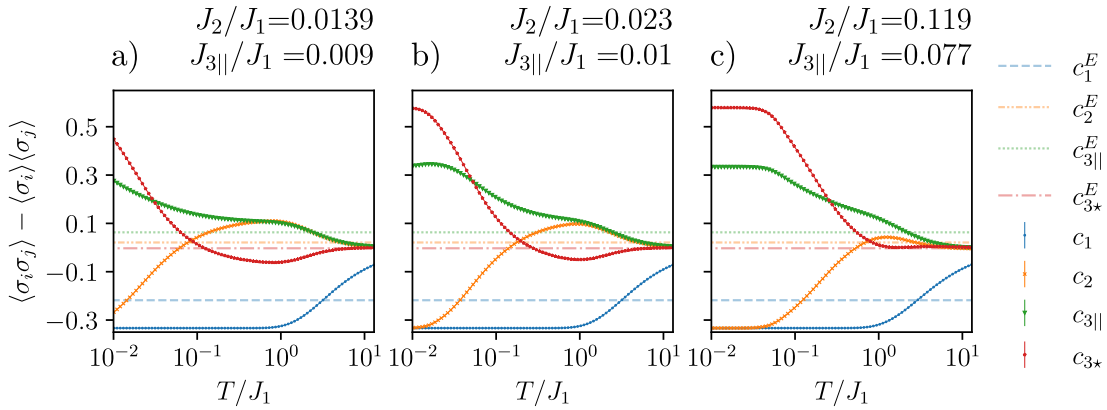


Figure 3.21 – Overview of the behavior of the first few correlations as a function of the temperature for the values of  $J_2$  and  $J_{3||}$  from micromagnetic simulations ((a): dipolar corrections to the nearest-neighbor model, (b) actual couplings with IP part, (c) purely dipolar model (no IP regions)), with Monte Carlo simulations for 2 system sizes ( $N = 576, 1296$ ). The smaller system size is shown with a line while the larger one is shown with symbols.

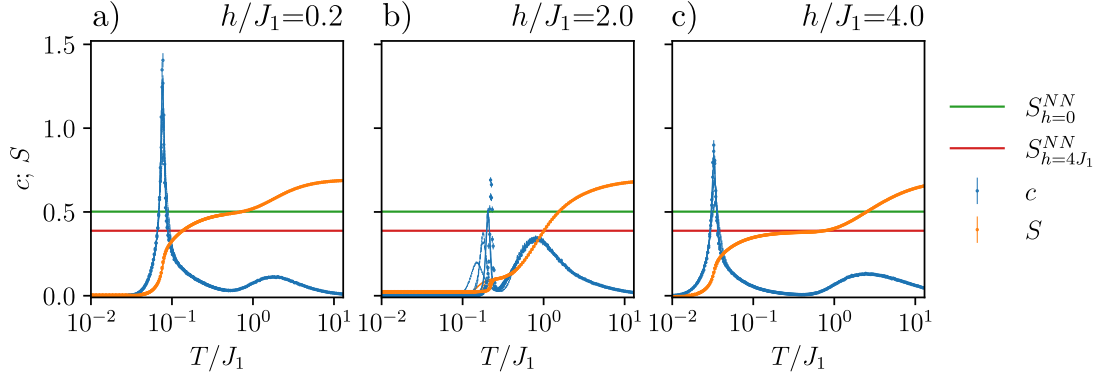


Figure 3.22 – Specific heat and residual entropy in the  $m = 1/3$  plateau for  $N = 36$  to  $N = 1296$  (markers). (a) At small fields there is an intermediate temperature region where the entropy corresponds to that of the nearest-neighbor model in zero field, whereas (c) at large fields there is an intermediate temperature region where the entropy corresponds to the nearest-neighbor model in a field at  $h = 4J_1$ . (b) We note that at intermediate fields there are strong finite size effects and the loss of residual entropy at the transition is not captured correctly by our simulations - the residual entropy in the ground state should be zero.

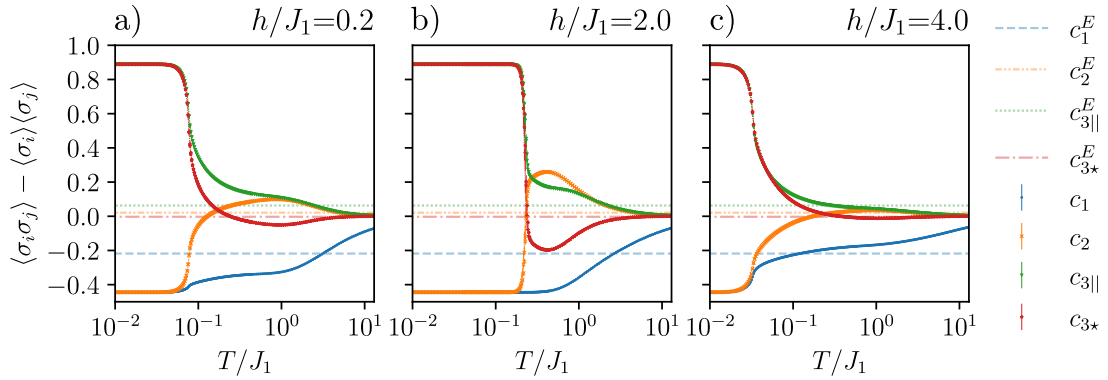


Figure 3.23 – Spin-spin correlations in the  $m = 1/3$  plateau for  $N = 900$  (dotted lines) and  $N = 1296$  (markers). The dashed lines indicate the experimental correlations, for comparison. (a) For small magnetic fields (Region A in Fig. 3.24) there is an intermediate range of temperatures where the correlations correspond to the model in zero field (Fig. 3.21). (b) At intermediate field, the  $c_2$  correlations again become larger than the  $c_{3||}$  correlations. (c) At large fields, there is an intermediate temperature region where the correlations are similar to those in the  $J_1 - h$  model at  $h = 4J_1$ , but with an effect of the farther-neighbor couplings which inverts the  $c_2$  and  $c_{3||}$  correlations.

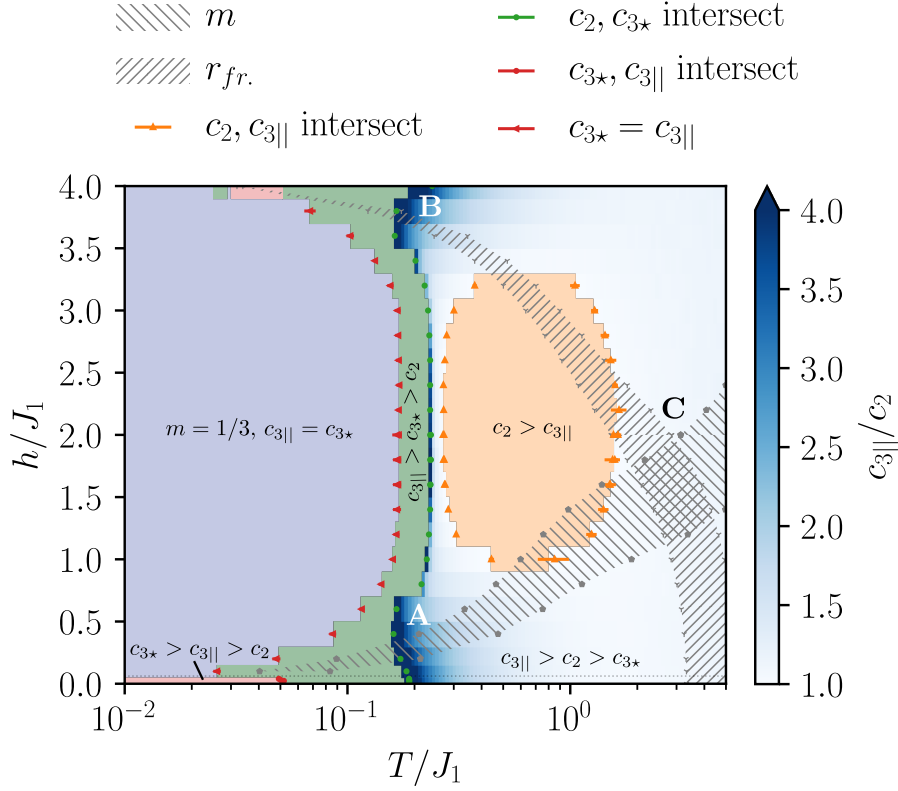


Figure 3.24 – Monte Carlo simulation results for the  $J_1 - J_2 - J_{3||} - h$  model as a function of the temperature. (A), (B) and (C) : the letters are placed just above three regions of interest, discussed in the main text. The various colored areas correspond to the values of temperature and fields where the correlations are in a certain descending order according to the Monte Carlo simulations. The “pixels” correspond to the 22 field points and 214 temperatures. With increasing temperature: in light blue, the region where the system is in the  $m = 1/3$  plateau ground state, with  $c_{3||} = c_{3*} = 8/9$ ; in light red, the region outside this plateau where  $c_{3||} < c_{3*}$ ; in green, the region where the  $c_2$  correlations are larger than  $c_1$  but still smaller than  $c_{3*}$ ; with the color map, the region where the descending order of the correlations is the same as in the experiment:  $c_{3||} \geq c_2 > c_{3*}$ ; in orange, the region where  $c_2 > c_{3||} > c_{3*}$ . The hatched regions indicate the values of the temperature and field where the Monte Carlo simulations results for the magnetization  $m$  and the proportion of ferromagnetic (“frustrated”) triangles  $r_{fr.}$  agree within the errors with the experimental values. The color map indicates the ratio of  $c_{3||}$  to  $c_2$  in the region where the descending order of the correlations is the same as in the experiment; experimentally, this ratio is of the order of 2 to 3 in most samples (but  $c_2$  can be negative in some samples, Fig. 3.5).

Besides the descending order of the correlations, a qualitative characteristic of the experimental results is the presence of a non-zero magnetization, which we try to account for by introducing a magnetic field. We have seen that if there is a field in the experiment, we expect it to be very roughly of the order of  $J_2 \lesssim h \lesssim J_1$ ; in addition, when considering the percentages of triangles with a given magnetization, the nearest-neighbor model predicts  $h \sim 1.6J_1$ . It thus seems sufficient to focus mainly on the two first magnetization plateaus. This is confirmed by the comparison between the experimental magnetization and the Monte Carlo simulations prediction for the magnetization in Fig. 3.20. This result shows that it is sufficient to study the behavior in temperature for fields  $6J_{3\parallel} < h < 4(J_1 + J_2) - 6J_{3\parallel}$  corresponding to the  $m = 1/3$  plateau. Figs. 3.20, 3.22, and 3.23 give a consistent picture of the behavior of the model as a finite temperature is applied on the  $m = 1/3$  plateau ground state. At small fields, there is an intermediate temperature region where the system essentially behaves as the farther-neighbor model in zero field: the residual entropy of the nearest-neighbor model is recovered (Fig. 3.22) but the  $c_2$  and  $c_{3\parallel}$  correlations are already inverted as compared to the nearest-neighbor model (Fig. 3.23). With increasing fields, the transition to the long range ordered ground state (stripe phase) happens at higher temperatures, with stronger and stronger finite size effects, reaches a maximum, then decreases again (Figs. 3.20 and 3.24). For  $h = 4J_1$ , at intermediate temperatures, we find approximately the residual entropy of the nearest-neighbor model (Fig. 3.22), with again an effect of the farther-neighbor couplings on the  $c_2$  and  $c_{3\parallel}$  correlations (Fig. 3.20).

We want to verify that the zero field  $c_{3\parallel} > c_2$  region is preserved in the presence of a magnetic field. In order to compare to the experimental results, we show a map of the descending order of the first four spin-spin correlations in Fig. 3.24, for  $J_2 = 0.023J_1$  and  $J_{3\parallel} = 0.0103J_1$ , as a function of the field and temperature. The region where the descending order of the correlations in the experiment ( $c_{3\parallel} > c_2 > c_{3\star}$ ) is reproduced by the Monte Carlo simulations is shown by a color map, which gives the  $c_{3\parallel}/c_2$  ratio. For small fields  $0 \leq h/J_1 \lesssim 0.5$  and temperatures  $0.1 \lesssim T/J_1 \lesssim 1$ , the  $c_{3\parallel} > c_2$  region indeed survives (with a reasonably large ratio of  $c_{3\parallel}/c_2$ ). At fields ranging from  $0.8J_1$  to  $3.2J_1$ ,  $c_2$  becomes larger than  $c_{3\parallel}$  for  $0.15 \leq T/J_1 \leq 1.5$ , which is consistent with the results of the nearest-neighbor model in a field, for which in this region the  $c_2$  correlations are much larger than the  $c_{3\parallel}$  correlations. At large fields,  $c_2$  decreases again such that  $c_{3\parallel} > c_2$  is valid for fields  $3.5 \lesssim h/J_1 \lesssim 4$ . Thus, even in the presence of an external magnetic field in the farther-neighbor model, there are still regions that account for the order of spin-spin correlations in the experiment, with a reasonable ratio of  $c_{3\parallel}$  to  $c_2$ .

In Fig. 3.24, the hatched regions correspond to the values of field and temperature where the theoretical magnetization and the proportion of ferromagnetic triangles agree within the error bars with the experimental values. Although it demonstrates that it is not possible to account for all the experimental results at once, this graph highlights three regions of interest:

- region **A** at low field  $h/J_1 \sim 0.2$  to  $0.5$  and temperatures  $0.2 \lesssim T/J_1 \lesssim 0.4$  where the Monte Carlo results for the magnetization match the experimental results and where the ratio of  $c_{3\parallel}$  to  $c_2$  is similar to the experimental value, but where the Monte Carlo

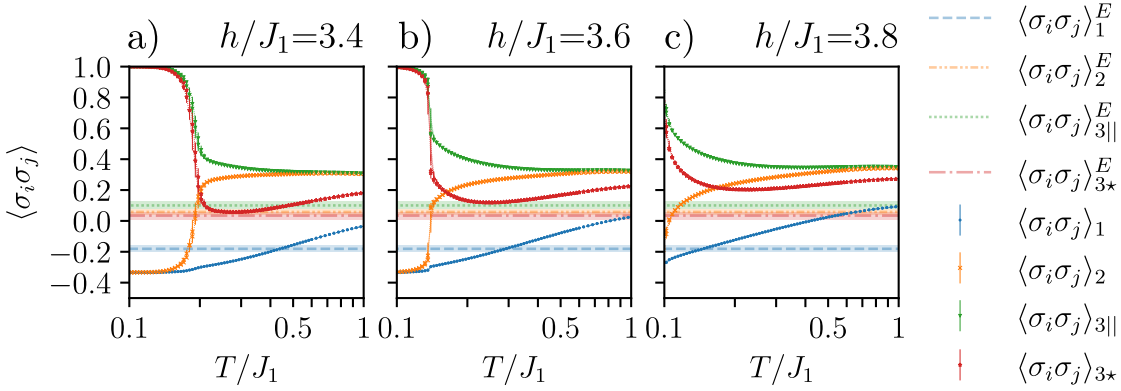


Figure 3.25 – (Region **B** in Fig. 3.24) Behavior of the first few (disconnected) correlations at large magnetic field, in the window where  $c_{3||}/c_2$  is of the same order of magnitude as in the experiment. The proportion of frustrated triangles is directly related to  $\langle \sigma_i \sigma_j \rangle_1$ ; in this region, both are in agreement with the experimental value. Since the magnetization is very different from the experimental value, we plot the disconnected correlations (i.e. the correlations without removal of the squared magnetization) for a valid comparison.

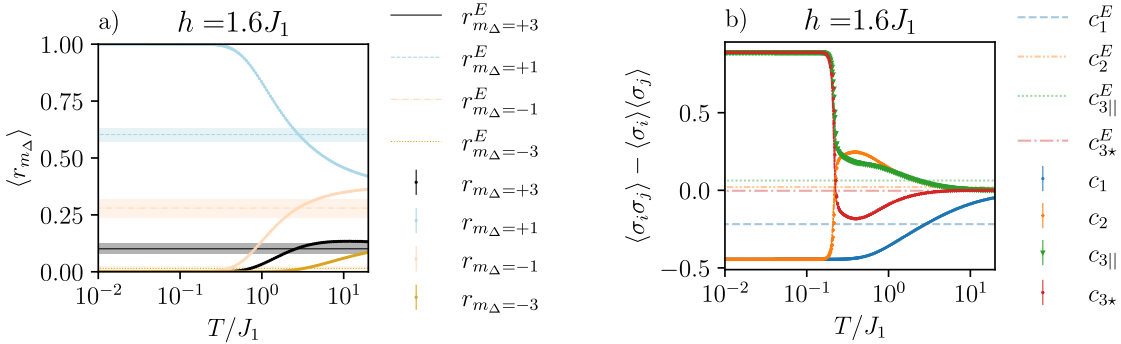


Figure 3.26 – (Region **C** in Fig. 3.24) Monte Carlo results for two sizes ( $N = 900, 1296$ ). (a) Expectation value for the proportion of triangles with magnetization  $m = -3, -1, +1, +3$  as a function of the temperature for an intermediate field. We recover the result of the nearest-neighbor model in a field (Fig. 3.13). (b) Behavior of the first few correlations at the same field. At intermediate temperatures,  $c_2 > c_{3||}$ , and at large temperatures,  $c_2 \lesssim c_{3||}$  (the two are essentially equal).

simulations predict zero ice-rule-breaking triangles. The corresponding correlation results are illustrated in the panel (a) ( $h = 0.2J_1$ ) of Fig. 3.23; it can be seen that they are quite different from the experimental results.

- region **B** at large field  $3.4 \lesssim h/J_1 \lesssim 3.8$  and intermediate temperatures  $0.15 \lesssim T/J_1 \lesssim 0.5$ , where the combined effect of the temperature and magnetic field reproduces the experimental proportion of ice-rule-breaking triangles, and where the ratio of  $c_{3\parallel}$  to  $c_2$  is again similar to the experimental value. However, in this region, the Monte Carlo simulations predict  $\langle r_{m_\Delta=-1} \rangle = \langle r_{m_\Delta=-3} \rangle = 0$  (all triangles are aligned with the field). Correspondingly, the magnetization predicted by the Monte Carlo simulations is around twice the experimental results ( $0.35 \lesssim m \lesssim 0.5$  instead of  $m \sim 0.2$ ). The disconnected correlations for this region are shown in Fig. 3.25; the farther-neighbor correlations are larger than their experimental counterpart.
- region **C** at intermediate field  $1 \lesssim h/J_1 \lesssim 2$  and high temperatures  $2 \lesssim T/J_1 \lesssim 4$  where the number of triangles and the magnetization are both compatible with the experiment. Just as in the nearest-neighbor model in a field, requiring that all the percentages of triangles with given magnetization match with the experiment gives  $h \cong 1.6J_1$  (Fig. 3.26a). However, Figs. 3.24 and 3.26b both show that, despite taking into account the farther-neighbor couplings, the correlations  $c_{3\parallel}$  and  $c_2$  remain essentially equal in this region.

### 3.5 Discussion

From the analysis of the experimental data, we extract the main observation that  $|c_1| > c_{3\parallel} > c_2 \gtrsim c_{3\star}$ . There are two additional qualitative observations: the systematic presence of a non-negligible proportion of ice-rule-breaking triangles and of a finite magnetization for all the samples, the magnetization of all the samples having the same sign. These two observations correspond to having precise proportions of triangles with magnetization  $-3, -1, +1$  and  $+3$ , given in Table 3.2.

From the micromagnetic simulations, we obtain that the effect of the IP regions in the samples is first and foremost to increase the nearest-neighbor couplings significantly (approximately by a factor of 10), and second to slightly increase the second and third neighbor couplings, resulting in a system where the next nearest-neighbor coupling  $J_2$  is of the order of 2% of the nearest-neighbor coupling  $J_1$ , and the third nearest-neighbor coupling  $J_{3\parallel}$  is of the order of 1% of  $J_1$ .

Basing our analysis on the Monte Carlo and tensor networks simulations, we have asked the following questions:

1. Considering an equilibrium distribution characterized by two Lagrange parameters - temperature and field - and corresponding to a model involving only nearest-neighbor couplings, can we reproduce the experimental proportions of triangles having a given

magnetization?

2. Considering this equilibrium distribution, is it possible to describe the descending order of the first spin-spin correlations in the experiment, or does one have to consider a model involving farther-neighbor couplings? If so, is there a limit on how small these couplings have to be to become negligible?
3. Finally, does the resulting equilibrium fully describe the experimental results, including the percentages of triangles with  $m = +3, +1, -1, -3$  and the actual values of the correlations?

The data in Fig. 3.13 allows us to easily determine that a simple model, the nearest-neighbor Ising antiferromagnet in a field, admits a region of field and temperature matching the experimental results for the number of triangles with a given magnetization. However, the corresponding temperature is quite large ( $T \sim 2.8J_1$ ).

When taking into consideration the experimental spin-spin correlations and comparing them to the nearest-neighbor Ising antiferromagnet (Figs. 3.8 and 3.14), it is quite clear that the system is not accurately modeled by an equilibrium distribution if one simply neglects the farther-neighbor couplings altogether. Instead, the simulations of the  $J_1 - J_2$  model confirm that even a small next nearest-neighbor coupling plays an essential role, affecting the correlations in a significant way (Figs. 3.16, 3.17 and 3.21). In the ground state, this is obviously the case because farther-neighbor couplings lift partially the macroscopic ground-state degeneracy of the nearest-neighbor model. What our results show is that, in addition, the correlations are also affected up to large temperatures, even for small values of  $J_2$ . For intermediate temperatures ( $0.1J_1 \lesssim T \lesssim 0.5J_1$ ), this modification can be sufficient to explain the descending order of the experimental correlations with respect to one another for  $J_2 \gtrsim 0.02$  (Fig. 3.16); for large temperatures ( $T \sim 3J_1$ ), the next nearest-neighbor couplings need to be larger ( $J_2 \gtrsim 0.06$ ) to obtain the same result. The micromagnetic simulations predict a third neighbor ( $J_{3||}$ ) coupling of the order of  $J_2/2$  (Fig. 3.4). This coupling naturally competes with the  $J_2$  coupling; in the ground state, it further lifts the degeneracy, leading to a reduced residual entropy (Eq. 3.41), and it affects the correlations (Fig. 3.18). At finite temperature, this third-neighbor coupling modifies the correlations as compared to the  $J_1 - J_2$  model, and therefore has to be taken into account. Despite this competition, a region with  $c_{3||} \gtrsim 2c_2$  is still present (Fig. 3.21).

In the farther-neighbor model, the magnetic field plays a similar role as in the nearest-neighbor model: combined with the temperature, it selects the proportion of triangles with a certain magnetization, setting the overall magnetization (Fig. 3.20) and the number of frustrated triangles (Fig. 3.24). Additionally, it affects the correlations both in the ground state and at finite temperature. In the ground state, depending on the value of the field, the degeneracy gets either partially or completely lifted (Fig. 3.18) and, at experimentally relevant fields, the third neighbor correlations can vary from  $c_{3||} = 26/81$  ( $m = 1/9$  plateau) to  $c_{3||} = 8/9$  ( $m = 1/3$  plateau). At finite temperature, the region where  $c_{3||}$  is larger than  $2c_2$  is preserved for two ranges of magnetic fields, illustrated by regions **A** and **B** in Fig. 3.24.



While the data in Fig. 3.24 demonstrates that the descending order of the correlations in the experiment can be recovered provided that farther-neighbor couplings are considered, this data also illustrates the impossibility of explaining simultaneously the entirety of the results based on these equilibrium distributions: the ratio of  $c_{3||}$  to  $c_2$  in most of the samples cannot be explained at the same time as the value of the magnetization and the proportion of ice-rule-breaking triangles. Based on the available information about the experiment, it is difficult to know in which further direction to push the models. Nevertheless, three interesting regions can be observed, at intermediate temperatures for small field (region **A**) and large field (region **B**), and at large temperatures for intermediate fields (region **C**).

In region **A**, the magnetization matches the experimental results, but there is no ice-rule-breaking triangle, and correspondingly the nearest-neighbor correlations take their ground-state value, which is qualitatively very different from the experiment. To fully account for the experimental results, an additional mechanism would thus have to be invoked. Starting from a region with a smaller magnetic field than region **A**, a possibility could be a source of disorder that would not be described by the temperature, such as a disorder in the coupling strengths generated by the IP regions or the presence of sites whose magnetization is not well defined, pinning ice-rule-breaking triangles at “domain walls” between low-energy states grown on the lattice, thus reducing the spin-spin correlations and fixing the magnetization.

Region **B** is different, in that the percentage of ferromagnetic triangles, and correspondingly the expectation value  $\langle \sigma_i \sigma_j \rangle_1$ , correspond to the experimental results, but that the magnetization and the expectation values  $\langle \sigma_i \sigma_j \rangle_k$  for the farther neighbors are larger than the experimental result. Again, in absence of additional insight regarding the experiment, we can only suggest hypotheses involving another effect. In this case, it could perhaps be that, by switching domains of a certain size, the demagnetization protocol would preserve the number of ice-rule-breaking triangles, while reducing the farther-neighbor correlations and the magnetization.

Finally, region **C** is interesting because the experimental proportion of triangles with a given magnetization is well reproduced by the magnetic field and the temperature: no additional mechanism would be needed to describe the magnetization or the number of ice-rule-breaking triangles. However, the second and third neighbor correlations  $c_2$  and  $c_{3||}$  are essentially equal (when  $J_2$  and  $J_{3||}$  take the values predicted by the micromagnetic simulations), which does not seem to be in full agreement with the experiments. Looking at Fig. 3.17, one can see that in the  $J_1 - J_2$  model and for temperatures  $T/J_1 \sim 3$ , the next nearest-neighbor couplings should be of order  $J_2 \sim 0.06J_1$  to  $J_2 \sim 0.11J_1$  to reproduce the experimental correlations. This would correspond to at least a factor of 3 for  $J_2/J_1$  as compared to the micromagnetic simulations. This seems unlikely, but we have to note that the micromagnetic simulations are performed for an idealized nanomagnet, and that the use of a square grid in the simulation did create a small difference between the nearest-neighbor couplings in two different directions ( $J_{1,h} = 1.868 \cdot 10^{-20} \text{J}$  while  $J_{1,d} = 1.884 \cdot 10^{-20} \text{J}$ ). However, the insight on the value of  $J_2$  based on Fig. 3.17 needs to be taken into account very carefully as it would be affected by the presence of third neighbor couplings and a magnetic field. We have not performed a systematic scan

for a range of values of  $J_{3||}$  vs  $J_2$ ; we can therefore not conclude what range of couplings would provide a complete match with the experimental results in this region. Another difficulty with this region is conceptual: the corresponding effective temperature seems large and could be interpreted as an attempt to model disorder in the coupling strengths; in this context, it is difficult to decide how far a precise comparison between the predicted and experimental correlations in this region can be pushed to draw meaningful conclusions.

## 3.6 Summary and outlook

In this Chapter, we have presented Monte Carlo and tensor network results for a series of short range antiferromagnetic Ising models on the kagome lattice, in the presence of a longitudinal field, computing the first few spin-spin correlations systematically. These models are combined to give the  $J_1 - J_2 - J_{3||} - h$  model, for which we established a candidate ground-state phase diagram as well as the temperature dependence of the magnetization and first correlations. In light of these simulations together with micromagnetic computations, we have studied the experimental results obtained from an array of chirally coupled nanomagnets on the kagome lattice.

The micromagnetic simulations show that arrays of chirally coupled nanomagnet using Dzyaloshinskii-Moriya interactions are a good basis for investigating models with extremely strong nearest-neighbor antiferromagnetic couplings. Indeed, even though short range farther-neighbor couplings are strengthened as well, the micromagnetic simulations suggest that they increase by a much smaller factor, resulting in an effective model which is significantly different from the dipolar Ising case.

Our Monte Carlo and tensor network simulations show that even very small farther-neighbor couplings significantly affect the first few spin-spin correlations, and that the next nearest-neighbor coupling  $J_2$  cannot be neglected even if it is as small as 2% of the nearest-neighbor coupling  $J_1$ . Additionally, our results show how the correlations are affected by the introduction of a third neighbor coupling  $J_{3||}$  and a magnetic field  $h$ . Their effect on the spin-spin correlations is summarized in Figs. 3.18 (for the ground state) and 3.24 (for the descending order of the correlations as a function of the temperature).

Although Fig. 3.24 shows that it is not possible to obtain a complete quantitative description of all the results of the experiment, it allows one to spot two regions of interest (**A** and **B**) at small and at large fields which seem to contain the essence of the experimental results (namely the descending order of the correlations) and might serve as a support to explain the observations modulo the introduction of an additional ingredient (a source of defects at weak field and a mechanism of reduction of the magnetization at large field). A third region (**C**) shows that a combination of an intermediate field and a surprisingly large temperature (suggesting the presence of disorder in the coupling strength due to local changes in the DMI or in the IP width, or disorder corresponding to the presence of nanomagnets whose local magnetization is not well determined from our measurements) can reproduce the experimental proportions

of triangles with a given magnetization, but not the difference between the second and third neighbor correlations.

We hope that our results can motivate and support further research both on the experimental and theoretical side. Experimentally, our contribution is to make a step in a new direction for tuning the ratios of the couplings in artificial spin systems emulating frustrated Ising models on the kagome lattice. Realizing a similar system but where the in-plane part separating three nearest-neighbor sites on the kagome lattice would have a triangular hole might change the effective model. *A priori*, one could expect that the nearest-neighbor couplings would remain large but that the effective second and third neighbor couplings would be smaller<sup>9</sup>. This is, however, a technical challenge because of the small size of the triangle that needs to be created. It is also not clear whether this could help to recover the nearest-neighbor correlations, since  $J_2$  should still be of the order of 1% of  $J_1$ ; as Figs. 3.16 and 3.21 show, the results will also depend on the ratio of  $J_{3||}$  to  $J_2$ . Another possible direction of improvement would be to have measurements allowing the determination of the configuration of the IP regions as well as the OOP regions, to confirm the micromagnetic simulations predictions and check that the IP regions do not get stuck in configurations which do not minimize the energy.

On the theoretical side, we have uncovered the phase diagram of the  $J_1 > J_2 > J_{3||}$  model in a field, exhibiting an interesting range of macroscopically degenerate phases, some with sub-extensive residual entropy, hopefully motivating further investigation. Besides the Hamiltonian considered here, we see two main directions for more involved models. The first is to determine whether the observed effects could be due to disorder in the switching fields, the coupling strengths or the presence of vacant sites, by modelling the effect that such disorder would have on the spin-spin correlations. In artificial spin systems in general, the role of structural disorder is a subtle problem. For instance, Budrikis et al. [85–87] showed that the intrinsic disorder in switching fields affects the dynamics of athermal artificial square ice and plays a role in reaching the ground state in experiments. In chirally coupled arrays, both because the nearest-neighbor exchange interactions are dominant and because of the macroscopic degeneracy of some of the ground state phases for truncated Hamiltonians, structural disorder might have a very different effect than that observed in in-plane square and kagome ice. From the numerical point of view, the loss of translation invariance could make this problem an interesting application of the tropical tensor networks [223].

The second direction for improving the model, assuming absence of disorder in coupling strength, would be to perform micromagnetic simulations on larger structures to determine the impact that the IP regions have on effective long range couplings in this system, and, in particular, to see if these long range couplings are different from the well-studied dipolar model. Comparing the values of these longer range couplings to the predicted short range four site couplings (Fig. 3.2) seems to be an essential step to build a more accurate model including the next order of interactions.

<sup>9</sup>This would perhaps give results similar to Eqs. 3.10.

#### Statement of contribution

The work detailed in this Chapter has been published in *J. Colbois, K. Hofhuis, Z. Luo, X. Wang, A. Hrabec, L. J. Heyderman, and F. Mila, Artificial out-of-plane Ising antiferromagnet on the kagome lattice with very small farther-neighbor couplings, Phys. Rev. B 104, 024418 (2021) [160]*, and is reproduced with permission from all co-authors.

The chirally coupled samples were fabricated by Z.L., and the MFM measurements were performed by X.W. with a magnetization protocol designed together with A.H. The MFM measurements analysis was performed in part by K.H. and in part by J.C. The micromagnetic simulations were performed by K.H. and analyzed in close collaboration with J. C.. The numerical analysis was performed by J.C., who implemented the Monte Carlo code and used the Ghent Quantum Group implementation of VUMPS for the tensor network simulations (Refs. 148–151). The linear program to compute the ground-state energy lower bounds was slightly adapted by J.C. from the code of Bram Vanhecke for Ref. 159. The manuscript was written by J.C. with inputs from K.H. for the experimental part, and with corrections and suggestions from all authors. The work was performed under the supervision of A.H., L. H. and F. M.

## 4 Progressive lifting of the KIAFM ground-state degeneracy

The motivation for the following project initially stems from the design and study of artificial spin systems on the kagome lattice with out-of-plane anisotropy [80, 81]. In these systems, the magnetostatic interactions are well-modeled by a dipolar approximation giving rise to an Ising Hamiltonian with long-range, antiferromagnetic couplings; the finite size of the nanomagnets as well as proximity effect have been shown to create corrections mostly in the nearest-neighbor couplings [81, 88], yielding a Hamiltonian of the following form for the dipolar kagome Ising antiferromagnet (DKIAFM):

$$H_{\text{DKIAFM}} = J_0 \sum_{\langle i,j \rangle} \sigma_i \sigma_j + D \sum_{(i,j)} \frac{\sigma_i \sigma_j}{|r_{i,j}|^3}. \quad (4.1)$$

These systems were originally investigated in Ref. 80; the development of the nearest-neighbor correlations in the out-of-plane kagome system have been compared to those of the then more well-studied in-plane kagome ice, and it was suggested that the similar development of the nearest-neighbor correlations corresponded to a universality in the artificial spin systems. As discussed in the general introduction, this can be understood from the equivalence between the nearest-neighbor Ising antiferromagnet on the kagome lattice and the ferromagnetic kagome spin ice model [93, 94].

However, Ref. 81 later found signatures of the dipolar couplings in the development of the spin-spin correlations, and even more clearly in the correlations between charges, defined up to a sign as the sum of the spins on each kagome triangle<sup>1</sup>. This occurs even in relatively high-temperature regimes accessible from demagnetization. This sparked an interest for the dipolar Ising antiferromagnet on the kagome lattice (DKIAFM). The model is particularly challenging to study using Monte Carlo simulations [82, 99]; despite this, Chioar et al. [82] managed to propose a ground-state candidate corresponding to a long-range order with a

---

<sup>1</sup>These are similar charges as those mentioned in the introduction for in-plane kagome ice. Although one has to be careful with the validity of the approximations when using the dumbbell picture in the case of out-of-plane anisotropy, the charges introduced as the sum of spins on a triangle still yield an interesting picture of the ground states.

12-sites unit cell (Fig. 4.2). Later, single-spin-flip Monte Carlo simulations of small systems using a modified Monte Carlo sweep compensating for the low acceptance ratio confirmed the proposed ground state and provided evidence that the transition to the long-range ordered ground state is first order [99]. Furthermore, the study of the autocorrelation function and the relaxation time showed that they are characteristic of fragile glasses. Finally, a treatment of the model at a mean-field level [100] showed a remarkable agreement with the Monte Carlo results, with a weakly first-order phase transition from the paramagnetic phase to the long-range ordered ground state, and a spin-glass transition occurring at the mean-field level which provides an interpretation for the dynamical slowing-down observed in Ref. 99.

When considering, on the one hand, the macroscopic ground-state degeneracy of the nearest-neighbor model, and on the other hand, the long-range ordered ground state of the dipolar model, it is natural to wonder how the ground-state degeneracy gets lifted. In particular, is this ground state already selected when the model is truncated to second- or third-neighbor interactions? This question is especially relevant given the recent development of new possibilities for tuning the couplings in artificial spin systems [108, 113, 160], which could give access to such short-range frustrated models.

In the Appendix of Ref. 99, the dipolar model truncated to second- and to third-nearest neighbors is also discussed. The  $J_1$ - $J_2$  model still exhibits a finite residual entropy, as discussed also in Ref. 102 (see [245] for a related model). For the model including third neighbors, the Monte Carlo simulations of Ref. 99 fall out of equilibrium, but a Pauling estimate suggests that the residual entropy should be zero and the system should order. Motivated by these results, we consider the model truncated to third-neighbor couplings, and investigate the ground-state phase diagram as a function of the second- and third-neighbor couplings.

We consider the following Hamiltonian:

$$H = J_1 \sum_{\langle i,j \rangle} \sigma_i \sigma_j + J_2 \sum_{\langle i,j \rangle_2} \sigma_i \sigma_j + J_{3||} \sum_{\langle i,j \rangle_{3||}} \sigma_i \sigma_j + J_{3\star} \sum_{\langle i,j \rangle_{3\star}} \sigma_i \sigma_j. \quad (4.2)$$

Since the dipolar interactions only depend on the distance, we consider  $J_{3||} = J_{3\star} =: J_3$  in most of the Chapter. The type of pairs are indicated in Fig. 4.1. In that Figure, it can be seen that the 2<sup>nd</sup> nearest-neighbor couplings form kagome sublattices, and the 3<sup>rd</sup> nearest-neighbor couplings form triangular sublattices (when  $J_{3||} = J_{3\star}$ ). For each of these couplings, there are three different sublattices.

In the remainder of this Chapter we start by discussing already known results in related models and for special points of this model that we will use to benchmark our code of the ground-state phase diagram. We also discuss predictions for the dipolar model that will be of interest to put our results in perspective. We then discuss the application of Kanamori's method to the case of the  $J_1 - J_2 - J_3$  model. Combining these lower bounds to upper bounds that we establish using a dual worm Monte Carlo algorithm, we give exact ground-state energies for the model in the region where  $J_1$  is antiferromagnetic and  $J_1 \gg J_2, J_3$ . After an overview of

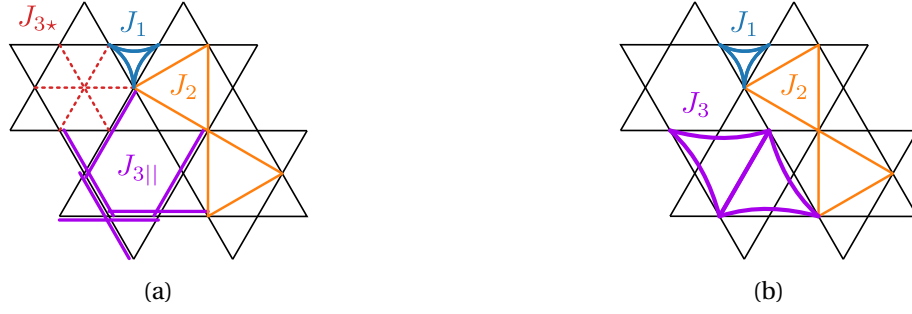


Figure 4.1 – The couplings for the Hamiltonian in Eq. 4.2, with (a) the distinction between the two types of third neighbor couplings  $J_{3||}$  and  $J_{3\star}$  and (b) the triangular sublattices associated with  $J_3 := J_{3||} = J_{3\star}$  which is the case that we are interested in.

the ground-state phase diagram, we focus the discussion on a detailed understanding of the ground-state phases, using tensor networks and the ground-state tiles construction [140, 159] to obtain very precise numerical results. We show that even with third-neighbor couplings, most of the ground-state phases still exhibit a finite residual entropy. In particular, we show that the dipolar ground state (Fig. 4.2) is one of the ground states for the model with  $J_3 < J_2/2$ , while the dipolar model truncated to third neighbor couplings ( $J_3 > J_2/2$ ) has a different set of ground states with a residual entropy corresponding to a twelfth of that of the TIAFM, a result that we are able to prove rigorously.

## 4.1 Known results and special points

We now discuss some known results at special points of the ground-state phase diagram of the  $J_1 - J_2 - J_3$  model and the related  $J_1 - J_2 - J_{3||}$  model. An overview of these results is given in Table 4.1, and the ground-state phase diagram of the  $J_1 - J_2 - J_{3||}$  model is given in Appendix F.

### 4.1.1 $J_1 - J_2$ model

The most well-studied model that we are interested in is the special case when  $J_3 = 0$ , namely the  $J_1 - J_2$  model. As we saw on the example in Chapter 1, Sec. 1.4.1, this model has four different ground-state phases depending on the signs of  $J_1$  and  $J_2$ . Considering the antiferromagnetic nearest-neighbor coupling ( $J_1 > 0$ ) in which we are interested, the model has two different ground-state phases depending on the sign of  $J_2$  [93, 94, 101–103]: when  $J_2$  is ferromagnetic, there is a  $\sqrt{3} \times \sqrt{3}$  LRO (see Fig. 4.4c) with ground-state energy

$$E_{\sqrt{3} \times \sqrt{3}} = -\frac{2}{3}J_1 + 2J_2, \quad (4.3)$$

whereas when  $J_2$  is antiferromagnetic, the ground-state energy is [93, 102]

$$E_{J_1 - J_2} = -\frac{2}{3}J_1 - \frac{2}{3}J_2. \quad (4.4)$$

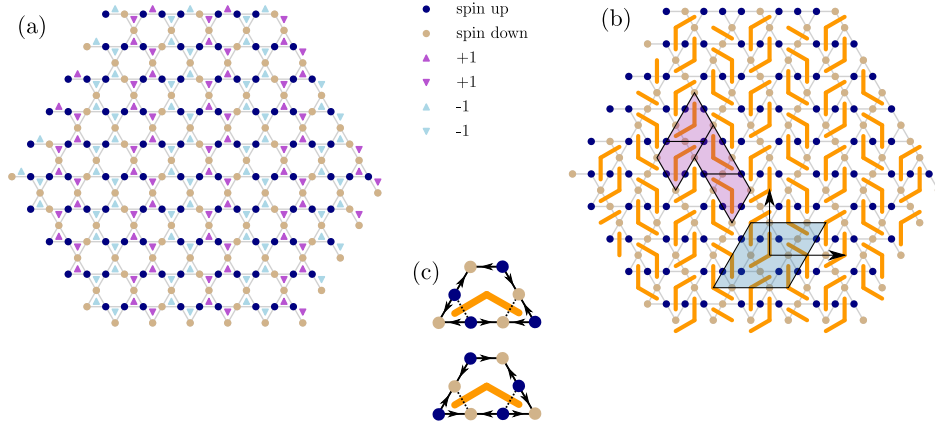


Figure 4.2 – Two views of the ground state of the dipolar Ising antiferromagnet on the kagome lattice [82, 99]. (a) The charge picture allows one to recognize an alternance of ferromagnetic stripes of charges[82, 99]. (b)The dimer picture will be useful for the comparison with the ground-state phases of the short-range model. The 12-sites magnetic unit cell is illustrated: in purple the 7-shaped unit cell which gives its name to the ground state in Ref. 82 and in blue the magnetic unit cell chosen by Hamp et al. [99]. In (c) we show the trapezoids construction [82] and the corresponding pair of dimers forming a chevron. The 7-shaped unit cell is a tessellation of four such trapezoids.

Model	Parameters	LRO?	$E_{G.S} + \frac{2}{3}J_1$	S		
				Pauling	Exact	MC
$J_1 - J_2$ <sup>(a)</sup>	$J_2 > 0$ $J_2 < 0$	No $\sqrt{3} \times \sqrt{3}$	$-\frac{2}{3}J_2$ $2J_2$	$\cong 0.31..$ 0	- 0	$\cong 0.297(3)$ <sup>(b)</sup> -
$J_1 - J_2 - J_{3  }$	Ferro. $J_2$ , $ J_2  >  J_{3  } $ <sup>(c)</sup>	$\sqrt{3} \times \sqrt{3}$	$2J_2 - \frac{2}{3}J_{3  }$	0	0	-
	Ferro. $J_{3  }$ , $ J_{3  }  >  J_2 $ <sup>(c)</sup>	Stripes	$-\frac{2}{3}J_2 + 2J_{3  }$	0	0	-
$J_1 - J_2 - J_{3  }$ , $J := J_{3  } = J_2$	Ferro. $J$ , $J_1 >  J $ <sup>(c)</sup>	No	$\frac{4}{3}J$	-	$\frac{1}{3}S_{\text{TIAFM}}$ $\cong 0.108$ <sup>(c)</sup>	-
	Antiferro. $J$ , $J_1 > 3J$ <sup>(d)</sup>	No (Hexamer CSL)	0	$\frac{1}{6} \ln\left(\frac{27}{4}\right)$ $\cong 0.32$	-	$\sim 0.32$
$J_1 - J_2 - J_3$	Dipolar point <sup>(b)</sup>	LRO dipolar?	$\geq -\frac{2}{3}J_2 - J_3$	$< 0?$	-	0?

Table 4.1 – Summary of known results in the  $J_1 - J_2 - J_3$  models. We only consider cases where the nearest-neighbor coupling  $J_1$  is strong and antiferromagnetic. The letters give the main references: (a) See Refs. 93, 94, 99, 101, 102, (b) See Ref. 99, (c) See Ref. 101, (d) See Ref. 222. The dipolar point corresponds to the dipolar model truncated to third-neighbor interactions; the value of the couplings for this point are given in Eq. 4.9.



It has been long known that the  $J_1$ - $J_2$  model exhibits a finite residual entropy for  $J_2 > 0$ . In fact, the exactly solvable model of Ref. 245, with  $J_2$  couplings only in one direction, has a set of ground states with a residual entropy per site of

$$S_{\text{Azaria}} = \frac{1}{3} \ln 2 \cong 0.23105... \quad (4.5)$$

It is easy to see that this ground-state degeneracy would not get lifted by the next-nearest-neighbor couplings in the other directions, which gives a lower bound for the residual entropy per site for the  $J_1 - J_2$  model. A better estimate can be obtained from Pauling estimates [40, 93]. For the nearest-neighbor kagome model, a Pauling estimate can be performed by noting that on each triangle with one fixed spin, there are four states of which only three satisfy the ice rule. If all the  $2N/3$  triangles of the kagome lattice were free, we would thus get an entropy [93]

$$S_P^{\text{NN}} = \ln(2) + \frac{2}{3} \ln\left(\frac{3}{4}\right) = \frac{1}{3} \ln\left(\frac{9}{2}\right) \cong 0.50136... \quad (4.6)$$

which is actually fairly close to the exact result [18]. Taking into account second-nearest neighbors, the residual entropy per site can be estimated roughly by including constraints on the three kagome superlattices, which gives [93, 99]

$$S_P^{2\text{nd N}} = \ln(2) + \frac{2}{3} \ln\left(\frac{3}{4}\right) + 3 \cdot \frac{2}{9} \ln\left(\frac{3}{4}\right) \cong 0.3096... \quad (4.7)$$

A very similar estimate is obtained using the known result for the residual entropy of the nearest-neighbor model:

$$S_P^{2\text{nd N}} = 2 \cdot S_{\text{NN}} - \ln(2) \cong 0.3105... \quad (4.8)$$

In Ref. 99, the  $J_1 - J_2$  model was studied for antiferromagnetic couplings using Monte Carlo simulations and it was seen on small systems ( $L = 3, N = 108$  sites) that the residual entropy is slightly below the Pauling estimate with  $S \cong 0.297 \pm 0.003^2$ . This model was also previously studied in Ref. 102 where it was suggested that there was a KT transition to a partially disordered state at low temperature. We computed the residual entropy in Chapter 3 (Ref. 160) with tensor networks, using a dual construction, and found  $S \cong 0.285299 \pm 1.4 \cdot 10^{-6}$  (Eq. 3.38).

#### 4.1.2 Dipolar point in the $J_1 - J_2 - J_3$ model

In Appendix A of Ref. 99, a brief study of the  $J_1 - J_2 - J_3$  model is presented, for the values of the couplings corresponding to the truncated version of the DKIAFM Hamiltonian (Eq. 4.1).

---

<sup>2</sup>This value is not given in the reference but we extracted it from their graph

Truncating the dipolar Hamiltonian (Eq. 4.1) to third neighbors gives<sup>3</sup>:

$$J_2/J_1 = \frac{2}{9\sqrt{3}} \cong 0.1283..., \quad J_3/J_1 = \frac{1}{12} \cong 0.0833..., \quad J_3/J_2 = \frac{3\sqrt{3}}{8} \cong 0.64952.... \quad (4.9)$$

In particular, the authors of Ref. 99 include the third-neighbor couplings in the Pauling estimate, either by assuming that these couplings impose an ice rule on the  $J_3$  triangles or by estimating a reduction factor from the known residual entropy of the TIAFM. In both cases, the residual entropy is negative. Let us note that this way of introducing  $J_3$  couplings assumes that both first-, second- and third-neighbor ice rules are imposed at the same time, corresponding to the following lower bound for the ground-state energy:

$$E_{J_1-J_2-J_3:\text{DKIAFM}} \geq -\frac{2}{3}J_1 - \frac{2}{3}J_2 - J_3. \quad (4.10)$$

They note that small-scale Monte Carlo simulations ( $L = 3, N = 108$ ) fall out of equilibrium at low temperatures but give evidence of a finite value of the order parameter associated with the long-range dipolar ground state; however they do not conclude decisively on the kind of order expected in the ground state of this truncated model. One of the main results of our Chapter will be to establish that the dipolar point lies within a phase with a macroscopic ground-state degeneracy (albeit a small one).

#### 4.1.3 $J_1 - J_2 - J_{3||}$ model

In Chapter 3 we discussed a close cousin of the model that we are interested in here: the  $J_1 - J_2 - J_{3||}$  model, where  $J_{3\star} = 0$ . The full ground-state phase diagram of this model in terms of ground-state energies has already been established [101] using Kanamori's method, and we reproduce it in Fig. F3 for completeness (see also Appendix F.1.1 for the list of Kanamori inequalities for this model). The residual entropies of the various ground-state phases have not all been studied. Wolf and Schotte [101] focused on the residual entropy for  $J_1$  antiferromagnetic,  $J_2 = J_{3||}$  ferromagnetic, and showed that it was exactly

$$S_{J_1, J_2=J_{3||}}^{\text{Wolf And Schotte}} = \frac{1}{3} S_{\text{TIAFM}}. \quad (4.11)$$

Since this model is quite close to the one that we are interested in, we will use this region where  $J_2 = J_{3||} < 0$  to benchmark the tensor network results for the residual entropy. Actually, this is the same kagome ice ground-state manifold that is obtained as the ground-state of the

---

<sup>3</sup>This corresponds to  $J_1 = 1.5$ ,  $J_2 = 1/2^{3/2} \cong 0.192$  and  $J_3 = 1/8 = 0.125$ , namely setting  $J_0 = 0.5$  and  $D = 1$  in Eq. 4.1. In Appendix A of Ref. 99, it seems that the the couplings are  $J_1 = 1.5$ ,  $J'_2 \cong 0.692$  and  $J'_3 = 0.625$ , which corresponds to adding a 0.5 term also for the  $J_2$  and the  $J_3$  couplings. Although this does not affect the ratio between  $J_2$  and  $J_3$ , both couplings are too large compared to  $J_1$  and correspond to a different ground-state phase of the  $J_1 - J_2 - J_3$  model. However, comparing the behavior of the specific heat in the  $J_1 - J_2$  model (Fig. 9b in Ref 99) to known results (Fig. 8a in 102 and Fig. 26d in 160), it seems that the couplings announced in Ref. 99 result from a typo; the results of the simulation seem more compatible with the couplings of Eq. 4.9.

$\langle 111 \rangle$  magnetization plateau in pyrochlores, and of the KIAFM in a field (except for the fact that in the  $J_1 - J_2 - J_{3\parallel}$  model there is spontaneous  $\mathbb{Z}_2$  symmetry breaking).

This macroscopic ground-state degeneracy occurs at the boundary between two ordered phases: when  $J_2$  is ferromagnetic and dominates, they find the same  $\sqrt{3} \times \sqrt{3}$  long-range ordered state as in the  $J_1 - J_2$  model with ferromagnetic  $J_2$ , whereas when  $J_{3\parallel}$  dominates, there is a stripe-ordered ground state with six-fold degeneracy. We will show that these two ordered phases also appear in the full  $J_1 - J_2 - J_3$  model, but that in that case, due to the  $J_{3\star}$  interaction, there is no macroscopic degeneracy at the boundary between the two phases.

For completeness, let us mention that Mizoguchi et al. [222] also focused on the  $J_2 = J_{3\parallel}$  line of this model but additionally studied the case of antiferromagnetic  $J := J_2 = J_{3\parallel}$ . It can be seen in Fig. E3 that this line is again at the boundary between two other phases. They showed that when  $J_1 \geq 3J$  there is a residual entropy

$$S_{\text{hexamer CSL}} \cong 0.32... \quad (4.12)$$

corresponding to a classical spin liquid that they name the hexamer classical spin liquid. Importantly this residual entropy is *not* that of the TIAFM, as we saw in Chapter 3 when studying this model. In that Chapter, we also showed that the phase for  $0 < J_{3\parallel} < J_2$  has also a finite residual entropy,  $S = 0.1439...$

Since  $J_{3\star}$  is competing with  $J_{3\parallel}$  and creates a triangular lattice, it can be expected that the ground-state phase diagram for the  $J_1 - J_2 - J_3$  model will be quite different from the results of Wolf and Schotte; we discuss the comparison of the full ground-state phase diagram in Appendix F. We should note that in their paper, Wolf and Schotte acknowledge J. Kanamori for “showing [them] his unpublished analysis of the ground states for a Kagome-Ising model, which also includes a fourth coupling constant  $J_4$ ”. Unfortunately, we were unable to find a trace of this unpublished work.

#### 4.1.4 Dipolar ground state and low energy configurations

Since the original motivation for studying the  $J_1 - J_2 - J_3$  model is to explore the lifting of the ground-state degeneracy from the nearest-neighbor model ground-state manifold to the dipolar ground state, let us review some features of the dipolar model’s long-range ordered ground state and some low energy states.

As noted by Chioar et al. [82], the dipolar ground state corresponds to a long-range order of “charges” defined on the triangles:

$$Q_{\Delta} = \sum_{i \in \Delta} \sigma_i \quad Q_{\nabla} = - \sum_{i \in \nabla} \sigma_i \quad (4.13)$$

This picture of the ground state is shown in Fig. 4.2a. In Fig. 4.2b we illustrate the corresponding dimer configuration. In terms of dimers, the first remark is that on all the hexagons, the pair

of dimers touching the center of the hexagon form a chevron. The dipolar ground state can be seen as a tiling of a unit cell with four chevrons. The connection with the trapezoids and the 7-shape of Ref. 82 can be done as follows (Fig. 4.2c): the trapezoids are constructed by associating with each kagome lattice bond either an arrow connecting the up spin to the down spin, or a dashed bond if the two spins are the same. Therefore, the trapezoids are essentially dual to the chevrons formed by the dimers. The unit cell of four trapezoids, or four chevrons, corresponds to the 7-shaped unit cell of Ref. 82, shown in purple in Fig. 4.2b. For convenience we can also chose a slightly different unit cell shown in blue in the same Figure. In this ground state there is three-fold sublattice rotation symmetry breaking and two-fold time-reversal symmetry breaking (as well as a four-fold translation symmetry breaking corresponding to the 12-site magnetic unit cell).

In Ref. 99 the charge picture is used to identify low-lying states in the dipolar model. The approach is inspired by the role of the charges in the in-plane kagome spin ice where, by approximating spins as charge dumbbells, the dipolar Hamiltonian can be rewritten (up to a constant and small corrections vanishing with distance at least as fast as  $1/r^5$ ) as [53, 95, 96, 99]

$$H_{\text{KSI}} = \frac{1}{2} \sum_{\alpha} v_0 Q_{\alpha}^2 + \frac{\mu_0}{8\pi} \sum_{\alpha \neq \beta} \frac{Q_{\alpha} Q_{\beta}}{r_{\alpha, \beta}}. \quad (4.14)$$

In this equation,  $v_0$  can be expressed in terms of the nearest neighbor coupling  $J$ , the dipolar coupling  $D$ , the magnetic moment  $\mu$  and the distance between charges  $a_h$ . Hamp et. al. propose to push this approach as follows: to go from the in-plane case to the DKIAFM, the spins are tilted progressively while the limit  $a_h \rightarrow \infty$  and at the same time  $q \rightarrow 0$  is taken such that the charges at the ends of the dumbbells keep overlapping at the center of the triangles. Eventually, the dumbbell picture will break down, but since the charges  $Q_{\alpha}$  are proportional to the charges introduced in Eq. 4.13 and the 7-shaped ground state corresponds to an ordering of those charges, one is tempted to push this picture beyond its scope of application and see if it provides an intuitive understanding of the low-lying states of the DKIAFM.

In this approximation, the charges are eventually separated in two triangular layers, namely charges living on up triangles and charges living on down triangles. In the first approximation, these layers are not interacting. At the same time, charges within a triangular layer have Coulomb interactions favoring charge-stripe patterns defined by an “antiferromagnetic” alternance of aligned directed strings of charges. Considering strings that span the lattice vertically, one can see that there is a subextensive degeneracy corresponding to all the strings going simultaneously left or right at each row.

To first order, one could ignore the interactions between the two triangular layers. But, having observed that the (spin-spin) dipolar interactions seem to favor a proximity between charges of the same sign from one layer to the other, a reasonable description for a family of low-lying state is to adjust the stripe pattern in one of the layers such as to maximize this proximity. That way, there is a subextensive degeneracy for the configurations in one layer, and the charge configuration in the second layer is fixed to be consistent with that of the first layer. This family

of states contains the 7-shaped ground state, has an entropy scaling with the linear size of the system, and according to Ref. 99 many of these states lie close in energy to the dipolar ground state, with an energy difference of order 1.3% .

## 4.2 Ground-state phase diagram

In this section, we give an overview of the ground-state phase diagram. We start by describing the application of the Kanamori approach to the  $J_1 - J_2 - J_3$  model. Having obtained the inequalities polytope for the  $J_1 - J_2 - J_3$  model, we simplify the problem by focusing on the phases for  $J_1 \gg J_2, J_3$  with  $J_1$  antiferromagnetic. With this, we establish the exact ground-state energies for these phases, and give an overview of the residual entropies that we will obtain in the remainder of the Chapter.

### 4.2.1 Applying Kanamori's method

To study the model

$$H = J_1 \sum_{\langle i,j \rangle_1} \sigma_i \sigma_j + J_2 \sum_{\langle i,j \rangle_2} \sigma_i \sigma_j + J_3 \sum_{\langle i,j \rangle_{3||}} \sigma_i \sigma_j + J_3 \sum_{\langle i,j \rangle_{3\star}} \sigma_i \sigma_j, \quad (4.15)$$

the inequalities must be written separating the two type of third-neighbor (disconnected) correlations:

$$c_{3||} := \frac{1}{2N} \sum_{\langle i,j \rangle_{3||}} \sigma_i \sigma_j, \quad \tilde{c}_{3\star} := \frac{1}{2N} \sum_{\langle i,j \rangle_{3\star}} \sigma_i \sigma_j, \quad (4.16)$$

where we have denoted  $-1/2 \leq \tilde{c}_{3\star} \leq 1/2$  to emphasize the fact that we divide by twice the number of type  $3\star$  bonds. The energy per site is given by

$$\frac{H}{N} = 2J_1 c_1 + 2J_2 c_2 + 2J_{3||} c_{3||} + 2J_{3\star} \tilde{c}_{3\star} \quad (4.17)$$

We find a list of inequalities for  $c_1$ ,  $c_2$ ,  $c_{3||}$  and  $\tilde{c}_{3\star}$  by applying the procedure presented in Chapter 1, Sec. 1.4.1. These inequalities can be written in the form:

$$a_1 c_1 + a_2 c_2 + a_{3||} c_{3||} + a_{3\star} \tilde{c}_{3\star} \geq -1. \quad (4.18)$$

and in Appendix F1.2, Table E3 we give a list of the 17 strongest inequalities we found using a systematic enumeration; we also illustrate the corresponding clusters. Some of these inequalities, that do not include  $\tilde{c}_{3\star}$ , are also present in the treatment of the  $J_1 - J_2 - J_{3||}$  model. Conversely, some inequalities constraining the correlations of the  $J_1 - J_2 - J_{3||}$  model are not sufficiently restrictive for the  $J_1 - J_2 - J_3$  model and are eliminated. The 17 inequalities are valid for any values of  $J_1$ ,  $J_2$ ,  $J_{3||}$  and  $J_{3\star}$ , and give rise to a four-dimensional polytope in the correlation space with 21 vertices

$$\{\vec{c}^{(i)}\}_{i=1,\dots,21} = \left\{ (c_1^{(i)}, c_2^{(i)}, c_{3||}^{(i)}, \tilde{c}_{3\star}^{(i)}) \right\}_{i=1,\dots,21}, \quad (4.19)$$

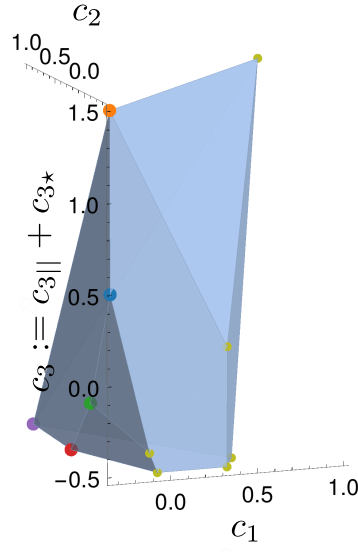


Figure 4.3 – Polytope from Kanamori’s method of inequalities reduced for  $J_{3||} = J_{3\star}$ . In this Chapter we focus on the corners highlighted with large color points (for  $c_1 = -\frac{1}{3}$ ).

listed in Appendix F.1.2, Table F.4. We do not immediately seek to find a state corresponding to each of these 21 vertices, which would be needed to establish the full ground-state phase diagram for  $J_1 - J_2 - J_{3||} - J_{3\star}$  models<sup>4</sup>; instead we start by specializing to the case where  $J_{3||} = J_{3\star}$ :

$$\frac{H}{N} = 2J_1 c_1 + 2J_2 c_2 + 2J_3 (c_{3||} + \tilde{c}_{3\star}). \quad (4.20)$$

The polytope in the  $(c_1, c_2, c_{3||} + \tilde{c}_{3\star})$  space is found as the convex hull of the set

$$\left\{ (c_1^{(i)}, c_2^{(i)}, c_{3||}^{(i)}, \tilde{c}_{3\star}^{(i)}) \cdot (0, 0, 1, 1) \right\}_{i=1, \dots, 21}, \quad (4.21)$$

where some of the 21 original corners might be “projected” onto the same point or end up in the interior of this new polytope. Computing this convex hull, we find a polytope illustrated in Fig. 4.3, whose 11 vertices are listed in Appendix F.1.2, Table F.5. With these corners, one obtains a candidate ground-state phase diagram which has to be checked by finding for each corner of the polytope a configuration that realizes it. Since we are mainly interested in the ground-state phase diagram for  $J_1 \gg J_2, J_3$ , we focus on this case in the remainder of this Chapter, and we relegate the discussion of the full candidate ground-state phase diagram to Appendix F.2.2. In that Appendix, we show that some of the corners of this polytope, not relevant to the current discussion, are not realized. Although we are not able to elucidate the ground-state phase diagram fully, we get an extensive insight into it.

<sup>4</sup>We give indications in Appendix F.2.2 that this would be a challenging process requiring the construction of even stronger lower bounds.

### 4.2.2 Overview of the ground-state phase diagram for $J_1 \gg J_2, J_3$

Since we are mainly interested in the ground-state phase diagram for  $J_1 \gg J_2, J_3$ , we can still operate one more simplification on the Kanamori polytope: by taking  $J_1$  to be large<sup>5</sup>, we can focus on the corners of the Kanamori polytope in Fig. 4.3 for which  $c_1$  is minimal; i.e. we can focus on the section of this polytope that lies in the  $c_1 = -\frac{1}{3}$  plane. This gives us the polygon in Fig. 4.4a. Given the correlations of the various corners, one still has to check that each corner can be realized by a spin configuration on the lattice. For this, we perform small-scale Monte Carlo simulations with periodic boundary conditions, using the worm algorithm discussed in Sec. 1.2, which corresponds to building an upper bound for the ground-state energy that will match the lower bound from the Kanamori approach. Note that each corner where we find a configuration then corresponds to a ground-state phase, as it corresponds to the extremal energy for a range of values of  $J_2, J_3$ . While the associated ground-state energy can be read directly on the graph (given Eq. 4.17), the Kanamori method tells nothing about the nature of the ground-state phase and whether it has a residual entropy.

For each corner in Fig. 4.4a we find a configuration, represented by a snapshot of the Monte Carlo simulations, which rigorously proves the energies of all these phases. The appearance of the configurations either in spin or in dimers gives the name to the corresponding phase, as detailed below.

We complement the exact results for the ground-state energies with tensor network computations for the residual entropies, using the method described in Chapter 2 to write the partition function. First, the Hamiltonian is split as a sum of local Hamiltonians on small clusters, with weights describing how each bond is shared between the cluster Hamiltonians. For any weights, the ground-state energy on the cluster is a lower bound on the global ground-state energy. We optimize for the weights which maximize this lower bound; if it matches the known global ground-state energy (from Kanamori's method) then it means that the frustration is relieved and that the total Hamiltonian can be minimized by minimizing each weighted cluster Hamiltonian simultaneously. All the ground states are then described as a tiling of the local ground-state configurations on the cluster, and one can build a tensor network to count them. In all the depicted ground-state phases, a star cluster is sufficient to support the ground-state tiles. We will discuss in more detail the results for each phase in the rest of the Chapter, but the overall results are summarized in Fig. 4.5 and in Table 4.2 for the residual entropies and ground-state energies.

Let us have a look at these results. Corresponding to the fact that we selected  $J_1 \gg J_2, J_3$  and that Fig. 4.4a corresponds to the  $c_1 = -1/3$  plane of the 3D inequalities polytope in Fig. 4.3, in all this ground-state phase diagram, the nearest-neighbor energy is always minimized in the sense that all the nearest-neighbor triangles always respect an ice rule. The diversity of the phases thus arises from a competition between the second- and third-nearest-neighbor

---

<sup>5</sup>According to the results of Appendix F2.2,  $J_1$  is large enough if  $\sqrt{\left(\frac{J_2}{J_1}\right)^2 + \left(\frac{J_3}{J_1}\right)^2} < 1/2$ .

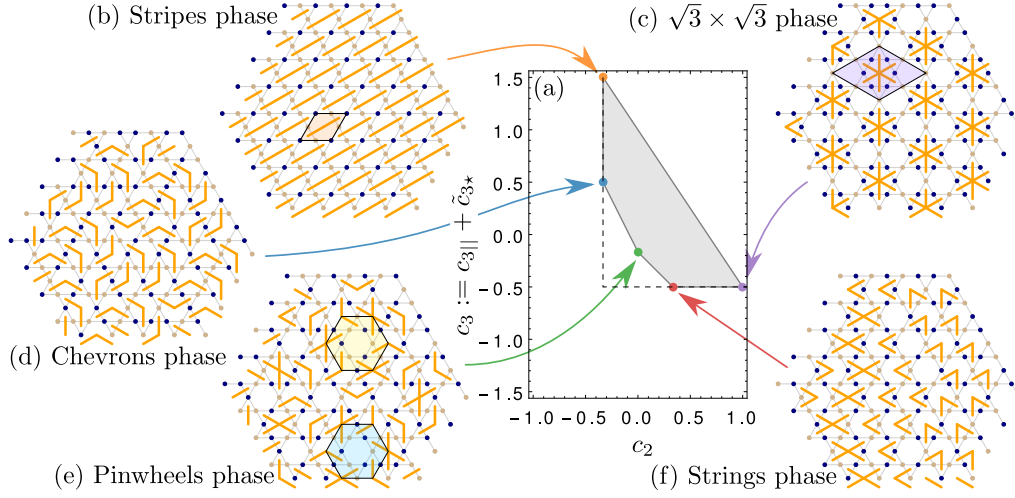


Figure 4.4 – (a) Polytope from Kanamori’s method of inequalities reduced for  $J_1 \gg J_2, J_3$ ,  $J_1 > 0$ . For reference, the dashed lines give the inequalities corresponding to minimizing the energy on all the  $J_2$  or all the  $J_3$  triangles respectively. For each corner we show one Monte Carlo snapshot which has these correlations. In all cases  $c_1 = -\frac{1}{3}$  (Fig. 4.3). The correlations correspond to states as follows. (b)  $(c_2, c_3) = (-1/3, 3/2)$ : long-range ordered Stripe states; (c)  $(c_2, c_3) = (1, -1/2)$ : long-range ordered  $\sqrt{3} \times \sqrt{3}$  states; (d)  $(c_2, c_3) = (-1/3, 1/2)$ : a phase where pair of dimers form chevrons; (e)  $(c_2, c_3) = (0, -1/6)$ : a phase where dimers rotate clockwise or anti-clockwise around empty hexagons as pinwheels (highlighted); (f)  $(c_2, c_3) = (1/3, -1/2)$ : a phase characterized by strings of crosses spanning the system.

couplings, which either partially or completely lift the ground-state degeneracy of the nearest-neighbor model.

There are two long-range ordered phases corresponding to either  $J_2$  or  $J_3$  being ferromagnetic (Fig. 4.4b and c). In these phases, the ground state is such that the sub-lattices corresponding to the dominant coupling are ferromagnetically ordered, yielding a  $\sqrt{3} \times \sqrt{3}$  order when  $J_2$  dominates (named this way because of the size of the unit cell as compared to the triangular sublattice spacing), and a long-range order with ferromagnetic stripes of spins when  $J_3$  dominates (stripes phase). As we mentioned earlier, these phases are also present in the  $J_1 - J_2 - J_{3||}$  model (i.e. when  $J_{3\star} = 0$ ).

More surprisingly, when both  $J_2 \geq 0$  and  $J_3 \geq 0$ , there is a number of phases with reduced but non-zero residual entropy. In Fig. 4.4, we indicated by dashed lines the inequalities  $c_2 \geq -1/3$  and  $c_3 \geq -1/2$  that correspond to satisfying the ice rule on each  $J_2$  triangle and each  $J_3$  triangle, respectively. The fact that we find more restrictive inequalities that cut the corner formed by these two inequalities shows that there is no state satisfying simultaneously the ice rule on all nearest, second-nearest and third-nearest neighbor triangles at once. Instead, we find stronger inequalities forming three corners and correspondingly three phases (Fig. 4.4d, e and f). The additional inequalities correspond to more involved rules on the lattice, which we can find in the form of tiles using the approach described in Chapter 2.



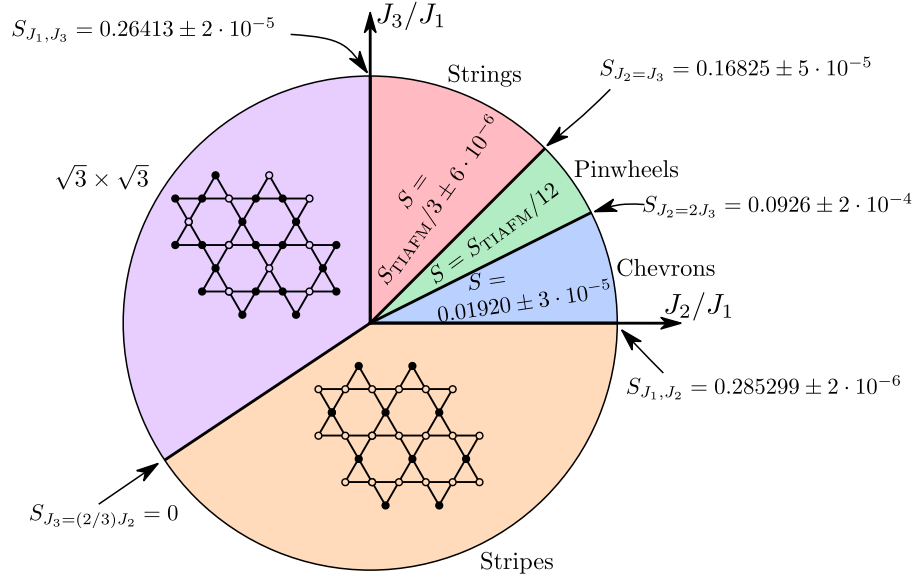


Figure 4.5 – The ground-state phase diagram of the  $J_1$ - $J_2$ - $J_3$  model for  $J_1$  antiferromagnetic and for farther-neighbor couplings in a radius of  $J_1/2$ . Positive couplings correspond to antiferromagnetic interactions. The residual entropies are obtained from contractions of tensor networks based on a star cluster.

Start from the  $J_1 - J_2$  model : its ground state is located on the leftmost phase boundary in Fig. 4.4a, at  $c_2 = -1/3$  corresponding to all next-nearest-neighbor triangles respecting the ice rule. This ground-state manifold is known to be macroscopically degenerate (Table 4.1, Chapter 3). Upon introducing a small  $J_3$  coupling, the corner corresponding to Fig. 4.4d is selected. With Monte Carlo, we validate this corner by finding a state which respects the ice rule for all 2nd-neighbor triangles but also has some constraint on the third-neighbor triangles giving rise to  $c_3 = 1/2$ . Illustrated in Fig. 4.4d, this state is characterized by all the dimers appearing in pairs forming chevrons (two dimers at a  $120^\circ$  angle), and we name this phase the “chevrons phase”.

Upon increasing  $J_3$  there is a transition to another ground-state phase (Fig. 4.4e) which we name the “pinwheels phase” because it is characterized by a lattice of empty hexagons surrounded by dimers with a well-defined chirality, turning either clockwise or counter-clockwise with respect to the hexagon center. In these ground states, some of the  $J_2$  triangles as well as some of the  $J_3$  triangles are ferromagnetic. When  $J_3$  becomes larger than  $J_2$  there is yet another phase, in which all the  $J_3$  triangles respect the ice rule. The Monte Carlo snapshots in this phase (Fig. 4.4e) are characterized by strings of crosses winding the systems; since we will show that these strings of crosses can be used to understand the finite residual entropy, we name this phase the strings phase. We will see that all three phases as well as their phase boundaries have a finite residual entropy (Fig. 4.5, Table 4.2).

## Chapter 4. Progressive lifting of the KIAFM ground-state degeneracy

Phase or boundary	Name	$E_{G.S} + \frac{2}{3}J_1$	$S$		
			Pauling / Lower bound	Exact	TN
$J_2 > 0, J_3 = 0$	$J_1 - J_2$	$-\frac{2}{3}J_2^{(a)}$	$\cong 0.31..^{(b)}$	-	$0.285299 \pm 2 \cdot 10^{-6(c)}$
$J_2 > 2J_3 > 0$	Chevrons	$-\frac{2}{3}J_2 + J_3$	-	-	$0.01920 \pm 3 \cdot 10^{-5}$
$J_3 = J_2/2 > 0$	-	$-\frac{1}{6}J_2$	-	-	$0.0926 \pm 2 \cdot 10^{-4}$
$J_2 > J_3 > J_2/2 > 0$	Pinwheels	$-\frac{1}{3}J_3$	-	$S_{\text{TIAFM}}/12 \cong 0.02692..$	$0.026922 \pm 3 \cdot 10^{-6}$
$J_3 = J_2 > 0$	-	$-\frac{1}{3}J_3$	-	-	$0.16825 \pm 5 \cdot 10^{-5}$
$J_3 > J_2 > 0$	Strings	$\frac{2}{3}J_2 - J_3$	$\geq \frac{1}{9} \ln 2 \cong 0.077$	$S_{\text{TIAFM}}/3 \cong 0.10769...$	$0.107689 \pm 2 \cdot 10^{-6}$
$J_2 = 0$	$J_1 - J_3$	$-J_3$	$\geq \frac{1}{27} \ln 559 \cong 0.2348$	-	$0.26413 \pm 2 \cdot 10^{-5}$
$J_2 < 0, J_3 > 2/3J_2$	$\sqrt{3} \times \sqrt{3}$	$2J_2 - J_3$	$0^{(d)}$	$0^{(d)}$	0
$J_3 = 2/3J_2 < 0$	-	$\frac{4}{3}J_2$	-	0	0
$J_3 < 0, J_2 > 3/2J_3$	Stripes	$-\frac{2}{3}J_2 + 3J_3$	$0^{(d)}$	$0^{(d)}$	0

Table 4.2 – Overview of the results discussed in this Chapter. We indicate the following references for known results (see also Table 4.1 and the discussion in Appendix F): (a) See Refs. 93, 94, 99, 101, 102 (b) See Ref. 93, 99, (c) See Chapter 3 of the present thesis (Ref. 160), (d) See Ref. 101 ( $J_1 - J_2 - J_{3\parallel}$  model) where these two ordered phases are also present. To the best of our knowledge, the rest of the results are new. We present them starting from the  $J_1 - J_2$  model and enumerating the phases in Fig. 4.5 counter-clockwise.

In the following, we present these results in detail. We start by describing the two ordered phases, which is the occasion to give a short reminder of the idea behind the tensor network construction once the ground-state tiles are obtained. We also make a remark about the boundary between the two ordered phases and contrast this result to that of Wolf and Schotte [101], which we use as a benchmark. Then, we move on to the chevrons phase; we show that the ground state of the long-range, dipolar model is a ground state in this phase, despite the fact that the dipolar Hamiltonian truncated to third neighbors would have couplings which would fit the pinwheels phase. Next, we study the pinwheels phase and show that it still exhibits a finite residual entropy which is a twelfth of the residual entropy of that of the TIAFM. Finally, we have a look at the strings phase and notice that the residual entropy there is a third of that of the TIAFM; we see how this result can be at least partially understood in terms of strings living on an effective honeycomb lattice.

### 4.3 Ferromagnetic farther-neighbor couplings and benchmark

Two ordered phases occur when  $J_2$  and/or  $J_3$  are ferromagnetic : the  $\sqrt{3} \times \sqrt{3}$  phase where  $J_2$  is ferromagnetic and  $J_3 > \frac{2}{3}J_2$ , and the stripes phase when  $J_3$  is ferromagnetic and  $J_2 > \frac{3}{2}J_3$ . These phases correspond to ferromagnetically ordered next-nearest- and third-nearest neighbor sublattices, respectively.

The ground-state tiles corresponding to the  $\sqrt{3} \times \sqrt{3}$  phase (ferromagnetic  $J_2$ ) and the stripes phase (ferromagnetic  $J_3$ ) are illustrated in Fig. 4.6. Here and in the following, we will always show one instance of each type of tile; it is implicit that all the tiles corresponding to rotations and global spin flips are also ground-state tiles. In Fig. 4.7, we recall the idea behind the tensor network construction: once the ground-state tiles are obtained, one wishes to count all the valid ways of tiling them. Two ground-state tiles can be tessellated if they have the same spin configuration on their shared sites. Thus, in spirit, one can build a tensor network to count the tiles by building a  $\Delta$ -tensor  $G$  associated to each cluster and whose bond dimension equals the number of ground-state tiles, and contracting these tensors with bond tensors  $P_h$  and  $P_v$  which impose that two neighboring ground-state tiles must have the same spin configuration on the sites that they share. The bond dimension can be reduced to at most  $2^{n_s}$ , where  $n_s$  is the number of shared sites, by performing an SVD on the sparse bond tensors.

In these two phases, contracting the tensor network with the VUMPS algorithm yields a leading eigenvalue of one, corresponding to a zero residual entropy and the expected long-range order. In the stripes phase, this occurs even with a bond dimension of one for the boundary MPS. In the  $\sqrt{3} \times \sqrt{3}$  phase, a bond dimension of four is sufficient to converge and get a zero residual entropy, even without allowing for the three-by-three translation symmetry breaking expected in this phase; if this symmetry-breaking is allowed for by using a multi-site VUMPS implementation [151], then the correct result is obtained for bond dimension one.

In the work of Wolf and Schotte [101], where they studied the case where  $J_3 = 0$  across the

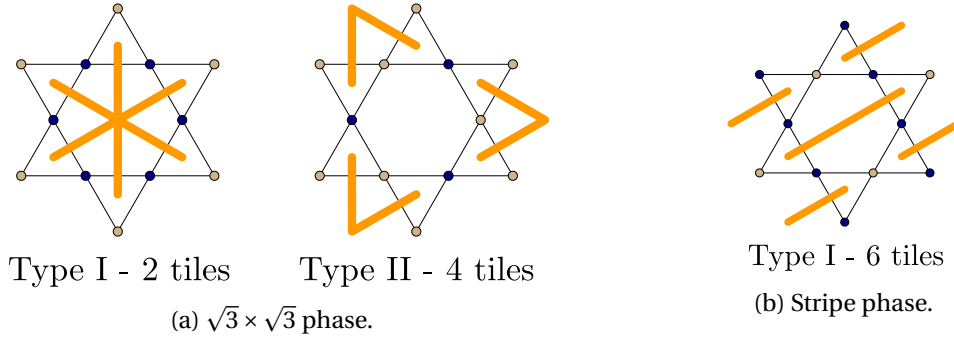


Figure 4.6 – The ground-state tiles in the two long-range ordered ground-state phases. The yellow dots correspond to down spins, the blue dots correspond to up spins, and the orange segments correspond to the dimer configuration on the dual, diced lattice. A dimer is put whenever two nearest-neighbor spins have the same signs.

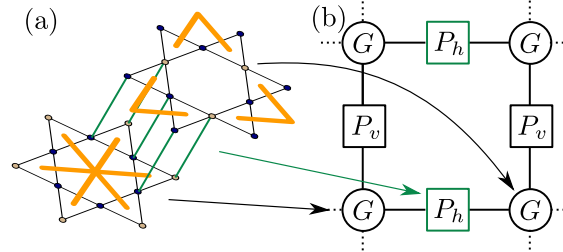


Figure 4.7 – A reminder of the idea behind the tensor network construction, illustrated with the ground-state tiles of the  $\sqrt{3} \times \sqrt{3}$  phase. In (a), it is shown that two tiles match horizontally if the five spins on the sites that they share have the same values. In the most straightforward construction, the tensor network in (b) is thus built with a four-legs  $\Delta$ -tensor  $G$  which associates a number to each ground-state configuration, and bond tensors  $P_h$  and  $P_v$  which enforce that neighboring tiles must match by taking value one if the neighboring tiles have the same values of the shared spins, and zero otherwise. The contraction of the tensor network thus counts the number of valid tilings of the ground-state tiles.

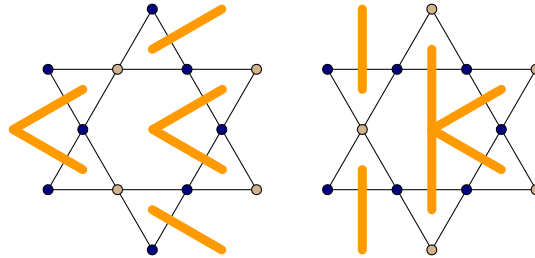


Figure 4.8 – Additional ground-state tiles at the phase boundary between the ordered phases when  $J_{3*}$  is zero, i.e. in the model of Wolf and Schotte [101]. These tiles cannot belong to the ground state when  $J_{3*}$  is non-zero and ferromagnetic.

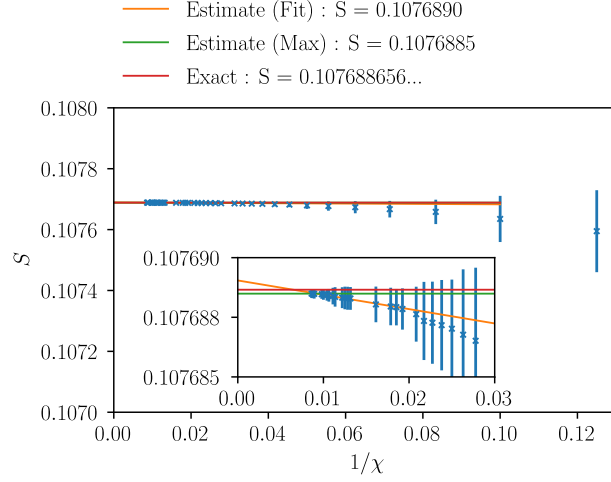


Figure 4.9 – Benchmark: residual entropy when  $J_3 = 0$  across the hexagon. The exact result is  $S_{\text{TIAFM}}/3$  [101]. The tensor network contraction is performed for bond dimensions ranging from  $\chi = 8$  to  $\chi = 116$ . The errorbars come from computing the variance. The fit is performed on the 15 largest bond dimensions and gives an estimate for the entropy, while another estimate is given by the largest residual entropy obtained over all considered bond dimensions. The inset is a simple zoom on the largest bond dimensions.

hexagons, the phase boundary between the stripe and the  $\sqrt{3} \times \sqrt{3}$  phases is found at  $J_2 = J_3$  and exhibits a finite residual entropy:

$$S_{J_1, J_2=J_{3||}}^{\text{Wolf And Schotte}} = \frac{1}{3} S_{\text{TIAFM}} \cong 0.1077... \quad (4.22)$$

The  $J_{3\star}$  coupling (the coupling across the hexagons) pushes this phase boundary to  $J_2 = \frac{3}{2} J_3$ , and completely lifts the macroscopic degeneracy at the boundary between the two phases. This is easily seen in terms of the ground-state tiles: while in our case there is no new tile at the boundary between the two ordered phases, if  $J_{3\star} = 0$  there is a number of new tiles illustrated in Fig. 4.8. Clearly, these tiles cannot be present when  $J_{3\star}$  is non-zero and ferromagnetic. In the case of Wolf and Schotte, these are the tiles which allow cost-free boundaries between the  $\sqrt{3} \times \sqrt{3}$  ground state and the stripe ground state.

Since the residual entropy at the phase boundary when  $J_{3\star} = 0$  is an exact result, we use it as a benchmark for the code. The results are presented in Fig. 4.9, where it can be seen that the tensor network contraction agrees perfectly with the predicted result. In this Figure and other similar Figures in the chapter, we fix the y-scale to the third decimal in the residual entropy. Since this is the order of magnitude of the error that one can typically hope to obtain with Monte Carlo simulations, it gives an idea of the precision of the tensor network results as compared to Monte Carlo thermodynamic integration. We use the insets to show the limit of the precision that we obtain.

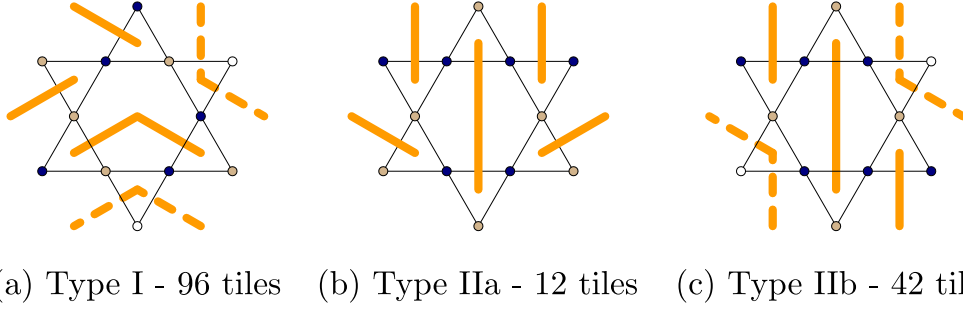


Figure 4.10 – The 150 ground-state tiles of the  $J_1$ - $J_2$  model. The dashed lines stand for a freedom in setting the dimer: when two dashed lines touch the center of a triangle, a dimer can be set on either of the dashed lines at the exclusion of the other. For instance, in (a), the bottom spin shown in white can be either down or up, which puts the dimer either to the right or to the left.

## 4.4 Chevrans phase

We now move on to the other ground-state phases of the model, with both  $J_2$  and  $J_3$  antiferromagnetic. We start with the  $J_1$ - $J_2$  model, and the chevrons phase which arises when a small non-zero  $J_3$  is introduced.

### 4.4.1 $J_1$ - $J_2$ model

When  $J_3 = 0$  the ground-state energy is [102]

$$E_{J_1-J_2} = -\frac{2}{3}J_1 - \frac{2}{3}J_2. \quad (4.23)$$

and we saw that there is a finite residual entropy (Table 4.1).

The construction of the tensor network associated with the  $J_1$ - $J_2$  model first requires obtaining the ground-state tiles, illustrated in Fig. 4.10. In this Figure and in the rest of this Chapter, we take a convention to describe the situation where there is some freedom in setting a spin: the spin is shown in white, and the dual bonds on which a dimer can be put are dashed. This means that the spin can be either up or down, and correspondingly we must put a dimer on one of the dual bonds at the exclusion of the other. The tiles of Type I exactly correspond to the chevrons that we identified to the trapezoids of Ref. 82 (see Fig. 4.2). One can check that the ground state of the DKIAFM corresponds to a tiling of these Type-I tiles, and therefore it immediately follows that the ground state of the DKIAFM *is* one of the ground states of the  $J_1$ - $J_2$  model (despite the fact that it was not explicitly reported in studies of the short-range models on the kagome lattice that preceded the work of Chioar et al.). We also show an example of a ground state obtained from Monte Carlo simulations in Fig. 4.12. Being aware that the  $J_1$  -  $J_2$  model corresponds to a phase boundary between the stripes and the chevrons phase, one can notice that dimer configurations associated with both phases can be seen in

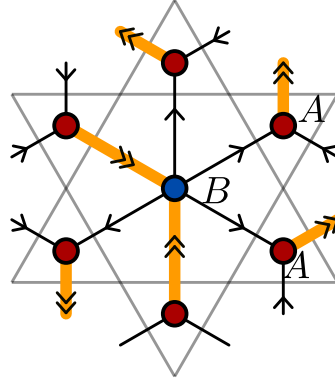


Figure 4.11 – Definition of the flux associated with the dimer configurations in the  $J_1 - J_2$  ground-state manifold.

that ground state.

Interestingly, in this ground-state manifold we can find an equivalent of a  $U(1)$  Gauss' law by defining fluxes associated with the dimers. For this, one has to notice that in this phase, corresponding to the constraints due to the nearest-neighbor coupling, there is exactly one dimer touching each three-coordinated vertex of the dice lattice ( $A$  sites). Additionally, corresponding to the constraints on the next-nearest-neighbor triangles, there is exactly two dimers touching each six-coordinated vertex of the dice lattice ( $B$  sites). We can therefore associate a flux with dimers on the dice lattice in this ground-state manifold with the following conventions (Fig. 4.11a):

with a dimer we associate a flux of 2 going from  $A$ -sites to  $B$ -sites (4.24)

with the absence of dimer we associate a flux of 1 going from  $B$ -sites to  $A$ -sites, (4.25)

such that the flux is conserved at each vertex. Importantly, these constraints describe a set of dimer configurations *wider* than just the  $J_1 - J_2$  ground-state manifold, since for instance the Type III tiles of the strings phase (Fig. 4.24e) also satisfy these constraints.

From the tensor network contraction, we obtain a precise estimate of the residual entropy per site (see Appendix G.1), which matches the result obtained in Chapter 3 with the construction using dimers:

$$S_{J_1 - J_2} = 0.285299 \pm 2 \cdot 10^{-6}. \quad (4.26)$$

#### 4.4.2 Introducing a small $J_3$ coupling

Introducing a small third-neighbor coupling only adds one term to Eq. 4.4, corresponding to the fact that among all the ground states of the  $J_1 - J_2$  model, some states can be selected that

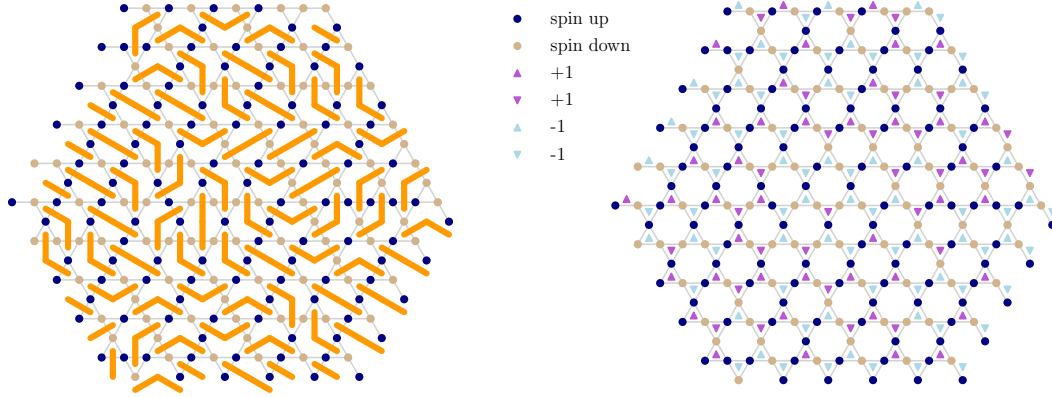


Figure 4.12 – Two views of a ground state of the  $J_1$ - $J_2$  Ising antiferromagnet on the kagome lattice. The tiles belonging to the stripe phase and the tiles belonging to the chevrons phase can be identified, together with additional ground-state tiles which only appear because  $J_3 = 0$ .

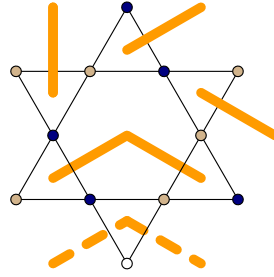
minimize the cost of the  $J_3$  interaction:

$$E_{\text{Chevrons}} = -\frac{2}{3}J_1 - \frac{2}{3}J_2 + J_3. \quad (4.27)$$

The corresponding ground-state tiles are illustrated in Fig. 4.13; they all correspond to the trapezoids described in Ref. 82, and give their name to this phase. Clearly, the DKIAFM ground state belongs to this ground-state manifold, despite the fact that truncating the dipolar Hamiltonian (Eq. 4.1) to third neighbors would *not* correspond to this phase. Indeed, the couplings in Eq. 4.9 would correspond to the pinwheels phase. We note that the ground-state manifold of the chevrons phase does *not* include all possible chevron tilings: the tiles in Fig. 4.13 enforce rules on how the chevrons must tile together. In Appendix G.2 we give an example of a chevron configuration that does not respect these tiling rules and therefore does not belong to the ground-state phase.

On large system sizes, our Monte Carlo simulations struggle to equilibrate or even reach the ground state. On a small system size (144 sites), though, we manage to find a set of ground states, two of which are depicted in Fig. 4.14. Interestingly, we only find non-local moves (i.e. torus-winding updates) between the various ground states. With only this information, it would seem as if the residual entropy of the model would be sub-extensive, with a zero residual entropy per site. This phase is also a challenge for the tensor network contraction. However, as can be seen in Fig. 4.15, when 2-stars translation symmetry breaking is allowed for in the Ansatz, the results consistently converge to a finite residual entropy per site which is





(a) Type I - 48 tiles

Figure 4.13 – The 48 ground-state tiles of the chevrons phase. The dashed lines and white site describe the fact that one can set the spin to be either up or down on the white site, and correspondingly put a dimer on one of the two dashed bonds at the exclusion of the other. Note that these tiles restrict how neighboring chevrons can be arranged.

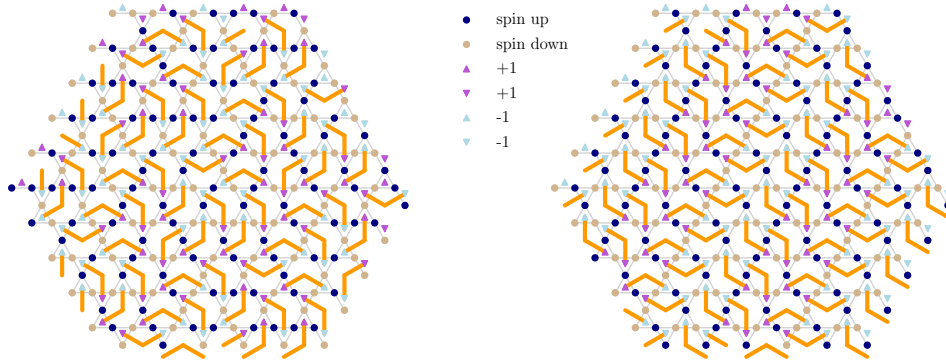


Figure 4.14 – Two ground states of the chevrons phase. The trapezoids of Ref. 82 can be identified. On the right panel, a charge ordering different from that in the DKIAFM ground state can be seen.

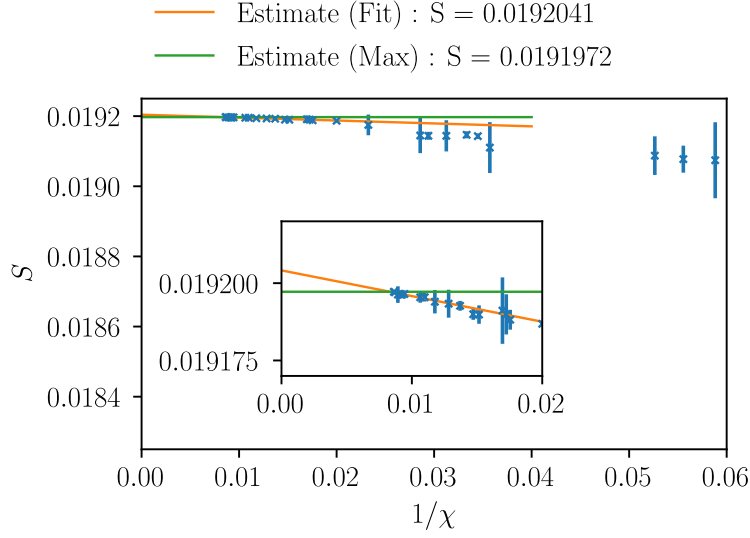


Figure 4.15 – Residual entropy per site of the chevrons phase from tensor network contractions. The tensor network contraction is performed for bond dimensions ranging from  $\chi = 17$  to  $\chi = 116$ . The errorbars come from computing the variance. The inset shows a zoom on the largest bond dimensions. We allow for two-site symmetry breaking in the Ansatz.

approximately

$$S_{\text{Chevrons}} = 0.01920 \pm 3 \cdot 10^{-5}. \quad (4.28)$$

This entropy is smaller than  $\ln 2/36$ , which suggests that, in the Monte Carlo simulations, if we were to find updates between ground states corresponding to flipping a cluster of spins, they might correspond to 36-sites unit cell (unless the scenario explaining the residual entropy per site is similar to what we observe in the pinwheels and strings phases); this might explain why we were unable to identify updates as being local in our 144-sites Monte Carlo simulations.

## 4.5 Pinwheels phase : a mapping to the triangular lattice Ising anti-ferromagnet

The pinwheels phase is located at

$$1/2 < J_3/J_2 < 1, \quad (4.29)$$

with the additional requirement that  $J_2$  and  $J_3$  should not be too big compared to  $J_1$  (see Appendix F for neighboring phases):

$$J_3 + 3/2 J_2 < J_1. \quad (4.30)$$

#### 4.5. Pinwheels phase : a mapping to the triangular lattice Ising antiferromagnet

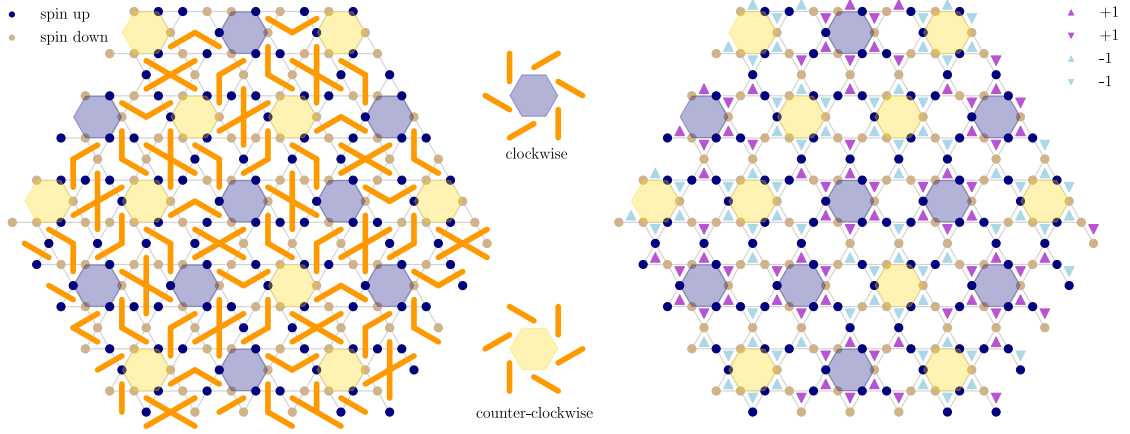


Figure 4.16 – Two views of the same snapshot of a ground state in the pinwheels phase. The blue and yellow dots correspond to up and down spins. On the left, the orange segments stand for the dimers living on the dice lattice (dual to kagome). A periodic structure of hexagons with no dimers can be seen (highlighted in blue or yellow). The dimers around the empty hexagons arrange as the wings of a pinwheel, which gives its name to this phase. The color in which the hexagon is highlighted corresponds to the direction in which the dimers turn around that hexagon: clockwise or counter-clockwise. On the right, the up and down purple and blue triangles correspond to +1 and -1 charges, respectively, with the convention of Ref. 99. The periodic structure of empty hexagons on the left corresponds here to a periodic structure of hexagons surrounded by a single type of charge, all +1 or all -1. They seem to respect a “charge ice rule”: three nearest-neighbor empty hexagons cannot all have the same charge.

Note that these equations are satisfied by the DKIAFM model truncated to third-neighbor couplings (Eq. 4.9). The ground-state energy per site is (Table 4.2)

$$E_{\text{Pinwheels}} = -\frac{2}{3}J_1 - \frac{1}{3}J_3. \quad (4.31)$$

In this section, we are going to argue that the pinwheels phase not only exhibits a finite residual entropy, albeit a small one, but also that the ground-state manifold admits a mapping to the ground state of the TIAFM, with 12-sites clusters behaving as effective Ising degrees of freedom (pinwheels with either clockwise or counter-clockwise chirality). In the following, we first give an intuition of this result based on a snapshot of the Monte Carlo simulations and the residual entropy obtained from the tensor network computations. Then, based on the ground-state tiles we give a rigorous characterization of the ground-state manifold of the pinwheels phase.

##### 4.5.1 Numerical results

In Fig. 4.16, we show a snapshot of a ground state obtained in the Monte Carlo simulations. With this, one can notice that the configuration in the ground state of the pinwheels phase has three possible hexagon configurations: either the hexagon is empty, or it hosts a chevron (two

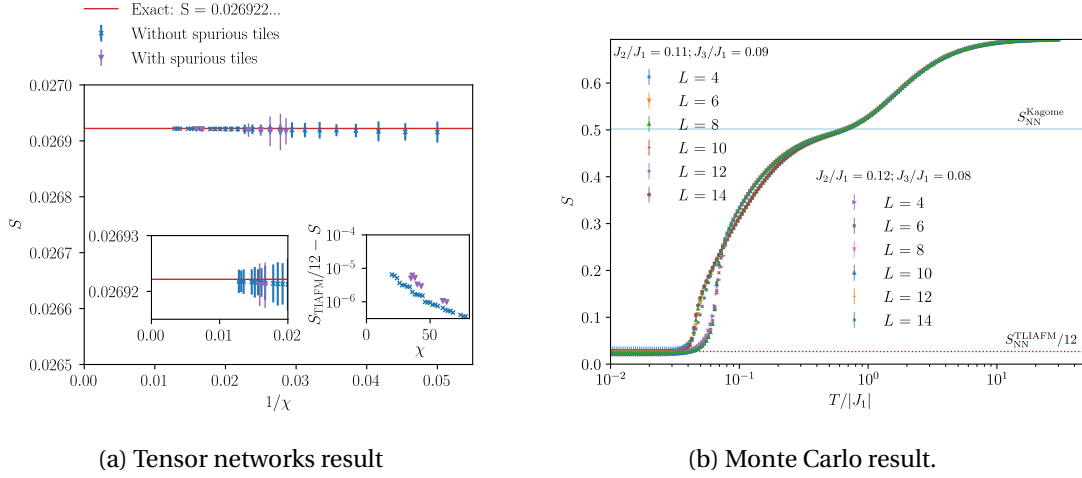


Figure 4.17 – Residual entropy in the pinwheels phase. (a) Tensor networks result for bond dimensions ranging from  $\chi = 18$  to  $\chi = 78$ . As we already suggested (Chapter 2), removing the spurious tiles (Type IV tiles in Fig. 4.18), makes it much easier to get a convergence at any bond dimension; the results with the spurious tiles are however also consistent with a residual entropy of  $S = \frac{1}{12} S_{\text{TIAFM}}$ . The insets show a zoom on the data and the difference to  $S_{\text{TIAFM}}/12$  in logarithmic scale. In the latter, the error bars are omitted for readability. (b) Monte Carlo results for sizes ranging from 144 up to 1764 sites, for two sets of couplings in the pinwheels phase.

dimers at a  $120^\circ$  angle), or a cross. Furthermore, the empty hexagons form a triangular lattice. As one can see, the dimers around empty hexagons all go in the same direction, effectively turning either clockwise or counter-clockwise; correspondingly, the charges around an empty hexagon all have the same value. Finally, this snapshot gives an intuition of what we are going to prove: the empty hexagons form a triangular lattice, and the clockwise/counter-clockwise (or hexagonal charge) degrees of freedom behave as effective Ising spins. These spins seem to respect an ice rule on the larger triangular lattice, hinting that the pinwheels phase might have as residual entropy one twelfth of that of the TIAFM.

From the tensor network computations, we indeed obtain (Fig. 4.17a)

$$S_{\text{Pinwheels}} = 0.026922 \pm 3 \cdot 10^{-6} \cong \frac{S_{\text{TIAFM}}}{12}. \quad (4.32)$$

To obtain this result, we need to allow for two-by-two site translation symmetry breaking (using a multi-site VUMPS implementation [151]). This is not surprising given the expected translation symmetry breaking corresponding to the triangular lattice of empty hexagons. Although the Monte Carlo simulations have large errors, the resulting residual entropies are compatible with the tensor networks result, and our prediction (Fig. 4.17b).

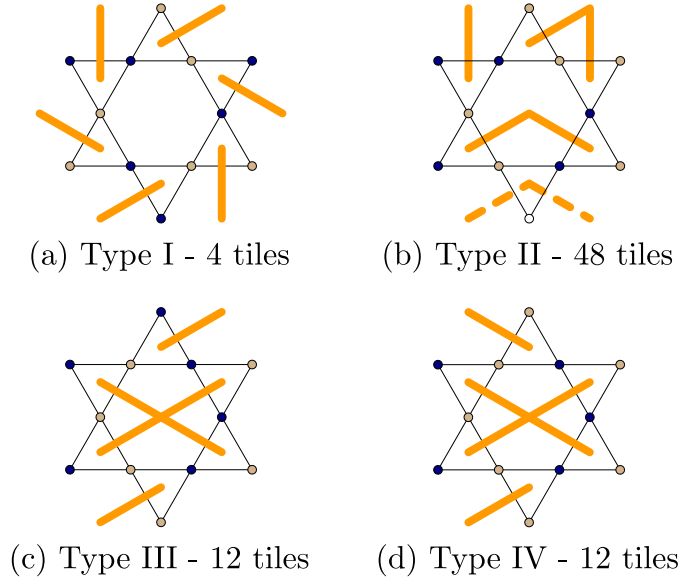


Figure 4.18 – The four types of ground-state tiles in the pinwheels phase. There are 76 tiles in total; if a tile belongs to the ground state, so do its counterparts corresponding to a global spin flip and/or lattice symmetries. The blue, respectively yellow dots correspond to up, respectively down spins. The orange segments represent the dimer configuration on the dual dice lattice. The dotted orange segment stands for the fact that the dimer can either be on the left or on the right. We will show that the 12 tiles of Type IV are spurious tiles.

#### 4.5.2 Mapping to the ground state of the TIAFM

The fact that the residual entropy of the pinwheels phase is related to that of the TIAFM does not imply that there is a direct mapping between the two families of ground states. For instance, there could be additional configurations in the former corresponding to sub-extensive corrections in the entropy. However, we will show that such a mapping exists. First, in the spirit of Chapter 2, we will see what are the tiles available in the ground state; second, we will prove that the only states one can build with these tiles are states with a triangular lattice of empty hexagons, respecting a clockwise/counter-clockwise ice rule; third, we will show that the hexagons bearing crosses play the same role as dimers in the TIAFM ground state; and fourth, we will see that this implies that there is an eight-to-one mapping from the pinwheels phase ground states to the TIAFM ground states.

##### Ground-state tiles

The 76 ground-state tiles are summarized in Fig. 4.18. There are four tiles corresponding to our tentative effective Ising d.o.f.; the other tiles either bear a cross or a chevron, confirming what was observed in the Monte Carlo snapshot. What all these tiles have in common is that the only allowed spin configurations around a hexagon are those with three spins up and three spins down. The empty hexagons (Fig. 4.18a) correspond to ferromagnetic  $J_2$  triangles

while the chevrons (Fig. 4.18b) and the crosses (Fig. 4.18b and c) correspond to  $J_2$  triangles respecting an ice rule. It is important to remember that when constructing a state with the tiles in Fig. 4.18, each tile shares two nearest-neighbor triangles with each of its neighbors (Fig. 4.7).

### **Proof that the ground-state configurations bear a triangular lattice of empty hexagons respecting an ice rule**

From the ground-state energy of the pinwheels phase (Eq. 4.31) we can deduce that  $3/4$  of the  $J_2$  triangles (kagome superlattices) are in their ground state and  $1/4$  are ferromagnetic. This in turn implies that over all,  $1/4$  of all hexagons in a given ground state must be empty, and  $3/4$  must bear either a cross or a chevron.

Fig. 4.18a shows that around an empty hexagon, the dimers must either turn clockwise or counterclockwise. This implies that a hexagon containing a cross cannot have an empty hexagon as a nearest neighbor in the cross's acute angles directions. At the same time, the cross cannot have another cross as a nearest neighbor in the direction of its acute angles (it would violate the ice rule on the  $J_1$  triangles); it must therefore have chevrons as nearest neighbors in these two directions. Furthermore, it is easy to see that two crosses cannot share their acute angle chevron without creating a defect in a nearest-neighbor triangle. Therefore, there must be at least two chevrons for each cross, which implies an upper bound on the overall ratio of hexagons bearing a cross (and a lower bound on the overall ratio of hexagons bearing a chevron):

$$r_{\text{cross}} \leq 1/4, \quad r_{\text{chevron}} \geq 1/2, \quad (4.33)$$

where we used that fact that the overall ratio of empty hexagons is fixed.

The tiles of Type II show that a chevron must always be nearest neighbor to at least one cross in the direction of the cross's acute angle. But this implies an upper bound on the ratio of crosses, since there must be at least one cross for two chevrons:

$$r_{\text{cross}} \geq \frac{1}{4}, \quad r_{\text{chevron}} \leq 1/2, \quad (4.34)$$

Therefore, the overall ratio of crosses in the pinwheels phase ground state also has to be  $1/4$ ; the ratio of chevrons is  $1/2$ .

We now want to show that these ratios are not only satisfied globally but also locally. For this, we first notice that two empty hexagons cannot be nearest neighbors (Type I tiles in Fig. 4.18); they must at least be next-nearest neighbors. It is easy to verify that this implies that an occupied hexagon - tiles of Type II, III and IV in Fig. 4.18 - can have at most two empty hexagons among its six nearest neighbors. Thus, at most, for each  $M$  occupied hexagons there are  $M/3$  empty hexagons (since an empty hexagon always has six occupied nearest neighbors). Since this corresponds to the overall ratio of empty hexagons being  $1/4$ , the bound has to be saturated, and an occupied hexagon has to have exactly two empty hexagons as nearest

#### 4.5. Pinwheels phase : a mapping to the triangular lattice Ising antiferromagnet

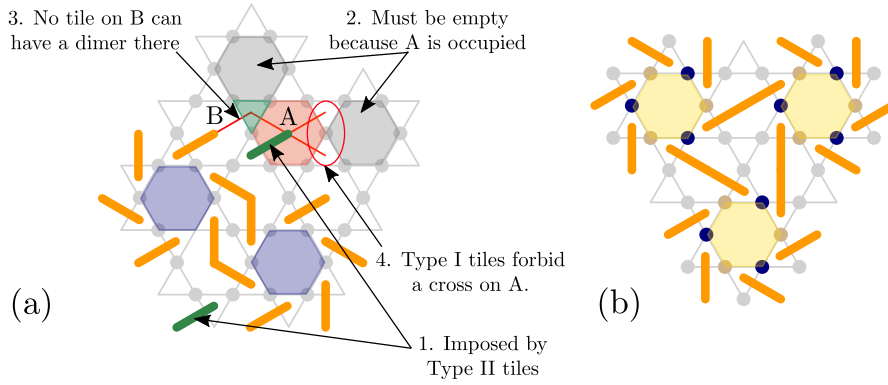


Figure 4.19 – Two illustrations to help understand the proof. (a) Graphical proof that two empty hexagons cannot be next-nearest neighbors in the pinwheels phase: we start with the configuration of the orange dimers (two next-nearest neighbor empty hexagons must have the same chirality). From the Type II tiles, the green dimers must be added. The hexagon A is thus occupied and has already three occupied nearest-neighbor hexagons. It has to have two nearest-neighbors which are empty, and these empty hexagons cannot be nearest-neighbors, which fixed their positions (highlighted in gray). The green triangle must be occupied by one dimer. However no tile on B can occupy it; similarly, no tile on A can occupy it, because the empty hexagon forbids putting a cross on A. Thus the plane cannot be tiled starting from two next-nearest-neighbor empty hexagons. (b) Three empty hexagons which are third neighbors cannot all have the same chirality.

neighbors.

Now, one can convince oneself that is not possible to tile starting from two empty hexagons which are next-nearest neighbors: fairly early on, one encounters a contradiction. We refer to Fig. 4.19a to show this explicitly. First, one can check that the two empty hexagons need to have the same chirality; this in turn implies that they are separated by two chevrons. This enforces the existence of an occupied hexagon (highlighted in red, labeled A) whose three neighbors on one side are already occupied. As we have seen, this occupied hexagon must have two empty hexagons as nearest-neighbors, whose position is thus fixed. With these two hexagons fixed, one can easily check that there is no way to find tiles that fit on hexagons A and B in Fig. 4.19a.

Therefore, all empty hexagons have to be third-nearest neighbors; the only way to have a ratio of empty hexagons of  $1/4$  in that case is that they form a triangular lattice. At the same time, it is easy to see that on each triangle on this larger lattice, the three empty hexagons cannot all have the same chirality: there is an ice rule for the rotation of the dimers around these empty hexagons (Fig. 4.19).

One should note that once the location of the empty hexagons is fixed, the spin configuration is fully determined by the Type I tiles placed there. This proves the result that all the ground states in the pinwheels phase can be seen as a triangular lattice of Type-I tiles respecting a “chiral” or “charge” ice rule.

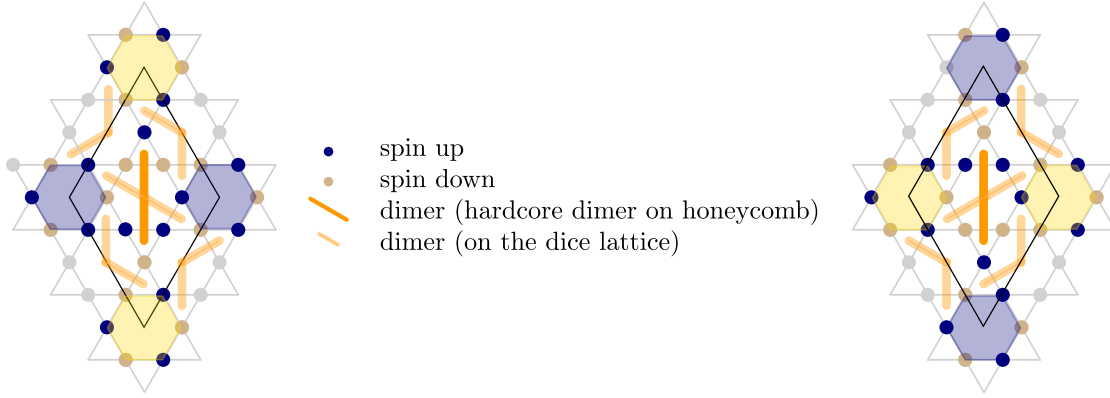


Figure 4.20 – The two rhombi to be considered in the pinwheels phase (two dimer configurations, four spin configurations). The black lines indicate the rhombi corresponding to the original TIAFM model. In the TIAFM, a rhombus corresponds to two triangles sharing a bond with aligned spins. Here, it corresponds to two triangles of pinwheels sharing a bond with aligned pinwheel chirality.

Finally, there are eight ground states of the pinwheels phase mapping to the same TIAFM ground state. Indeed, there is a four-fold degeneracy corresponding to the translation symmetry breaking (selecting which hexagons are going to bear the effective Ising degrees of freedom), and a two-fold degeneracy corresponding to a global spin flip in the pinwheels phase ground state (for a given chirality, there are two Type I tiles).

#### Any configuration of the TIAFM ground state is represented

To conclude the proof, we still have to show that *any* spin configuration in the TIAFM ground state maps to eight ground states of the pinwheels phase. For this, we will make use of the rhombus tiling of the triangular lattice and its connection to the hardcore dimer model on honeycomb and the TIAFM ground states (introduced in the context of solid-on-solid models, see e.g. Refs. 26, 62). To each dimer on honeycomb, one can associate a pair of triangles forming a rhombus; thus, a configuration of dimers on honeycomb respecting the hardcore constraints corresponds to a tiling of the plane with rhombi. Given this, we want to show that any rhombi tiling can be mapped to a pinwheels phase ground state. A rhombus corresponds to two triangles sharing a bond with aligned spins in the original TIAFM model; there are thus only two types of rhombi to consider. For each type, the corresponding pinwheels phase tiling is uniquely defined (up to a global spin flip). We show the corresponding configurations in Fig. 4.20. From there, one can easily check that the pinwheels phase tiles do not create additional constraints for the rhombi to fit, which immediately implies that any rhombi tiling can be mapped to a pinwheels phase ground state. Therefore, the dimer configuration in the pinwheels phase is fully fixed by the TIAFM configuration up to translations of the pinwheel center location (four-fold degeneracy). For a given dimer configuration, there are only two possible spin configurations, corresponding to a global spin flip. Therefore the spin



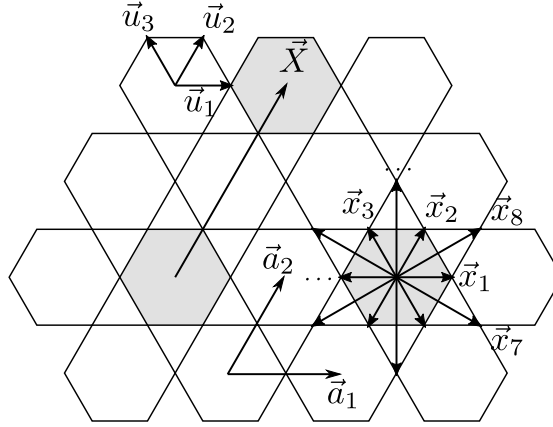


Figure 4.21 – Two conventions for labeling the sites of kagome. Either we label the hexagon centers ( $\vec{R} = R_1 \vec{a}_1 + R_2 \vec{a}_2$  with  $R_1$  and  $R_2$  integers) and the three sites in the unit cell ( $\vec{u}_1$  to  $\vec{u}_3$ ), or we label the pinwheel centers ( $\vec{X} = 2n\vec{a}_1 + 2m\vec{a}_2$  with  $n, m$  integers) and the twelve sites in the unit cell ( $\vec{x}_1$  to  $\vec{x}_{12}$ ).

configuration in the pinwheels phase is fixed up to an eight-fold degeneracy by the TIAFM ground-state configuration. This concludes our proof.

### 4.5.3 Consequences for the ground-state correlations in the pinwheels phase

The mapping from the pinwheels phase ground states to the TIAFM teaches us about the correlations in the ground-state manifold. Below, we discuss the various types of spin-spin correlations. The essential argument is first that there is algebraic decay of the correlations between the pinwheel orientations, second that the long-range order associated with the pinwheel centers translates into a partial long-range order for the spins on a certain sublattice, and finally that the pinwheel orientations being fixed, the spin configuration is also fixed (up to a global spin flip).

The approach amounts to describing the spin configuration based on David stars centered on empty hexagons: there is long-range order for the spins on the hexagon at the center of the stars, and algebraic decay for the spins on the branches of the star. In the following, we label by  $\vec{r}_i$  the positions of the spins, by  $\vec{R}_\alpha$  the positions of the hexagon centers, and by  $\vec{u}_k$  ( $k = 1, 2, 3$ ) the positions of the spins in the unit cell, such that  $\vec{r}_{k,\alpha} = \vec{R}_\alpha + \vec{u}_k$ . We take the original kagome lattice spacing to be 1, so the basis vectors of the triangular lattice supporting the kagome lattice are  $\vec{a}_1 = (2, 0)$  and  $\vec{a}_2 = (1, \sqrt{3})$  (Fig. 4.21).

#### Pinwheel center

The location of the pinwheels is characterized by the presence of an empty hexagon, which corresponds to having two ferromagnetic next-nearest-neighbor triangles instead of two ice-rule-respecting next-nearest-neighbor triangles. We can introduce an operator on the

hexagons

$$P_{\square} = \frac{1}{4} \left( \sum_{\Delta_2 \in \square} (\sigma_i \sigma_j + \sigma_j \sigma_k + \sigma_k \sigma_i) - 2 \right) = \begin{cases} 1 & \text{if the hexagon is a pinwheel center} \\ -1 & \text{otherwise} \end{cases}, \quad (4.35)$$

or equivalently, in terms of dimers,

$$P_{\square} = \frac{1}{4} \left( \sum_{i=0}^5 (d_i d_{i+1}) - 2 \right) = \begin{cases} 1 & \text{if the hexagon is a pinwheel center} \\ -1 & \text{otherwise} \end{cases}, \quad (4.36)$$

where  $i$  goes through the dimers bonds touching the hexagon center and where  $d_6 = d_0$ . This operator has clearly long-range order in any of the four translation-symmetry-broken sectors of the pinwheel phase, since <sup>6</sup>:

$$\langle P_{\alpha} P_{\beta} \rangle = \begin{cases} 1 & \text{if } (\vec{R}_{\alpha} - \vec{R}_{\beta}) = 2n\vec{a}_1 + 2m\vec{a}_2 \\ -1 & \text{otherwise} \end{cases} \quad (4.37)$$

The order parameter associated with the selection of the translation-symmetry-broken sectors can be built on the triangular sublattice of hexagon centers (labeled by  $\alpha$ ) as

$$M = \frac{3}{N} \sum_{\alpha} P_{\alpha} e^{i\frac{1}{2}\vec{Q} \cdot \vec{R}_{\alpha}} \quad (4.38)$$

where  $\vec{Q} = (\pi, 0)$ . In the ground state, this parameter can take four values, with  $M = |M|e^{i\phi}$  where  $|M| = 1/2$  and the phase  $\phi = n\pi/2$  with  $n$  an integer.

This being established we can adjust the notation to work directly in a translation-symmetry-broken sector. Instead of labeling the sites based on  $\vec{u}_i$  taking three possible values, we label the sites based on an empty star center  $\vec{X}_{\alpha} = 2n\vec{a}_1 + 2m\vec{a}_2$  and a 12-sites motif describing the star  $\vec{x}_i$   $i = 1, \dots, 12$ . We take the convention that  $i = 1, \dots, 6$  describes the hexagon sites, and  $i = 7, \dots, 12$  describes the branches of the star (Fig. 4.21).

### Pinwheel correlations

Only looking at pinwheels, we could compute the chirality by averaging the number of dimers turning in one direction or the other. If we are only looking at the ground-state manifold, since around an empty hexagon the chirality is fixed once we know a single dimer position, the simplest version is

$$C_{\alpha} = \delta_{P_{\alpha}, 1} \sigma_{\vec{R}_{\alpha} + \vec{u}_1} \sigma_{\vec{R}_{\alpha} + \vec{a}_1 + \vec{u}_2} = \delta_{P_{\alpha}, 1} d_{\vec{R}_{\alpha} + \vec{u}_1, \vec{R}_{\alpha} + \vec{a}_1 + \vec{u}_2} = \begin{cases} 1 & \text{if clockwise} \\ -1 & \text{otherwise} \end{cases}. \quad (4.39)$$

---

<sup>6</sup>Note that the correlations averaged over the four translation-symmetry-broken sectors give zero if  $(\vec{R}_{\alpha} - \vec{R}_{\beta}) \neq 2n\vec{a}_1 + 2m\vec{a}_2$ .

#### 4.5. Pinwheels phase : a mapping to the triangular lattice Ising antiferromagnet

or, in the new notation,

$$C_\alpha = \sigma_{\vec{X}_\alpha + \vec{x}_1} \sigma_{\vec{X}_\alpha + \vec{x}_8} = \begin{cases} 1 & \text{if clockwise} \\ -1 & \text{otherwise} \end{cases}. \quad (4.40)$$

In the ground-state manifold of the TIAFM, the spin-spin correlations decay asymptotically as [35, 246]

$$\langle s_i s_j \rangle = \epsilon_0 \frac{\cos(\vec{q} \cdot \vec{r})}{\sqrt{|\vec{r}|}}, \quad \vec{r} = \vec{r}_j - \vec{r}_i, \quad (4.41)$$

where we denoted by  $s_i$  the Ising spins, and where the structure factor is characterized by  $\vec{q} = (\pm \frac{2\pi}{3}, \frac{2\pi}{\sqrt{3}})$ . It has been argued using numerical evidence [35] that along a row of the triangular lattice, the proportionality factor  $\epsilon_0$  related to the decay amplitude  $E_0^T$  of the pair correlations at the critical point of the triangular *ferromagnet* as

$$\epsilon_0 = \sqrt{2}(E_0^T)^2 \cong 0.632226080... \quad (4.42)$$

which can be checked directly using the tensor network construction (Appendix G.3).

This implies that in the pinwheels ground-state manifold, in a given symmetry-broken sector, the pinwheel chirality correlations decay as

$$\langle C_\alpha C_\beta \rangle = \epsilon_0 \delta_{P_\alpha, 1} \delta_{P_\beta, 1} \frac{\cos\left(\frac{\vec{q} \cdot \vec{X}}{4}\right)}{\sqrt{|\vec{X}|/4}}, \quad \vec{X} = \vec{X}_\beta - \vec{X}_\alpha, \quad (4.43)$$

where we used  $\vec{X}_\beta - \vec{X}_\alpha = 2n\vec{a}_1 + 2m\vec{a}_2$ .

#### Partial long-range order and critical correlations

The pinwheels correlations imply spin-spin correlations which we now explore, and summarize in Fig. 4.22. An empty hexagon corresponding to a pinwheel center has two possible associated spin configurations for a given chirality: either the one depicted in Fig. 4.18a (spin up on  $\vec{u}_1$ ) or the one depicted in the Monte Carlo snapshot in Fig. 4.16 (spin down on  $\vec{u}_1$ ). We now argue that, together with the long-range order in the pinwheel center locations, there comes a long-range order in the spins living on the empty hexagons. First, fixing the spin on  $\vec{u}_1$  in a given empty hexagon fixes all the other spins on that hexagon. Second, it is easy to see (Fig. 4.20) that a spin  $\sigma_1$  in  $\vec{r}_1 = \vec{X}_\alpha + \vec{u}_i$ , and another  $\sigma_2$  in  $\vec{r}_2 = \vec{X}_\alpha + \vec{a}_i + \vec{u}_i$ , where  $i = 1, 2, 3$  and  $\vec{a}_3 = -\vec{a}_1 + \vec{a}_2$ , must have opposite values  $\sigma_2 = -\sigma_1$ . Indeed, they are separated by a hexagon bearing either a cross or a chevron, and the path connecting them must cross either the two branches of the cross or chevron, or no branches. Thus we must have  $\sigma_3 = \sigma_1$  if  $\vec{r}_3 = \vec{X}_\alpha + 2\vec{a}_i + \vec{u}_i$ .

This implies that two nearest-neighbor empty hexagons have the same spin configuration.

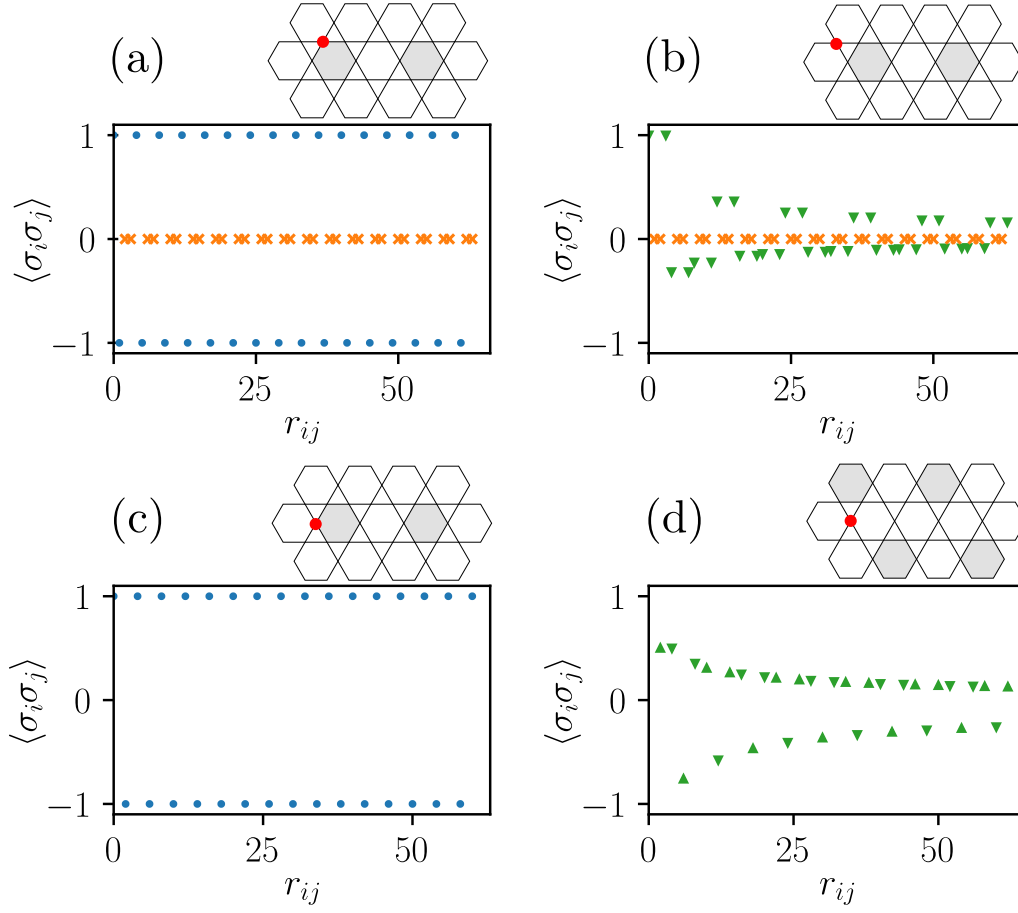


Figure 4.22 – Prediction for the horizontal spin-spin correlations in the pinwheels phase, in a translation symmetry-broken sector. We show in blue the correlations between sites in the center of the David stars centered on empty hexagons, in green the correlations between sites in the branches of the David stars, and in orange the mixed correlations. The correlations depend on the specific site chosen as the origin and we show the four possible set of correlations, with the red dot in the insets signaling the site selected as the origin. In the insets the stars with empty hexagons are highlighted in grey.

Therefore, by simple extension,

$$\sigma_{\vec{X}_\beta + \vec{x}_j} \sigma_{\vec{X}_\alpha + \vec{x}_i} = \begin{cases} 1 & \text{if } \text{mod}(i, 2) = \text{mod}(j, 2) \\ -1 & \text{otherwise} \end{cases}, \quad i, j = 1, \dots, 6 \quad (4.44)$$

where  $\vec{X}_\beta = \vec{X}_\alpha + 2n\vec{a}_1 + 2m\vec{a}_2$ , and the long-range order in the pinwheel centers translates into a long-range order in the spins living on the empty hexagons (Figs. 4.22a and 4.22c).

For the product of spins belonging to the branches of a pinwheel we have

$$\sigma_{\vec{X}_\beta + \vec{x}_j} \sigma_{\vec{X}_\alpha + \vec{x}_i} = \begin{cases} C_\alpha C_\beta & \text{if } \text{mod}(i, 2) = \text{mod}(j, 2) \\ -C_\alpha C_\beta & \text{otherwise} \end{cases}, \quad i, j = 7, \dots, 12 \quad (4.45)$$

where  $\vec{X}_\beta = \vec{X}_\alpha + 2n\vec{a}_1 + 2m\vec{a}_2$ . Therefore, the algebraic decay of the spin-spin correlations in the TIAFM must translate into an algebraic decay of the spin-spin correlations for spins on the branches of the pinwheels in the pinwheels phase (Figs. 4.22b and 4.22d).

Finally,

$$\sigma_{\vec{X}_\beta + \vec{x}_j} \sigma_{\vec{X}_\alpha + \vec{x}_i} = \begin{cases} -C_\beta & \text{if } \text{mod}(i, 2) = \text{mod}(j, 2) \\ C_\beta & \text{otherwise} \end{cases}, \quad i = 1, \dots, 6 \quad j = 7, \dots, 12. \quad (4.46)$$

Since  $\langle C_\beta \rangle = 0$ , these correlations are identically zero in the ground-state (Figs. 4.22a and 4.22b).

## 4.6 Strings phase and relation to the triangular lattice Ising antiferromagnet

### 4.6.1 $J_2 = 0$

We now look at the last missing part of the ground-state phase diagram, where  $J_3$  is antiferromagnetic and large compared to  $J_2$ . At  $J_2 = 0$ , the ground-state energy per site is

$$E_{J_1-J_3} = -\frac{2}{3}J_1 - J_3, \quad (4.47)$$

corresponding to the fact that every nearest-neighbor triangle and every third-nearest-neighbor triangle are in their ground state. A lower bound on the residual entropy can be obtained by recognizing the following set of ground states of the  $J_1$ - $J_3$  model: fixing one  $J_2$  kagome sublattice to be up and another to be down, the spins on the third sublattice can be set at random without changing the energy. This gives a lower bound

$$S_{J_1-J_3} \geq \frac{1}{3} \ln 2 \cong 0.231... \quad (4.48)$$

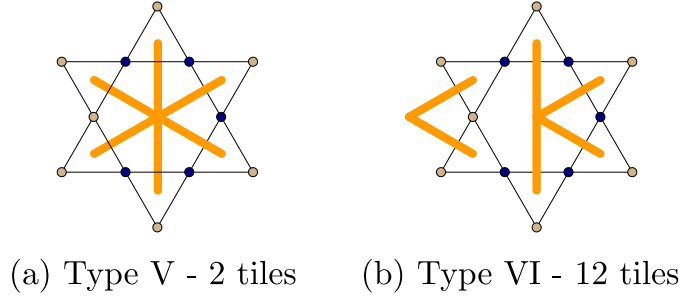


Figure 4.23 – Together with the 200 ground-state tiles of the strings phase (Fig. 4.24), these 14 ground-state tiles belong to the ground state of the  $J_1$ - $J_3$  model. The Type V tiles also belong to the  $\sqrt{3} \times \sqrt{3}$  ordered phase, while the Type VI tiles are new tiles only existing at the boundary.

In fact, we can push this lower bound up by noticing that in some of the configurations taken by the spins set on the third sublattice, one of the central spins is freed. Counting the corresponding configurations, one gets

$$S_{J_1-J_3} \geq \frac{1}{27} \ln 559 \cong 0.234... \quad (4.49)$$

Finally, another possible estimate can be made in the same spirit as what Hamp et. al. attempted for the dipolar point: since the residual entropy of the KIAFM and the TIAFM is known, we can use them to determine reduction factors for the number of ground states as

$$f_{\text{KIAFM}} := e^{S_{\text{KIAFM}}/2} \cong 0.8259... \quad f_{\text{TIAFM}} := e^{S_{\text{TIAFM}}/2} \cong 0.6907..., \quad (4.50)$$

yielding

$$S_{J_1-J_3} \sim \ln(2 \cdot f_{\text{KIAFM}} \cdot f_{\text{TIAFM}}^{2/3}) \cong 0.255... \quad (4.51)$$

where we have assumed that if two of the three third-neighbor triangular sublattices are fixed together with the nearest-neighbor model, the third sublattice is implicitly fixed. Although this is a hand-waving argument, it goes to show how the lower residual entropy of the TIAFM should make the residual entropy that we obtain at  $J_2 = 0$  smaller than the one at  $J_3 = 0$ . This is indeed what we find with the tensor network contraction (Fig. 4.5, see also Appendix G.1):

$$S_{J_1-J_3} = 0.26413 \pm 10^{-5}. \quad (4.52)$$

In this ground state phase, there are 214 ground-state tiles; some of them are illustrated in Fig. 4.23, but 200 of these tiles also belong to the ground-state when a small antiferromagnetic  $J_2$  coupling is introduced, and are shown in Fig. 4.24.

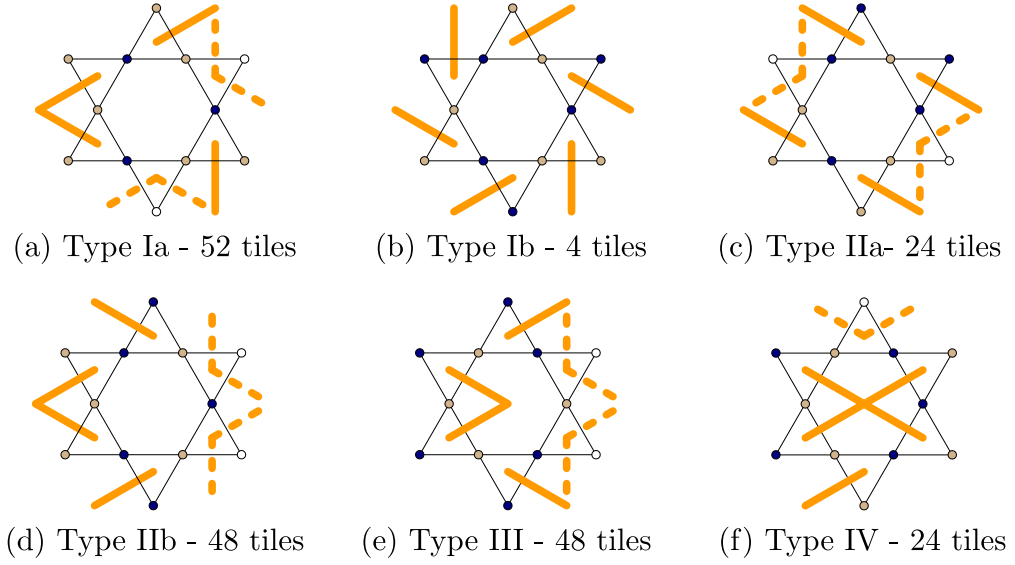


Figure 4.24 – The various types of ground-state tiles in the phase at small  $J_2$  values (strings phase). There are 200 tiles in total. See the caption of Fig. 4.18 for a detailed legend. We suspect that the Type I tiles (a and b) are spurious, while the tiles of Type II (a and b), III and IV are not. Notice that tiles of Types I and II correspond to two ferromagnetic next-nearest-neighbor triangles, Type III tiles correspond to one ferromagnetic and one ice-rule-respecting next-nearest-neighbor triangle, and Type IV tiles correspond to two next-nearest-neighbor triangles in their ground state.

#### 4.6.2 Overview of the strings phase

When a small  $J_2$  coupling is introduced, the ground-state energy of the  $J_1$ - $J_3$  model gets modified as:

$$E_{\text{Strings}} = -\frac{2}{3}J_1 + \frac{2}{3}J_2 - J_3. \quad (4.53)$$

This corresponds to a selection of states for which the contribution due to the second-neighbor coupling is minimized. The ground-state tiles in Fig. 4.24 give rise to a macroscopic number of ground states where there are as many ice-rule-respecting second-neighbor triangles as ferromagnetic second-neighbor triangles. It is easy to put a lower bound on this number by considering Fig. 4.25: each spin on a green site can be flipped without changing the ground-state energy, which gives a lower bound of

$$S_{\text{Strings}} \geq \frac{1}{9} \ln(2) \cong 0.077... \quad (4.54)$$

The tensor network contraction results in a larger residual entropy (Fig. 4.27), corresponding to one third of that of the TIAFM:

$$S_{\text{Strings}} = 0.107689 \pm 2 \cdot 10^{-6} \cong \frac{1}{3} S_{\text{TIAFM}}. \quad (4.55)$$

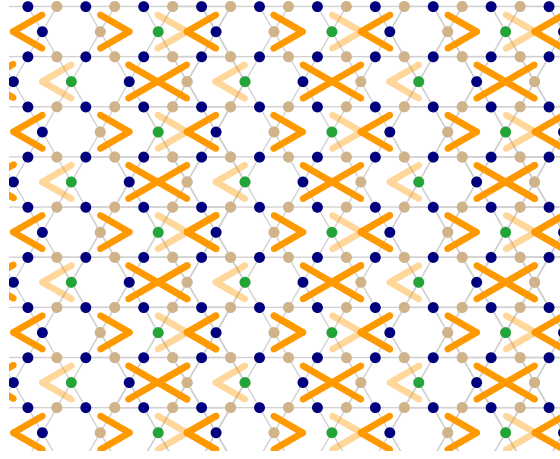


Figure 4.25 – A set of ground states of the strings phase providing a lower bound for the residual entropy. Without any change in the energy, the green spins can be flipped independently. The light-orange dimers illustrate the dimer configuration when all the green spins are down (light yellow). Flipping the spin on a green site flips the light-orange dimer arrow horizontally. In all cases there are strings of crosses that wind through the sample.

This of course makes one wonder whether it is possible to find a mapping from the ground states of the strings phase to the TIAFM ground states. There are two obvious directions to pursue. The first is to find effective Ising d.o.f. corresponding to grouping three spins. Looking at the ground states obtained from Monte Carlo simulations, it does indeed seem like the charges defined on either all the up or all the down triangles of the kagome lattice respect some kind of ice rule (Fig. 4.26). However, this is challenging since for a given charge configuration there could be many spin configurations. Another obvious direction is to notice by looking at the ground-state tiles in Fig. 4.24 that all the dimers in the strings phase ground-states must belong to an arrow-like pair of dimers (forming an acute angle, either on its own, such as in the middle of tiles of Type III, or belonging to a cross, such as in the middle of Type IV tiles). This means one could define hardcore dimers living on a honeycomb lattice by associating to each acute angle a new dimer variable, connecting two kagome triangles. However, we find that the maximally flippable state is not realized, which eliminates this direction of study.

A third possibility is to notice, in the ground states obtained from Monte Carlo simulations, that crosses form strings that seem to be directed. This points to a different connection to the TIAFM, relying on configurations of directed strings on the honeycomb lattice. In the rest of this section, we will first discuss the relation between the TIAFM and directed, non-crossing strings on the honeycomb lattice. Then, we will show how to associate to any such string configuration at least one of the ground states of the strings phase. We will see that some string configurations are associated to a macroscopic number of ground states of the strings phase, and we will argue that this number is subextensive. Finally, we use the tiles to prove the result that crosses *have* to form strings, and that any ground state of the strings phase maps to a well-defined configuration of directed, non-crossing strings on the honeycomb lattice.



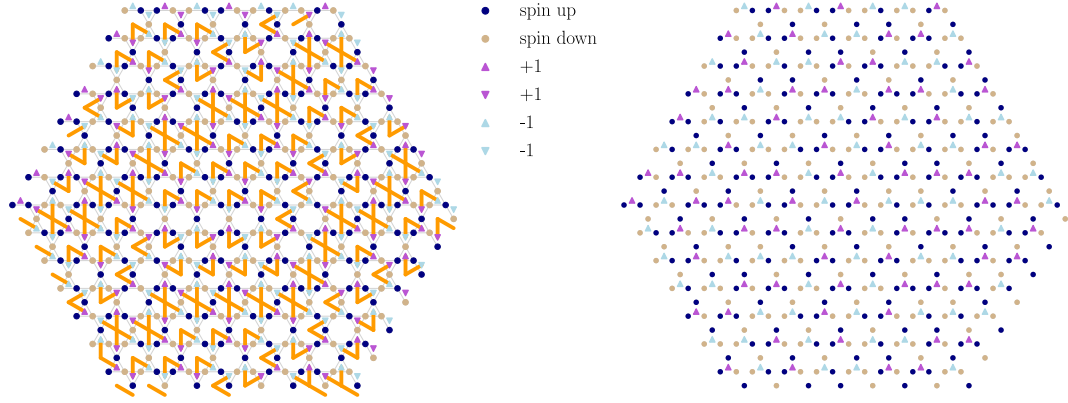


Figure 4.26 – A ground state of the strings phase. On the left panel, we show the full charge and dimer configuration, while on the right panel, we only show the configuration of charges on up triangles. In the dimer configuration, one should notice the strings of crosses winding the system. In the charge configuration, one should notice it does seem to behave as a ground state of the TIAFM.

Although this is not an exact mapping, it gives an interesting insight into the strings phase and its residual entropy.

### 4.6.3 TIAFM and strings on the honeycomb lattice

The core of the understanding of the residual entropy of the strings phase relies on an existing mapping between the ground-state configurations of the TIAFM and configurations of strings on the honeycomb lattice. This well-known mapping is described in detail in References 246–248, but we reproduce the argument here as it will be useful for understanding the strings phase.

As we discussed in Sec. 1.1, the TIAFM ground state maps to classical dimers on the honeycomb lattice with hardcore constraints. It is easy to see that two different dimer configurations  $\mathcal{C}$  and  $\mathcal{C}'$  on honeycomb must be related by the rotation of dimers around loops of even length, with the dimers around the loop belonging alternatively to  $\mathcal{C}$  and to  $\mathcal{C}'$ . Thus, choosing a reference configuration, one can associate to any dimer configuration a configuration of loops on honeycomb. If the reference configuration corresponds to stripes of spins (Fig. 4.28a), then there are further restrictions on these loops: they must consist in directed strings (i.e. strings which cannot turn back on themselves), which span the system and do not cross. Furthermore, if periodic boundary conditions are imposed on the spin configuration, there strings must come in pairs. In Fig. 4.28b and in the rest of this section, we show pairs of string with one green and one red string.

Since for each dimer configuration there is a single corresponding string configuration, the

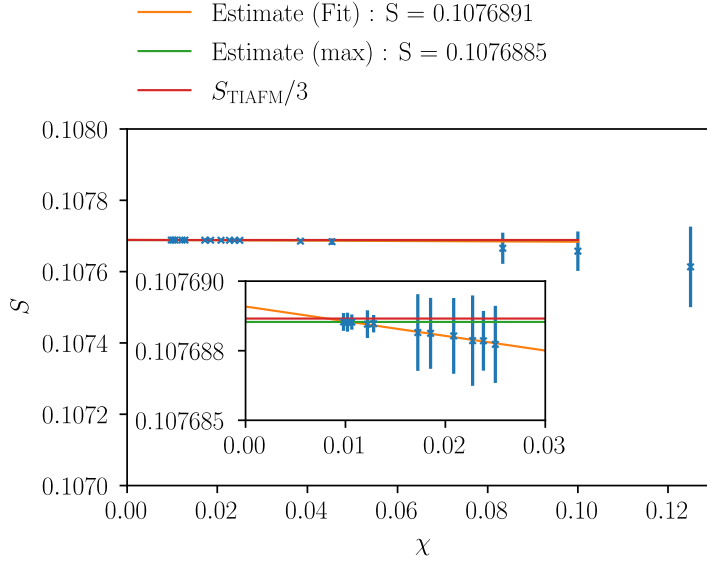


Figure 4.27 – Residual entropy per site in the strings phase for bond dimensions ranging from  $\chi = 8$  to  $\chi = 98$ , and comparison to the residual entropy of the TIAFM.

number of ground states of the TIAFM can also be obtained as the number of configurations of any even number of directed strings on the honeycomb lattice which do not cross.

In the following, we will see how the residual entropy of the strings phase can be understood in terms of strings on the honeycomb lattice, up to sub-extensive contributions.

#### 4.6.4 Any string configuration on the honeycomb lattice maps to at least one ground state of the strings phase

##### An ordered ground state of the strings phase

As shown in Fig. 4.24, there are 200 tiles that can *a priori* be used to construct ground states in the strings phase. In particular, these tiles can be differentiated based on their contribution to the next-nearest-neighbor correlations. Indeed, the tiles of Types I and II (Fig. 4.24a to d) correspond to two ferromagnetic 2nd-neighbor triangles; the tiles of Type III to one ferromagnetic and one ice-rule-respecting 2nd-neighbor triangle; and the tiles of Type IV to two ice-rule-respecting 2nd-neighbor triangles.

At the same time, because there are two next-nearest-neighbor triangles for three sites, the factor  $\frac{2}{3}$  in front of  $J_2$  in the ground-state energy of this phase (Eq. 4.53) implies that half of the 2nd-neighbor triangles must be ferromagnetic and half must be in their ground state. An easy way to satisfy this constraint together with the tiling constraints is to make a long-range ordered configuration as shown in Fig. 4.29a. It is easy to check that all the nearest-neighbor

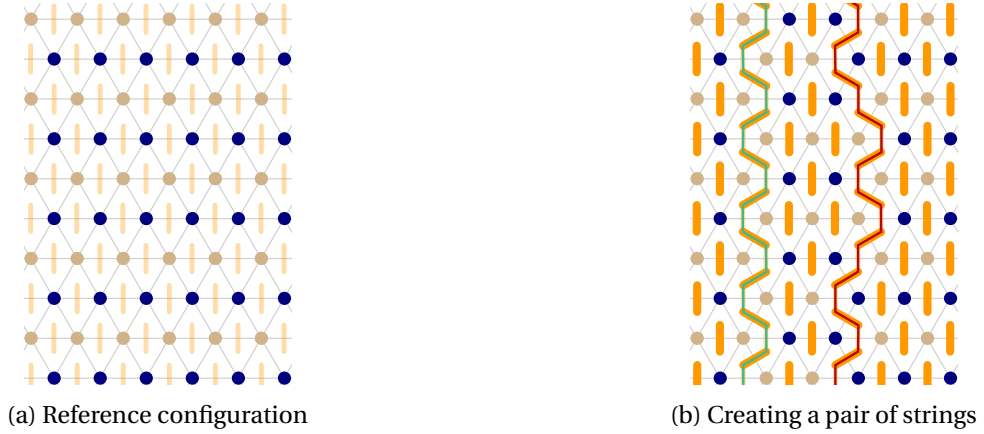


Figure 4.28 – Mapping between Ising configurations in the ground state of the TIAFM and string configurations on the honeycomb lattice. (a) The stripe configuration is used as a reference (b) The difference between the dimer configurations associated with the new configuration and the reference one corresponds to directed strings on honeycomb.

triangles as well as all the 3rd-nearest-neighbor triangles are in their ground state in this state, which proves that it is a ground state of the strings phase. This ground state will be of crucial importance in our discussion because we are going to use it as a reference configuration.

#### Creating and moving pairs of strings

To prove that any string configuration on the honeycomb lattice maps to at least one ground state of the strings phase, we are going to explicitly show how to construct ground states associated with given string configurations.

First, we notice that flipping a column of arrows compared to the reference configuration does not change the energy, since all the tiles in the resulting configuration belong to the ground-state tiles<sup>7</sup>. This allows one to create a pair of strings: as depicted in Fig. 4.29b, we adopt the convention that a red string runs along the right ends of crosses, and that the corresponding green string runs along the left end of crosses or of the leftmost right-pointing arrows from a column of crosses. This means that the green string can be moved to the left by flipping a left-pointing arrow which stands to its left, as in Fig. 4.29c, without changing the energy. Similarly, the red string can be moved to the right by flipping a left-pointing arrow which stands to its left (destroying a cross and creating a new one), as in Fig. 4.29d. This implies that any valid configuration of two pairs of strings on honeycomb maps to at least one ground state of the Small  $J_2$  phase.

For completeness we now want to show that without changing the reference configuration we can have a green string to the right of a red string. The same prescription as in Fig. 4.29b allows one to create a new pair of strings next to the already existing one, as shown in Fig. 4.29e. The

<sup>7</sup>Notice also that the total number of ferromagnetic  $J_2$  triangles is conserved by this move.

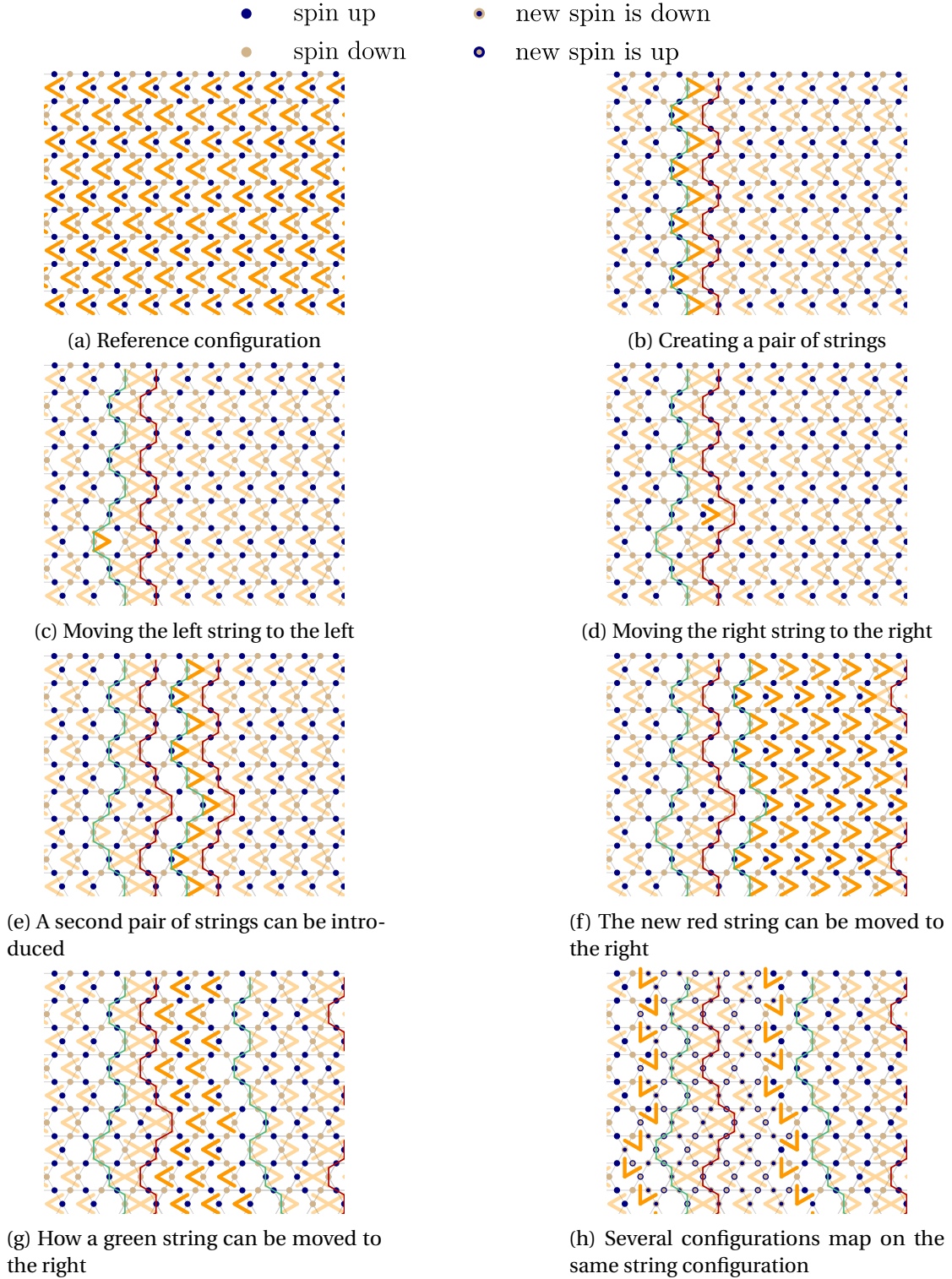


Figure 4.29 – Creating and moving strings in the strings phase. The dark orange dimers are the ones which are modified with respect to the preceding panel, while the light-orange dimers are left untouched. In panel (h) the flipped spins are depicted differently to highlight the need of creating two strings of rotated arrows.

red string in this new pair can be moved all the way to the right (Fig. 4.29f), leaving behind a trail of right-pointing arrows. The green string can also be moved to the right by flipping these arrows again (Fig. 4.29g).

Finally, we show in Fig. 4.29h how trying to rotate an arrow creates a string of arrows spanning the whole system and following the neighboring string of crosses. It also imposes a global spin flip to the left that can only be “absorbed” by another string of rotated arrows. This suggests that there is a sub-extensive number of configurations that map onto the same string configuration. To convince ourselves that this number is growing exponentially only with the linear system size, we compute the residual entropy per site associated with the set of ground-state tiles without the tiles containing crosses. In that case, VUMPS tends to struggle to converge but systematically eventually gives an eigenvalue of one, and thus a zero residual entropy<sup>8</sup>. Although this is not a rigorous proof, we consider it sufficient numerical evidence. Notice also that it is because of the initial choice of reference configuration that such global updates can be made between a red string on the left and a green string on the right, but not between a red string on the left and a green string on the right. There is no fundamental asymmetry there, only a matter of convention.

### 4.6.5 Any ground-state configuration of the strings phase maps to a string configuration on the honeycomb lattice

We have thus shown that any valid string configuration on the honeycomb lattice maps to a ground state of the strings phase. The converse still has to be proven, however. First, we consider ground-state configurations which do not have any crosses or empty hexagons. With periodic boundary conditions, there are 12 such ground states, all rotations or global spin flip with respect to our reference configuration in Fig. 4.29a. These ground state all map to the configuration with no strings. We now must take care of showing that all the other ground states - which have crosses and empty hexagons - map to a valid string configuration.

#### Crosses have to form strings

We start by showing that crosses have to form strings. For this, we consider the Tiles in Fig. 4.24, and in particular the tiles of Type IV. These are the only tiles which bear crosses. Given such a tile, with the cross oriented horizontally, it has two lower nearest-neighbor tiles, of which at least one has to bear a dimer. From looking at the tiles of Types III and IV, it is obvious that this dimer has to belong to a cross, since no tile of Type III can fit there. Thus, one of the nearest-neighbor tiles below a cross has to be another cross. It is obvious that only one of these two tiles can be a cross, and thus crosses have to form strings on a triangular lattice of hexagons. It is also immediately clear that, given the orientation of the first cross, these strings can then only progress in one direction. According to the mapping we introduced in Sec. 4.6.4,

<sup>8</sup>Note that this corresponds to working with open boundary conditions and thus the absence of crosses in the bulk does not remove the possibility of non-local moves due to the presence of empty hexagons on the boundary.

a string of crosses immediately defines a string on the honeycomb lattice: one only needs to connect the right ends of the crosses. Thus, we have shown how to find the configuration of “red strings” associated with a ground state of the strings phase. But this is only half of the description of the associated string configuration.

### Finding the second string

As we have seen above, in the case of periodic boundary conditions, strings have to come in pairs; and we still have to show how to associate a “green strings” configuration to a given ground state of the strings phase. For this, it is sufficient to show how to build the green string that runs to the left of a string of crosses.

In spirit, the prescription to find the location of the green string to the left of a string of crosses is simple: start from the string of crosses, and push the green string to the left until it meets a hexagon which is not a right-pointing arrow. We only have to prove that this way, the green string is always well-constructed; more precisely, that a situation like in figure 4.30a, where the green string has a “jump” and does not live on the honeycomb lattice, is prevented.

This is easily seen from the following procedure: at any point in the process of pushing the green string to the left, one finds the situation depicted in Fig. 4.30b (or its vertical mirror), where one has to see if the green string can be pushed past the hexagon in blue. There are two possibilities. One is that the blue hexagon contains a right-pointing arrow, and the process has to be repeated with a new hexagon (highlighted in yellow in Fig. 4.30b). The other is that it corresponds to a tile which leaves empty the triangle highlighted in red. In this case the green string cannot be pushed further to the left. As illustrated in Fig. 4.30d, the green string is then well constructed: indeed, the red triangle can be occupied only in two ways (dotted line) which both forbid a right-pointing arrow in the triangle highlighted in yellow. Thus, iterating the procedure, one gets a well-defined green string. This shows that any ground state of the strings phase corresponds to a well-defined configuration of directed strings on the honeycomb lattice, and explain the residual entropy that we obtain.

## 4.7 Discussion and outlook

In this Chapter we studied the  $J_1 - J_2 - J_3$  Ising model on the kagome lattice with antiferromagnetic nearest-neighbor and small antiferromagnetic and/or ferromagnetic second- and third-nearest-neighbor interactions. Applying the inequalities method originally proposed by Kanamori [155], we established the ground-state phase diagram exactly. Furthermore, using the tensor network approach we introduced in Chapter 2, we were able to determine the residual entropy with a very high numerical precision.

For antiferromagnetic values of  $J_2$  and  $J_3$  we find three macroscopically degenerate phases with varying residual entropies, the smallest in chevrons phase. This result is surprising when

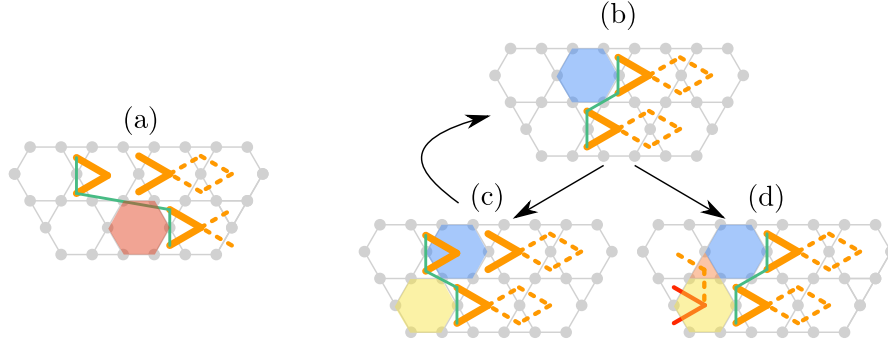


Figure 4.30 – Proving that the strings to the left of strings of crosses are well constructed. We want to show that the situation in (a), where the red hexagon does *not* contain a right-pointing arrow, *never* occurs. The orange segments stand for dimers, the dashed orange segments stand for two dimer possibilities. The initial position of the green string, connecting the left edges of crosses, is well-defined. Pushing the green string to the left creates situation like (b), where one has to decide whether to stop or to bring the green string across the hexagon highlighted in blue. There are two possible cases depending on whether a right-pointing arrow is in that hexagon. If there is, as in (c), the green string can be brought across the blue hexagon, and we are back in a situation like in (b), and we can iterate. If there is not, then we are in situation (d) and cannot bring the green string further to the left. We have to show that (a) does not occur. However, since we are not in situation (c), the red triangle has to be occupied by some other dimer, which forbids putting a right-pointing arrow in the yellow triangle. Thus, the green string cannot be pushed further to the left, and the process stops.

compared with the TIAFM, for instance, whose residual entropy gets immediately lifted by second-neighbor interactions. Although there are some examples in the literature showing that on the kagome lattice, interactions up to third neighbor do not necessarily lift the degeneracy (see for instance [101, 102, 222, 244, 245, 249]), it was mostly known in the case of fine-tuned regions of the phase diagram, for instance  $J_{3\parallel} = J_2$ . Our results show that this is also the case when interactions are solely based on distance and without a fine-tuning of the second- to third-nearest-neighbor interactions, giving a wide range of parameters for the exploration of classical spin liquids.

In the pinwheels phase we were able to understand the residual entropy, which is a twelfth of that of the TIAFM, as the emergence of effective Ising spins on the level of a star unit, and to prove the mapping exactly using the ground-state tiles, which gives us exact results for the decay of the spin-spin correlations. This result shows the power of combining the Kanamori approach of inequalities with its dual, that gives the knowledge of the ground-state tiles and allows for tensor network computations, and with small-scale Monte Carlo simulations that provide an intuition of the ground-state manifold.

It is intriguing that the DKIAFM truncated to third-neighbors has the pinwheel ground-state manifold, and not the chevrons one. This points to a strong competition between the various states when farther-neighbor are taken into account, and asks the question of the range of



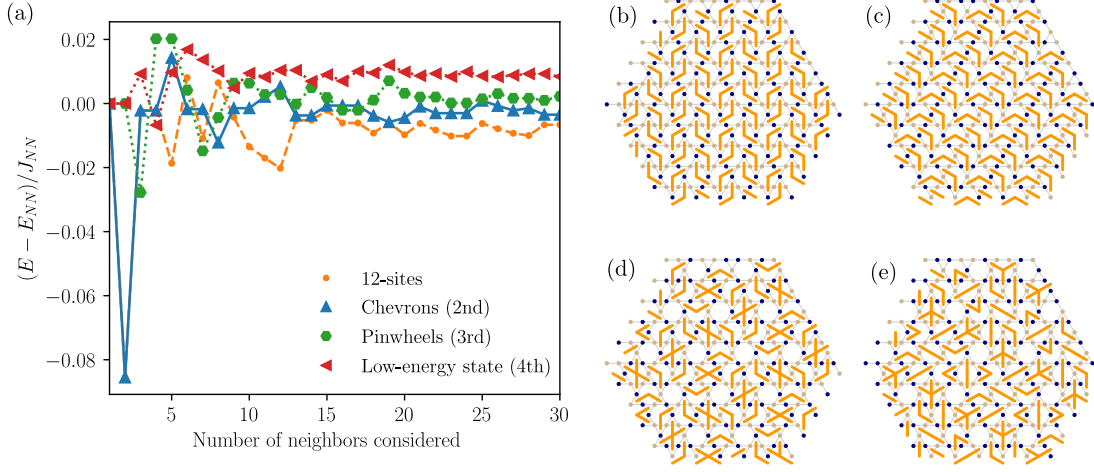


Figure 4.31 – (a) Energy competition between four different states as a function of the range of neighbors taken into account with dipolar couplings (as in Eq. 4.1, with  $J_0 = 1/2, D = 1$ ). The 12-site DKIAFM ground state is only the lowest in energy when the range is of nine neighbors or more. The energies of the four following states are compared (b) 12-site DKIAFM ground state (c) A ground-state in the chevrons phase (different from (b)) (d) A state in the pinwheels ground-state manifold (e) A low energy state when truncating to 4-neighbors (possibly not the ground state).

neighbors couplings that has to be taken into account to find the 12-site long-range-ordered ground state of the DKIAFM. As a simple look into this question, we compute the energy of four different low-energy states as a function of the range of farther-neighbor interactions included. The results are shown in Fig. 4.31. A range of nine neighbors is required to reach the point where the 12-site DKIAFM ground-state systematically has the lowest energy. It is also occasionally degenerate with the specific chevron state that we selected in even further ranges. This strong competition suggests that a large range of neighbors have to be taken into account to fully understand the progressive lifting of the ground-state degeneracy and the selection of the 12-site long-range order in the DKIAFM.

In the chevrons phase, which among other ground states contains the long-range-ordered ground state of the DKIAFM, we find numerical evidence of a macroscopic ground-state degeneracy from the tensor network contraction, although with such a low residual entropy per site that we are unable to detect it in small Monte Carlo simulations, where we only find a sub-extensive entropy. Interestingly, Hamp et al. [99] have discussed a possibly sub-extensive set of states with low energy in the DKIAFM based on the dumbbell picture, and it is tempting to wonder about a possible connection with our chevrons phase. However, one can easily check that the state in Fig. 4.31c does not match the description in terms of strings of charges given in Sec. 4.1.4, yet it is a low energy state. One can also construct states based on strings of charges which do not respect the chevrons tilings.



Despite being a bit further from the initial motivation which was to study the truncated DKIAFM, we find that the results of the strings phase are particularly interesting: indeed, if one would obtain such strings in an experimental setting, the first intuition might be that one is looking at excitations and that the system has not reached the ground state. Yet, here, the strings of crosses are a fundamental feature of the ground state phase. One should therefore be careful and not immediately interpret the presence of such apparent domain walls as a failure of the system to reach its ground-state manifold.

Let us note that in this chapter we have not discussed detailed tensor network evidence for the existence of algebraic correlations in the various ground-state phases. The essential challenge lies in that the top and bottom leading eigenvectors of the horizontal transfer matrix are not necessarily hermitian conjugates in all of these models (see e.g. [140]), which means that we *a priori* lack a good argument for selecting the correct bottom environment when computing observables in the presence of symmetry breaking. In particular, this is ongoing work for the case of the  $J_1 - J_2$  model. We have checked that the approach works well for the TIAFM and an exactly solvable  $J_1 - J_2$  model [245], and are studying the case of the  $J_1 - J_2$  model with ferromagnetic  $J_2$  interactions which is known to have a long-range-ordered ground state and shows two Kosterlitz-Thouless transitions in accordance with its mapping to the six-state clock model [94, 102, 103, 129]. The case with  $J_2$  antiferromagnetic is expected to have a finite-temperature Kosterlitz-Thouless transition [102]. The main remaining effort in this project is therefore the evaluation of the spin-spin correlations. By computing the stiffness from the spin-spin correlations using the Monte Carlo simulations or the tensor networks, we could probably argue much more strongly for an infinite correlation length.

More generally, if the ground-state manifold is critical, there is the question that one cannot *a priori* distinguish between various scenarios: the existence of a finite-temperature Kosterlitz-Thouless transition, a zero-temperature critical point in the Villain-Stephenson universality class, as in the TIAFM, or even a second-order transition as in the dipolar spin ice where the transition between the two ice regimes is in the Ising universality class [94, 95]. For instance, in the pinwheel phase the existence of a spontaneous translation symmetry breaking could translate in a second-order phase transition at finite-temperature, which would also be interesting to explore.

## Statement of contribution

This chapter corresponds to a work under preparation, resulting from a collaboration between Jeanne Colbois, Bram Vanhecke, Laurens Vanderstraeten, Andrew Smerald, Frank Verstraete and Frédéric Mila.

The Monte Carlo simulations have been implemented and performed by J. C. The tensor network simulations are performed by J. C. using the Ghent Quantum Group implementation of the VUMPS algorithm [148–151]. The ground-state energy lower bounds are studied by J. C. using her own code for the Kanamori approach and the code developed by B. V. for

#### **Chapter 4. Progressive lifting of the KIAFM ground-state degeneracy**

---

Chapter 2 for the Huang approach. Overall the work was performed by J. C. and B. V. in close collaboration, supervised by A. S., L. V. , F. V. and F. M. . The chapter is written by J. C. . The chapter has not yet been shared *in extenso* with all collaborators and any flaw or mistake is due to J. C. .

## 5 Summary and outlook

Although transfer matrices and more recently tensor networks have always been a method of choice for studying two dimensional classical spin systems, in the last few years there seems to have been a regained interest in the topic. This is evidenced by a number of recent examples of application of the tensor network framework to (sometimes long-standing) statistical mechanics problems (selected examples : [125, 127, 129–133, 140, 224, 250–254]). In this sense, the present work is a contribution in a more long-term tendency to establish tensor network methods as extremely useful complementary methods or even stand-alone alternatives to Monte Carlo.

In this thesis, we have introduced a systematic approach to compute the ground-state local rule of frustrated Ising models, which naturally gives rise to contractible tensor networks, providing a direct access to the ground-state properties of finite-range frustrated Ising models. The second part of this thesis has shown how rich the short-range antiferromagnetic Ising models on the kagome lattice are; in multiple occasions we have encountered models where a whole range of values of the first- to third-neighbor couplings (and not just fine-tuned points) correspond to a macroscopically degenerate ground-state phase. In Appendix F we also give an overview of the  $J_1 - J_2 - J_{3\parallel}$  and  $J_1 - J_2 - J_3$  models, where most of the ground-state energies can be established exactly, and where we encounter some additional macroscopically degenerate phases. Our Monte Carlo results in Chapters 2 and 4 as well as the results of Refs. 99, 211, 212, 222 illustrate the challenge of determining the residual entropy via thermodynamic integration: even when the Monte-Carlo update is well-designed and the energy is measured accurately over the whole range of temperatures, it is a considerable investment of resources to evaluate the entropy to the third decimal. To push to higher precision, the model has to be studied extensively to predict the finite-size scaling behavior correctly. By contrast, the tensor network approach gives a direct access to the ground-state properties independently of the finite-temperature behavior, and provides an accurate evaluation of the residual entropy even with somewhat modest bond dimensions. In most phases the results can be obtained down to the fifth decimal without an excessive investment of computational resources: instead of requiring a deep understanding of the model, the evaluation of the residual entropy becomes

a first step that can tell us what properties to look for.

Our approach to the contraction problem of tensor networks for frustrated spin systems seems complementary to the tropical tensor networks approach introduced in Ref. 223, in that our ground-state tiles technique can be applied for the approximate contraction of the TN partition function related to translation-invariant problems while their method is, for now, applicable to exact contraction of finite-size tensor networks related to spin glass models, with random interactions. In the case of very small residual entropies, as we encountered in Chapter 4, one could expect the finite size (order of  $32 \times 32$  for the square lattice Ising model) to play a significant role, just as it does in Monte Carlo. It would be interesting to see if their approach could be adapted to make the most out of the translation invariance.

The first step to build the tensor network is to obtain a ground-state energy lower bound and the corresponding ground-state tiles. This means that we can now make the most of what the tensor network and Monte Carlo algorithms are best at: tensor networks are very powerful to evaluate the leading eigenvalue of the transfer matrix, and Monte Carlo is a great generator of examples. Having access to the ground-state energy lower bound (from the MIN-MAX or the Kanamori approach) means that even a single Monte Carlo sample allows us to get a proof of the ground-state energy. Having access to the ground-state tiles in conjunction with a precise evaluation of the residual entropy means that we can look for exact results such as mappings to the ground-state manifold of the TIAFM; the intuition can be guided by Monte Carlo snapshots even if the simulations fail to equilibrate properly.

We discussed future prospects in the conclusions of the respective Chapters, but there is one more point that we would like to raise. In Chapter 2, we have argued that spurious tiles should be avoided as much as possible. We have seen an example of this in Chapter 4, where in the pinwheels phase the convergence of the VUMPS algorithm is much better when some tiles - which are proven to be spurious - are removed. Interestingly, we have also seen the case of the  $J_1 - J_2$  model where the convergence with the dual construction in Chapter 3 is as good as with the tiles construction in Chapter 4, even though in the former spurious tiles are actually included. This is an observation that we have yet to understand.

In a broader picture, the ground-state rule approach holds a lot of potential. As described in Chapter 2, it gives access to finite-temperature regimes that would not be available using tensor networks in the standard formulation. In the absence of frustration, it is well known that tensor networks can significantly improve results in two-dimensional systems as compared to Monte-Carlo, and we can hope that this will also be the case for frustrated systems. We have an ongoing project to apply the finite-temperature approach on the  $J_1 - J_2$  model on kagome. More generally, it would be interesting to study the nature of the transitions to the  $J_1 - J_2 - J_3$  ground-state phases. We also note that, in the MIN-MAX approach to build ground-state tiles, we do not rely on the fact that the degrees of freedom are Ising in nature, and our method could be applied to frustrated models with higher local degree-of-freedom. In this regard, we also note that the principle of building the tensor such that the ground-state

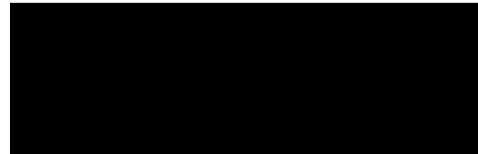
---

rule is correctly encoded was recently extended to solve a frustrated model with continuous degrees-of-freedom, also at finite temperature [224]. Finally, we note that in principle, the ground-state tiles approach is not restricted to two-dimensional problems. In fact, in three-dimensional models where the ground-state local rule was already known, it has been shown in Ref. 140 that tensor networks do provide a very good evaluation of the residual entropy. There is therefore some potential to apply our method to three-dimensional frustrated models, although it would be a technical challenge from the point of view of the bond dimension.

There is a quote from Alan Turing (concluding his paper about the development of artificial intelligence) which, to me, summarizes perfectly what research feels like: “We can only see a short distance ahead, but we can see plenty there that needs to be done” [255]. We have discussed at the end of each Chapter the work that lies ahead – the further development of tensor networks for classical frustrated systems, a more systematic study of chirally coupled artificial spin systems on kagome, the exploration of the phase transitions of farther-neighbor Ising models on the kagome lattice – and, although our plans are of course not as ambitious as those of Alan Turing, hopefully we have convinced the reader that these directions are worth exploring.



## Appendices







# A Complement: Monte Carlo

## A.1 A short introduction to Monte Carlo

In this appendix, we review the basics of the Metropolis-Hastings algorithm. In terms of reference, we especially recommend the lecture notes by M. Troyer [256] for the introduction to importance sampling and error estimations (binning and jackknife analysis). The lecture notes by A. W. Sandvik [221] are also a great introduction to the topic; so is the book of Landau and Binder [257]. For a more mathematical background, we suggest the book by M. Benaïm and N. El Karoui [258] (in French).

### A.1.1 Markov Chain Monte Carlo methods

The Metropolis-Hastings algorithm is an example of a Markov Chain Monte Carlo (or MCMC) method. Therefore, we start by giving some definitions and properties related to Markov chains. There can be some variation in the precise definition depending on the type of stochastic processes that are considered, but for this thesis we will consider the following. First, we are interested in discrete time and discrete space stochastic processes: a set of random variables  $X_t$  defined over the discrete probability space  $E$  and that are indexed by the discrete time  $t$ . A Markov chain is a particular kind of stochastic process that satisfies the “Markov property”, namely, it is memoryless. This property states that the conditional probability distribution of the future states of the process, instead of depending on all the history of the process, is only dependent on the current state:

$$\mathcal{P}(X_{t+1} = j | X_t = i_t, \dots, X_0 = i_0) = \mathcal{P}(X_{t+1} = j | X_t = i_t) \quad (\text{A.1})$$

To describe Markov chains it is useful to introduce the transition probability from state  $i$  to state  $j$ :

$$p_{ij}^t := \mathcal{P}(X_{t+1} = j | X_t = i) \quad (\text{A.2})$$

which describes the probability of going from a state  $i$  to a state  $j$  and in principle can depend on time. If this transition probability does not depend on time, namely, for any initial

distribution  $\mu$ :

$$\mathcal{P}(X_{n+1} = j | X_n = i) = \mathcal{P}(X_n = j | X_{n-1} = i), \quad (\text{A.3})$$

then the Markov chain is said to be time homogeneous. For the rest of this discussion we only consider time homogeneous Markov chains. We can gather the transition probabilities of the Markov chain in a transition matrix  $P = (p_{ij})_{(i,j) \in E^2}$  which, together with the initial distribution  $\mathcal{P}(X_0 = i_0)$ , characterizes the Markov chain. Indeed:

$$\mathcal{P}(X_0 = i_0, X_1 = i_1, \dots, X_n = i_n) = \mathcal{P}(X_0 = i_0) p_{i_0 i_1} p_{i_1 i_2} \dots p_{i_{n-1} i_n}. \quad (\text{A.4})$$

**Stationary distribution.** We consider a subspace  $E$  of states, and a transition matrix  $P$  defining a Markov chain on  $E$ . A measure  $\pi = \{p_i\}_{i \in E}$  is a stationary measure of the Markov chain defined by  $P$  over  $E$  if it is an eigenfunction of  $P$  with eigenvalue one. If  $\pi$  is a distribution, namely  $\pi_i \geq 0 \forall i \in E$  and  $\sum_{i \in E} \pi_i = 1$ , then  $\pi$  we call it a stationary distribution of the Markov chain.

The purpose of Monte Carlo Markov chain algorithms is to design a transition matrix  $P$  for a homogeneous Markov chain such that the distribution  $\pi$  that we want to sample is the stationary distribution of  $P$ , namely

$$P^k \mu \xrightarrow[k \rightarrow \infty]{} \pi. \quad (\text{A.5})$$

The ergodic theorem states that if the transition matrix  $P$  is irreducible aperiodic and positive recurrent, the unicity of the limiting distribution  $\pi$  and the independence of  $\pi$  on  $\mu$  is guaranteed. It is in spirit a Perron-Frobenius theorem for stochastic matrices.

### A.1.2 Metropolis-Hastings algorithm

One way of generating a Markov chain with stationary distribution  $\pi$  when this distribution is known up to a multiplicative constant is to implement the Metropolis-Hastings algorithm. The basis of this approach is the detailed balance principle, which is a sufficient but not necessary way to ensure the convergence of the Markov chain and the unicity of its stationary distribution<sup>1</sup>. The detailed balance equation describes the fact that the probability of being in state  $x$  and going to state  $x'$  should be the same as the probability of being in state  $x'$  and going to state  $x$  in one step:

$$\pi(x)P(x'|x) = \pi(x')P(x|x'). \quad (\text{A.6})$$

The key idea behind the algorithm is the splitting of the process of going from state  $x$  to state  $x'$  into two steps: first, the selection of a candidate  $x'$  with a *selection* probability  $g(x'|x)$ <sup>2</sup> and

---

<sup>1</sup>More precisely, the transition matrix  $P$  that we give below is reversible for  $\pi$ , is irreducible if the selection matrix is irreducible, and if the acceptance probability  $A < 1$ , it is aperiodic.

<sup>2</sup>corresponding to the selection matrix  $Q$ .

second, the acceptance or rejection of this candidate with an *acceptance* probability  $A(x'|x)$ :

$$P(x'|x) = \begin{cases} g(x'|x) A(x'|x) & \text{if } x' \neq x \\ 1 - \sum_{y \neq x} P(y|x) & \text{if } x' = x \end{cases}. \quad (\text{A.7})$$

In practice, this means that the algorithm unfolds as:

1. If  $n = 0$  : Initialize the state  $x_0$
2. At step  $n$  : Generate  $y_{n+1}$  with law  $g(y_{n+1}|x_n)$
3. Select a number  $a$  in  $[0, 1]$  randomly with uniform probability
4. If  $a < A(y_{n+1}|x_n)$  : accept the selected value and set  $x_{n+1} = y_{n+1}$ . Else, reject the value :  $x_{n+1} = x_n$ . Go to 2.

The key point is therefore to find  $A$  and  $g$  such that  $P$  satisfies Eq. A.6. We must have  $g(x|y) > 0 \Rightarrow g(y|x) > 0$ , and therefore we can rewrite the detailed balance equation as:

$$\frac{A(x'|x)}{A(x|x')} = \frac{\pi(x')}{\pi(x)} \frac{g(x|x')}{g(x'|x)} \quad (\text{A.8})$$

Given  $\pi$  and  $g$ , the general way of building  $A$  to satisfy the detailed balance is to build a function  $F : ]0, \infty[ \rightarrow ]0, 1]$  which is such that

$$F(u) = u F\left(\frac{1}{u}\right). \quad (\text{A.9})$$

For instance:  $F(u) = \min(1, u)$ . Constructing

$$A(x'|x) = \begin{cases} F\left(\frac{\pi(x')}{\pi(x)} \frac{g(x|x')}{g(x'|x)}\right) & \text{if } g(x'|x) \neq 0 \\ 0 & \text{otherwise} \end{cases} \quad (\text{A.10})$$

ensures that the detailed balance equation is satisfied.

### A.1.3 Applications of the Metropolis-Hastings algorithm

Here, we give two examples of algorithms based on the Metropolis-Hastings algorithms, which are relevant in this thesis.

#### The single-spin-flip algorithm

This is the most well-known algorithm for the study of at-equilibrium thermodynamics of spin systems. The states are sampled based on their Boltzmann weights  $\pi(\vec{\sigma}) = \frac{1}{Z} e^{-\beta E(\vec{\sigma})}$  where  $Z$  is the partition function (we work with  $k_B = 1$  and therefore  $\beta = \frac{1}{T}$ ). Considering a system of  $N$

spins on a lattice, the selection distribution is:

$$g(\vec{\sigma}'|\vec{\sigma}) = \begin{cases} 1/N & \text{if } \vec{\sigma} \text{ and } \vec{\sigma}' \text{ differ by a single spin flip,} \\ 0 & \text{otherwise} \end{cases} \quad (\text{A.11})$$

Notice that  $g(\vec{\sigma}'|\vec{\sigma}) = g(\vec{\sigma}|\vec{\sigma}')$  in this case. The acceptance probability is then chosen as

$$A(\vec{\sigma}'|\vec{\sigma}) = \min\left(1, \frac{\pi(\vec{\sigma}')}{\pi(\vec{\sigma})}\right) = \min\left(1, e^{-\beta(E(\vec{\sigma}')-E(\vec{\sigma}))}\right). \quad (\text{A.12})$$

### Parallel tempering

An easy way to avoid thermalization issues at low temperature that can arise in the single-spin-flip algorithm is the parallel tempering approach. It relies on simulating simultaneously (in parallel) a number of systems in a range of temperatures, and periodically propose to swap two states at neighboring temperatures. This respects the detailed balance of the ensemble of walkers (see e.g. [259] and references therein)

At a given step:

$$g(\vec{\sigma}'|\vec{\sigma}) = \begin{cases} 1 & \text{if } \vec{\sigma} \text{ and } \vec{\sigma}' \text{ are states in neighboring temperature threads,} \\ 0 & \text{otherwise.} \end{cases} \quad (\text{A.13})$$

In this case, we have to consider the joint distributions of the states in the two different temperature threads  $\beta_a, \beta_b$  to compute the acceptance probability:

$$A(x' = (\vec{\sigma}_2, \vec{\sigma}_1) | x = (\vec{\sigma}_1, \vec{\sigma}_2)) = \min\left\{1, e^{(\beta_a - \beta_b)(E(\vec{\sigma}_1) - E(\vec{\sigma}_2))}\right\}. \quad (\text{A.14})$$

#### A.1.4 Computing the residual entropy via thermodynamic integration

The specific heat per site  $c$  is computed using the variance of the energy as described above, and the residual entropy per site is obtained from thermodynamic integration as:

$$S = \ln 2 - \int_0^\infty \frac{c}{T} dT. \quad (\text{A.15})$$

Alternatively, the residual entropy is computed from a thermodynamic integration of the energy [211]. At inverse temperature  $\beta$ , one has:

$$S(\beta) = \ln(2) + \beta E(\beta) - \int_0^\beta E(\beta') d\beta', \quad (\text{A.16})$$

where here  $E$  stands for the energy per site. We typically compute both estimates to ensure that they agree.

## A.2. Probability table, zero-bounce and one-bounce solutions

Note that in practice, we integrate numerically up to some maximal temperature  $T_{\max}$ . For the temperatures from  $T_{\max}$  to infinity, one can compute the behavior of the specific heat from a high-temperature expansion. It is fairly easy to show that the first relevant term is

$$c_{\text{High T}} = \beta^2 \sum_k z_k J_k^2 \quad (\text{A.17})$$

where  $z_k$  is the number of couplings of type  $k$  per site, allowing an easy evaluation of the integral from  $T_{\max}$  to infinity.

## A.2 Probability table, zero-bounce and one-bounce solutions

In this section we describe the construction of the probability table  $T_{b^{(k)}, b^{(k+1)}}^{v^{(k)}}$  that plays an essential role for imposing the detailed balance condition in the construction of the worm. It describes the probability for the worm to exit on bond  $b^{(k+1)}$  when it arrives to  $v^{(k)}$  from  $b^{(k)}$  (Fig. 1.3b, Alg. 1 line 12). Defining the Boltzmann weight of the dimer configuration before flipping the dimer variable on bonds  $b^{(k)}$  and  $b^{(k+1)}$  as  $\mathcal{W}_{b^{(k)}}^{v^{(k)}}$ , and that of the dimer configuration after flipping as  $\mathcal{W}_{b^{(k+1)}}^{v^{(k+)}}$ , at the probabilistic step  $k$  of the worm construction, the local detailed balance equation has to take the form:

$$\mathcal{W}_{b^{(k)}}^{v^{(k)}} T_{b^{(k)}, b^{(k+1)}}^{v^{(k)}} = \mathcal{W}_{b^{(k+1)}}^{v^{(k+)}} T_{b^{(k+1)}, b^{(k)}}^{v^{(k+)}} \quad (\text{A.18})$$

imposing that the probability to be in a configuration and flip both dimers must be the same as the probability to be in the resulting configuration and flip back both dimers. Clearly, the weights  $\mathcal{W}$  in Eq. A.18 only differ by a few factors depending on the configuration of dimers in a small neighborhood around the vertex  $v^{(k)}$ . The local detailed balance can be rewritten

$$w_{b^{(k)}}^{v^{(k)}} T_{b^{(k)}, b^{(k+1)}}^{v^{(k)}} = w_{b^{(k+1)}}^{v^{(k+)}} T_{b^{(k+1)}, b^{(k)}}^{v^{(k+)}} \quad (\text{A.19})$$

with the renormalized weights  $w_{b^{(k)}}^{v^{(k)}}$  only containing the relevant factors: denoting  $\gamma^{(k)}$  the set of three nearest-neighbor bonds of the direct lattice surrounding  $v^{(k)}$  and  $d^{(k)}$  ( $d^{(k+1)}$ ) the dimer configuration before (after) flipping, we can write

$$\begin{aligned} w_{b^{(k)}}^{v^{(k)}} = & \prod_{\substack{\Gamma_1 \text{ s.t.} \\ \Gamma_1 \cap \gamma^{(k)} \neq \emptyset}} \left( e^{-\beta J_1 d_{b_{\Gamma_1}}^{(k)}} \right) \prod_{\substack{\Gamma_2 \text{ s.t.} \\ \Gamma_2 \cap \gamma^{(k)} \neq \emptyset}} \left( e^{-\beta J_2 \left( \prod_{a \in \Gamma_2} d_{b_a}^{(k)} \right)} \right) \\ & \cdot \prod_{\substack{\Gamma_{3||} \text{ s.t.} \\ \Gamma_{3||} \cap \gamma^{(k)} \neq \emptyset}} \left( e^{-\beta J_{3||} \left( \prod_{a \in \Gamma_{3||}} d_{b_a}^{(k)} \right)} \right) \prod_{\substack{\Gamma_{3\star} \text{ s.t.} \\ \Gamma_{3\star} \cap \gamma^{(k)} \neq \emptyset}} \left( e^{-\beta \frac{J_{3\star}}{2} \left( \prod_{a \in \Gamma_{3\star}} d_{b_a}^{(k)} \right)} \right) \end{aligned} \quad (\text{A.20})$$

(and similarly for  $w_{b^{(k+1)}}^{v^{(k+)}}$ , with  $d^{(k)} \rightarrow d^{(k+1)}$ ). The set of dual bonds playing a role in this local weight is denoted as  $l(v)$  and illustrated in Fig. 1.4 for our case. The probability table therefore only depends on this local configuration of dimers on the dual bonds around vertex  $v^{(k)}$ . We can take some convention clarifying that the probability table does not depend on the actual

## Appendix A. Complement: Monte Carlo

---

vertex but only on the local configuration  $\vec{d}_{l(v)}$  and the entry and exit bonds. One can rewrite the weights and the probability table

$$W_i^{l(v)} := w_{b^{(k)}}^{v^{(k)}}, \quad W_j^{l(v)} := w_{b^{(k+1)}}^{v^{(k)}} \text{ and } Tas_{i,j}^{l(v)} = T_{b^{(k)}, b^{(k+1)}}^{v^{(k)}} \quad (\text{A.21})$$

if  $b^{(k)}$  ( $b^{(k+1)}$ ) is the  $i^{\text{th}}$  ( $j^{\text{th}}$ ) neighbor<sup>3</sup> of  $v^{(k)}$ . Taking the usual approach [172, 173] and defining

$$A_{i,j}^{l(v)} := W_i^{l(v)} M_{i,j}^{l(v)} \quad (\text{A.22})$$

a three-by-three matrix (no Einstein summation), the local detailed balance Eq. A.19 and the constraint  $\sum_{j=0}^2 T_{b^{(k)}, b_j}^{v^{(k)}} = 1$  become

$$A_{i,j}^{l(v)} = A_{j,i}^{l(v)} \quad \text{with the constraints } \sum_j A_{i,j}^{l(v)} = W_i^{l(v)}. \quad (\text{A.23})$$

These equations, together with the fact that we want to minimize the bounce weights  $M_{i,i}^{l(v)}$  can be rewritten as a linear program (for readability, the index  $l(v)$  is omitted)

$$\min A_{0,0} + A_{1,1} + A_{2,2} \quad \text{with} \quad \begin{cases} A_{i,j} = A_{j,i} \\ \sum_j A_{i,j} = W_i \\ A_{i,j} \geq 0 \forall i, j \end{cases} \quad (\text{A.24})$$

There are two types of solutions, depending on the value of the maximum of the three weights  $W_0, W_1, W_2$ . The zero-bounce solution reads:

$$A_{i,i} = 0 \quad \forall i \quad \text{and} \quad A_{i,j} = \frac{W_i + W_j - |\epsilon_{ijk} W_k|}{2} \quad \forall i \neq j \quad (\text{A.25})$$

(with  $\epsilon_{ijk}$  is the Levi-Civita symbol). Such a solution only exists as long as

$$W_\Lambda \leq W_{\lambda_1} + W_{\lambda_2} \quad (\text{A.26})$$

where  $W_\Lambda$  is the maximum of the weights and  $W_{\lambda_1}, W_{\lambda_2}$  are the two other weights<sup>4</sup>.

If

$$W_\Lambda > W_{\lambda_1} + W_{\lambda_2}, \quad (\text{A.27})$$

it is easy to check that there is no solution such that  $A_{\Lambda,\Lambda} = 0$ . However, this bounce probability can be minimized by the one-bounce solution

$$A_{\lambda_i,\Lambda} = W_{\lambda_i}, \quad A_{\lambda_1,\lambda_2} = A_{\lambda_i,\lambda_i} = 0 \quad (i \in \{1,2\}), \quad \text{and} \quad A_{\Lambda,\Lambda} = W_\Lambda - W_{\lambda_1} - W_{\lambda_2}. \quad (\text{A.28})$$

---

<sup>3</sup>There are various possible conventions for the selection of  $i$  and  $j$ : for creating a lookup table, it is practical to number the bonds around a vertex  $v$  in a systematic way, while for computing the table during the execution of the algorithm, it is more practical to select  $i = 0$  as the entry bond and  $i = 1, 2$  as the two exit bonds.

<sup>4</sup>If  $W_\Lambda > W_{\lambda_1} + W_{\lambda_2}$ , Eq. A.25 implies  $A_{\lambda_1,\lambda_2} < 0$ , and is therefore not a solution.

### A.3. Proof of detailed balance for Alg. 1 and dealing with periodic boundary conditions

All possible cases for the weights can be dealt with using the zero and the one-bounce solutions. We finally obtain the probability table as  $T_{i,j}^{l(v)} = A_{i,j}^{l(v)} / W_i^{l(v)}$ .

### A.3 Proof of detailed balance for Alg. 1 and dealing with periodic boundary conditions

We give the proof of detailed balance for Alg. 1 following Refs. 114, 164, 260, 261, and discuss the treatment of periodic boundary conditions.

The probability of creating a *particular* worm bringing an initial dimer configuration  $\vec{d}^i$  to a final dimer configuration  $\vec{d}^f$  is

$$g_w(\vec{d}^f | \vec{d}^i) = \frac{1}{6} T_{b^{(1)}, b^{(2)}}^{v^{(1)}} \frac{1}{5} T_{b^{(2)}, b^{(3)}}^{v^{(2)}} \cdots \frac{1}{5} T_{b^{(n-1)}, b^{(n)}}^{v^{(n)}}, \quad (\text{A.29})$$

with  $n$  the length of the worm. The probability of generating the reverse worm to bring  $\vec{d}^f$  to  $\vec{d}^i$  is

$$g_w(\vec{d}^i | \vec{d}^f) = \frac{1}{6} T_{b^{(n)}, b^{(n-1)}}^{v^{(n)}} \frac{1}{5} T_{b^{(n-1)}, b^{(n-2)}}^{v^{(n-1)}} \cdots \frac{1}{5} T_{b^{(2)}, b^{(1)}}^{v^{(1)}}. \quad (\text{A.30})$$

Using the initial and final weights

$$\mathcal{W}_{b^{(1)}}^{v^{(1)}} = \mathcal{W}(\vec{d}^i) \quad \text{and} \quad \mathcal{W}_{b^{(n)}}^{v^{(n)}} = \mathcal{W}(\vec{d}^f), \quad (\text{A.31})$$

the relation

$$\mathcal{W}_{b^{(k+1)}}^{v^{(k)}} = \mathcal{W}_{b^{(k+1)}}^{v^{(k+1)}}, \quad (\text{A.32})$$

and the local detailed balance Eq. A.18, we obtain

$$\begin{aligned} \mathcal{W}(\vec{d}^i) g_w(\vec{d}^f | \vec{d}^i) &= \mathcal{W}_{b^{(1)}}^{v^{(1)}} \frac{1}{6} T_{b^{(1)}, b^{(2)}}^{v^{(1)}} \frac{1}{5} T_{b^{(2)}, b^{(3)}}^{v^{(2)}} \cdots \frac{1}{5} T_{b^{(n-1)}, b^{(n)}}^{v^{(n)}} \\ &= \frac{1}{6} T_{b^{(2)}, b^{(1)}}^{v^{(1)}} \mathcal{W}_{b^{(2)}}^{v^{(1)}} \frac{1}{5} T_{b^{(2)}, b^{(3)}}^{v^{(2)}} \cdots \frac{1}{5} T_{b^{(n-1)}, b^{(n)}}^{v^{(n)}} \\ &= \frac{1}{6} T_{b^{(2)}, b^{(1)}}^{v^{(1)}} \frac{1}{5} \mathcal{W}_{b^{(2)}}^{v^{(2)}} T_{b^{(2)}, b^{(3)}}^{v^{(2)}} \cdots \frac{1}{5} T_{b^{(n-1)}, b^{(n)}}^{v^{(n)}} \\ &\quad \dots \\ &= \frac{1}{6} T_{b^{(2)}, b^{(1)}}^{v^{(1)}} \frac{1}{5} T_{b^{(2)}, b^{(3)}}^{v^{(2)}} \cdots \frac{1}{5} T_{b^{(n-1)}, b^{(n-2)}}^{v^{(n-1)}} \frac{1}{5} T_{b^{(n)}, b^{(n-1)}}^{v^{(n)}} \mathcal{W}_{b^{(n)}}^{v^{(n)}} \\ &= \frac{1}{6} T_{b^{(n)}, b^{(n-1)}}^{v^{(n)}} \frac{1}{5} T_{b^{(n-1)}, b^{(n-2)}}^{v^{(n-1)}} \cdots \frac{1}{5} T_{b^{(2)}, b^{(1)}}^{v^{(1)}} \mathcal{W}(\vec{d}^f) \\ &= g_w(\vec{d}^i | \vec{d}^f) \mathcal{W}(\vec{d}^f). \end{aligned} \quad (\text{A.33})$$

This proves the detailed balance for one particular worm construction. The probability of going from  $\vec{d}^i$  to  $\vec{d}^f$  in a single worm update reads

$$P(\vec{d}^f | \vec{d}^i) = \sum_w g_w(\vec{d}^f | \vec{d}^i), \quad (\text{A.34})$$

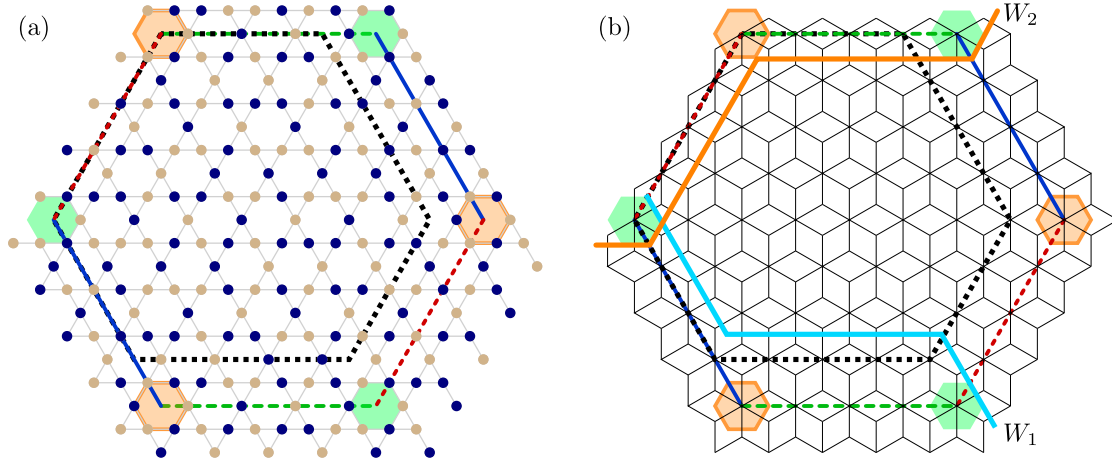


Figure A.1 – Periodic boundary conditions and reference lines for the winding numbers. (a) An instance of a spin configuration is plotted. The lines of the same color (blue, red, green) correspond to the periodic boundary conditions; the highlighted hexagons help to visualize the periodic boundary conditions. In practice, we only plot the configuration of spins on the hexagons in the area surrounded by the black dashed line. (b) The same periodic boundary conditions shown on the dice lattice. The lines  $W_1$  and  $W_2$  wind the torus in opposite directions and are used as reference lines for counting the winding numbers of the worm updates.

where the sum is over all possible worms bringing  $\vec{d}^i$  to  $\vec{d}^f$  (remember that the acceptance probability is set to one). This gives

$$\begin{aligned}
 \mathcal{W}(\vec{d}^i) P(\vec{d}^f | \vec{d}^i) &= \sum_w \mathcal{W}(\vec{d}^i) g_w(\vec{d}^f | \vec{d}^i) \\
 &= \sum_w g_w(\vec{d}^i | \vec{d}^f) \mathcal{W}(\vec{d}^f) \\
 &= P(\vec{d}^i | \vec{d}^f) \mathcal{W}(\vec{d}^f),
 \end{aligned} \tag{A.35}$$

which proves detailed balance for the dimer model updates.

As we discussed in Sec. 1.1, having periodic boundary conditions in the spin model (Fig. A.1) creates an additional constraint, and the only valid dimer configurations are those for which any torus-winding loop in the spin model crosses an even number of empty dual bonds. The initial configuration  $\vec{d}^i$ , which is obtained from an initial spin configuration, satisfies those constraints automatically, but after a worm update, the final configuration  $\vec{d}^f$  might not satisfy them anymore. Since the *parity* of the number of empty dual bonds in a given direction on the torus only depends on the number of times the worm update winds the torus in the other direction, it is sufficient to know the parity of the winding number of the worm update in each direction to decide whether the final configuration  $\vec{d}^f$  is valid. In Fig. A.1a, we illustrate our choice of periodic boundary conditions, and in Fig. A.1b, we illustrate the two winding directions taken into account when checking the winding number of the worm updates.



A first possibility would be to simply reject worm updates which have an odd winding number, and repeat the previous configuration in the Monte Carlo chain [114, 164]. An alternative approach [260, 261] is to keep the illegal worm updates and build additional updates until the total winding number parity is even in both directions. That this creates an ergodic Markov Chain is proven in Ref. 261 and rests upon the following result (see Refs. 261, 262 for a rigorous formulation and a proof):

Let  $P$  be an irreducible transition matrix on a finite state space  $\mathcal{S}$  with stationary distribution  $\pi$ . Define a new Markov chain by only observing the original chain corresponding to  $P$  when it visits a state in  $S \in \mathcal{S}$ . The new chain is an irreducible Markov chain on  $S$  with stationary distribution

$$\bar{\pi}_s = \frac{\pi_s}{\sum_{s' \in S} \pi_{s'}}, \quad s \in S. \quad (\text{A.36})$$

Here, the state space  $\mathcal{S}$  is the space of generalized dimer configurations having either odd or even parity of the winding numbers in each direction, while  $S$  is the “quadrant” with even parity in both direction, corresponding to periodic boundary conditions. Since the Boltzmann weight of the dimer configurations in this quadrant match those of the corresponding spin configurations, the distribution obtained by never rejecting updates and only observing the Markov Chain when the dimer configuration respects the winding number constraints does correspond to the target distribution.

## A.4 Monte Carlo parameters

### A.4.1 Monte Carlo simulations parameters and remarks for Chapter 2

For the Monte Carlo simulations, as a complement to the standard single spin flip update which is rapidly failing, we use a dual worm algorithm based on Ref. 114 as detailed in Chapter 1, Sec. 1.2, as well as parallel tempering (also known as temperature replica method). For this, we use 216 walkers with a temperature associated to each walker. In a given Monte Carlo step, we first update each state with twice as many single spin flip attempts as there are sites in the system; then we perform worm updates until the total length of the worms corresponds to twice the number of dual sites of the system (see below); finally, we make a parallel tempering step. At each step, detailed balance is respected.

These features of the Monte Carlo simulations allow one to reach the ground states. This is verified by computing the expectation value of the energy at the lowest temperature and checking that it is systematically within  $10^{-9}$  of the exact ground state energies.

For each size, 16 independent runs are performed (for each run, 16'384 thermalization steps are followed by 1'048'576 measurement steps).

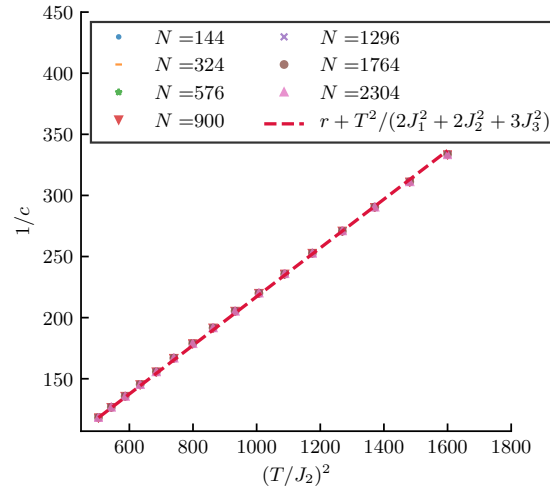


Figure A.2 – Comparison of the specific heat near the maximal temperature, and the high temperature expansion. The constant offset  $r \cong 18$  corresponds to a correction of order  $\beta^4$  in the high temperature expansion, whose contribution to the entropy is negligible.

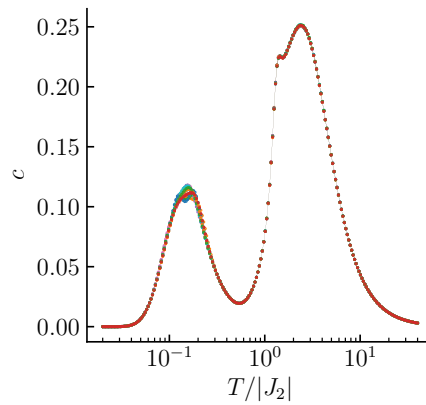


Figure A.3 – Specific heat for independent runs. In the lower heap, the various runs do not agree (simulations for  $L = 12$ ).

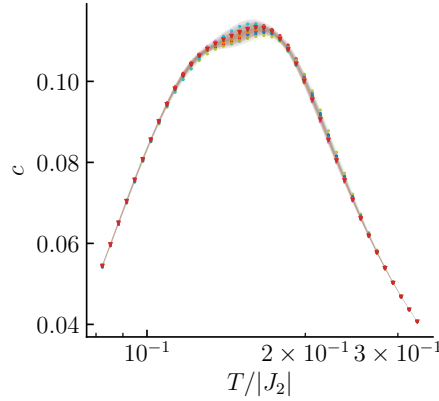


Figure A.4 – Performing a bootstrap analysis, the various averages of the runs agree within errorbars (zooming in on the heap at lower temperature for  $L = 12$ ).

The specific heat in the lowest heap shows a dependence on the run for large sizes (Fig. A.3). This is compensated for by taking the average over the 16 simulations. By a bootstrap analysis, we show that the errorbars obtained from merging the 16 independent simulations are reasonable (Fig. A.4). The errorbars on the specific heat (2 standard deviations) are used to give errorbars on the residual entropy by integrating the smallest, respectively the largest possible value of the specific heat over  $T$  at any temperature.

In practice, we simulate the system only until  $T_{\max}/|J_2| = 40$ . Plotting  $1/c$  as a function of  $T^2$ , we can check that at  $T \cong T_{\max}$  the first order term in Eq. A.17 already captures the behavior very well, Fig. A.2). The integral for the specific heat contribution is obtained as

$$\int_{T_{\max}}^{\infty} \frac{c}{T} dT \cong 1.568 \cdot 10^{-4}. \quad (\text{A.37})$$

The specific heat in the lowest heap shows a dependence on the run for large sizes (Fig. A.3). This is compensated for by taking the average over the 16 simulations. By a bootstrap analysis, we show that the errorbars obtained from merging the 16 independent simulations are reasonable (Fig. A.4). The errorbars on the specific heat (2 standard deviations) are used to give errorbars on the residual entropy by integrating the smallest, respectively the largest possible value of the specific heat over  $T$  at any temperature. Finally, we note that the residual entropy can alternatively be computed by integrating over the energy (see e.g. Ref. 263 and references therein). We did this and kept only those sizes for which the simulations had been ran long enough that the two ways of computing the residual entropy would agree within errorbars.

This model seems to have extremely strong, hard to characterize finite-size effects. We show the residual entropy as a function of the inverse of  $N$ , the number of spins, and of  $L$ , the linear

system size, in Fig. 2.12. Justifying finite-size corrections is a challenge, that often requires a prior understanding of the ground state phase, and here we only show these two graphs as a guide to the eye. The extrapolation as a function of  $1/N$  would seem to work best, at least compared to the tensor network result. However, the slope of  $S(N)$  would indicate a huge prefactor to the number of ground states that we cannot explain. The extrapolation in  $1/L$  would seem most plausible based on the observation that the type-II tiles form domain walls, especially since they are irrelevant to the extensive entropy. But the extrapolation in  $1/L$  doesn't look too convincing and would dramatically underestimate the lower bound of  $S = \frac{1}{3} S_{\text{TLLAF}}$ . To solve this problem, one would need to study even larger system sizes, which turns out to be very difficult with MC, at least with our algorithm.

### A.4.2 Monte Carlo simulations parameters for Chapter 3

The Monte Carlo simulations algorithms depend on the problems we are studying. In zero field, we use the algorithm of Rakala and Damle [114], which consists in mapping spin configurations to dimer configurations on the dual (dice) lattice, and building loop updates in this dual space which respect local detailed balance and can thus be accepted once they close. In the presence of a field, the dual updates are typically rejected, and we resort to a simpler single-spin-flip update. This is, however, not sufficient, as those updates are typically rejected at low temperature. To alleviate the problem, we use replicas in field and in temperature (known as parallel tempering in the case of the replicas in temperature) [239, 264, 265]. When we cannot compare to the tensor networks results, the simulations are always completed for a number of sizes until convergence, and for at least two independent runs for each size. The correlations are always computed as an average over the sample, and then an ensemble average over the set of measurements. The errors are estimated from a binning analysis [266]. Each Monte Carlo step (MCS) consists of  $(N_{\text{spin}}, N_{\text{worm}}, N_{\text{rep}})$  single spin flip, worm and replica updates. The parameters for the various Figures are as follows:

1. Fig. 3.8 :  $(8N_{\text{sites}}, 8N_{\text{sites}}, 1)$ ; thermalization - 1024 MCS, measurements - 16384 spaced by 3 MCS;
2. Fig. 3.14 :  $(8N_{\text{sites}}, 8N_{\text{sites}}, 1)$ ; thermalization - 1024 MCS, measurements - 16384 spaced by 3 MCS;
3. Figs. 3.16 and 3.15 :  $(4N_{\text{sites}}, 4N_{\text{sites}}, 1)$ ; thermalization - 4096 MCS, measurements - 32768 spaced by 8 MCS;
4. Fig. 3.17 :  $(4N_{\text{sites}}, 4N_{\text{sites}}, 1)$ ; thermalization - 4096 MCS, measurements - 8192 spaced by 8 MCS;
5. Fig. 3.20  $(4N_{\text{sites}}, 0, 1)$  : thermalization - 262144 MCS, measurements - 16384 spaced by 16 MCS (except for the  $1/3$  plateau, see parameters for Figs. 3.23 and 3.22).

6. Figs. 3.21 and E.3 :  $(4N_{\text{sites}}, 4N_{\text{sites}}, 1)$ ; thermalization - 16384 MCS, measurements - 32768 spaced by 8 MCS;
7. Figs. 3.22, 3.23 and 3.25:  $(4N_{\text{sites}}, 0, 1)$ : thermalization - 65536 MCS, measurements - 8192 spaced by 8 MCS;
8. Fig. 3.26 :  $(4N_{\text{sites}}, 0, 1)$ : thermalization - 65536 MCS, measurements - 8192 spaced by 8 MCS



## B Complement: tensor networks

## B.1 Introduction to uniform MPSs

In the most general case, we describe a vector (or, in the quantum case, a state)  $|\phi\rangle \in \otimes_j \mathbb{C}^d$ , where  $j$  indexes the sites of the one-dimensional lattice, and  $d$  is the dimension of the (Hilbert) space on each site:

$$|\phi\rangle = \sum_{\{s_i\}} \phi_{\dots, s_{j-1}, s_j, s_{j+1}, \dots} |\dots, s_{j-1}, s_j, s_{j+1}, \dots\rangle \quad (\text{B.1})$$

as a tensor:

$$\begin{array}{c} \overline{\hspace{10em}} \\ \begin{array}{ccccccc} & & & \phi & & & \\ & & & | & & & \\ \dots & | & & | & & | & \dots \\ & s_{j-1} & & s_j & & s_{j+1} & \end{array} \end{array} \quad (\text{B.2})$$

### Single site unit cell

We introduce the uniform matrix product state (MPS) Ansatz as an approximation of such a tensor. For a thorough introduction, we refer the reader to the 2019 lecture notes by Vanderstraeten et al. [150] and references therein. Since we want to be able to work in the thermodynamic limit, we need an Ansatz that is translation invariant. One way to build such an Ansatz is to approximate  $|\phi\rangle$  by a *state*  $|\psi(A)\rangle$  defined as a *uniform product* of a single three-legged tensor  $A_{\alpha_i, \alpha_{i+1}}^{s_j}$  repeated on every site in the lattice:

$$|\psi(A)\rangle := \cdots \text{---} \boxed{A} \text{---} \boxed{A} \xrightarrow{\alpha_j} \underset{s_j}{\boxed{A}} \xrightarrow{\alpha_{j+1}} \boxed{A} \text{---} \boxed{A} \text{---} \cdots, \quad (\text{B.3})$$

hence the name “uniform MPS”. Here we slightly misusing the notation since the tensor product represents the matrix of coefficients as in Eq. B.1 and not the state directly. In this construction, the tensor  $A_{\alpha_j, \alpha_{j+1}}^{s_j}$  can be thought of as a map  $A: \mathbb{C}^\chi \otimes \mathbb{C}^\chi \rightarrow \mathbb{C}^d$  from the virtual space labeled by  $\alpha_j, \alpha_{j+1}$  to the physical space labeled by  $s_j$ . The dimension  $\chi$  of the virtual space is called the *bond dimension* and will be the parameter for refining the Ansatz.

When one studies quantum problems, or classical problems with symmetric row-to-row

## Appendix B. Complement: tensor networks

transfer matrices, an extremely useful object to consider is the transfer matrix

$$E := \begin{array}{c} \boxed{A} \\ | \\ \boxed{A^*} \end{array}, \quad (\text{B.4})$$

which corresponds to the contraction of  $A$  with its conjugate on the physical index, resulting in an operator on the space of  $\chi \times \chi$  matrices. This transfer matrix is not necessarily hermitian; yet, in the generic case<sup>1</sup>, it has a non-degenerate leading eigenvalue  $\lambda_0$ . Considering MPSs for which the leading eigenvalue is non-degenerate is essentially equivalent to requiring that the MPS be injective, namely that there must exist an  $L$  such that the set of matrices  $\{A^{s_1} \cdots A^{s_L} | 1 \leq s_1, \dots, s_L \leq d\}$  spans the space of  $\chi \times \chi$  matrices<sup>2</sup>. In the following we assume that this condition is satisfied, in which case the leading eigenvalue  $\lambda_0$  of this transfer matrix is also positive<sup>3</sup>. Let us consider the associated left and right eigenvectors:

$$\begin{array}{c} \textcircled{l} \\ | \\ \boxed{A} \\ | \\ \boxed{A^*} \end{array} = \lambda_0 \textcircled{l} \quad \begin{array}{c} \boxed{A} \\ | \\ \boxed{A^*} \\ | \\ \textcircled{r} \end{array} = \lambda_0 \textcircled{r}. \quad (\text{B.6})$$

They are not necessarily equal to each other. When viewing  $l$  and  $r$  as  $\chi \times \chi$  matrices, they are Hermitian by construction, and furthermore are positive semi-definite [184]. In the quantum case we typically normalize  $A \rightarrow A/\sqrt{\lambda_0}$ .

$A$  defines  $|\psi(A)\rangle$  uniquely, but the converse is not true, since the transformation

$$\text{triangle}_{A_L} = \textcircled{L} - \boxed{A} - \textcircled{L^{-1}}, \quad (\text{B.7})$$

does not change the state in Eq. B.3. In particular, we can make the practical choice of selecting  $L$  such that  $l = L^\dagger L$  which implies (remember that we have normalized  $A$  such that the leading eigenvalue is one):

$$\begin{array}{c} \text{triangle}_{A_L} \\ | \\ \text{triangle}_{A_L^*} \end{array} = \left( \begin{array}{c} \text{---} \\ \text{---} \end{array} \right). \quad (\text{B.8})$$

An MPS in this form is said to be left-orthonormal, or to be in the left gauge. Similarly, we can

<sup>1</sup>By generic, we mean that the set of MPSs for which this eigenvalue is degenerate is of measure zero, c.f. [267, 268] and references therein

<sup>2</sup>This is equivalent to requiring the injectivity of the map [267]

$$\Gamma : X \rightarrow \sum_{s_1, \dots, s_L}^d \text{Tr}(X A^{s_1} \cdots A^{s_L}) |s_1, \dots, s_L\rangle. \quad (\text{B.5})$$

Non-injective MPSs give rise to macroscopic superpositions of states.

<sup>3</sup>The positiveness can be proven using the quantum Perron-Frobenius theorem, see [184] and references therein



construct the equivalent MPS in the right gauge:

$$\begin{array}{c} \text{---} \triangleleft A_R \text{---} \\ | \\ \text{---} \end{array} = \text{---} \bigcirc R^{-1} \text{---} \boxed{A} \text{---} \bigcirc R \text{---} \quad \text{s.t.} \quad \begin{array}{c} \triangleleft A_R \\ | \\ \triangleleft A_R^* \end{array} \text{---} = \text{---} \bigcirc \text{---} \bigcirc \text{---} \quad (B.9)$$

The left and right gauges are most useful when they are combined appropriately to write an MPS in the mixed gauge:

$$|\psi(A)\rangle = \cdots \text{---} \triangleleft A_L \text{---} \triangleleft A_L \text{---} \bigcirc L \text{---} \boxed{A} \text{---} \bigcirc R \text{---} \triangleleft A_R \text{---} \triangleleft A_R \text{---} \cdots, \quad (B.10)$$

$$= \cdots \text{---} \triangleleft A_L \text{---} \triangleleft A_L \text{---} \triangleleft A_L \text{---} \bigcirc L \text{---} \bigcirc R \text{---} \triangleleft A_R \text{---} \triangleleft A_R \text{---} \cdots. \quad (B.11)$$

This allows us to define the center-site tensor  $A_C$  and the gauge tensor  $C$  as

$$\text{---} \bigcirc C \text{---} = \text{---} \bigcirc L \text{---} \bigcirc R \text{---}, \quad \boxed{A_C} \text{---} = \text{---} \bigcirc L \text{---} \boxed{A} \text{---} \bigcirc R \text{---}. \quad (B.12)$$

$C$  implements the map from the left-gauge tensor  $A_L$  to the right-gauge tensor  $A_R$ . We now notice that there is still an additional gauge that is not fixed by selecting the right- or left-orthonormal form: a unitary transformation on  $A_L$  or  $A_R$  does not affect the left or right fixed point, respectively. Furthermore, since the right fixed point of the transfer matrix based on  $A_L$  still corresponds to a hermitian matrix, it can be brought into a diagonal form by this unitary transformation (and vice versa for the right gauge tensor). Using a singular value decomposition on  $C$

$$\text{---} \bigcirc C \text{---} = \text{---} \bigcirc U \text{---} \diamond S \text{---} \bigcirc V^\dagger \text{---}, \quad (B.13)$$

we can rename (the left-hand tensor is the new tensor):

$$\begin{array}{c} \diamond C \leftarrow \diamond S, \quad \triangleleft A_L \leftarrow \text{---} \bigcirc U^\dagger \text{---} \triangleleft A_L \text{---} \bigcirc U \text{---} \\ \text{and } \triangleleft A_R \leftarrow \text{---} \bigcirc V^\dagger \text{---} \triangleleft A_R \text{---} \bigcirc V \text{---} \end{array}, \quad (B.14)$$

where we indicate with tilted squares tensors corresponding to diagonal matrices. There are several nice properties with this construction. First, writing the state as

$$|\psi(A)\rangle = \cdots \text{---} \triangleleft A_L \text{---} \triangleleft A_L \text{---} \diamond C \text{---} \triangleleft A_R \text{---} \triangleleft A_R \text{---} \cdots \quad (B.15)$$

$\underbrace{\quad\quad\quad}_{|\psi_L(A_L)\rangle}$

$\underbrace{\quad\quad\quad}_{|\psi_R(A_R)\rangle}$

it is clear that  $C$  directly encodes the entanglement spectrum of the state and that the Schmidt

## Appendix B. Complement: tensor networks

decomposition of the state is given by

$$|\psi(A)\rangle = \sum_{\alpha} C_{\alpha} |\psi_L^{\alpha}(A_L)\rangle \otimes |\psi_R^{\alpha}(A_R)\rangle \quad (\text{B.16})$$

since by construction

$$\dots \begin{array}{c} \triangleleft A_L \triangleleft A_L \triangleleft A_L \\ \vdots \\ \triangleleft A_L^* \triangleleft A_L^* \triangleleft A_L^* \end{array} = \left( , \quad (\text{B.17})$$

$$\text{and} \quad \begin{array}{c} \triangleleft A_R \triangleleft A_R \triangleleft A_R \\ \vdots \\ \triangleleft A_R^* \triangleleft A_R^* \triangleleft A_R^* \end{array} \dots = \left) . \quad (\text{B.18})$$

Furthermore, in the quantum case, the value of any single site observable is efficiently evaluated in the mixed gauge (we use the fact that  $|\psi(A)\rangle$  is normalized:

$$\frac{\langle \psi(A^*) | O | \psi(A) \rangle}{\langle \psi(A^*) | \psi(A) \rangle} = \dots \quad \begin{array}{c} \square A \square A \square A \square A \square A \\ \vdots \\ \square A^* \square A^* \square A^* \square A^* \square A^* \end{array} \dots \quad (\text{B.19})$$

$$= \dots \quad \begin{array}{c} \triangleleft A_L \triangleleft A_L \triangleleft A_C \triangleleft A_R \triangleleft A_R \\ \vdots \\ \triangleleft A_L^* \triangleleft A_L^* \triangleleft A_C^* \triangleleft A_R^* \triangleleft A_R^* \end{array} \quad \dots = \left( \begin{array}{c} \square A_C \square \\ \square O \square \\ \square A_C^* \square \end{array} \right) . \quad (\text{B.20})$$

## B.2 Derivation of the tangent space projector

In the following we will denote by

$$|\phi(B; A)\rangle := B^v \frac{\partial}{\partial A^v} |\psi(A)\rangle \quad (\text{B.21})$$

the tangent vector to the manifold at point  $|\psi(A)\rangle$  defined by the tensor  $B$ . The index  $v$  stands for all three indices of the tensors  $A$  and  $B$ . In the uniform gauge this tangent vector is given by

$$|\phi(B; A)\rangle = \sum_n \dots \begin{array}{c} \square A \square A \square B \square A \square A \\ \vdots \\ \square A_{s_{n-1}} \square A_{s_n} \square B_{s_{n+1}} \square A_{s_{n+1}} \square A_{s_{n+2}} \end{array} \dots , \quad (\text{B.22})$$

and in the mixed gauge it is given by

$$|\phi(B; A_L, A_R)\rangle = \sum_n \dots \begin{array}{c} \triangleleft A_L \triangleleft A_L \triangleleft B_C \triangleleft A_R \triangleleft A_R \\ \vdots \\ \triangleleft A_{L,s_{n-1}} \triangleleft A_{L,s_n} \triangleleft B_{C,s_{n+1}} \triangleleft A_{R,s_{n+1}} \triangleleft A_{R,s_{n+2}} \end{array} \dots , \quad (\text{B.23})$$

where it is understood that  $B_C$  is  $B$  with absorbed left and right gauge tensors  $L$  and  $R$ .

## B.2. Derivation of the tangent space projector

It can be shown that there is a gauge freedom in  $B$ . We refer the interested reader to Ref. 150 and simply note that this gauge freedom can be fixed in the case of the MPS in the uniform gauge using the following parametrization, which enforces that we only look at vectors in the tangent space that are orthogonal to  $|\psi(A)\rangle^4$  ( $l$  and  $r$  being the left- and right-eigenvectors of the MPS transfer matrix):

$$\text{---} \boxed{B} \text{---} = \text{---} \boxed{l^{-\frac{1}{2}}} \text{---} \boxed{V_L} \text{---} \boxed{X} \text{---} \boxed{r^{-\frac{1}{2}}} \text{---} , \quad \text{---} \boxed{B_C} \text{---} = \text{---} \boxed{V_L} \text{---} \boxed{X} \text{---} , \quad (\text{B.24})$$

where the parameter  $X$  is of dimension  $\chi(d-1) \times \chi$ , and where  $V_L$  is of dimensions  $\chi \times d \times \chi(d-1)$  and satisfies

$$\begin{array}{c} \boxed{V_L} \\ | \\ \boxed{V_L^*} \end{array} = \left( \begin{array}{c} \boxed{V_L} \\ | \\ \boxed{A^*} \end{array} \right) = 0 \quad \text{i. e.} \quad \begin{array}{c} \boxed{V_L} \\ | \\ \boxed{A_L^*} \end{array} = 0 . \quad (\text{B.25})$$

This choice of gauge has the advantage that the overlap between two tangent vectors is given by (independently of the gauge)

$$\langle \phi(B'(X'); A) | \phi(B(X); A) \rangle = \sum_{n, n'} \text{---} \boxed{l} \text{---} \begin{array}{c} \boxed{B} \\ | \\ \boxed{A^*} \end{array} \text{---} \boxed{A} \text{---} \boxed{A} \text{---} \boxed{r} \text{---} \begin{array}{c} \boxed{A^*} \\ | \\ \boxed{B'^*} \end{array} \text{---} \text{---} \quad (\text{B.26})$$

$$= \sum_n \text{---} \boxed{l} \text{---} \begin{array}{c} \boxed{B} \\ | \\ \boxed{B'^*} \end{array} \text{---} \boxed{r} \text{---} = \sum_n \text{---} \boxed{X} \text{---} \begin{array}{c} \boxed{X'^*} \end{array} \text{---} = \sum_n \text{Tr}((X')^\dagger X) . \quad (\text{B.27})$$

This result allows us to derive the orthogonal projection of a vector  $|\nu\rangle$  in the Hilbert space onto the linear subspace which is the tangent space associated with  $|\psi(A)\rangle$ . Indeed, we can find  $X$  such that  $|\phi(B(X); A)\rangle$  corresponds to the orthogonal projection by minimizing the norm of the difference:

$$\min_X \| |\nu\rangle - |\phi(B(X); A)\rangle \|^2, \quad (\text{B.28})$$

which amounts to minimizing

$$\min_X \left( \sum_n \text{Tr}(X^\dagger X) - \langle \nu | \phi(B(X); A) \rangle - \langle \phi(B^*(X); A^*) | \nu \rangle \right). \quad (\text{B.29})$$

The solution is given by

$$\sum_n X = \frac{\partial}{\partial X^*} \langle \phi(B^*(X); A^*) | \nu \rangle. \quad (\text{B.30})$$

Considering (one-site) translation invariant  $|\nu\rangle$  we have that its projection on the tangent

<sup>4</sup>See Ref. 196 for an example of why this is useful.

## Appendix B. Complement: tensor networks

space is given by

$$|\phi(B(X); A)\rangle = \sum_n \text{Diagram} \quad (B.31)$$

in the uniform gauge, or by

$$|\phi(B(X); A_L, A_R)\rangle = \sum_n \text{Diagram} \quad (B.32)$$

in the mixed gauge. With this, we can define the tangent space projector  $\mathcal{P}_A$  in the uniform gauge (it can directly be read in Eq. B.31), and most importantly we can find it in the mixed gauge as

$$\mathcal{P}_A = \sum_n \text{Diagram}_1 - \sum_n \text{Diagram}_2 \quad (B.33)$$

To eliminate the expression of  $V_L$  in Eq. B.32 we used that the identity can be rewritten

$$\text{Diagram} = \text{Diagram}_1 + \text{Diagram}_2 \quad (B.34)$$

# C Complement: the Kanamori method of inequalities

## C.1 List of references

Table C.1 is a reproduction of the very useful table of Ref. [25], listing the applications of Kanamori's method of inequalities and of similar methods to determine the ground states of (generalized) Ising models and related problems. In italics we added some related works that came out after the book by Ducastelle; we hope this is helpful but by no means do we warrant the exhaustiveness of this list.

Structure	References	Interactions taken into account
Linear chain	Ducastelle Sec. 3.3.3, 3.4. 4, 5.3 [25]	
	Morita 1974 [269, 270], Finel 1987 [271]	general results for interactions of finite range; specific results for 4th and 5th neighbours
	Kaburagi and Kanamori 1975 [203]	3rd neighbors
	Ducastelle Sec. 3.3.3, <i>Garbulsky et al.</i> 1992 [272]	2nd neighbors
	Hubbard 1978 [273], Pokrovsky and Uimin 1978 [274], Ducastelle Sec. 3.4.3	positive and convex pair interactions
	Fisher and Selke 1981 [275], Pokrovsky and Uimin 1982 [276]	3D ANNNI model at low temperatures
	Tonegawa et al. 1985 [277, 278]	1st and 2nd neighbors in ternary alloys (Potts model)
Square lattice	Ducastelle Sec. 5.2.1	
	Kaburagi 1978a [279], Kanamori and Kaburagi 1983 [280]	3rd neighbors
	Takasaki et al. 1988 [281]	1st and 2nd neighbors in ternary alloys (Potts model)
Centered	Kanamori 1966 [155]	2nd

## Appendix C. Complement: the Kanamori method of inequalities

---

rectangular lattice	Kaburagi 1978b [282]	4th
	Kaburagi and Kanamori 1977 [283]	7th
Triangular lattice	Ducastelle Sec. 3.3.1 and 5.2.2	
	Tanaka and Uryu 1975 [284]	2nd
	Kaburagi and Kanamori 1978 [204]	3rd
	<i>Dublenych 2009</i> [285]	19th
	<i>Dublenych 2011</i> [286, 287]	2nd + triplet
	Kanamori 1984, 1985, 1986 [288–290], Kanamori and Okamoto 1985 [291]	7th and triplets (semiconductor surfaces)
	<i>Huang 2016</i> [158]	up to quadruplets
Honeycomb lattice	Ducastelle Sec. 3.4.2	
	Kudo and Katsura 1976 [200], Kanamori 1984 [205]	3rd
	<i>Dublenych 2009</i> [285]	3rd
Kagome lattice	Wolf and Schotte 1988 [101]	3rd
	<i>Colbois et al. 2021</i> [160]	3rd   and field (to be completed)
	<i>This thesis</i>	3rd   and 3rd★ (to be completed)
Shastry-Sutherland	<i>Dublenych 2012</i> [292]	2nd
Simple cubic	Kanamori 1966 [155]	2nd
	Kaburagi and Kanamori 1975 [203]	3rd
	Lipkin 1988 [293]	1-, 2- and 3-body
Cubic lattices	Mouritsen et al. 1983 [294]	4-spin interactions
	<i>Seko et al. 2014</i> [295]	4th
BCC	Ducastelle Sec. 3.5.3	
	Kanamori 1966 [155], Richards and Cahn 1971 [161], Allen and Cahn 1972 [156]	2nd
	Kanamori and Kakehashi 1977 [296]	4th
	Finel and Ducastelle 1984 [297], Finel 1987 [271]	5th
Body centered tetragonal	Kanamori 1966 [155]	2nd
	Narita and Katsura 1974 [298, 299]	3rd
	Moriya and Ino 1979 [300]	6th
	<i>Seko et al. 2014</i> [295]	4th
FCC	Ducastelle Sec. 3.5.1	

## C.2. Relation between the MAX-MIN approach and Kanamori's polytope

hcp	Kanamori 1966 [155], Richards and Cahn 1971 [161], Allen and Cahn 1972, 1973 [156, 301], <i>Cenedese and Cahn</i> 1994 [302]	2nd
	Kanamori and Kakehashi 1977 [296]	4th
	Kanamori 1979 [303]	5th
	Cahn and Kikuchi 1979 [304], Sanchez and de Fontaine 1981 [305]	multiatom interactions
	<i>Wolverton et al.</i> 1993 [306], <i>Seko et al.</i> 2014 [295]	4th
	<i>De Meulenaere et al.</i> 1994 [307]	1st and 4th
	Ducastelle Sec. 3.5.2	
	Kudo and Kastura 1976 [200]	2nd
	<i>Singh and Lele</i> 1991-1992 [308–312]	3rd
	<i>Seko et al.</i> 2014 [295]	4th
	<i>McCormack et al.</i> 1992-1993 [313, 313], <i>Sarma et al.</i> 1994 [314]	up to 4-body
	Ono and Oguchi 1968 [315]	1st
	<i>Seko et al.</i> 2014 [295]	5th
	<i>Kaburagi et al.</i> 1984 [316]	ANNI
Simple hexagonal lattice		

Table C.1 – Compilation of ground-state determinations (Reproduced from Ref. [25] and completed). Note that these works often consist in improvements of the Kanamori method of inequalities, and in some of the most recent works the methods are actually somewhat different (MAX-MIN approach, basic rays methods, convex hull from the interior polytope, ...). Another useful reference for an overview is D. de Fontaine [317].

## C.2 Relation between the MAX-MIN approach and Kanamori's polytope

The two LPs obtained from the configurational polytope method and the MAX-MIN approach are actually very closely related, as discussed in Ref. 158. To see this, we first need to rewrite Eq. 1.73 in a slightly more general way, easier to relate to our notation for the MAX-MIN

approach:

$$\frac{H}{N} = \frac{1}{N} \sum_{k \in \mathbf{C}} J_k \sum_{\Gamma_k} \prod_{i \in \Gamma_k} \sigma_i \quad (\text{C.1})$$

$$= \sum_{k \in \mathbf{C}} J_k \frac{N_k}{N} \frac{1}{N_k} \sum_{\Gamma_k} \prod_{i \in \Gamma_k} \sigma_i \quad (\text{C.2})$$

$$= \sum_{k \in \mathbf{C}} J_k \frac{N_k}{N} c_k, \quad (\text{C.3})$$

which defines the generalization of the correlations  $c_k$  for arbitrary cluster interactions.

We can now start from the LP for the MAX-MIN approach (Eq. 1.98, and explicitly write the inequalities  $H_u^{\tilde{\alpha}}(\tilde{\sigma}|_u) \geq n_u E$  using

$$H_u^{\tilde{\alpha}}(\tilde{\sigma}|_u) = \sum_{k \in \mathbf{C}} \sum_{\Gamma_k \subseteq u} J_k \alpha_{\Gamma_k}^u \prod_{i \in \Gamma_k} \sigma_i. \quad (\text{C.4})$$

Given a LP there is a systematic procedure to write its dual LP [199]. Applying the procedure to Eq. 1.98 with Eq. C.4, we have to define for each constraint a corresponding dual variable. The constraints on the energy define dual variables  $\rho_{\tilde{\sigma}|_u}$ , while the constraints on the weights  $\alpha_{\Gamma_k}^u$  define dual variables  $\rho_k$ , and we get the dual LP [156]:

$$\min_{\tilde{\rho}} \sum_{k \in \mathbf{C}} \rho_k J_k, \quad \text{with} \quad \begin{cases} \rho_k = \frac{1}{n_u} \sum_{\tilde{\sigma}|_u} \rho_{\tilde{\sigma}|_u} \prod_{i \in \Gamma_k} \sigma_i \quad \forall k \in \mathbf{C} \quad \forall \Gamma_k \subseteq u \\ \sum_{\tilde{\sigma}|_u} \rho_{\tilde{\sigma}|_u} = 1 \\ \rho_{\tilde{\sigma}|_u} \geq 0 \end{cases}. \quad (\text{C.5})$$

The variables  $\rho_{\tilde{\sigma}|_u}$  can be interpreted as the frequency at which a certain configuration  $\tilde{\sigma}|_u$  appears on the cluster  $u$ . Clearly these must be larger than zero and sum to one. With this, we get (for  $\Gamma_k \subseteq u$ )

$$\rho_k = \frac{1}{n_u} \sum_{\tilde{\sigma}|_u} \rho_{\tilde{\sigma}|_u} \prod_{i \in \Gamma_k} \sigma_i = \frac{1}{N} \sum_{\Gamma_k} \prod_{i \in \Gamma_k} \sigma_i = \frac{N_k}{N} c_k, \quad (\text{C.6})$$

where we used that  $N = n_u \cdot N_{\mathcal{T}_u}$ . Eq. C.6 essentially states that computing the correlations by translating and rotating an interacting cluster through all the bonds is the same as computing them by selecting a specific interacting cluster  $\Gamma_k$  in the reference cluster  $u$  and summing the correlations on this cluster by weighting all the possible configurations  $\tilde{\sigma}|_u$  obtained in a certain configuration. The configurational polytope of Kanamori is thus hidden in the constraints on  $\rho_{\tilde{\sigma}|_u}$  and their relation to the correlations  $c_k$ . The minimization C.5 is therefore equivalent to the minimization 1.76 under the configurational polytope constraints. Thus, Kanamori's method is essentially the dual LP to the MAX-MIN approach<sup>1</sup>.

The dual transformation does not change the complexity of the problem. However, both

---

<sup>1</sup>This is especially clear from the formulation of Kanamori's method in the work of Allen and Cahn, Ref. 156



methods have some advantages depending on the problem that one wants to tackle. In particular, for finding the ground-state energy of a specific Ising Hamiltonian, the MAX-MIN approach has the advantage that the exponential number of constraints can be incorporated in an efficient manner (most of the constraints are not relevant to determine the ground-state energy of a specific Hamiltonian). Additionally, it yields results that are particularly appropriate for tensor network construction (Chapter 2). At the same time, for getting a first look at a ground-state phase diagram, Kanamori's configurational polytope method is particularly useful, especially when the problem is such that a high number of corners can be easily constructed.



## D Pseudocode for the linear program to find ground state tiles

*The statement of contribution for Chapter 2 also applies to this Appendix.*

Alg. 3 describes a method to find a simplex of maximal dimension that fits inside a convex set  $A$ . The idea is to take a small simplex inside  $A$  and try to make it bigger until it has the dimension of  $A$ . For this, the origin is first moved to the interior of the small simplex, and a vector orthogonal to the current simplex is constructed. One then looks for a vector in  $A$  of maximal overlap (in absolute value) with this vector. If the maximal overlap is 0 the simplex is of maximal dimension inside  $A$ , if not, one adds the result to the simplex and starts over.

Alg. 3 finds the interior simplex once the set  $A$  that solves the problem

$$E_u \leftarrow \max_{\tilde{a}} E, \quad \text{with} \quad \left\{ \begin{array}{l} H_u^{(\alpha)}(C) \geq E \quad \forall C \\ \sum_{c \in \mathcal{T}_u | n \in c} \alpha_n^c = 1 \end{array} \right\}, \quad (\text{D.1})$$

has been found. For large clusters, where there is a large number of configurations, even finding this cluster can pose memory issues. Alg. 4 offers a solution to this problem which automatically finds an interior simplex of D.1 using as few configurations  $C$  as possible. The algorithm turns the memory load into a time load.

The idea is to take a restricted set of configurations  $\{c_i\}$  and solve Eq. D.1 just for them, to estimate the full solution. This amounts to finding a convex set that contains  $A$ . We then look for an interior simplex of the solution-set of this problem. Solving equation D.1, we get a temporary estimate for the ground state energy. In each corner of the simplex, the  $\tilde{a}$  define a Hamiltonian associating an energy to all the configurations of the clusters. The estimate is compared to the energy of each configuration in each corner. If we find a configuration which has an energy below the estimate, the associated inequality is useful; the configuration is added to the set  $\{c_i\}$  and we restart. On the other hand, if in each corner, the energy of each configuration is greater than or equal to the estimate, we are sure to have a solution of Eq. D.1 with all configurations considered, and the problem is solved. This way, we work around most of the redundancy in the set of inequalities associated with all the configurations, and only inequalities that bring insight are used to build the convex set  $A$ .

## Appendix D. Pseudocode for the linear program to find ground state tiles

---

Note that Alg. 3 can just about handle the example from the paper, but larger clusters, say two or three kagome stars could only be considered using Alg. 4.

---

### Algorithm 3 Build interior simplex of convex set $A$

---

```
1:  $\vec{R} \leftarrow$  random vector
2:  $\vec{\alpha}_1 \leftarrow \max \vec{R} \cdot \vec{\alpha}$  with  $\alpha \in A$ 
3: while do
4:    $\vec{\beta} \leftarrow$  a point in simplex $[\{\vec{\alpha}_i\}]$ 
5:   Translate  $\vec{\alpha}$ -space by  $-\vec{\beta}$ 
6:    $\{\vec{w}_i\} \leftarrow$  a basis of orthogonal vectors to all  $\{\vec{\alpha}_i\}$ 
7:   for  $\vec{v} \in \{\vec{w}_i, -\vec{w}_i\}$  do
8:      $\vec{\alpha} \leftarrow \max \vec{v} \cdot \vec{\alpha}$  with  $\alpha \in A$ 
9:     if  $\vec{v} \cdot \vec{\alpha} \neq 0$  then
10:       Add  $\vec{\alpha}$  to the set  $\{\vec{\alpha}_i\}$ 
11:       Return to the top of the while loop
12:   Stop the while loop
13: return  $\{\vec{\alpha}_i\}$ 
```

---

---

### Algorithm 4 Build interior simplex of $A^u$

---

```
1:  $\{c_i\} \leftarrow$  choose some random configurations
2:
3: Add random configurations to  $\{c_i\}$  until there
4: is a finite  $E$  and a finite interior simplex
5:
6: while do
7:   for  $\vec{\alpha} \in \{\vec{\alpha}_i\}$  do
8:     for  $c : H_u^{\vec{\alpha}}(c) < E_{\text{temp}}$  do
9:       if  $c \notin \{c_i\}$  then
10:         Add  $c$  to  $\{c_i\}$ 
11:          $E_{\text{temp}} \leftarrow$  solve Eq. D.1 for configurations  $\{c_i\}$ 
12:          $\{\vec{\alpha}_i\} \leftarrow$  Update interior simplex for  $\{c_i\}$ 
13:         Return to the top of the while loop
14:   Stop the while loop
15: return  $E_{\text{temp}}, \{\vec{\alpha}_i\}$ 
```

---

# E Details related to the chirally coupled artificial spin systems

*The statement of contribution for Chapter 3 also applies to this Appendix.*

## E.1 Experiments

The fabrication of the samples is performed using electron beam lithography. First, films of Pt(6 nm)/Co(1.6 nm)/Al(2 nm) are deposited on a 200 nm-thick SiNx layer on a silicon substrate by DC magnetron sputtering at a base pressure of  $2 \cdot 10^{-8}$  mbar and at a deposition pressure of  $3 \cdot 10^{-3}$  mbar. After patterning a polymethyl methacrylate (PMMA) mask with an electron beam writer, the trilayers are milled with Ar ions. The anisotropy of the various regions is determined by whether the Al layer is covered by the mask: the future IP regions are protected by 2 nm Ta, while the future OOP regions are exposed to oxygen plasma at a power of 30 W and an oxygen pressure of 0.013 mbar. For statistics, 20 samples of size  $20 \times 20 \mu\text{m}^2$  are patterned on the same substrate. With an IP length of 50 nm and an OOP edge length of 100 nm, this amounts to approximately 2300 sites per sample.

All 20 samples have been AC demagnetized by a field-based protocol of sinusoidal OOP fields with decreasing amplitudes. The sinusoidal amplitude decreased from 900 Oe to 30 Oe linearly in 4000 steps over a period of two hours. At each step, a single sinusoidal period is applied with a frequency of 2 Hz. Several demagnetization protocols with different parameters were tested using the net magnetization of a specific array on a sample as a measure of success. However, the spread in the net magnetization for different samples was larger than any improvement in the magnetization achieved with the protocols when going from a 1 hour protocol to 4 hours (Fig. E.1), and a zero net magnetization was not reached. This is different from results for dipolar coupled nanomagnets, where it has been found advantageous to use longer protocols [67], as is demonstrated for instance by Ref. 318. While we did not observe such a clear trend in our demagnetization protocols, we should note that our samples and protocols are significantly different from the usual dipolar coupled nanomagnets as our samples have chirally interacting IP and OOP regions. In addition, we do not rotate the sample in the demagnetizing field. In our chirally coupled systems, rotating the sample would induce strong

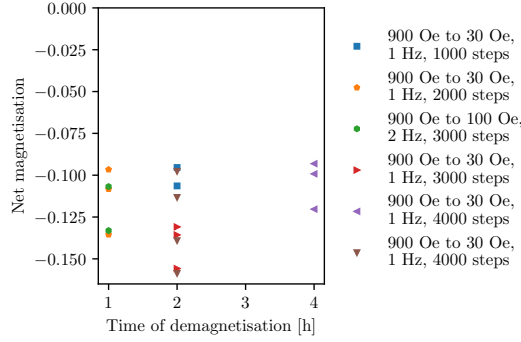


Figure E.1 – MFM optimization of the demagnetization protocol, displaying various 1, 2, and 4 hours protocols. Different colors at each protocol time indicate different protocols, and each point represents an individual array whose net magnetization is computed. The net magnetization cannot be driven closer to zero than -0.09. The more extended protocols do not show a clear trend towards reducing the net magnetization. The larger spread at 2 hours is due to more samples being tested. In order to be efficient in measuring our 20 arrays, the 2 hours protocol was chosen.

interactions between external fields and the IP regions.

Magnetic force microscopy (MFM) measurements are performed after the demagnetization protocol to extract the OOP spin configurations. A protective layer of PMMA is spin coated on each sample for the MFM measurements. The MFM tips, coated by CoCr, are sensitive to magnetic stray fields. The tip is scanned over the sample at a frequency of 1 Hz and 512 pixels/line.

### E.2 Micromagnetic simulations

We performed micromagnetic simulations using MuMax<sup>3</sup> (v3.10) [233, 234] to determine the (relative) coupling constants of the chirally coupled nanomagnet geometry. The simulations are carried out with a cell size of 0.866 by 0.866 by 1.6 nm<sup>3</sup> (1.6 nm being smaller than the exchange length of the system) and with 2048 by 2048 by 1 simulation world size. The cell sizes are chosen such that the angled edges are accurately simulated.

Typical material parameters for cobalt (Co) are used: a saturation magnetization  $M_s = 600$  kA/m, an exchange stiffness  $A = 16 \times 10^{-12}$  J/m, and a magnetocrystalline anisotropy  $K_u = 570$  kJ/m<sup>3</sup> in the OOP region and  $K_u = 0$  in the IP region. Interfacial DMI is introduced by setting  $D_{\text{ind}} = 0.9 \pm 0.1$  mJ/m<sup>2</sup> [113]. The Gilbert damping  $\alpha$  is set to 1.0 to allow the simulation to relax quickly to the state we are interested in, i.e. the state after energy minimization. The various coupling constants follow from simulating different OOP and IP configurations.

The aim is to estimate the values of the various coupling constants relative to the full nearest-neighbor coupling, to determine if they are large enough to explain the inversion of the  $c_2$

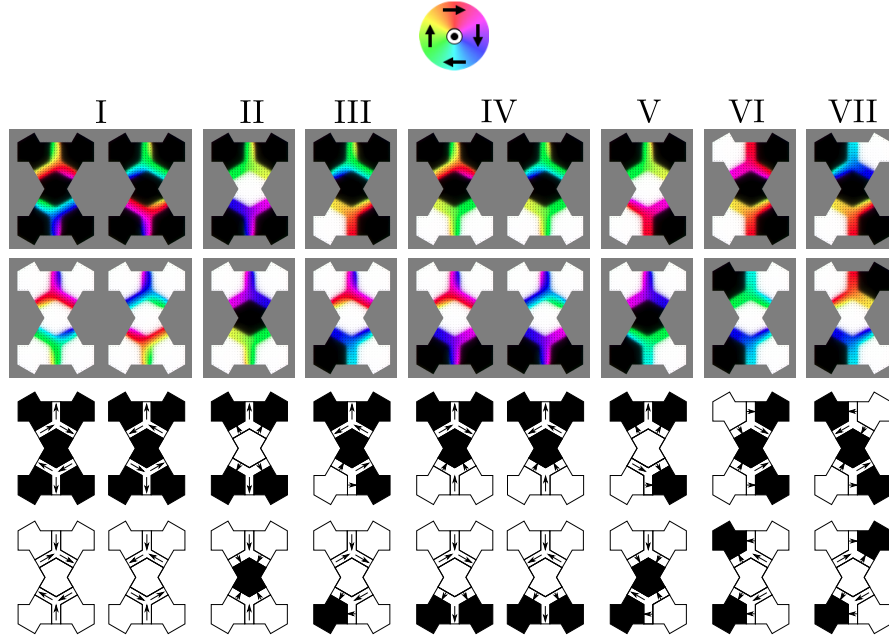


Figure E.2 – First row: micromagnetic simulations results (after relaxation) for each OOP configuration from Fig. 3.2. For each OOP configuration, we show the IP configuration that minimizes the energy. The colored disk at the top gives the legend for the IP magnetization. For the OOP regions, black means up Ising spin, white means down Ising spin. Second row: IP configurations that minimize the energy when all the spins are flipped. Here, we do not show the micromagnetic results for applying rotations and/or mirror symmetries, but they have been used in determining the average energy and the error bars for the results in Table E.1. Third and fourth rows: sketch illustrating the OOP and IP configurations from the first and second rows, for readability.

	Expression of the Energy	Energy (pure OOP) [ $10^{-17}$ J]	Energy (OOP + IP) [ $10^{-17}$ J]
I	$E_0 + 4J_{1,d} + 2J_{1,h} + 2J_2 + 2J_{3  } + Q_1 + 4Q_2$	$-1.645897 \pm 6 \cdot 10^{-7}$	$-1.2408601 \pm 5 \cdot 10^{-7}$
II	$E_0 - 4J_{1,d} + 2J_{1,h} + 2J_2 + 2J_{3  } + Q_1 - 4Q_2$	$-1.6609718 \pm 2 \cdot 10^{-7}$	$-1.367404 \pm 1 \cdot 10^{-6}$
III	$E_0 + 2J_{1,d} - Q_1 - 2Q_2$	$-1.65413964 \pm 8 \cdot 10^{-7}$	$-1.3064207 \pm 4 \cdot 10^{-7}$
IV	$E_0 + 2J_{1,h} - 2J_2 - 2J_{3  } + Q_1$	$-1.6549028 \pm 2 \cdot 10^{-7}$	$-1.3062638 \pm 4 \cdot 10^{-7}$
V	$E_0 - 2J_{1,d} - Q_1 + 2Q_2$	$-1.6616731 \pm 7 \cdot 10^{-7}$	$-1.3693708 \pm 5 \cdot 10^{-7}$
VI	$E_0 - 2J_{1,h} + 2J_2 - 2J_{3  } + Q_1$	$-1.661483 \pm 2 \cdot 10^{-7}$	$-1.3699101 \pm 6 \cdot 10^{-7}$
VII	$E_0 - 2J_{1,h} - 2J_2 + 2J_{3  } + Q_1$	$-1.661797 \pm 9 \cdot 10^{-7}$	$-1.3707522 \pm 5 \cdot 10^{-7}$

Table E.1 – Results of the micromagnetic simulations for the energies of the various configurations from Fig. 3.2, for an IP width of 50 nm.

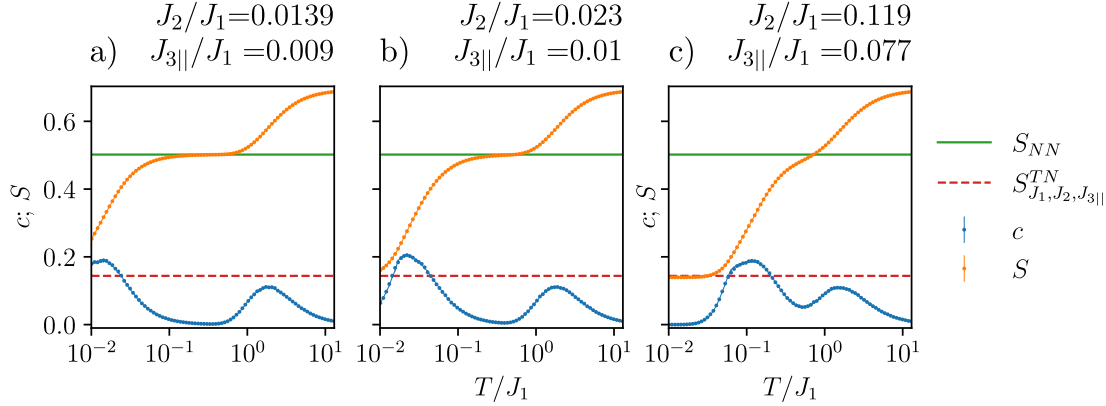


Figure E.3 – Overview of the behavior of the specific heat and entropy as a function of the temperature for the values of  $J_2$  and  $J_{3||}$  from Sec. 3.1.2, with Monte Carlo simulations for 3 system sizes ( $N = 576, 1296$ ). The smaller system size is shown with a line while the larger is shown with symbols.

and  $c_{3||}$  correlations observed in Fig. 3.5 as compared to the nearest-neighbor models in Figs. 3.8, 3.14. To do this, we simulate the various configurations of Fig. 3.2 for the Ising spins, and let the system relax. We then compare their respective energies to extract the effective couplings. For the configurations of Fig. 3.2, indexed by roman numbers, we obtain the micromagnetic results shown in Fig. E.2. In Table E.1, we summaries the expression of the energy (based on Fig. 3.2), and the value of the energy in the micromagnetic simulations, first in the pure out-of-plane case (dipolar couplings, no IP region), and second in the complete case shown in Fig. E.2. The errors in the energies are estimated from the differences in the energies of configurations that belong to the same group.

### E.3 More about the $J_1 - J_2 - J_{3||}$ model in zero field

In Fig. E.3, we show the specific heat and the entropy per site as a function of the temperature for two different system sizes in the  $J_1 - J_2 - J_{3||}$  model in zero field. The selected values of  $J_2$  and  $J_{3||}$  correspond to the panels of Fig. 3.21, i.e. to the values that have been discussed in the micromagnetic simulations section. Again, we find two peaks in the specific heat. Exactly as in the  $J_1 - J_2$  case, the feature at larger temperatures corresponds to the nearest-neighbor model. The second feature is actually a combined effect of the  $J_2$  and  $J_{3||}$  couplings. The  $J_2$  ice rule is imposed, but additionally, the  $c_{3||}$  correlations are restricted to the minimum that they can reach in the  $J_1 - J_2$  set of ground states. An example ground state is shown in Fig. E.4.



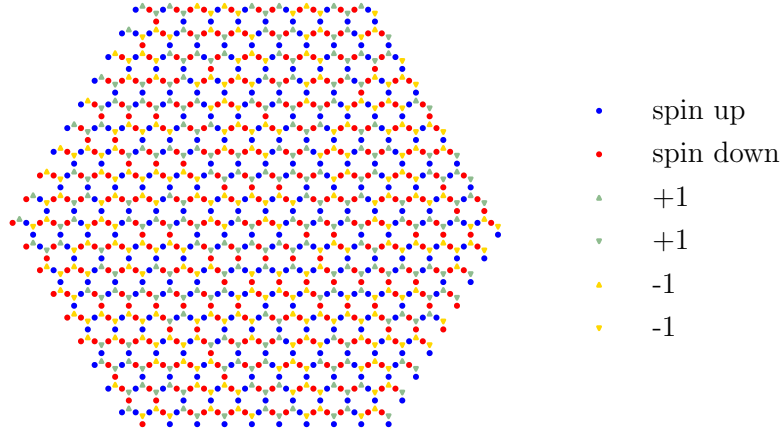


Figure E.4 – An example of a ground-state configuration for the  $J_1 - J_2 - J_{3||}$  model, including the corresponding charge configuration.

#### E.4 Detail of the $J_1 - J_2 - J_{3||} - h$ ground states

As discussed in the main text, the phase diagram of the farther-neighbor model in a field arises from a selection of a different set of states depending on the value of the magnetic field. In zero field, tensor network results, as well as Monte Carlo results, show that there is a residual entropy even for  $0 < J_{3||} < J_2$ . Upon introducing the magnetic field, this macroscopic ground-state degeneracy is immediately partially lifted. Two examples of such ground states are shown in Fig. 3.19. The difference between the two configurations illustrates the type of torus-winding updates that can be found (i.e., non-local updates that cross the sample and close in on themselves through the periodic boundary conditions). Each such update can be performed independently. Together with the fact that the tensor network contraction gives zero residual entropy, this provides evidence that the ground-state degeneracy is macroscopic but grows exponentially with the linear system size.

Upon increasing the magnetic field, there is a first-order phase transition in the ground state between the  $m = 1/9$  and  $m = 1/3$  plateaus. There, the states are a mixture of the  $m = 1/9$  ground states and the stripe state of the  $1/3$  plateau, and the average magnetization shows a strong dependence in system size (only sizes with a linear size of a multiple of 3 match), Fig. E.5.

In the  $m = 1/3$  plateau, the charge state is the same as in the corresponding plateau of the nearest neighbor model, but the farther-neighbor couplings select a long-range ordered stripe state (as long as  $J_{3||} < J_2$ ; for  $J_{3||} > J_2$  another long-range ordered state is selected).

At the transition to the  $m = 5/9$  plateau, we again find a strong size dependence of the magnetization (Fig. E.6). The  $m = 5/9$  plateau seems again characterized by a sub-extensive

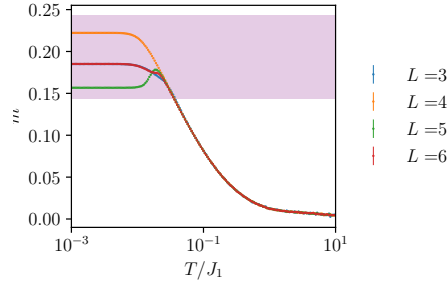


Figure E.5 – Magnetization as a function of the temperature for the  $J_1 - J_2 - J_{3||}$  model at  $h = 6J_{3||}$ , for various small system sizes. The number of sites is  $N = 9L^2$ . The shaded region corresponds to the experimental value.

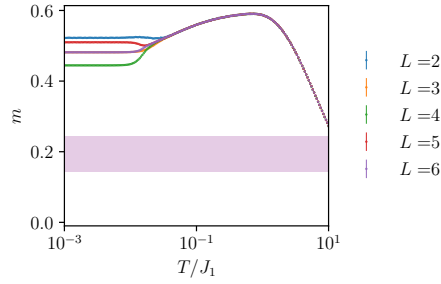


Figure E.6 – Magnetization as a function of the temperature for the  $J_1 - J_2 - J_{3||}$  model at  $h = 4(J_1 + J_2) - 6J_{3||}$ , for various small system sizes. The shaded region corresponds to the experimental value.

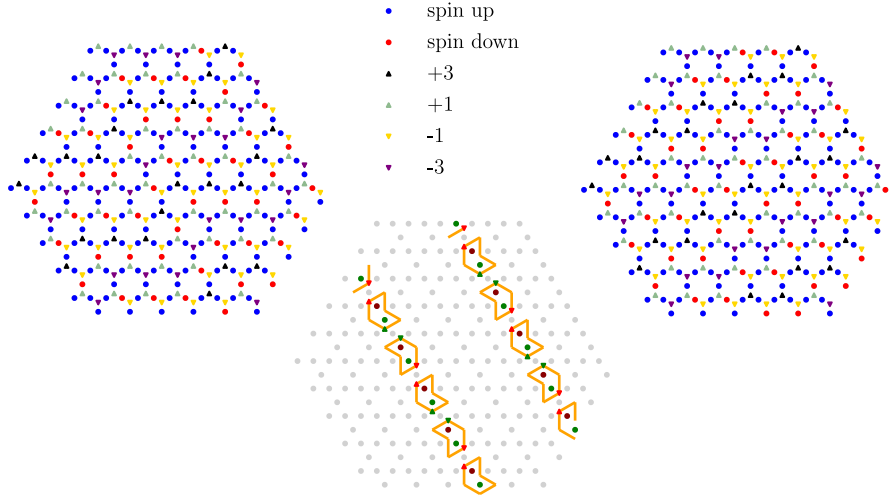


Figure E.7 – Two examples of ground-state configurations for the  $J_1 - J_2 - J_{3||}$  model, including the corresponding charge configuration, for a magnetic field  $4(J_1 + J_2) - 6J_{3||} < h < 4(J_1 + J_2) - 2J_{3||}$  ( $m = 5/9$ ). The central panel shows the difference between the two configurations (see the caption Fig. 3.19 for the convention regarding the updates).

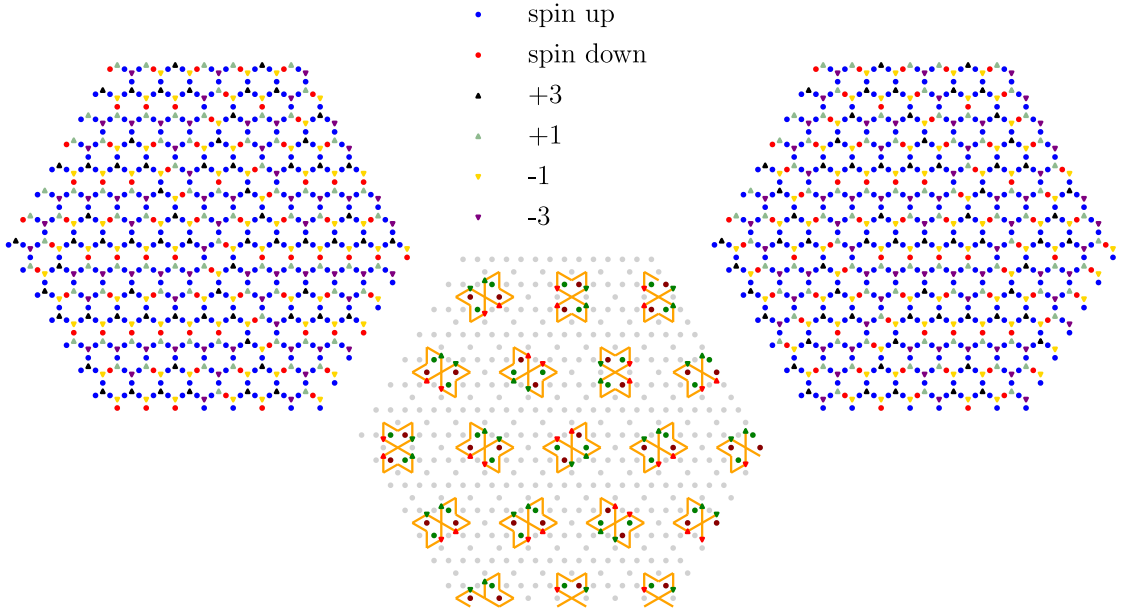


Figure E.8 – Two examples of ground-state configurations for the  $J_1 - J_2 - J_{3||}$  model, including the corresponding charge configuration, for a magnetic field  $4(J_1 + J_2) - 2J_{3||} < h < 4(J_1 + J_2 + J_{3||})$  ( $m = 17/27$ ). Local updates shown in the central panel bring the system from one configuration to the other (see the caption of Fig. 3.19 for detail).

ground-state degeneracy, with non-local updates winding the torus (Fig. E.7); however we do not have tensor networks results in this phase. Finally, in the  $m = 17/27$  plateau, we find that there are local updates, shown in Fig. E.8, yielding a lower bound for the residual entropy in that phase  $S \geq \frac{1}{27} \ln(2)$ .

The present discussion is a preliminary study of this ground-state phase diagram, and much is left to be clarified. Nevertheless, it shows that on the kagome lattice, the residual entropy gets lifted only very progressively - in contrast to the triangular lattice Ising antiferromagnet, for instance. In particular, we want to underline that unlike Refs. 222, 244, the case where  $J_{3||} < J_2$  is *not* at a phase boundary between two ground-state phases of the  $J_1 - J_2 - J_{3||}$  model. It is all the more surprising that a finite residual entropy is preserved at some values of the magnetic field.



# F Ground-state phase diagrams

In this Appendix we discuss more broadly the results for the  $J_1 - J_2 - J_{3||}$  models and the  $J_1 - J_2 - J_3$  models. We start by presenting the Kanamori inequalities. We then proceed to plotting the ground-state phase diagram in the the  $J_1 - J_2 - J_{3||}$  models as obtained by Wolf and Schotte [101], which we complement with further results from Refs. 160, 222 and some of our own additional tensor network computations. Then, we show the candidate ground-state phase diagram for the  $J_1 - J_2 - J_3$  models with arbitrary values of the couplings (instead of only focusing on the cases when  $J_1 \gg J_2, J_3$  as in the main text in Chapter 4), and discuss additional required work to fully understand this ground-state phase diagram. We also compare the two ground-state phase diagrams.

## F.1 Kanamori inequalities

In this section, we discuss the results obtained by applying the method of inequalities (Sec. 1.4.1) to two models : the  $J_1 - J_2 - J_{3||}$  model studied by Wolf and Schotte [101], and the  $J_1 - J_2 - J_{3||} - J_{3\star}$  model. Unless otherwise specified, the inequalities are obtained following the approach of Kudo and Katsura [200] which we presented in Chapter 1.

### F.1.1 $J_1 - J_2 - J_{3||}$ models

The model

$$H = J_1 \sum_{\langle i,j \rangle_1} \sigma_i \sigma_j + J_2 \sum_{\langle i,j \rangle_2} \sigma_i \sigma_j + J_{3||} \sum_{\langle i,j \rangle_{3||}} \sigma_i \sigma_j \quad (\text{F1})$$

is studied in Ref. 101 using Kaburagi and Kanamori's method, as we described in Sec. 1.4.1. The inequalities for the correlations can be put in the form

$$a_1 c_1 + a_2 c_2 + a_{3||} c_{3||} \geq -1. \quad (\text{F2})$$

## Appendix F. Ground-state phase diagrams

Inequality	$a_1$	$a_2$	$a_{3  }$	Cluster
W1	3	0	0	
W2	0	3	0	
W3	-2	1	0	
W4	-2	0	1	
W5	2	0	1	
W6	3	1	1	
W7	-1	1	1	
W8	1	-1	-1	
W9	-1	1	-1	
W10	-1	-1	1	

Table F.1 – Coefficient of the 10 relevant inequalities (Eq. F.2) for  $J_1 - J_2 - J_{3||}$  models on the kagome lattice [101]. The clusters together with the signs taken into account to establish the inequalities are given. When only some of the signs are given, one should assume that they are placed in a way that respects the cluster's symmetries.

Corner	$c_1$	$c_2$	$c_{3  }$	Instance
1	1	1	1	Ferromagnetic state
2	$-\frac{1}{3}$	1	$-\frac{1}{3}$	$\sqrt{3} \times \sqrt{3}$ (Fig. 4.4c)
3	$-\frac{1}{3}$	$-\frac{1}{3}$	1	Stripes (Fig. 4.4b)
4	0	0	-1	Ferro. hexagons (Fig. F.1a)
5	0	$-\frac{1}{3}$	$-\frac{2}{3}$	Zigzags (Fig. F.1b)
(*)6	$-\frac{1}{3}$	$-\frac{1}{3}$	$\frac{1}{3}$	Chevrons and dimers (Fig. F.1c)
(*)7	$-\frac{1}{3}$	$\frac{1}{3}$	$-\frac{1}{3}$	Arrows and dimers (Fig. F.1d)
8	$\frac{1}{3}$	$-\frac{1}{3}$	$\frac{1}{3}$	Stripes II (Fig. F.1e)
(*)9	$\frac{1}{3}$	$-\frac{1}{3}$	$-\frac{1}{3}$	Triangle-based TIAFM (Fig. F.1f)

Table F.2 – The 9 corners describing the Kanamori polytope for  $J_1 - J_2 - J_{3||}$  models as obtained by Wolf and Schotte. The names of the phases are given by us on the basis of the states configurations. The corners marked with a star correspond to ground-state phases which we determined have a finite residual entropy.

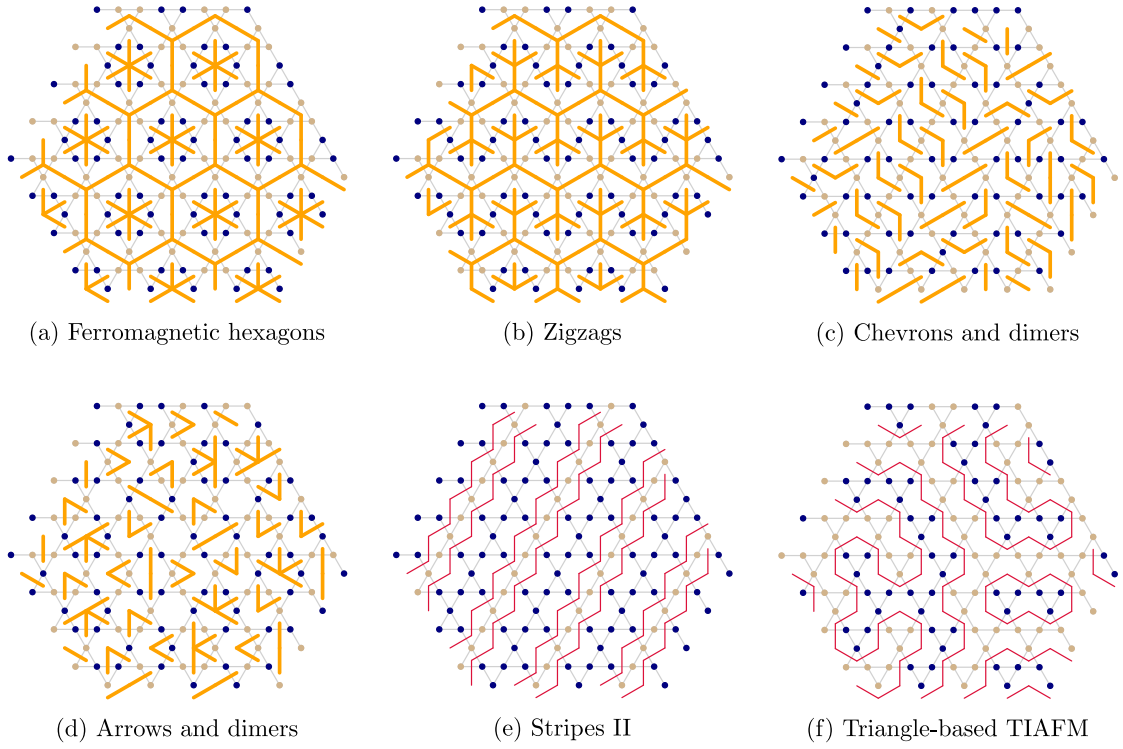


Figure F.1 – Configurations appearing in the ground-state phase diagram of the  $J_1 - J_2 - J_{3||}$  models.

The values of  $a_1$ ,  $a_2$  and  $a_{3||}$  are tabulated in Table F.1, which is a reproduction of Table 1 in [101], where we additionally included the clusters and signs generating the corresponding inequalities. These 10 inequalities generate the 9 corners found by Wolf and Schotte and given in Table F.2. We note that in this case, the set of 10 inequalities is sufficient, as each corner in this table is realized. Not all the corners correspond to long-range ordered ground states, as we have seen in Chapter 3 for the phase corresponding to corner number 6, and as we will discuss in more detail when presenting the phase diagram. In that table, we also give the name of an instance of a configuration realizing each corner. These are shown in Fig. F.1 unless they have been discussed in the main body of the thesis.

### F.1.2 $J_1 - J_2 - J_{3||} - J_{3\star}$ models

To study the model

$$H = J_1 \sum_{\langle i,j \rangle_1} \sigma_i \sigma_j + J_2 \sum_{\langle i,j \rangle_2} \sigma_i \sigma_j + J_3 \sum_{\langle i,j \rangle_{3||}} \sigma_i \sigma_j + J_{3\star} \sum_{\langle i,j \rangle_{3\star}} \sigma_i \sigma_j, \quad (\text{F.3})$$

the inequalities must be written separating the two type of third neighbor correlations:

$$c_{3||} := \frac{1}{2N} \sum_{\langle i,j \rangle_{3||}} \sigma_i \sigma_j, \quad \tilde{c}_{3\star} := \frac{1}{2N} \sum_{\langle i,j \rangle_{3\star}} \sigma_i \sigma_j. \quad (\text{F.4})$$

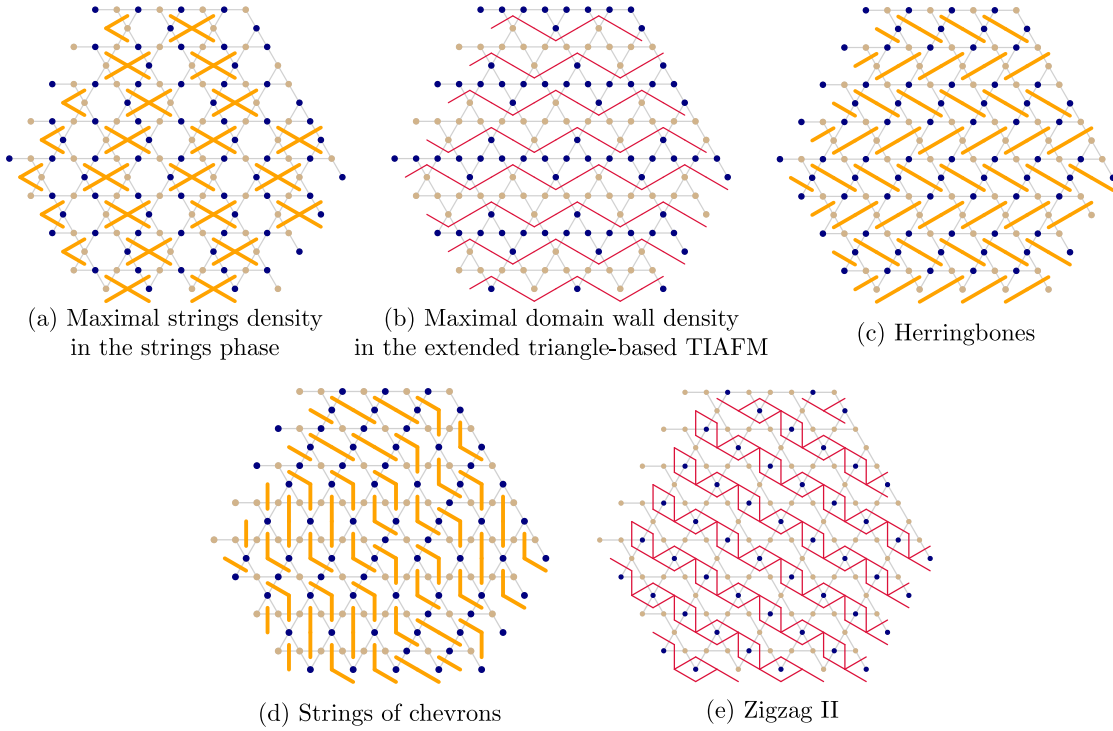


Figure E2 – Configurations appearing in the ground-state phase diagram of the  $J_1 - J_2 - J_{3||} - J_{3\star}$  models.

Note that with this definition  $-1/2 \leq \tilde{c}_{3\star} \leq 1/2$ , and the energy per site is given by

$$\frac{H}{N} = 2J_1 c_1 + 2J_2 c_2 + 2J_{3||} c_{3||} + 2J_{3\star} \tilde{c}_{3\star}. \quad (\text{E5})$$

The inequalities for the correlations can be put in the form

$$a_1 c_1 + a_2 c_2 + a_{3||} c_{3||} + a_{3\star} \tilde{c}_{3\star} \geq -1, \quad (\text{E6})$$

and the coefficients are given in Table E3. The corresponding 21 corners are given in Table E4. Importantly, we note that not all these corners are realized, and that additional inequalities would certainly be needed. A number of the corners can be related to the phases of the  $J_1 - J_2 - J_{3||}$  model. Some other corners will remain present when  $J_{3||} = J_{3\star}$  and can be related to states found there.

## F.2 Ground-state phase diagrams

### F.2.1 $J_1 - J_2 - J_{3||}$

In Sec. F.1.1 we enumerated the inequalities and corners found by Wolf and Schotte [101] for the  $J_1 - J_2 - J_{3||}$  ground-state phase diagram. In Fig. F.3 we plot this ground-state phase diagram,



## F.2. Ground-state phase diagrams

Inequality	$a_1$	$a_2$	$a_{3  }$	$a_{3\star}$	Cluster
(W1) 1	3	0	0	0	
(W2) 2	0	3	0	0	
(W3) 3	-2	1	0	0	
(W4) 4	-2	0	1	0	
(W5) 5	2	0	1	0	
(W6) 6	3	1	1	0	
(W8) 7	1	-1	-1	0	
(W10) 8	-1	-1	1	0	
9	0	0	2	2	
10	0	0	-2	2	
11	1	-1	0	-2	
12	-1	-1	0	2	
13	2	2	0	2	
14	-2	2	0	-2	
15	$\frac{5}{2}$	1	0	1	
16	$\frac{1}{2}$	-1	-1	1	
17	$-\frac{3}{2}$	-1	1	1	

Table F3 – The 17 inequalities for  $J_1 - J_2 - J_{3||} - J_{3\star}$  models on the kagome lattice as obtained from the procedure described in Sec. 1.4.1, and the corresponding clusters. These inequalities give rise to 21 corners given in Table F4.

## Appendix F. Ground-state phase diagrams

Corner	$c_1$	$c_2$	$c_{3  }$	$\tilde{c}_{3\star}$	Instance
(*)1	$-\frac{1}{3}$	$-\frac{1}{3}$	$\frac{1}{3}$	$\frac{1}{6}$	Chevrons phase(Fig. 4.4d)
2	$-\frac{1}{3}$	$-\frac{1}{3}$	1	$\frac{1}{2}$	Stripes (Fig. 4.4b)
(*)3	$-\frac{1}{3}$	0	0	$-\frac{1}{6}$	Pinwheels phase (Fig. 4.4e)
4	$-\frac{1}{3}$	$\frac{1}{3}$	$-\frac{1}{3}$	$-\frac{1}{6}$	Strings phase reference state (Fig. 4.29a)
5	$-\frac{1}{3}$	$\frac{1}{3}$	0	$-\frac{1}{2}$	Strings phase with maximal density of strings (Fig. F.2a)
6	$-\frac{1}{3}$	1	$-\frac{1}{3}$	$-\frac{1}{6}$	$\sqrt{3} \times \sqrt{3}$ (Fig. 4.4c)
7	$-\frac{1}{9}$	$-\frac{1}{3}$	$-\frac{1}{3}$	$-\frac{1}{18}$	-
8	$-\frac{1}{15}$	$-\frac{1}{3}$	$-\frac{7}{15}$	$-\frac{1}{30}$	-
9	$-\frac{1}{15}$	$-\frac{1}{3}$	$-\frac{2}{5}$	$-\frac{1}{10}$	-
10	$\frac{1}{3}$	$-\frac{1}{3}$	0	$-\frac{1}{2}$	Maximal domain wall density in the extended triangle-based TIAFM (Fig. F.2b)
(*)11	$\frac{1}{3}$	$-\frac{1}{3}$	$-\frac{1}{3}$	$-\frac{1}{6}$	Triangle-based TIAFM(Fig. F.1f)
12	$\frac{1}{3}$	$-\frac{1}{3}$	$\frac{1}{3}$	$-\frac{1}{6}$	Stripes II (Fig. F.1e)
13	$\frac{3}{7}$	$-\frac{1}{7}$	$-\frac{1}{7}$	$-\frac{5}{14}$	-
14	1	1	1	$\frac{1}{2}$	Ferromagnetic state
15	$-\frac{1}{3}$	$\frac{1}{3}$	$-\frac{1}{3}$	$\frac{1}{6}$	-
16	$-\frac{1}{3}$	$\frac{1}{3}$	$\frac{1}{3}$	$-\frac{1}{6}$	Zigzag II (Fig. F.2e)
17	$-\frac{1}{3}$	$-\frac{1}{3}$	$\frac{2}{3}$	$\frac{1}{6}$	Strings of chevrons (Fig. F.2d)
18	$-\frac{1}{3}$	$-\frac{1}{3}$	$\frac{1}{3}$	$\frac{1}{2}$	Herringbones (Fig. F.2c).
19	$\frac{1}{5}$	$\frac{1}{5}$	$-\frac{3}{5}$	$\frac{1}{10}$	-
20	0	0	-1	$\frac{1}{2}$	Ferromagnetic hexagons (Fig. F.1a)
21	0	$-\frac{1}{3}$	$-\frac{2}{3}$	$\frac{1}{6}$	Zigzag (Fig. F.1b)

Table F.4 – The 21 corners obtained from the inequalities in Table F.3. Some of the states found in studying the related  $J_1 - J_2 - J_3$  models and  $J_1 - J_2 - J_{3||}$  models can be directly identified to some of these corners; when it is the case or when the corner is easily realized the corresponding states are mentioned. Otherwise, one would have to look for configurations corresponding to these corners or find more restrictive lower bounds. The corners marked with a star correspond to macroscopically degenerate ground-state phases. Some other corners might have either subextensive entropy or extensive entropy, but what is important here is that there are at least two phases which still have a macroscopic degeneracy even when  $0 \neq J_{3||} \neq J_{3\star} \neq 0$ .

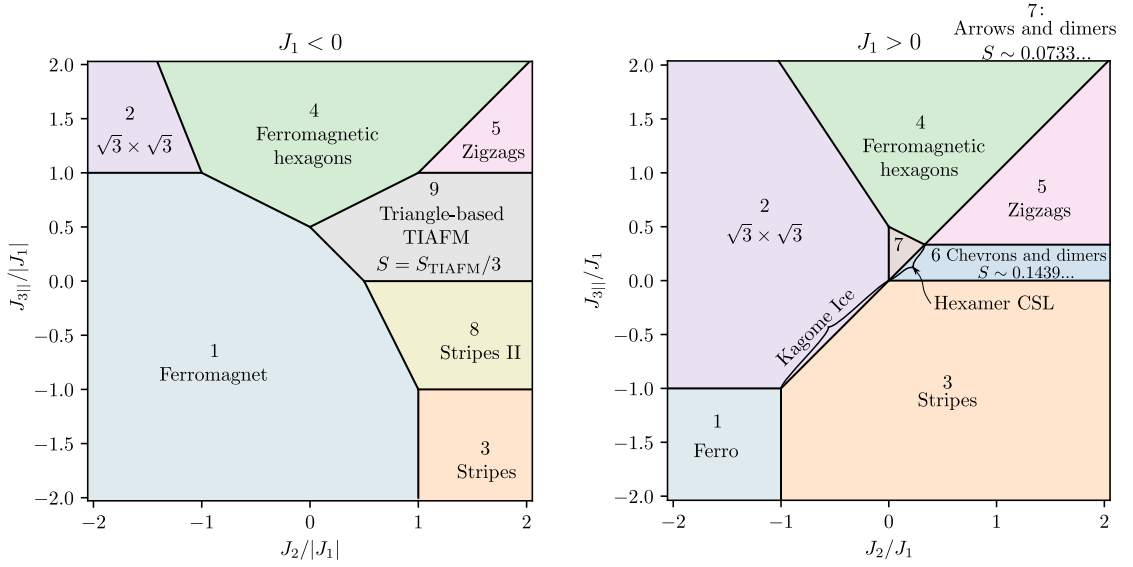


Figure F.3 – Ground-state phase diagram for  $J_1 - J_2 - J_{3||}$  models. The numbers correspond to the labels of the corners in Table F.2. Left panel: ferromagnetic nearest-neighbor couplings. Right panel: antiferromagnetic nearest-neighbor couplings. This ground-state phase diagram was first obtained in Ref. 101 for the ground-state energies. The Kagome Ice phase boundary was also studied in that work, while the Hexamer spin liquid was first studied in Ref. 222. In Ref. 160 we studied the phase for  $J_1 \gg J_2 \gg J_{3||} > 0$ . The residual entropy for the phase number 7 is a new result and was evaluated based on tensor network contractions up to  $\chi = 128$ . The phase number 9 can be related to the work we discussed in Chapter 2 (Ref. 159), so the result there is only partially new.

which is for  $J_1 - J_2 - J_{3||}$  models. Note that in that reference in Fig. 3, the labels for phases 2 and 3 were swapped in the plot (which can be checked intuitively since for ferromagnetic  $J_2$  there must be a  $\sqrt{3} \times \sqrt{3}$  ground state, or numerically by computing the locations of the phase boundaries).

On top of the results of Wolf and Schotte, we also include the residual entropies in the phases that have a macroscopic ground-state degeneracy. We note that the Kagome Ice phase boundary was already studied by Wolf and Schotte, while the Hexamer spin liquid was first studied in Ref. 222. In Ref. 160 we studied the phase for  $J_1 \gg J_2 \gg J_{3||} > 0$ . The residual entropy for the phase number 7 is a new result (to the best of our knowledge) and was evaluated based on tensor network contractions up to  $\chi = 128$ . Interestingly, we find that phase number 9 is closely related to the phase that we studied in Chapter 2, as we will discuss below when comparing Fig. F.3 to the ground-state phase diagram for  $J_{3\star} = J_{3||}$ .

Interestingly, we find that the triangle-based TIAFM phase in this case is only generated by the Type-I tiles of Chapter 2 and Ref. 159 (namely, there are no domain walls between reflection symmetry broken sectors).

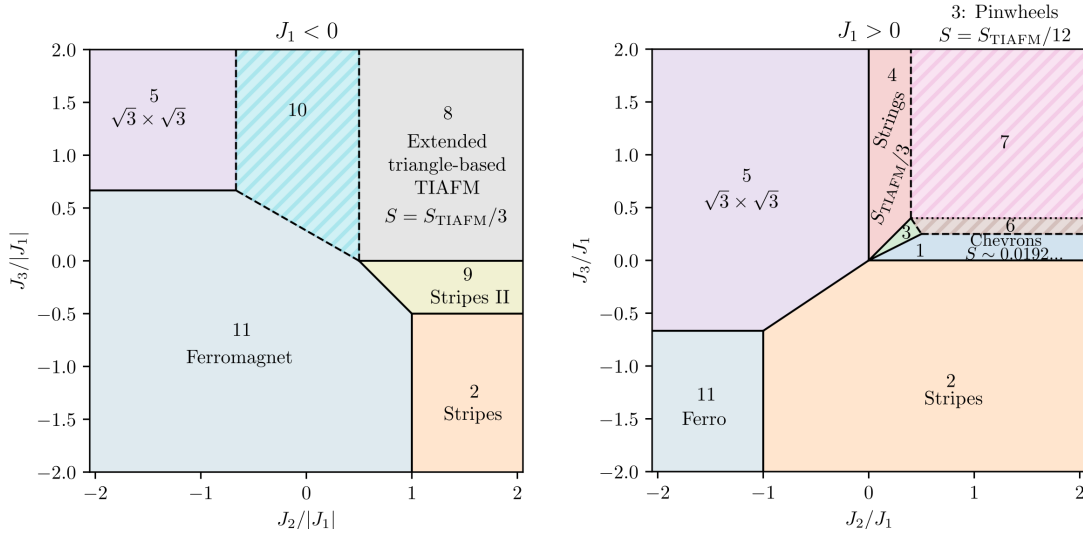


Figure F.4 – Candidate ground-state phase diagram based on the Kanamori polytope established in Chapter 4. The hatched regions correspond to corners for which no state was found, and are explored in further detail in Fig. F.10. The phases where no residual entropy is indicated are long-range ordered. The numbers refer to the number of the corresponding corner in Table F.5. The phase number 8 was studied in Chapter 2, and phases 1 to 5 in Chapter 4. The dashed boundaries are not fully established but can only potentially move towards the interior of the hatched regions.

### F.2.2 $J_1 - J_2 - J_3$

In Appendix F.1.2 we discussed the Kanamori inequalities for the  $J_1 - J_2 - J_{3||} - J_{3\star}$  model and listed 21 corners corresponding to the inequalities. Here, we want to discuss the specialization to the case where  $J_{3||} = J_{3\star} = J_3$  which is of main interest for Chapter 4.

#### Candidate ground-state phase diagram

We construct the polytope in the three-dimensional  $(c_1, c_2, c_{3||} + \tilde{c}_{3\star})$  space as detailed in Chapter 4, Sec. 4.2.1. The corners corresponding to the polytope in Fig. 4.3 are summarized in Table F.5. They give the candidate ground-state phase diagram pictured in Fig. F.4. In that Figure, the regions related to corners of the polytope for which we did not find a corresponding spin configuration are hatched. These are the regions which we focus on in detail below. Among the phases already fixed in Fig. F.4, those with a finite residual entropy are the chevrons, the pinwheels and the strings phase when  $J_1$  is antiferromagnetic, as discussed in Chapter 4, and, when  $J_1$  is ferromagnetic, the phase number 8 which is characterized by Ising degrees of freedom living on the triangles as discussed in Chapter 2. The Stripes II phase is long-range ordered.

Corner	$c_1$	$c_2$	$c_3$	Instance
(★)1	$-\frac{1}{3}$	$-\frac{1}{3}$	$\frac{1}{2}$	Chevrons phase(Fig. 4.4d)
(★)2	$-\frac{1}{3}$	$-\frac{1}{3}$	$\frac{3}{2}$	Stripes (Fig. 4.4b)
(★)3	$-\frac{1}{3}$	0	$-\frac{1}{6}$	Pinwheels phase (Fig. 4.4e)
(★)4	$-\frac{1}{3}$	$\frac{1}{3}$	$-\frac{1}{2}$	Strings phase (Fig. 4.4f)
5	$-\frac{1}{3}$	1	$-\frac{1}{2}$	$\sqrt{3} \times \sqrt{3}$ (Fig. 4.4c)
6	$-\frac{1}{9}$	$-\frac{1}{3}$	$-\frac{7}{18}$	-
7	$-\frac{1}{15}$	$-\frac{1}{3}$	$-\frac{1}{2}$	-
(★)8	$\frac{1}{3}$	$-\frac{1}{3}$	$-\frac{1}{2}$	Extended Triangle-based TIAFM (Fig. 2.11)
9	$\frac{1}{3}$	$-\frac{1}{3}$	$\frac{1}{6}$	Stripes II (Fig. F.1e)
10	$\frac{3}{7}$	$-\frac{1}{7}$	$-\frac{1}{2}$	-
11	1	1	$\frac{3}{2}$	Ferromagnetic state

Table F.5 – The 11 corners describing the polytope in Fig. 4.3. The first five corners correspond to the five phases studied in the main text. The phase 8 was studied in Chapter 2. The corners 6, 7 and 10 are not realized. The corners marked with a star correspond to ground-state phases where we established that the residual entropy is finite.

### Missing phases

In Table F.5, there are still three corners for which we did not find a configuration. We are now going to find the ground state in some of these phases and we will show that the energy lower bounds are higher than those obtained by the application of the method of Kudo and Katsura. Unfortunately, we won't be able to exhibit inequalities, but we will discuss how one should proceed from the current state of the phase diagram.

The first remark is that corners which are not (yet) realized correspond to candidate ground-state phases, shown with a hatching in Fig. F.4. Importantly, the dashed lines that stand for phase boundaries between a known phase and a candidate ground-state phase can only be left invariant or move further into the unknown phases. Indeed, let us remember that phases correspond to corners of the polytope, phase boundaries to 1-dimensional edges, and so on. Now, consider two candidate phases sharing a phase boundary (i.e. two corners sharing an edge), of which one (phase/corner  $A$ ) corresponds to a proven corner while the other does not (phase/corner  $B$ ). Consider the additional inequalities needed to remove corner  $B$ . There are two possibilities for each such inequality: either the corresponding plane goes through corner  $A$ , or it does not. If it does not, the faces of the polytope in a close neighborhood of  $A$  are left invariant and the location of the phase boundaries of phase  $A$  are not affected.

If the plane does go through corner  $A$ , by convexity and because it corresponds to an inequality

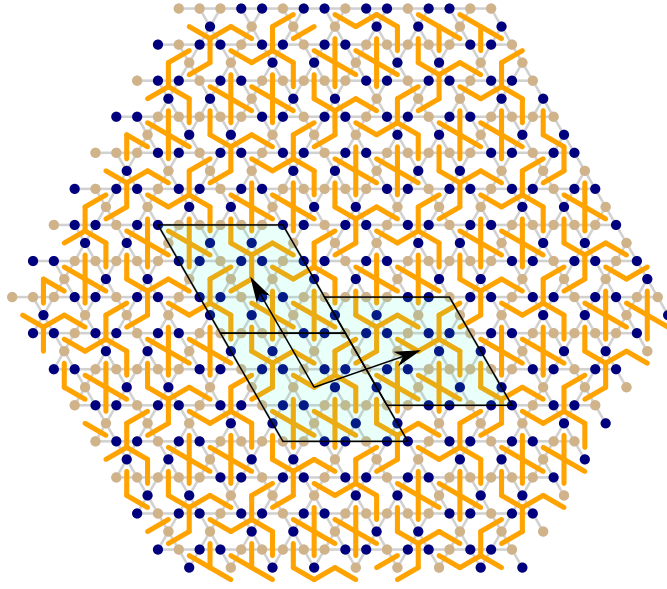


Figure E5 – Long-range ordered ground state corresponding to the energy in Eq. E8 (Phase 6A, see Fig. F10).

that removes corner  $B$ , it has to correspond to an inequality that eliminates the  $\overline{AB}$  edge. The question is then whether the vectors  $\vec{J} \perp \overline{AB}$  that (from corner  $A$ ) point to the interior of the polytope, and which in the phase diagram are on the phase boundary between phases  $A$  and  $B$ , then fall into phase  $A$  or not when that inequality is included. For each such vector, its orthogonal plane contains the  $\overline{AB}$  segment, which is *excluded* of the polytope by the new inequalities. Therefore, the corner  $A$  now corresponds to the most extremal point in the polytope for this set of vectors. Hence, the former phase boundary falls into phase  $A$  when additional inequalities are included that eliminate the  $\overline{AB}$  edge.

Now, let us see if we can find stricter lower bounds for phases 6, 7 and 10 in Fig. F4, corresponding to corners 6, 7 and 10 in Table E5. There are several ways to proceed. One possibility would be to follow the approach suggested by A. de Walle in his thesis [157]. Another option, since the phase diagram is now somewhat reduced, is to target the specific phases using the lower bounds from the Huang approach together with upper bounds from Monte-Carlo. This has the advantage that we can directly test candidate ground-state lower bounds by constructing the tensor network and trying to contract it, which allows to eliminate some options before running the challenging Monte Carlo simulations. Furthermore, the ground-state tiles typically give a good indication of the type of configuration that is to be expected. The cost of applying this method is that one does not obtain planes of the inequality polytope but rather corners.

Let us start with phase number 6. The energy lower bound from the Kanamori polytope is

$$E_6^{\text{Polytope}} \geq -\frac{2}{9}J_1 - \frac{2}{3}J_2 - \frac{7}{9}J_3. \quad (\text{E7})$$

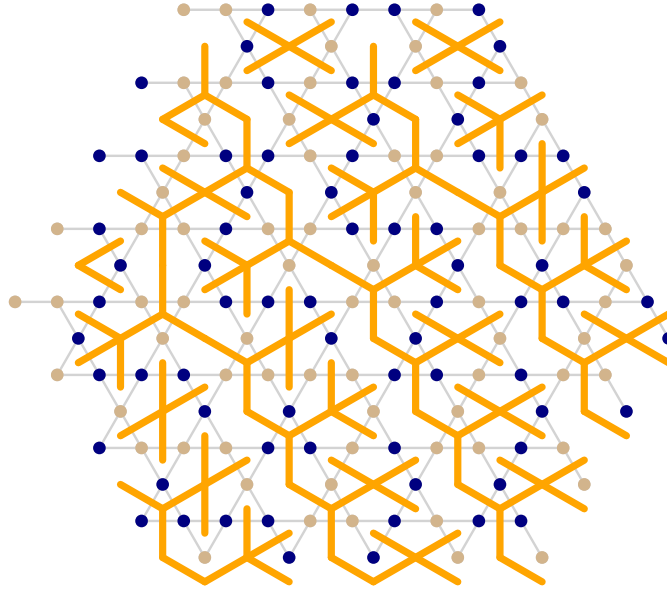


Figure E.6 – An example ground-state for phase 7A (see Fig. E.10).

However, we are not able to find states with the Monte-Carlo simulations that correspond to such correlations. Furthermore, when trying to compute this energy lower bound for points well within the phase  $((J_1, J_2, J_3) = \{(1, 1, 0.3), (1, 0.8, 0.3), (1, 1, 0.35)\})$  with the method of Chapter 2, we find that the lower bound constructed that way corresponds to

$$E_6^{\text{Tiles}} \geq -\frac{1}{3}J_1 - \frac{2}{3}J_2 - \frac{1}{3}J_3. \quad (\text{E.8})$$

Additionally, the tensor network contraction converges with eigenvalue 1. Importantly, we have

$$E_6^{\text{Tiles}} \geq E_6^{\text{Polytope}} \iff 4J_3 \geq J_1 = E_{6A} \quad (\text{E.9})$$

which means that this lower bound is larger than that obtained from the Kanamori method everywhere above the  $J_3/J_1 = 1/4$  line which denotes the transition with the Chevrons phase. This implies that there must be stronger inequalities removing corner number 6 in Table E.5 and instead giving rise to a corner corresponding to Eq. E.8. Furthermore, we find that this new corner must be realized, since the configuration in Fig. E.5 has correlations corresponding to Eq. E.8. Therefore, even though we are not using the Kanamori approach here, we just found a new phase whose ground-state energy is proven rigorously, and we found evidence that this phase has long range order. Interestingly, in this ground-state phase we find 96 ground-state tiles based on a single star, while the unit cell in Fig. E.5 requires 9 hexagons, which illustrates the power of the tessellation approach where weights are optimized to find the ground-state tiles (note that we had to allow for two-site symmetry breaking for the tensor network contraction to converge). Below, we will refer to this phase as phase number 6A.

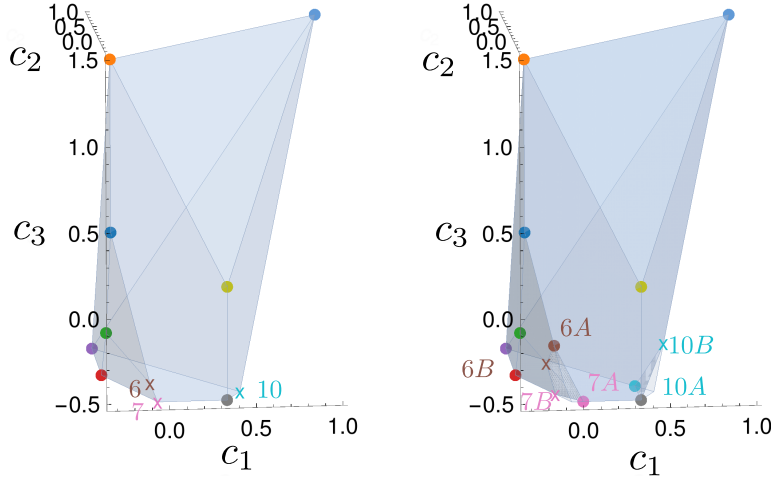


Figure E7 – Polytope of inequalities before and after taking into account the new ground-state phases. The corners marked with a cross need to be verified while the ones marked with a point have at least one associated configuration.

Let us now have a look at phase number 7 in Fig. F4 and Table F4. From the polytope we have

$$E_7^{\text{Polytope}} \geq -\frac{2}{15}J_1 - \frac{2}{3}J_2 - J_3. \quad (\text{F.10})$$

First, note that this energy becomes lower than that of phase number 6 at some point, so we still have to consider that corner. We start by considering the region where  $J_2, J_3$  are both bigger than  $J_1$ , which is well into that phase. Now, using the same approach as for phase 6, we find a very interesting result: not only does the tiling construction give a ground-state energy lower bound which is slightly higher than that obtained by the Kanamori method:

$$E_7^{\text{Tiles}} \geq -\frac{2}{3}J_2 - J_3, \quad (\text{F.11})$$

but the tensor network contraction of the 150 ground-state tiles converges to a finite value of the residual entropy. We only tried small bond dimensions as of the writing of this thesis, but for  $\chi = 18$  we obtain  $S \cong 0.1075$  which is strongly suggestive of another phase with the TIAFM residual entropy. Interestingly, this corner was already present in the  $J_1 - J_2 - J_{3\parallel}$  ground-state phase diagram, and also in the  $J_1 - J_2 - J_{3\parallel} - J_{3\star}$  list of corners, where it corresponds to the Zigzag phase. But in the process of selecting the  $J_{3\parallel} = J_{3\star}$  case, it has been screened by another, spurious corner of the polytope. We show an instance of ground state for this phase in Fig. F6, where we can see a modification of the simple zigzag pattern. Below, we will refer to this phase as phase number 7A.

Again, the ground-state energy in Eq. F.11 is larger than the polytope lower bound everywhere where  $J_1 > 0$  so the former phase 7 is completely eliminated.



It looks like we have found the ground-state energies for phases number 6 and 7. However, a very important point to recognize is that the lower bounds obtained from the tiles, unlike the Kanamori lower bounds, are not computed for a full range of couplings, and therefore require a more thorough look at the phase diagram to check for additional phases. Let us go back to the Kanamori polytope and include these new corners (Fig. E.7). The corner 6A is on the  $\overline{1-6}$  edge and the corner 7A is on the  $\overline{1-8}$  edge. From their position, we can immediately tell that there must be at least one additional phase. Indeed, consider whether one can add one or more inequalities to remove corners 6 and 7 and corresponding to planes going through corners 6A and/or 7A but without creating another corner. This can only be done by having an inequality corresponding to a plane that goes through both corners 6A and 7A. But this inequality will create a new corner unless it is also saturated at corners 3 and 4. However, one can easily check that corners 6A, 7A, 3 and 4 do not all belong to the same plane, so there must be at least one additional corner.

We will not find these new corners exactly but we can give an outline of the phase diagram with stronger ground-state energy lower bounds. Let us note that a more systematic study should probably involve going back to the original approach of Kanamori (see e.g [205]) as reformulated by Ducastelle [25] and van De Walle [157] to eliminate corners of the Kanamori polytope. Here, we simply see how far the approach we applied so far can take us.

First, we note that at large  $J_2$ , exactly at the phase boundary between the phases 6A and 7A, we find a ground-state energy lower bound which matches the energy of phases 6A and 7A. Therefore, there must be a phase boundary there and correspondingly an edge in the Kanamori polytope between these two corners. Doing the same at the phase boundary between phase 7A and phase 4, we find instead that the ground-state energy lower bound is lower than the energy expected at the phase boundary, indicative of an additional phase, with 66 tiles. Similarly, exploring the phase boundary between phases 6A and 3, we also find another ground-state energy lower bound with 76 tiles. We find a direct boundary between the two phases, however in this whole region the tensor network contractions do not converge, indicating that these two ground-state energy lower bounds are probably not saturated.

Therefore, we now stand with two new ground-state phases with energies

$$E_{6A} = -\frac{1}{3}J_1 - \frac{2}{3}J_2 - \frac{1}{3}J_3, \quad E_{7A} = -\frac{2}{3}J_2 - J_3, \quad (\text{E.12})$$

and two new candidate ground-state phases with energies

$$E_{6B} \geq -\frac{2}{5}J_1 - \frac{2}{5}J_2 - \frac{3}{5}J_3, \quad E_{7B} \geq -\frac{2}{7}J_1 - \frac{2}{7}J_2 - J_3. \quad (\text{E.13})$$

These are shown in Figs. E.7 and E.10.

We now move to phase number 10. Again, we find that the lower bound

$$E_{10}^{\text{Polytope}} \geq \frac{6}{7}J_1 - \frac{2}{7}J_2 - J_3 \quad (\text{E.14})$$

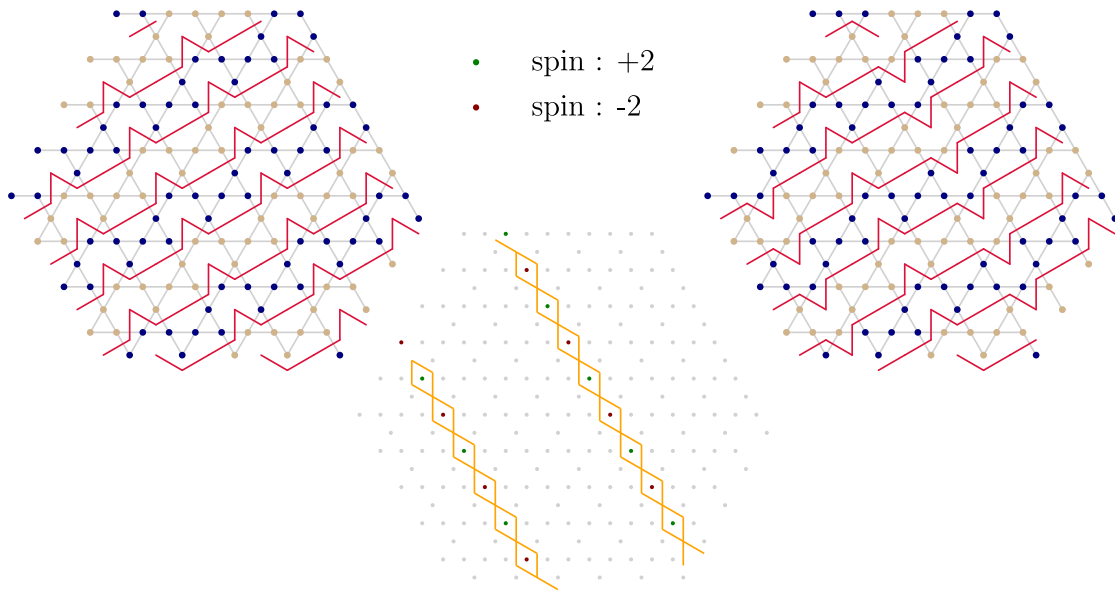


Figure F8 – Ground states suggesting a sub-extensive degeneracy in phase 10A (“Stripes III phase” see Fig. F.10).

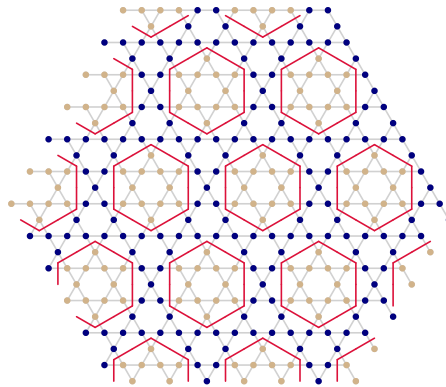


Figure F9 – State giving a ground-state energy upper bound for phase 10B (see Fig. F.10, Eq. F.16)

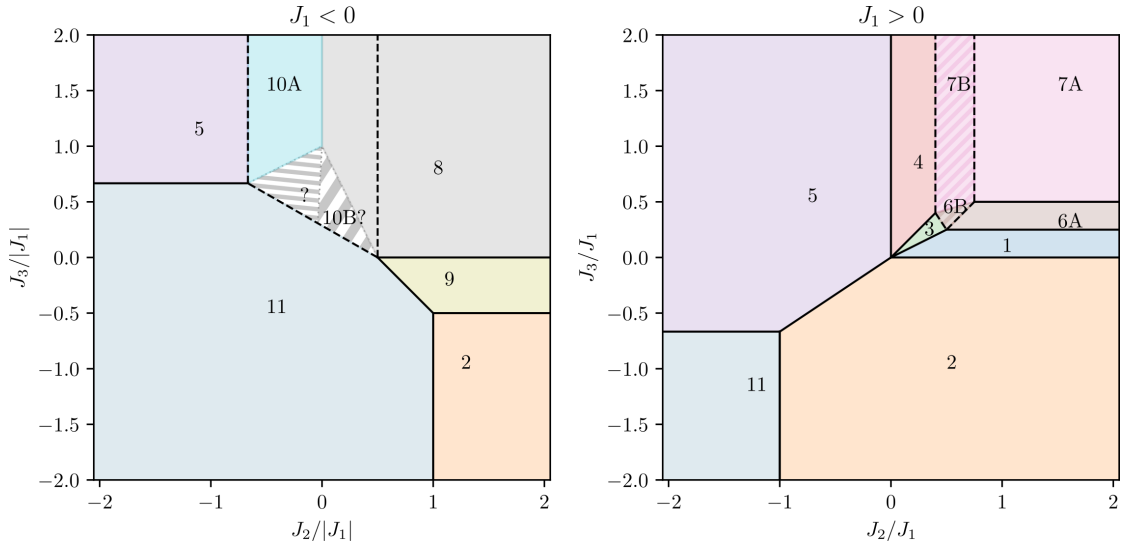


Figure F.10 – Updated candidate ground-state phase diagram as compared to Fig. F.4. The numbers refer to the number of the corresponding corner in Table E.5 or to the equations discussed in the main text. Phase 6A is long-range ordered, phase 7A has a finite residual entropy per site of the order of  $S_{\text{TIAFM}}/3$ , and phase 10A has probably a sub-extensive residual entropy. The hatched regions correspond to corners for which no state was found. In regions 6B and 7B we found a ground-state energy lower bound stronger than the one from the original polytope, but still probably not saturated. The region 10B with a question mark requires additional work, and for now we only have a ground-state energy lower bound stronger than the Kanamori one at  $J_2 > 0$ .

is probably too low, as we do obtain it with the one-star lower bound construction but the related tensor network contraction does not converge. Using a two-stars unit cell instead, we find

$$E_{10A} = \frac{2}{3}J_1 - J_3 \quad (\text{F.15})$$

with 44 ground-state tiles. The tensor network based on these tiles converges to a zero residual entropy per site. Interestingly, the corresponding Monte-Carlo simulations show the possibility of “topological” updates, as illustrated in Fig. F.8, which, together with the tensor network result, gives extremely strong evidence of a sub-extensive residual entropy in that phase.

We find that this new phase has direct transitions to the triangle-based TIAFM (phase 8) and the  $\sqrt{3} \times \sqrt{3}$  phase (phase 5). However, both the Monte-Carlo simulations and the one-star and two-star lower bound computations show that it does not have a direct transition to the ferromagnetic ground state. Instead, there, for positive  $J_2$  we find another phase with ground-state energy

$$E_{10B} \geq J_1 - \frac{1}{2}J_3, \quad E_{10B} \leq \frac{10}{9}J_1 + \frac{2}{9}J_2 - \frac{1}{9}J_3 \quad (\text{F.16})$$

where the upper bound is obtained from the Monte-Carlo snapshot in Fig. F.9 and the lower bound is found using the linear program with one and/or two stars. However the contraction

of the tensor network does not converge, and in fact with two stars we obtain that all the tiles are spurious. This suggests that one ought to look for larger clusters. What's more, when  $J_2$  is negative, we find, with one star, the same lower bound as with the Kanamori approach, and with two stars, results suggesting that another phase must be also present. However, for the points that we sampled, the results are not consistent enough to provided a new lower bound equation, and a further investigation is required in this region of the phase diagram.

The results are summarized on the Kanamori polytope in Fig. E.7 and on the phase diagram in Fig. E.10. Overall, we found a number of complex phases with either extensive residual entropy, sub-extensive residual entropy (phase 10A), or long-range order. In Fig. E.10, the ground-state energy is proven exactly in all the non-hatched regions. A more systematic approach is required for the hatched regions, and our next step will be to dive into the approaches suggested in Refs. 25, 157, 205, 286, 287. The ground-state energy upper bound for phase 10B also suggests that the approach for the energy-lower bounds based on tilings would gain from being able to look at larger clusters: to allow this, a first step is to systematically implement the use of cluster symmetries, as hinted to in Chapter 2.

### F.2.3 Comparison of the phase diagrams

With this in hands we can now discuss and contrast the ground-state phase diagrams of the  $J_1 - J_2 - J_3||$  (Fig. E.3) and  $J_1 - J_2 - J_3$  models (Figs. E.4 and E.10). Clearly, the difference between these two ground-state phase diagrams mostly comes from the fact that the  $J_{3||}$  interactions form three independent square sublattices in the model of Wolf and Schotte, while the  $J_3$  interactions form three triangular sublattices in the  $J_1 - J_2 - J_3$  model.

For a ferromagnetic  $J_3$  coupling, this change of sublattices has only a limited effect on the ground-state phases:

1. It changes slightly the location of the phase boundaries,
2. It lifts the degeneracy of the Kagome ice phase boundary between the stripes and  $\sqrt{3} \times \sqrt{3}$  phases.

In contrast, for an antiferromagnetic  $J_3$  coupling, the change from square sublattices to triangular sublattices introduces some additional frustration in the system, and this in turn affects the very nature of the ground-state phases.

Let us start this discussion with the ferromagnetic nearest-neighbor couplings case. When  $J_2$  is also ferromagnetic and large, both models select the ferromagnetic or the  $\sqrt{3} \times \sqrt{3}$  configurations as ground states depending on the value of the third-neighbor couplings. When  $J_2$  is *antiferromagnetic* and large, we obtain two related ground-state phases in the two models: when  $J_{3\star} = 0$ , the selected ground-state phase has a direct mapping to the TIAFM ground-state phase with degrees of freedom living on either up or down triangles (corresponding to the

Type-I tiles ensemble of Chapter 2; setting  $J_{3\star} = J_{3||}$  adds a number of tiles to the ground state, however without changing the entropy, as we established in Chapter 2. Interestingly, looking back at table F.4 we can notice that corners 10 and 11 correspond to a long-range ordered state (Fig. F.2b) and to the triangle-based TIAFM, respectively. We can therefore interpret the results from Chapter 2 and Fig. F.4 regarding the extended triangle-based TIAFM as the fact that the edge between these two corners is in the plane perpendicular to  $J_{3\star} = J_{3||}$  in this region of the phase diagram, and that the tiles from both corners are allowed to tile without an energy cost.

Now, when  $J_2$  is small in absolute value and  $J_3$  dominates, we find two completely different behaviors depending on whether  $J_{3\star} = 0$  or not. This can be understood partially by noticing that the ferromagnetic hexagons long-range ordered state (Fig. F.1a), which is favored when  $J_{3\star} = 0$ , and although it does correspond to an ice-rule respecting configuration for the  $J_3$  triangles, does not optimize the nearest-neighbor energy. At the same time, the Stripes III phase (10A Fig. F.8), which has a sub-extensive degeneracy, is only optimal when considering triangular sublattices and does not optimize the third-neighbor energy on the square sublattices. The fact that the Zigzag phase at large  $J_2, J_{3||}$  is eliminated by  $J_{3\star} = J_{3||}$  can be understood in a similar fashion.

We turn to the antiferromagnetic nearest-neighbor couplings case. There, we find that the changes essentially occur in the antiferromagnetic second- and third-neighbor couplings quadrant. In particular, while only a small region of the phase diagram has macroscopic ground-state degeneracy in the  $J_1 - J_2 - J_{3||}$  model (phases 6 and 7), which can be understood as mainly a partial lifting of the nearest-neighbor ground-state degeneracy, almost all the phases that we were able to identify in the  $J_1 - J_2 - J_3$  model have a macroscopic ground-state degeneracy and the competition between these phases gives rise to a complex phase diagram that we did not elucidate completely.

We discuss the main results for  $J_1 \gg J_2, J_3$  in Chapter 4, but let us make two more remarks. First, that in phase 7A we identify yet another phase with the TIAFM ground-state entropy. And second, that the difference in the partial lifting of the  $J_1 - J_2$  ground-state degeneracy depending on the value of  $J_{3\star}$  can be mostly understood from the fact that  $J_{3\star}$  will tend to eliminate ground-state tiles containing straight dimers.

Finally, it should be noted that by working on these two reduced models, we can actually conclude that there are some macroscopically degenerate ground-state phases in the complete  $J_1 - J_2 - J_{3||} - J_{3\star}$  model (not only for not fine-tuned points), and we are able to identify most of the corners for this more general ground-state phase diagram.



# G Complementary plots for the $J_1 \gg J_2, J_3$ model

## G.1 Residual entropy and phase boundaries

The  $J_1 - J_2$  model was discussed in Chapter 3 and 4. In the first case we obtained the residual entropy using a dual tensor network construction; here, we show the results based on the ground-state tiles construction (Fig. G.1), which gives us the same result.

What is interesting is that based on the discussion in Sec. 2.5, one can note that the dual tensor network construction in Chapter 3 is actually not optimal, in that it will include spurious tiles in the ground state manifold. Yet, the tensor network contraction converges and the results are independent of the presence of these spurious tiles. At the same time, in other models we have seen that the spurious tiles can really spoil the convergence. It would therefore be interesting to explore deeper the heuristic argument of Chapter 2, using these seemingly contradictory examples as a basis.

At the phase boundary between the chevrons and the pinwheels phases, there are no new tiles. Additionally, it is easy to see from Figs. 4.13 and 4.18 that there are no tiles belonging to both phases. One can wonder whether the two phases can coexist; this simply relates to whether tiles belonging to both phases can tile together. If such phase mixing is possible, then the residual entropy can be larger than in both neighboring phases (otherwise, it will be the maximum of the two). A Monte Carlo snapshot on a small system size, in Fig. G.2, shows that the tiles from both phases can tile together. This is in agreement with the tensor network result, shown in Fig. G.3:

$$S = 0.0926 \pm 2 \cdot 10^{-4} \quad (\text{G.1})$$

The phase boundary between the pinwheels and the strings phase has a residual entropy which is approximately

$$S_{J_2=J_3} = 0.16825 \pm 5 \cdot 10^{-5}. \quad (\text{G.2})$$

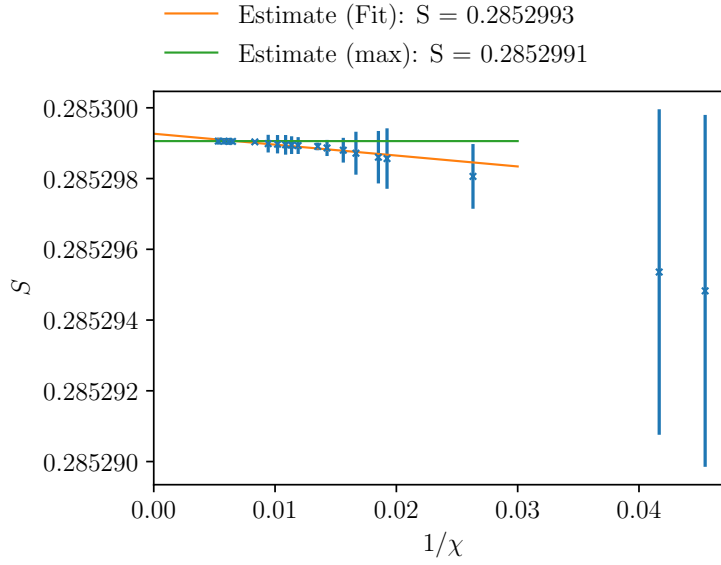


Figure G.1 – Residual entropy per site of the  $J_1$ - $J_2$  model.

Finally, when  $J_2 = 0$  and  $J_3$  is antiferromagnetic, we also find a finite residual entropy:

$$S_{J_1-J_3} = 0.24613 \pm 2 \cdot 10^{-5}. \quad (\text{G.3})$$

## G.2 State not belonging to the chevrons phase

In Fig. G.6 we show a configuration that has chevrons but is not made by the tiles shown in Fig. 4.13.

## G.3 TIAFM spin-spin correlations

In Fig. G.7 we plot the spin-spin correlations in the ground-state phase of the TIAFM based on the tensor network construction, which we compare to the results by Stephenson, showing an excellent agreement.



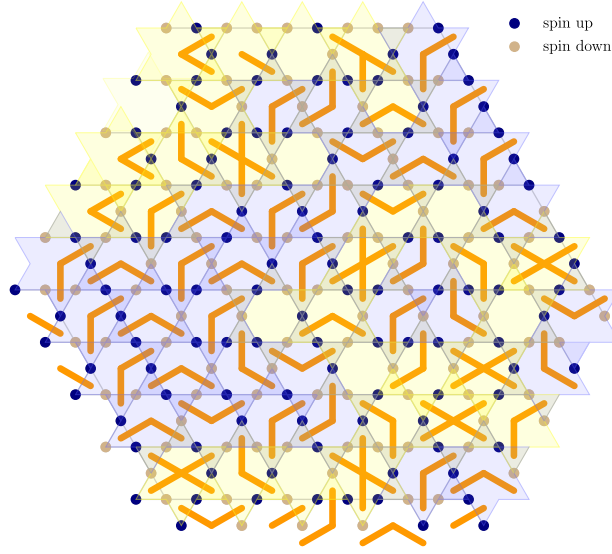


Figure G.2 – Monte Carlo snapshot - phase mixing at the boundary between the chevrons and the pinwheels phases. The tiles can be associated with either the trapezoidal phase (in blue, see Fig. 4.13) or the pinwheel phase (in yellow, see Fig. 4.18)

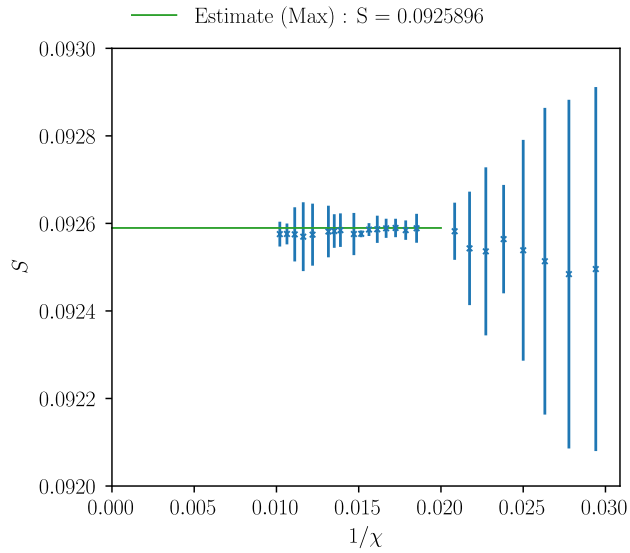


Figure G.3 – Residual entropy of the model at the  $J_3 = J_2/2$  point (boundary between the chevrons and pinwheels phases), from tensor networks, for bond dimensions ranging from  $\chi = 34$  to  $\chi = 108$

## Appendix G. Complementary plots for the $J_1 \gg J_2, J_3$ model

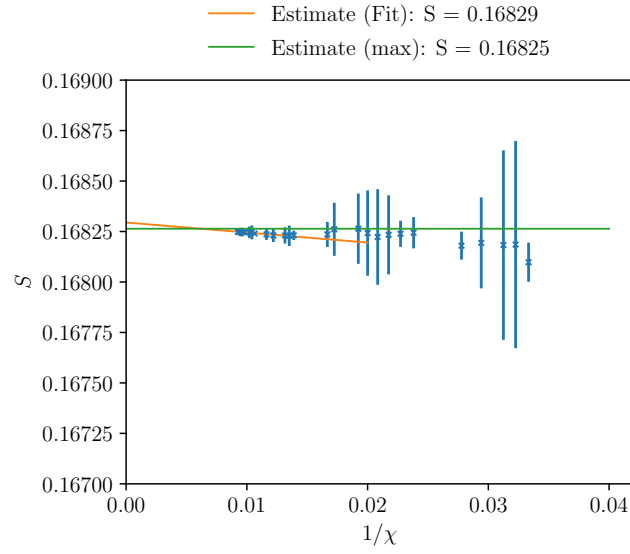


Figure G.4 – Residual entropy of the model at the  $J_3 = J_2$  point, from tensor networks, for bond dimensions ranging from  $\chi = 34$  to  $\chi = 98$

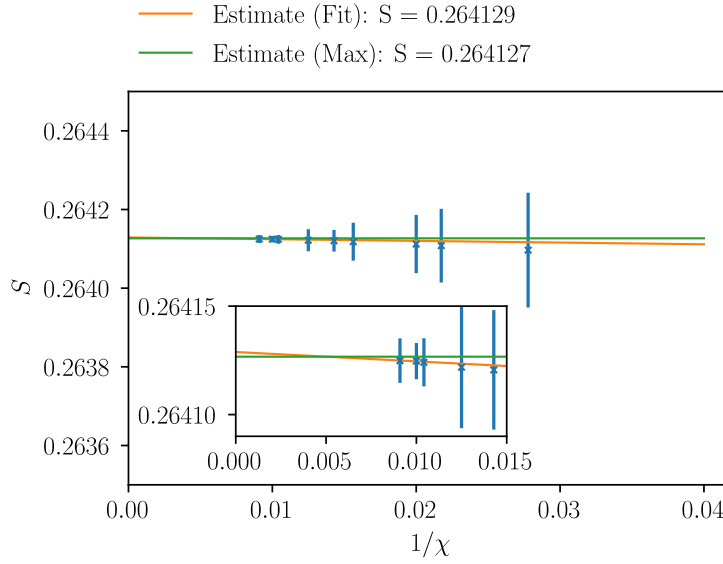


Figure G.5 – Residual entropy per site of the  $J_1$ - $J_3$  model (boundary between the strings phase and the  $\sqrt{3} \times \sqrt{3}$  phase), from tensor networks, for bond dimensions ranging from  $\chi = 36$  to  $\chi = 110$ .

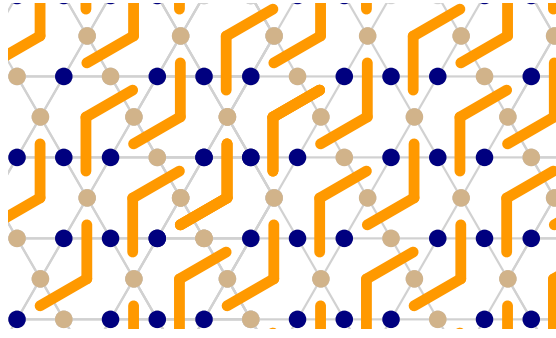


Figure G.6 – Example of configuration that does not belong to the chevrons phase.

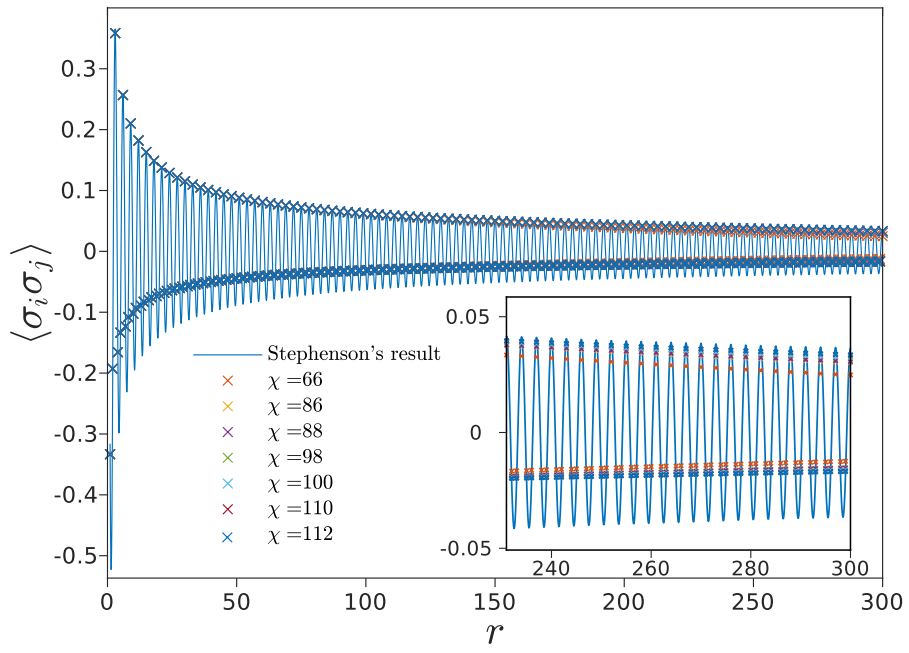


Figure G.7 – Spin-spin correlations in the TIAFM ground-state manifold from tensor network computations as compared to the result by Stephenson [35]



# Bibliography

- [1] W. Lenz, Beitrag zum Verständnis der magnetischen Erscheinungen in festen Körpern, [Phys. Zetischr. \*\*21\*\*, 613–615 \(1920\)](#).
- [2] W. Pauli, [Le Magnétisme, Rapports et Discussions du Sixième Conseil de Physique tenu à Bruxelles du 20 au 25 octobre 1930 \(1932\)](#).
- [3] E. Ising, *Beitrag zur Theorie des Ferro- und Paramagnetismus*, [Ph.D. thesis](#), Universität Hamburg (1924).
- [4] E. Ising, [Contribution to the theory of ferromagnetism \(translation\)](#) (1925).
- [5] E. Ising, Beitrag zur Theorie des Ferromagnetismus, [Z. Phys. \*\*31\*\*, 253–258 \(1925\)](#).
- [6] W. Heisenberg, Zur Theorie des Ferromagnetismus, [Z. Phys. \*\*49\*\*, 619–636 \(1928\)](#).
- [7] T. Ising, R. Folk, R. Kenna, B. Berche, and Y. Holovatch, The fate of Ernst Ising and the fate of his model, [Journal of Physical studies \*\*21\*\*, 3002 \(2017\)](#).
- [8] S. G. Brush, History of the Lenz-Ising model, [Rev. Mod. Phys. \*\*39\*\*, 883–893 \(1967\)](#).
- [9] H. A. Kramers and G. H. Wannier, Statistics of the two-dimensional ferromagnet. Part I, [Phys. Rev. \*\*60\*\*, 252–262 \(1941\)](#).
- [10] H. A. Kramers and G. H. Wannier, Statistics of the two-dimensional ferromagnet. Part II, [Phys. Rev. \*\*60\*\*, 263–276 \(1941\)](#).
- [11] R. J. Baxter, Dimers on a rectangular lattice, [J. Math. Phys. \*\*9\*\*, 650–654 \(1968\)](#).
- [12] K. Husimi and I. Syôzi, The statistics of honeycomb and triangular lattice. I, [Prog. Theor. Phys. \*\*5\*\*, 177–186 \(1950\)](#).
- [13] Y. Nambu, A note on the eigenvalue problem in crystal statistics, [Prog. Theor. Phys. \*\*5\*\*, 1–13 \(1950\)](#).
- [14] G. H. Wannier, Antiferromagnetism. The triangular Ising net, [Phys. Rev. \*\*79\*\*, 357–364 \(1950\)](#).

## Bibliography

---

- [15] G. H. Wannier, Antiferromagnetism. The triangular Ising net, [Phys. Rev. B \*\*7\*\*, 5017–5017 \(1973\)](#).
- [16] R. Houtappel, Order-disorder in hexagonal lattices, [Physica \*\*16\*\*, 425–455 \(1950\)](#).
- [17] I. Syôzi, Statistics of kagomé Lattice, [Prog. Theor. Phys. \*\*6\*\*, 306–308 \(1951\)](#).
- [18] K. Kanô and S. Naya, Antiferromagnetism. The kagomé Ising net, [Prog. Theor. Phys. \*\*10\*\*, 158–172 \(1953\)](#).
- [19] L. Onsager, Crystal statistics. I. A two-dimensional model with an order-disorder transition, [Phys. Rev. \*\*65\*\*, 117–149 \(1944\)](#).
- [20] B. Kaufman, Crystal statistics. II. Partition function evaluated by spinor analysis, [Phys. Rev. \*\*76\*\*, 1232–1243 \(1949\)](#).
- [21] M. E. Fisher, On the dimer solution of planar Ising models, [J. Math. Phys. \*\*7\*\*, 1776–1781 \(1966\)](#).
- [22] D. Poland, S. Rychkov, and A. Vichi, The conformal bootstrap: Theory, numerical techniques, and applications, [Rev. Mod. Phys. \*\*91\*\*, 015002 \(2019\)](#).
- [23] S. F. Edwards and P. W. Anderson, Theory of spin glasses, [J. Phys. F: Met. Phys. \*\*5\*\*, 965–974 \(1975\)](#).
- [24] D. Sherrington and S. Kirkpatrick, Solvable model of a spin-glass, [Phys. Rev. Lett. \*\*35\*\*, 1792–1796 \(1975\)](#).
- [25] F. Ducastelle, *Order and Phase Stability in Alloys*, edited by F. de Boer and D. Perrifor, Cohesion and Structure No. 3 (North-Holland, Elsevier Science Publisher, Amsterdam, 1991) (No online source found).
- [26] B. Nienhuis, H. J. Hilhorst, and H. W. J. Blote, Triangular SOS models and cubic-crystal shapes, [J. Phys. A: Math. Gen. \*\*17\*\*, 3559–3581 \(1984\)](#).
- [27] C. Castellano, S. Fortunato, and V. Loreto, Statistical physics of social dynamics, [Rev. Mod. Phys. \*\*81\*\*, 591–646 \(2009\)](#).
- [28] W.-X. Zhou and D. Sornette, Self-organizing Ising model of financial markets, [Eur. Phys. J. B \*\*55\*\*, 175–181 \(2007\)](#).
- [29] G. Toulouse, Theory of the frustration effect in spin glasses: I, in [Spin Glass Theory and Beyond](#), World Scientific Lecture Notes in Physics, Vol. 9, edited by M. Mezard, G. Parisi, and M. A. Virasoro (World Scientific, Singapore, 1987) pp. 99–103, original article in [30].
- [30] G. Toulouse, Theory of the frustration effect in spin glasses: I, [Comm. Phys. \*\*2\*\*, 115–119 \(1977\)](#).

- 
- [31] J.-F. Sadoc and R. Mosseri, Preface, in *Geometrical Frustration*, Collection Alea-Saclay: Monographs and Texts in Statistical Physics (Cambridge University Press, 1999) pp. xi–xii.
- [32] J.-F. Sadoc and R. Mosseri, Quasiperiodic order and frustration, in *Geometrical Frustration*, Collection Alea-Saclay: Monographs and Texts in Statistical Physics (Cambridge University Press, 1999) pp. 196–213.
- [33] P. Ronceray and B. Le Floch, Range of geometrical frustration in lattice spin models, *Phys. Rev. E* **100**, 052150 (2019).
- [34] S. E. Korshunov, F. Mila, and K. Penc, Degeneracy and ordering of the noncoplanar phase of the classical bilinear-biquadratic heisenberg model on the triangular lattice, *Phys. Rev. B* **85**, 174420 (2012).
- [35] J. Stephenson, Ising-model spin correlations on the triangular lattice. III. Isotropic antiferromagnetic lattice, *J. Math. Phys.* **11**, 413–419 (1970).
- [36] A. Sütő, Models of superfrustration, *Z. Phys. B* **44**, 121–127 (1981).
- [37] W. Apel and H.-U. Everts, Correlations in the Ising antiferromagnet on the anisotropic kagome lattice, *J. Stat. Mech.* **2011**, P09002 (2011).
- [38] R. Kotecký, J. Salas, and A. D. Sokal, Phase transition in the three-state Potts antiferromagnet on the diced lattice, *Phys. Rev. Lett.* **101**, 030601 (2008).
- [39] W. F. Giauque and M. F. Ashley, Molecular rotation in ice at 10°K. Free energy of formation and entropy of water, *Phys. Rev.* **43**, 81–82 (1933).
- [40] L. Pauling, The structure and entropy of ice and of other crystals with some randomness of atomic arrangement, *J. Am. Chem. Soc.* **57**, 2680–2684 (1935).
- [41] J. D. Bernal and R. H. Fowler, A theory of water and ionic solution, with particular reference to hydrogen and hydroxyl ions, *J. Chem. Phys.* **1**, 515–548 (1933).
- [42] P. W. Anderson, Ordering and antiferromagnetism in ferrites, *Phys. Rev.* **102**, 1008–1013 (1956).
- [43] M. J. Harris, S. T. Bramwell, D. F. McMorrow, T. Zeiske, and K. W. Godfrey, Geometrical frustration in the ferromagnetic pyrochlore  $\text{Ho}_2\text{Ti}_2\text{O}_7$ , *Phys. Rev. Lett.* **79**, 2554–2557 (1997).
- [44] S. T. Bramwell and M. J. Harris, Frustration in Ising-type spin models on the pyrochlore lattice, *J. Phys.: Condens. Matter* **10**, L215–L220 (1998).
- [45] A. S. Wills, A. Harrison, C. Ritter, and R. I. Smith, Magnetic properties of pure and diamagnetically doped jarosites: Model kagomé antiferromagnets with variable coverage of the magnetic lattice, *Phys. Rev. B* **61**, 6156–6169 (2000).

## Bibliography

---

- [46] P. Mendels and A. S. Wills, Kagome antiferromagnets: Materials vs spin liquid behaviors, in [47], pp. 207–238.
- [47] C. Lacroix, P. Mendels, and F. Mila, *Introduction to Frustrated Magnetism: Materials, Experiments, Theory*, edited by C. Lacroix, P. Mendels, and F. Mila (Springer-Verlag, Berlin, Heidelberg, 2001).
- [48] L. Balents, Spin liquids in frustrated magnets, [Nature](#) **464**, 199–208 (2010).
- [49] P. Mendels and F. Bert, Quantum kagome antiferromagnet  $\text{ZnCu}_3(\text{OH})_6\text{Cl}_2$ , [J. Phys. Soc. Jpn.](#) **79**, 011001 (2010).
- [50] M. R. Norman, Colloquium: Herbertsmithite and the search for the quantum spin liquid, [Rev. Mod. Phys.](#) **88**, 041002 (2016).
- [51] B. Fåk, E. Kermarrec, L. Messio, B. Bernu, C. Lhuillier, F. Bert, P. Mendels, B. Koteswararao, F. Bouquet, J. Ollivier, A. D. Hillier, A. Amato, R. H. Colman, and A. S. Wills, Kapellasite: A kagome quantum spin liquid with competing interactions, [Phys. Rev. Lett.](#) **109**, 037208 (2012).
- [52] M. J. Gingras, Spin ice, in [47], pp. 293–329.
- [53] C. Castelnovo, R. Moessner, and S. L. Sondhi, Magnetic monopoles in spin ice, [Nature](#) **451**, 42–45 (2008).
- [54] R. Moessner and S. L. Sondhi, Theory of the [111] magnetization plateau in spin ice, [Phys. Rev. B](#) **68**, 064411 (2003).
- [55] R. Moessner and S. L. Sondhi, Ising models of quantum frustration, [Phys. Rev. B](#) **63**, 224401 (2001).
- [56] R. Moessner, S. L. Sondhi, and P. Chandra, Two-dimensional periodic frustrated Ising models in a transverse field, [Phys. Rev. Lett.](#) **84**, 4457–4460 (2000).
- [57] N. Rougemaille and B. Canals, Cooperative magnetic phenomena in artificial spin systems: spin liquids, Coulomb phase and fragmentation of magnetism – a colloquium, [Eur. Phys. J. B](#) **92**, 62 (2019).
- [58] J. T. Chalker, [Spin liquids and frustrated magnetism](#) (2010), Lecture Notes.
- [59] P. W. Anderson, Resonating valence bonds: A new kind of insulator?, [Mat. Res. Bull.](#) **8**, 153–160 (1973).
- [60] J. Villain, Insulating spin glasses, [Z. Phys. B](#) **33**, 31–42 (1979).
- [61] C. L. Henley, The “Coulomb phase” in frustrated systems, [Annu. Rev. Condens. Matter Phys.](#) **1**, 179–210 (2010).



- 
- [62] H. W. J. Blote and H. J. Hilhorst, Roughening transitions and the zero-temperature triangular Ising antiferromagnet, *J. Phys. A: Math. Gen.* **15**, L631–L637 (1982).
- [63] S. V. Isakov, K. Gregor, R. Moessner, and S. L. Sondhi, Dipolar spin correlations in classical pyrochlore magnets, *Phys. Rev. Lett.* **93**, 167204 (2004).
- [64] R. F. Wang, C. Nisoli, R. S. Freitas, J. Li, W. McConville, B. J. Cooley, M. S. Lund, N. Samarth, C. Leighton, V. H. Crespi, and P. Schiffer, Artificial ‘spin ice’ in a geometrically frustrated lattice of nanoscale ferromagnetic islands, *Nature* **439**, 303–306 (2006).
- [65] M. Tanaka, E. Saitoh, H. Miyajima, T. Yamaoka, and Y. Iye, Magnetic interactions in a ferromagnetic honeycomb nanoscale network, *Phys. Rev. B* **73**, 052411 (2006).
- [66] S. H. Skjærvø, C. H. Marrows, R. L. Stamps, and L. J. Heyderman, Advances in artificial spin ice, *Nat. Rev. Phys.* **2**, 13–28 (2020).
- [67] R. F. Wang, J. Li, W. McConville, C. Nisoli, X. Ke, J. W. Freeland, V. Rose, M. Grimsditch, P. Lammert, V. H. Crespi, and P. Schiffer, Demagnetization protocols for frustrated interacting nanomagnet arrays, *J. Appl. Phys.* **101**, 09J104 (2007).
- [68] X. Ke, J. Li, C. Nisoli, P. E. Lammert, W. McConville, R. F. Wang, V. H. Crespi, and P. Schiffer, Energy minimization and AC demagnetization in a nanomagnet array, *Phys. Rev. Lett.* **101**, 037205 (2008).
- [69] C. Nisoli, R. Moessner, and P. Schiffer, Colloquium: Artificial spin ice: Designing and imaging magnetic frustration, *Rev. Mod. Phys.* **85**, 1473–1490 (2013).
- [70] C. Nisoli, J. Li, X. Ke, D. Garand, P. Schiffer, and V. H. Crespi, Effective temperature in an interacting vertex system: Theory and experiment on artificial spin ice, *Phys. Rev. Lett.* **105**, 047205 (2010).
- [71] Y. Qi, T. Brintlinger, and J. Cumings, Direct observation of the ice rule in an artificial kagome spin ice, *Phys. Rev. B* **77**, 094418 (2008).
- [72] A. Farhan, P. M. Derlet, A. Kleibert, A. Balan, R. V. Chopdekar, M. Wyss, J. Perron, A. Scholl, F. Nolting, and L. J. Heyderman, Direct observation of thermal relaxation in artificial spin ice, *Phys. Rev. Lett.* **111**, 057204 (2013).
- [73] V. Kapaklis, U. B. Arnalds, A. Harman-Clarke, E. T. Papaioannou, M. Karimipour, P. Korilis, A. Taroni, P. C. W. Holdsworth, S. T. Bramwell, and B. Hjörvarsson, Melting artificial spin ice, *New J. Phys.* **14**, 035009 (2012).
- [74] A. Farhan, P. M. Derlet, A. Kleibert, A. Balan, R. V. Chopdekar, M. Wyss, L. Anghinolfi, F. Nolting, and L. J. Heyderman, Exploring hyper-cubic energy landscapes in thermally active finite artificial spin-ice systems, *Nature Phys.* **9**, 375–382 (2013).

- [75] J. P. Morgan, J. Akerman, A. Stein, C. Phatak, R. M. L. Evans, S. Langridge, and C. H. Marrows, Real and effective thermal equilibrium in artificial square spin ices, [Phys. Rev. B \*\*87\*\*, 024405 \(2013\)](#).
- [76] S. Zhang, I. Gilbert, C. Nisoli, G. W. Chern, M. J. Erickson, L. O'Brien, C. Leighton, P. E. Lammert, V. H. Crespi, and P. Schiffer, Crystallites of magnetic charges in artificial spin ice, [Nature \*\*500\*\*, 553–557 \(2013\)](#).
- [77] U. B. Arnalds, M. Ahlberg, M. S. Brewer, V. Kapaklis, E. T. Papaioannou, M. Karimipour, P. Korelis, A. Stein, S. Ólafsson, T. P. A. Hase, and B. Hjörvarsson, Thermal transitions in nano-patterned XY-magnets, [Appl. Phys. Lett. \*\*105\*\*, 042409 \(2014\)](#).
- [78] V. Kapaklis, U. B. Arnalds, A. Farhan, R. V. Chopdekar, A. Balan, A. Scholl, L. J. Heyderman, and B. Hjörvarsson, Thermal fluctuations in artificial spin ice, [Nature Nanotech. \*\*9\*\*, 514–519 \(2014\)](#).
- [79] K. Hofhuis, A. Hrabec, H. Arava, N. Leo, Y.-L. Huang, R. V. Chopdekar, S. Parchenko, A. Kleibert, S. Koraltan, C. Abert, C. Vogler, D. Suess, P. M. Derlet, and L. J. Heyderman, Thermally superactive artificial kagome spin ice structures obtained with the interfacial Dzyaloshinskii-Moriya interaction, [Phys. Rev. B \*\*102\*\*, 180405 \(2020\)](#).
- [80] S. Zhang, J. Li, I. Gilbert, J. Bartell, M. J. Erickson, Y. Pan, P. E. Lammert, C. Nisoli, K. K. Kohli, R. Misra, V. H. Crespi, N. Samarth, C. Leighton, and P. Schiffer, Perpendicular magnetization and generic realization of the Ising model in artificial spin ice, [Phys. Rev. Lett. \*\*109\*\*, 087201 \(2012\)](#).
- [81] I. A. Chioar, N. Rougemaille, A. Grimm, O. Fruchart, E. Wagner, M. Hehn, D. Lacour, F. Montaigne, and B. Canals, Nonuniversality of artificial frustrated spin systems, [Phys. Rev. B \*\*90\*\*, 064411 \(2014\)](#).
- [82] I. A. Chioar, N. Rougemaille, and B. Canals, Ground-state candidate for the classical dipolar kagome Ising antiferromagnet, [Phys. Rev. B \*\*93\*\*, 214410 \(2016\)](#).
- [83] L. J. Heyderman and R. L. Stamps, Artificial ferroic systems: novel functionality from structure, interactions and dynamics, [J. Phys.: Condens. Matter \*\*25\*\*, 363201 \(2013\)](#).
- [84] I. A. Chioar, B. Canals, D. Lacour, M. Hehn, B. Santos Burgos, T. O. Menteş, A. Locatelli, F. Montaigne, and N. Rougemaille, Kinetic pathways to the magnetic charge crystal in artificial dipolar spin ice, [Phys. Rev. B \*\*90\*\*, 220407 \(2014\)](#).
- [85] Z. Budrikis, P. Politi, and R. L. Stamps, Diversity enabling equilibration: Disorder and the ground state in artificial spin ice, [Phys. Rev. Lett. \*\*107\*\*, 217204 \(2011\)](#).
- [86] Z. Budrikis, J. P. Morgan, J. Akerman, A. Stein, P. Politi, S. Langridge, C. H. Marrows, and R. L. Stamps, Disorder strength and field-driven ground state domain formation in artificial spin ice: Experiment, simulation, and theory, [Phys. Rev. Lett. \*\*109\*\*, 037203 \(2012\)](#).

- 
- [87] Z. Budrikis, P. Politi, and R. L. Stamps, A network model for field and quenched disorder effects in artificial spin ice, *New J. Phys.* **14**, 045008 (2012).
- [88] N. Rougemaille, F. Montaigne, B. Canals, A. Duluard, D. Lacour, M. Hehn, R. Belkhou, O. Fruchart, S. El Moussaoui, A. Bendounan, and F. Maccherozzi, Artificial kagome arrays of nanomagnets: A frozen dipolar spin ice, *Phys. Rev. Lett.* **106**, 057209 (2011).
- [89] Y. Perrin, B. Canals, and N. Rougemaille, Extensive degeneracy, Coulomb phase and magnetic monopoles in artificial square ice, *Nature* **540**, 410–413 (2016).
- [90] S. Ladak, D. E. Read, G. K. Perkins, L. F. Cohen, and W. R. Branford, Direct observation of magnetic monopole defects in an artificial spin-ice system, *Nature Phys.* **6**, 359–363 (2010).
- [91] E. Mengotti, L. J. Heyderman, A. F. Rodríguez, F. Nolting, R. V. Hügli, and H.-B. Braun, Real-space observation of emergent magnetic monopoles and associated Dirac strings in artificial kagome spin ice, *Nature Phys.* **7**, 68–74 (2011).
- [92] A. Farhan, P. M. Derlet, L. Anghinolfi, A. Kleibert, and L. J. Heyderman, Magnetic charge and moment dynamics in artificial kagome spin ice, *Phys. Rev. B* **96**, 064409 (2017).
- [93] A. S. Wills, R. Ballou, and C. Lacroix, Model of localized highly frustrated ferromagnetism: The kagomé spin ice, *Phys. Rev. B* **66**, 144407 (2002).
- [94] G.-W. Chern and O. Tchernyshyov, Magnetic charge and ordering in kagome spin ice, *Phil. Trans. R. Soc. A* **370**, 5718–5737 (2012).
- [95] G. Möller and R. Moessner, Magnetic multipole analysis of kagome and artificial spin-ice dipolar arrays, *Phys. Rev. B* **80**, 140409(R) (2009).
- [96] G.-W. Chern, P. Mellado, and O. Tchernyshyov, Two-stage ordering of spins in dipolar spin ice on the kagome lattice, *Phys. Rev. Lett.* **106**, 207202 (2011).
- [97] L. Anghinolfi, H. Luetkens, J. Perron, M. G. Flokstra, O. Sendetskyi, A. Suter, T. Prokscha, P. M. Derlet, S. L. Lee, and L. J. Heyderman, Thermodynamic phase transitions in a frustrated magnetic metamaterial, *Nat. Commun.* **6**, 8278 (2015).
- [98] B. Canals, I.-A. Chioar, V.-D. Nguyen, M. Hehn, D. Lacour, F. Montaigne, A. Locatelli, T. O. Menteş, B. S. Burgos, and N. Rougemaille, Fragmentation of magnetism in artificial kagome dipolar spin ice, *Nat. Commun.* **7**, 11446 (2016).
- [99] J. Hamp, R. Moessner, and C. Castelnovo, Supercooling and fragile glassiness in a dipolar kagome Ising magnet, *Phys. Rev. B* **98**, 144439 (2018).
- [100] L. F. Cugliandolo, L. Foini, and M. Tarzia, Mean-field phase diagram and spin-glass phase of the dipolar kagome Ising antiferromagnet, *Phys. Rev. B* **101**, 144413 (2020).
- [101] M. Wolf and K. D. Schotte, *J. Phys. A: Math. Gen.* **21**, 2195–2209 (1988).

## Bibliography

---

- [102] T. Takagi and M. Mekata, Magnetic ordering of Ising spins on kagomé lattice with the 1st and the 2nd neighbor interactions, *J. Phys. Soc. Jpn.* **62**, 3943–3953 (1993).
- [103] M. K. Ramazanov, A. K. Murtazaev, M. A. Magomedov, and M. K. Badiev, Phase transitions and thermodynamic properties of antiferromagnetic Ising model with next-nearest-neighbor interactions on the kagome lattice, *Phase Transitions* **91**, 610–618 (2018).
- [104] S. Kempinger, R. D. Fraleigh, P. E. Lammert, S. Zhang, V. H. Crespi, P. Schiffer, and N. Samarth, Imaging the stochastic microstructure and dynamic development of correlations in perpendicular artificial spin ice, *Phys. Rev. Research* **2**, 012001 (2020).
- [105] Y. Perrin, B. Canals, and N. Rougemaille, Quasidegenerate ice manifold in a purely two-dimensional square array of nanomagnets, *Phys. Rev. B* **99**, 224434 (2019).
- [106] J. Drisko, S. Daunheimer, and J. Cumings, FePd<sub>3</sub> as a material for studying thermally active artificial spin ice systems, *Phys. Rev. B* **91**, 224406 (2015).
- [107] V. Schanilec, Y. Perrin, S. L. Denmat, B. Canals, and N. Rougemaille, Artificial vertex systems by design (2019), [arXiv:1902.00452 \[cond-mat.mes-hall\]](https://arxiv.org/abs/1902.00452) .
- [108] S. Kempinger, Y.-S. Huang, P. Lammert, M. Vogel, A. Hoffmann, V. H. Crespi, P. Schiffer, and N. Samarth, Field-tunable interactions and frustration in underlayer-mediated artificial spin ice, *Phys. Rev. Lett.* **127**, 117203 (2021).
- [109] K. Hofhuis, S. H. Skjærvø, S. Parchenko, H. Arava, Z. Luo, A. Kleiber, P. Derlet, and L. J. Heyderman, *Real-space imaging of phase transitions in bridged artificial kagome spin ice* (2021), preprint.
- [110] G. Möller and R. Moessner, Artificial square ice and related dipolar nanoarrays, *Phys. Rev. Lett.* **96**, 237202 (2006).
- [111] L. A. S. Mól, W. A. Moura-Melo, and A. R. Pereira, Conditions for free magnetic monopoles in nanoscale square arrays of dipolar spin ice, *Phys. Rev. B* **82**, 054434 (2010).
- [112] A. Farhan, M. Saccone, C. F. Petersen, S. Dhuey, R. V. Chopdekar, Y.-L. Huang, N. Kent, Z. Chen, M. J. Alava, T. Lippert, A. Scholl, and S. van Dijken, Emergent magnetic monopole dynamics in macroscopically degenerate artificial spin ice, *Sci. Adv.* **5**, eaav6380 (2019).
- [113] Z. Luo, T. P. Dao, A. Hrabec, J. Vijayakumar, A. Kleibert, M. Baumgartner, E. Kirk, J. Cui, T. Savchenko, G. Krishnaswamy, L. J. Heyderman, and P. Gambardella, Chirally coupled nanomagnets, *Science* **363**, 1435–1439 (2019).
- [114] G. Rakala and K. Damle, Cluster algorithms for frustrated two-dimensional Ising antiferromagnets via dual worm constructions, *Phys. Rev. E* **96**, 023304 (2017).

- 
- [115] S. R. White, Density matrix formulation for quantum renormalization groups, [Phys. Rev. Lett. \*\*69\*\*, 2863–2866 \(1992\)](#).
- [116] S. R. White, Density-matrix algorithms for quantum renormalization groups, [Phys. Rev. B \*\*48\*\*, 10345–10356 \(1993\)](#).
- [117] U. Schollwöck, The density-matrix renormalization group in the age of matrix product states, [Annals of Physics \*\*326\*\*, 96–192 \(2011\)](#).
- [118] I. P. McCulloch, Infinite size density matrix renormalization group, revisited (2008), [arXiv:0804.2509 \[cond-mat.str-el\]](#) .
- [119] U. Schollwöck, The density-matrix renormalization group, [Rev. Mod. Phys. \*\*77\*\*, 259–315 \(2005\)](#).
- [120] R. Orús, A practical introduction to tensor networks: Matrix product states and projected entangled pair states, [Annals of Physics \*\*349\*\*, 117–158 \(2014\)](#).
- [121] Y. Hieida, K. Okunishi, and Y. Akutsu, Numerical renormalization approach to two-dimensional quantum antiferromagnets with valence-bond-solid type ground state, [New J. Phys. \*\*1\*\*, 7–7 \(1999\)](#).
- [122] F. Verstraete and J. I. Cirac, Renormalization algorithms for quantum-many body systems in two and higher dimensions (2004), [arXiv:0407.066 \[cond-mat.str-el\]](#) .
- [123] F. Verstraete, M. M. Wolf, D. Perez-Garcia, and J. I. Cirac, Criticality, the area law, and the computational power of projected entangled pair states, [Phys. Rev. Lett. \*\*96\*\*, 220601 \(2006\)](#).
- [124] J. Jordan, R. Orús, G. Vidal, F. Verstraete, and J. I. Cirac, Classical simulation of infinite-size quantum lattice systems in two spatial dimensions, [Phys. Rev. Lett. \*\*101\*\*, 250602 \(2008\)](#).
- [125] K. Okunishi, T. Nishino, and H. Ueda, Developments in the tensor network – from statistical mechanics to quantum entanglement (2021), [arXiv:2111.12223 \[cond-mat.stat-mech\]](#) .
- [126] W. Li, S.-S. Gong, Y. Zhao, S.-J. Ran, S. Gao, and G. Su, Phase transitions and thermodynamics of the two-dimensional Ising model on a distorted kagome lattice, [Phys. Rev. B \*\*82\*\*, 134434 \(2010\)](#).
- [127] L. Vanderstraeten, B. Vanhecke, A. M. Läuchli, and F. Verstraete, Approaching the Kosterlitz-Thouless transition for the classical XY model with tensor networks, [Phys. Rev. E \*\*100\*\*, 062136 \(2019\)](#).
- [128] Y. Sasagawa, H. Ueda, J. Genzor, A. Gendiar, and T. Nishino, Entanglement entropy on the boundary of the square-lattice  $\pm J$  Ising model, [J. Phys. Soc. Jpn. \*\*89\*\*, 114005 \(2020\)](#).

## Bibliography

---

- [129] H. Ueda, K. Okunishi, K. Harada, R. Krčmár, A. Gendiar, S. Yunoki, and T. Nishino, Finite- $m$  scaling analysis of Berezinskii-Kosterlitz-Thouless phase transitions and entanglement spectrum for the six-state clock model, [Phys. Rev. E \*\*101\*\*, 062111 \(2020\)](#).
- [130] S. Nyckees, J. Colbois, and F. Mila, Identifying the Huse-Fisher universality class of the three-state chiral Potts model, [Nucl. Phys. B \*\*965\*\*, 115365 \(2021\)](#).
- [131] S. Nyckees and F. Mila, Commensurate-incommensurate transition in the chiral Ashkin-Teller model (2021), [arXiv:2109.01415 \[cond-mat.stat-mech\]](#) .
- [132] H. Li and L.-P. Yang, Tensor network simulation for the frustrated  $J_1 - J_2$  Ising model on the square lattice, [Phys. Rev. E \*\*104\*\*, 024118 \(2021\)](#).
- [133] P. Schmoll, A. Kshetrimayum, J. Eisert, R. Orús, and M. Rizzi, The classical two-dimensional Heisenberg model revisited: An  $SU(2)$ -symmetric tensor network study, [SciPost Phys. \*\*11\*\*, 98 \(2021\)](#).
- [134] T. Nishino and K. Okunishi, A density matrix algorithm for 3d classical models, [J. Phys. Soc. Jpn. \*\*67\*\*, 3066–3072 \(1998\)](#).
- [135] T. Nishino, K. Okunishi, Y. Hieida, N. Maeshima, and Y. Akutsu, Self-consistent tensor product variational approximation for 3d classical models, [Nucl. Phys. B \*\*575\*\*, 504–512 \(2000\)](#).
- [136] T. Nishino, Y. Hieida, K. Okunishi, N. Maeshima, Y. Akutsu, and A. Gendiar, Two-Dimensional Tensor Product Variational Formulation, [Prog. Theor. Phys. \*\*105\*\*, 409–417 \(2001\)](#).
- [137] A. Gendiar and T. Nishino, Latent heat calculation of the three-dimensional  $q = 3, 4$ , and 5 Potts models by the tensor product variational approach, [Phys. Rev. E \*\*65\*\*, 046702 \(2002\)](#).
- [138] A. Gendiar, N. Maeshima, and T. Nishino, Stable Optimization of a Tensor Product Variational State, [Prog. Theor. Phys. \*\*110\*\*, 691–699 \(2003\)](#).
- [139] A. Gendiar and T. Nishino, Phase diagram of the three-dimensional axial next-nearest-neighbor Ising model, [Phys. Rev. B \*\*71\*\*, 024404 \(2005\)](#).
- [140] L. Vanderstraeten, B. Vanhecke, and F. Verstraete, Residual entropies for three-dimensional frustrated spin systems with tensor networks, [Phys. Rev. E \*\*98\*\*, 042145 \(2018\)](#).
- [141] M. Levin and C. P. Nave, Tensor renormalization group approach to two-dimensional classical lattice models, [Phys. Rev. Lett. \*\*99\*\*, 120601 \(2007\)](#).
- [142] Z. Y. Xie, H. C. Jiang, Q. N. Chen, Z. Y. Weng, and T. Xiang, Second renormalization of tensor-network states, [Phys. Rev. Lett. \*\*103\*\*, 160601 \(2009\)](#).

- 
- [143] Z. Y. Xie, J. Chen, M. P. Qin, J. W. Zhu, L. P. Yang, and T. Xiang, Coarse-graining renormalization by higher-order singular value decomposition, [Phys. Rev. B \*\*86\*\*, 045139 \(2012\)](#).
- [144] G. Evenbly and G. Vidal, Tensor network renormalization, [Phys. Rev. Lett. \*\*115\*\*, 180405 \(2015\)](#).
- [145] G. Evenbly, Algorithms for tensor network renormalization, [Phys. Rev. B \*\*95\*\*, 045117 \(2017\)](#).
- [146] T. Nishino and K. Okunishi, Corner Transfer Matrix Renormalization Group Method, [J. Phys. Soc. Jpn. \*\*65\*\*, 891–894 \(1996\)](#).
- [147] R. Orús and G. Vidal, Infinite time-evolving block decimation algorithm beyond unitary evolution, [Phys. Rev. B \*\*78\*\*, 155117 \(2008\)](#).
- [148] V. Zauner-Stauber, L. Vanderstraeten, M. T. Fishman, F. Verstraete, and J. Haegeman, Variational optimization algorithms for uniform matrix product states, [Phys. Rev. B \*\*97\*\*, 045145 \(2018\)](#).
- [149] M. T. Fishman, L. Vanderstraeten, V. Zauner-Stauber, J. Haegeman, and F. Verstraete, Faster methods for contracting infinite two-dimensional tensor networks, [Phys. Rev. B \*\*98\*\*, 235148 \(2018\)](#).
- [150] L. Vanderstraeten, J. Haegeman, and F. Verstraete, Tangent-space methods for uniform matrix product states, [SciPost Phys. Lect. Notes , \*\*7\*\* \(2019\)](#).
- [151] A. Nietner, B. Vanhecke, F. Verstraete, J. Eisert, and L. Vanderstraeten, Efficient variational contraction of two-dimensional tensor networks with a non-trivial unit cell, [Quantum \*\*4\*\*, 328 \(2020\)](#).
- [152] G. Vidal, Efficient classical simulation of slightly entangled quantum computations, [Phys. Rev. Lett. \*\*91\*\*, 147902 \(2003\)](#).
- [153] G. Vidal, Classical simulation of infinite-size quantum lattice systems in one spatial dimension, [Phys. Rev. Lett. \*\*98\*\*, 070201 \(2007\)](#).
- [154] R. Orús and G. Vidal, Simulation of two-dimensional quantum systems on an infinite lattice revisited: Corner transfer matrix for tensor contraction, [Phys. Rev. B \*\*80\*\*, 094403 \(2009\)](#).
- [155] J. Kanamori, Magnetization Process in an Ising Spin System, [Prog. Theor. Phys. \*\*35\*\*, 16–35 \(1966\)](#).
- [156] S. M. Allen and J. W. Cahn, Ground state structures in ordered binary alloys with second neighbor interactions, [Acta Metallurgica \*\*20\*\*, 423–433 \(1972\)](#).
- [157] A. van de Walle, *The Effect of Lattice Vibrations on Substitutional Alloy Thermodynamics*, [Ph.D. thesis](#), Massachusetts Institute of Technology (2000).



## Bibliography

---

- [158] W. Huang, D. A. Kitchaev, S. T. Dacek, Z. Rong, A. Urban, S. Cao, C. Luo, and G. Ceder, Finding and proving the exact ground state of a generalized Ising model by convex optimization and MAX-SAT, *Phys. Rev. B* **94**, 134424 (2016).
- [159] B. Vanhecke, J. Colbois, L. Vanderstraeten, F. Verstraete, and F. Mila, Solving frustrated Ising models using tensor networks, *Phys. Rev. Research* **3**, 013041 (2021).
- [160] J. Colbois, K. Hofhuis, Z. Luo, X. Wang, A. Hrabec, L. J. Heyderman, and F. Mila, Artificial out-of-plane Ising antiferromagnet on the kagome lattice with very small farther-neighbor couplings, *Phys. Rev. B* **104**, 024418 (2021).
- [161] M. J. Richards and J. W. Cahn, Pairwise interactions and the ground state of ordered binary alloys, *Acta Metall.* **19**, 1263–1277 (1971).
- [162] P. W. Kasteleyn, Dimer statistics and phase transitions, *J. Math. Phys.* **4**, 287–293 (1963).
- [163] N. Prokof'ev and B. Svistunov, Worm algorithms for classical statistical models, *Phys. Rev. Lett.* **87**, 160601 (2001).
- [164] P. Hitchcock, E. S. Sørensen, and F. Alet, Dual geometric worm algorithm for two-dimensional discrete classical lattice models, *Phys. Rev. E* **70**, 016702 (2004).
- [165] U. Wolff, Collective Monte Carlo updating for spin systems, *Phys. Rev. Lett.* **62**, 361–364 (1989).
- [166] R. H. Swendsen and J.-S. Wang, Nonuniversal critical dynamics in Monte Carlo simulations, *Phys. Rev. Lett.* **58**, 86–88 (1987).
- [167] F. Alet and E. S. Sørensen, Cluster Monte Carlo algorithm for the quantum rotor model, *Phys. Rev. E* **67**, 015701 (2003).
- [168] F. Alet and E. S. Sørensen, Directed geometrical worm algorithm applied to the quantum rotor model, *Phys. Rev. E* **68**, 026702 (2003).
- [169] A. W. Sandvik and R. Moessner, Correlations and confinement in nonplanar two-dimensional dimer models, *Phys. Rev. B* **73**, 144504 (2006).
- [170] A. Sen, F. Wang, K. Damle, and R. Moessner, Triangular and kagome antiferromagnets with a strong easy-axis anisotropy, *Phys. Rev. Lett.* **102**, 227001 (2009).
- [171] F. Alet, J. L. Jacobsen, G. Misguich, V. Pasquier, F. Mila, and M. Troyer, Interacting classical dimers on the square lattice, *Phys. Rev. Lett.* **94**, 235702 (2005).
- [172] O. F. Syljuåsen and A. W. Sandvik, Quantum Monte Carlo with directed loops, *Phys. Rev. E* **66**, 046701 (2002).
- [173] O. F. Syljuåsen, Directed loop updates for quantum lattice models, *Phys. Rev. E* **67**, 046701 (2003).



- 
- [174] N. V. Prokof'ev, B. V. Svistunov, and I. S. Tupitsyn, "Worm" algorithm in quantum Monte Carlo simulations, [Phys. Lett. A \*\*238\*\*, 253–257 \(1998\)](#).
- [175] H. Suwa, Geometric allocation approach to accelerating directed worm algorithm, [Phys. Rev. E \*\*103\*\*, 013308 \(2021\)](#).
- [176] R. J. Baxter, Variational approximations for square lattice models in statistical mechanics, [J. Stat. Phys. \*\*19\*\*, 461–478 \(1978\)](#).
- [177] S. K. Tsang, Square lattice variational approximations applied to the Ising model, [J. Stat. Phys. \*\*20\*\*, 95–114 \(1979\)](#).
- [178] R. J. Baxter, *Exactly solved models in statistical mechanics* (Academic Press, New York, 1982).
- [179] I. Affleck, T. Kennedy, E. H. Lieb, and H. Tasaki, Rigorous results on valence-bond ground states in antiferromagnets, [Phys. Rev. Lett. \*\*59\*\*, 799–802 \(1987\)](#).
- [180] S. Östlund and S. Rommer, Thermodynamic limit of density matrix renormalization, [Phys. Rev. Lett. \*\*75\*\*, 3537–3540 \(1995\)](#).
- [181] T. Nishino, Density matrix renormalization group method for 2d classical models, [J. Phys. Soc. Jpn. \*\*64\*\*, 3598–3601 \(1995\)](#).
- [182] T. Nishino and K. Okunishi, Corner transfer matrix algorithm for classical renormalization group, [J. Phys. Soc. Jpn. \*\*66\*\*, 3040–3047 \(1997\)](#).
- [183] T. Nishino, [Dmrg webpage](#) (2022), Last visited on 20.01.2022.
- [184] J. I. Cirac, D. Pérez-García, N. Schuch, and F. Verstraete, Matrix product states and projected entangled pair states: Concepts, symmetries, theorems, [Rev. Mod. Phys. \*\*93\*\*, 045003 \(2021\)](#).
- [185] T. Nishino, [Tensor networks for classical statistical mechanics](#) (2021), Conference: "Entanglement in strongly correlated systems", Benasque.
- [186] T. Nishino, T. Hikihara, K. Okunishi, and Y. Hieida, Density matrix renormalization group: introduction from a variational point of view, [Int. J. Mod. Phys. B \*\*13\*\*, 1–24 \(1999\)](#).
- [187] J. Haegeman and F. Verstraete, Diagonalizing Transfer Matrices and Matrix Product Operators: A Medley of Exact and Computational Methods, [Annu. Rev. Condens. Matter Phys. \*\*8\*\*, 355–406 \(2017\)](#).
- [188] I. V. Oseledets, Tensor-train decomposition, [SIAM J. Sci. Comput. \*\*33\*\*, 2295–2317 \(2011\)](#).
- [189] H. H. Zhao, Z. Y. Xie, Q. N. Chen, Z. C. Wei, J. W. Cai, and T. Xiang, Renormalization of tensor-network states, [Phys. Rev. B \*\*81\*\*, 174411 \(2010\)](#).

## Bibliography

---

- [190] H. W. J. Blöte and M. P. Nightingale, Antiferromagnetic triangular Ising model: Critical behavior of the ground state, [Phys. Rev. B \*\*47\*\*, 15046–15059 \(1993\)](#).
- [191] X. Qian, M. Wegewijs, and H. W. J. Blöte, Critical frontier of the triangular Ising antiferromagnet in a field, [Phys. Rev. E \*\*69\*\*, 036127 \(2004\)](#).
- [192] P. Corboz, J. Jordan, and G. Vidal, Simulation of fermionic lattice models in two dimensions with projected entangled-pair states: Next-nearest neighbor Hamiltonians, [Phys. Rev. B \*\*82\*\*, 245119 \(2010\)](#).
- [193] P. Corboz, Variational optimization with infinite projected entangled-pair states, [Phys. Rev. B \*\*94\*\*, 035133 \(2016\)](#).
- [194] M. Frías-Pérez, M. Mariën, D. P. García, M. C. Bañuls, and S. Iblisdir, Collective Monte Carlo updates through tensor network renormalization (2021), [arXiv:2104.13264 \[cond-mat.stat-mech\]](#) .
- [195] J. Haegeman, M. Mariën, T. J. Osborne, and F. Verstraete, Geometry of matrix product states: Metric, parallel transport, and curvature, [J. Math. Phys. \*\*55\*\*, 021902 \(2014\)](#).
- [196] B. Vanhecke, M. V. Damme, J. Haegeman, L. Vanderstraeten, and F. Verstraete, Tangent-space methods for truncating uniform MPS, [SciPost Phys. Core \*\*4\*\*, 4 \(2021\)](#).
- [197] L. Vanderstraeten, L. Burgelman, B. Ponsioen, M. V. Damme, B. Vanhecke, P. Corboz, J. Haegeman, and F. Verstraete, Variational contractions of projected entangled-pair states (2021), [arXiv:2110.12726 \[cond-mat.str-el\]](#) .
- [198] P. W. Anderson, Limits on the energy of the antiferromagnetic ground state, [Phys. Rev. \*\*83\*\*, 1260–1260 \(1951\)](#).
- [199] M. Grötschel, L. Lovász, and A. Schrijver, *Geometric algorithms and combinatorial optimization* (Springer-Verlag Berlin Heidelberg, 1993).
- [200] T. Kudō and S. Katsura, A Method of Determining the Orderings of the Ising Model with Several Neighbor Interactions under the Magnetic Field and Applications to Hexagonal Lattices, [Prog. Theor. Phys. \*\*56\*\*, 435–449 \(1976\)](#).
- [201] U. Brandt and J. Stolze, Ground states of the triangular Ising model with two- and three-spin interactions, [Z. Phys. B \*\*64\*\*, 481–490 \(1986\)](#).
- [202] U. Brandt and J. Stolze, Ground states of extended Hubbard models in the atomic limit, [Z. Phys. B \*\*62\*\*, 433–441 \(1986\)](#).
- [203] M. Kaburagi and J. Kanamori, A Method of Determining the Ground State of the Extended-Range Classical Lattice Gas Model, [Prog. Theor. Phys. \*\*54\*\*, 30–44 \(1975\)](#).
- [204] M. Kaburagi and J. Kanamori, Ground state structure of triangular lattice gas model with up to 3rd neighbor interactions, [J. Phys. Soc. Jpn. \*\*44\*\*, 718–727 \(1978\)](#).

- 
- [205] J. Kanamori, Infinite series of ground states of the Ising model on the honeycomb lattice, *J. Phys. Soc. Jpn.* **53**, 250–260 (1984).
- [206] J. Villain, On the ground state of Ising models, *Ferroelectrics* **66**, 143–150 (1986).
- [207] Z. Wang and M. Navascués, Two-dimensional translation-invariant probability distributions: approximations, characterizations and no-go theorems, *Proc. R. Soc. A.* **474**, 20170822 (2018).
- [208] Z. Wang, S. Singh, and M. Navascués, Entanglement and nonlocality in infinite 1d systems, *Phys. Rev. Lett.* **118**, 230401 (2017).
- [209] I. Frérot and T. Roscilde, Detecting many-body bell nonlocality by solving Ising models, *Phys. Rev. Lett.* **126**, 140504 (2021).
- [210] S. Kourtis, C. Chamon, E. R. Mucciolo, and A. E. Ruckenstein, Fast counting with tensor networks, *SciPost Phys.* **7**, 60 (2019).
- [211] F. Romá, F. Nieto, E. E. Vogel, and A. J. Ramirez-Pastor, Ground-state entropy of  $\pm J$  Ising lattices by Monte Carlo simulations, *J. Stat. Phys.* **114**, 1325–1341 (2004).
- [212] J. Kolafa, Residual entropy of ices and clathrates from Monte Carlo simulation, *J. Chem. Phys.* **140**, 204507 (2014).
- [213] C. Wang, S.-M. Qin, and H.-J. Zhou, Topologically invariant tensor renormalization group method for the Edwards-Anderson spin glasses model, *Phys. Rev. B* **90**, 174201 (2014).
- [214] Z. Zhu and H. G. Katzgraber, Do tensor renormalization group methods work for frustrated spin systems? (2019), [arXiv:1903.07721 \[cond-mat.dis-nn\]](https://arxiv.org/abs/1903.07721) .
- [215] M. M. Rams, M. Mohseni, D. Eppens, K. Jałowiecki, and B. Gardas, Approximate optimization, sampling, and spin-glass droplet discovery with tensor networks, *Phys. Rev. E* **104**, 025308 (2021).
- [216] J. Villain, Spin glass with non-random interactions, *J. Phys. C: Solid State Phys.* **10**, 1717–1734 (1977).
- [217] H. Wang, Proving theorems by pattern recognition — II, *Bell Syst. Tech. J.* **40**, 1–41 (1961).
- [218] R. M. Robinson, Undecidability and nonperiodicity for tilings of the plane, *Inventiones mathematicae* **12**, 177–209 (1971).
- [219] H. Wang, Notes on a class of tiling problems, *Fundamenta Mathematicae* **82**, 295–305 (1975).
- [220] C. Bachoc, D. C. Gijswijt, A. Schrijver, and F. Vallentin, Invariant Semidefinite Programs, in *Handbook on Semidefinite, Conic and Polynomial Optimization*, International Series in Operations Research & Management Science, edited by M. F. Anjos and J. B. Lasserre (Springer US, Boston, MA, 2012) pp. 219–269.

## Bibliography

---

- [221] A. W. Sandvik, Computational Studies of Quantum Spin Systems, [AIP Conference Proceedings](#) **1297**, 135–338 (2010).
- [222] T. Mizoguchi, L. D. C. Jaubert, and M. Udagawa, Clustering of topological charges in a kagome classical spin liquid, [Phys. Rev. Lett.](#) **119**, 077207 (2017).
- [223] J.-G. Liu, L. Wang, and P. Zhang, Tropical tensor network for ground states of spin glasses, [Phys. Rev. Lett.](#) **126**, 090506 (2021).
- [224] F.-F. Song and G.-M. Zhang, Tensor network approach to the two-dimensional fully frustrated XY model and a bosonic metallic phase with chirality order (2021), [arXiv:2112.03550 \[cond-mat.str-el\]](#) .
- [225] H. Le Roy, *Elasticity of self assembling bio-materials*, [Theses](#), Université Paris-Saclay (2021).
- [226] O. Brunn, Y. Perrin, B. Canals, and N. Rougemaille, Signatures of farther neighbor couplings in artificial square ice, [Phys. Rev. B](#) **103**, 094405 (2021).
- [227] I. Dzyaloshinsky, A thermodynamic theory of “weak” ferromagnetism of antiferromagnetics, [J. Phys. Chem. Solids](#) **4**, 241–255 (1958).
- [228] T. Moriya, Anisotropic superexchange interaction and weak ferromagnetism, [Phys. Rev.](#) **120**, 91–98 (1960).
- [229] A. Fert, Magnetic and transport properties of metallic multilayers, in [Metallic Multilayers](#), Materials Science Forum, Vol. 59 (Trans Tech Publications Ltd, 1991) pp. 439–480.
- [230] A. Crépieux and C. Lacroix, Dzyaloshinsky–Moriya interactions induced by symmetry breaking at a surface, [J. Magn. Magn. Mater.](#) **182**, 341–349 (1998).
- [231] M. Saccone, K. Hofhuis, Y.-L. Huang, S. Dhuey, Z. Chen, A. Scholl, R. V. Chopdekar, S. van Dijken, and A. Farhan, Dipolar Cairo lattice: Geometrical frustration and short-range correlations, [Phys. Rev. Materials](#) **3**, 104402 (2019).
- [232] A. Farhan, M. Saccone, C. F. Petersen, S. Dhuey, K. Hofhuis, R. Mansell, R. V. Chopdekar, A. Scholl, T. Lippert, and S. van Dijken, Geometrical frustration and planar triangular antiferromagnetism in quasi-three-dimensional artificial spin architecture, [Phys. Rev. Lett.](#) **125**, 267203 (2020).
- [233] A. Vansteenkiste, J. Leliaert, M. Dvornik, M. Helsen, F. Garcia-Sanchez, and B. Van Waeyenberge, The design and verification of MuMax<sup>3</sup>, [AIP Advances](#) **4**, 107133 (2014).
- [234] J. Leliaert, M. Dvornik, J. Mulkers, J. De Clercq, M. Milošević, and B. Van Waeyenberge, Fast micromagnetic simulations on gpu—recent advances made with MuMax<sup>3</sup>, [J. Phys. D: Appl. Phys.](#) **51**, 123002 (2018).

- 
- [235] J. H. Barry and M. Khatun, Exact solutions for correlations in the kagomé Ising antiferromagnet, *Int. J. Mod. Phys. B* **11**, 93–101 (1997).
- [236] K. A. Muttalib, M. Khatun, and J. H. Barry, Perpendicular susceptibility and geometrical frustration in two-dimensional Ising antiferromagnets: Exact solutions, *Phys. Rev. B* **96**, 184411 (2017).
- [237] M. M. Rams, P. Czarnik, and L. Cincio, Precise extrapolation of the correlation function asymptotics in uniform tensor network states with application to the Bose-Hubbard and XXZ models, *Phys. Rev. X* **8**, 041033 (2018).
- [238] M. Udagawa, M. Ogata, and Z. Hiroi, Exact result of ground-state entropy for Ising pyrochlore magnets under a magnetic field along [111] axis, *J. Phys. Soc. Jpn.* **71**, 2365–2368 (2002).
- [239] Y. L. Loh, D. X. Yao, and E. W. Carlson, Thermodynamics of Ising spins on the triangular kagome lattice: Exact analytical method and Monte Carlo simulations, *Phys. Rev. B* **77**, 134402 (2008).
- [240] B. D. Metcalf and C. P. Yang, Degeneracy of antiferromagnetic Ising lattices at critical magnetic field and zero temperature, *Phys. Rev. B* **18**, 2304–2307 (1978).
- [241] C.-O. Hwang, S.-Y. Kim, D. Kang, and J. M. Kim, Ising antiferromagnets in a nonzero uniform magnetic field, *J. Stat. Mech.* **2007**, L05001–L05001 (2007).
- [242] M. Semjan and M. Žukovič, Magnetocaloric Properties of an Ising Antiferromagnet on a Kagome Lattice, *Acta Physica Polonica A* **137**, 622–624 (2020).
- [243] J. Colbois and K. Hofhuis, [Data related to the present work](#) (2021), doi: 10.5281/zenodo.4620851.
- [244] K. Tokushuku, T. Mizoguchi, and M. Udagawa, Field-selective classical spin liquid and magnetization plateaus on kagome lattice, *J. Phys. Soc. Jpn.* **89**, 053708 (2020).
- [245] P. Azaria, H. T. Diep, and H. Giacomini, Coexistence of order and disorder and reentrance in an exactly solvable model, *Phys. Rev. Lett.* **59**, 1629–1632 (1987).
- [246] A. Smerald and F. Mila, Spin-liquid behaviour and the interplay between Pokrovsky-Talapov and Ising criticality in the distorted, triangular-lattice, dipolar Ising antiferromagnet, *SciPost Phys.* **5**, 30 (2018).
- [247] Y. Jiang and T. Emig, Ordering of geometrically frustrated classical and quantum triangular Ising magnets, *Phys. Rev. B* **73**, 104452 (2006).
- [248] C. S. O. Yokoi, J. F. Nagle, and S. R. Salinas, Dimer pair correlations on the brick lattice, *J. Stat. Phys.* **44**, 729–747 (1986).

## Bibliography

---

- [249] M. Hering, H. Yan, and J. Reuther, Fracton excitations in classical frustrated kagome spin models, *Phys. Rev. B* (2021).
- [250] V. Zauner, D. Draxler, L. Vanderstraeten, J. Haegeman, and F. Verstraete, Symmetry breaking and the geometry of reduced density matrices, *New J. Phys.* **18**, 113033 (2016).
- [251] R. Krčmár, A. Gendiar, and T. Nishino, Entanglement-entropy study of phase transitions in six-state clock model, *Acta Physica Polonica A* , 598–600 (2020).
- [252] F.-F. Song and G.-M. Zhang, Hybrid Berezinskii-Kosterlitz-Thouless and Ising topological phase transition in the generalized two-dimensional XY model using tensor networks, *Phys. Rev. B* **103**, 024518 (2021).
- [253] R. Vanhove, L. Lootens, H.-H. Tu, and F. Verstraete, Topological aspects of the critical three-state Potts model (2021), [arXiv:2107.11177 \[math-ph\]](https://arxiv.org/abs/2107.11177) .
- [254] H. Ueda, K. Okunishi, S. Yunoki, and T. Nishino, Corner transfer matrix renormalization group analysis of the two-dimensional dodecahedron model, *Phys. Rev. E* **102**, 032130 (2020).
- [255] A. Turing, I.—Computing Machinery and intelligence, *Mind* **LIX**, 433–460 (1950).
- [256] M. Troyer, *Classical and Quantum Monte Carlo Algorithms and Exact Diagonalization* (2004), Lecture Notes.
- [257] D. Landau and K. Binder, *A Guide to Monte Carlo Simulations in Statistical Physics*, 5th ed. (Cambridge University Press, 2021).
- [258] M. Benaïm and N. El Karoui, *Promenade aléatoire: Chaînes de Markov et simulations; martingales et stratégies* (Editions de l'Ecole Polytechnique, 2005).
- [259] H. G. Katzgraber, S. Trebst, D. A. Huse, and M. Troyer, Feedback-optimized parallel tempering Monte Carlo, *J. Stat. Mech.* , P03018–P03018 (2006).
- [260] A. Smerald, S. Korshunov, and F. Mila, Topological aspects of symmetry breaking in triangular-lattice Ising antiferromagnets, *Phys. Rev. Lett.* **116**, 197201 (2016).
- [261] W. Zhang, T. M. Garoni, and Y. Deng, A worm algorithm for the fully-packed loop model, *Nucl. Phys. B* **814**, 461–484 (2009).
- [262] J. G. Kemeny and J. L. Snell, *Finite Markov Chains* (Springer-Verlag, New York, 1976).
- [263] M. Žukovič, Residual entropy of spin-s triangular Ising antiferromagnet, *Eur. Phys. J. B* **86**, 283 (2013).
- [264] K. Soldatov, A. Peretyatko, P. Andriushchenko, K. Nefedev, and Y. Okabe, Comparison of diluted antiferromagnetic Ising models on frustrated lattices in a magnetic field, *Phys. Lett. A* **383**, 1229–1234 (2019).

- 
- [265] K. Hukushima and K. Nemoto, Exchange Monte Carlo method and application to spin glass simulations, *J. Phys. Soc. Jpn.* **65**, 1604–1608 (1996).
- [266] V. Ambegaokar and M. Troyer, Estimating errors reliably in Monte Carlo simulations of the Ehrenfest model, *Am. J. Phys.* **78**, 150–157 (2010).
- [267] D. Pérez-García, F. Verstraete, M. M. Wolf, and J. I. Cirac, Matrix product state representations, *Quantum Inf. Comput.* **7**, 401–430 (2007).
- [268] M. Fannes, B. Nachtergaele, and R. F. Werner, Finitely correlated states on quantum spin chains, *Commun. Math. Phys.* **144**, 443–490 (1992).
- [269] T. Morita, Orderings of one-dimensional Ising systems with an arbitrary interaction of finite range, *J. Phys. A: Math. Nucl. Gen.* **7**, 289–300 (1974).
- [270] T. Morita, Orderings of one-dimensional Ising systems with an arbitrary interaction of finite range. II, *J. Phys. A: Math. Nucl. Gen.* **7**, 1613–1616 (1974).
- [271] A. Finel, *Contribution à l'étude des effets d'ordre dans le cadre du modele d'Ising: états de base et diagrammes de phase*, Ph.D. thesis, Université Paris 6 (1987).
- [272] G. D. Garbulsky, P. D. Tepesch, and G. Ceder, Ground State Analysis on the Fcc Lattice With Four Pair Interactions, *MRS Proceedings* **291**, 259 (1992).
- [273] J. Hubbard, Generalized Wigner lattices in one dimension and some applications to tetracyanoquinodimethane (TCNQ) salts, *Phys. Rev. B* **17**, 494–505 (1978).
- [274] V. L. Pokrovsky and G. V. Uimin, On the properties of monolayers of adsorbed atoms, *J. Phys. C: Solid State Phys.* **11**, 3535–3549 (1978).
- [275] M. E. Fisher and W. Selke, Low temperature analysis of the Axial Next-Nearest Neighbour Ising model near its multiphase point, *Phil. Trans. R. Soc. A* **302**, 1–44 (1981).
- [276] V. Pokrovsky and G. V. Uimin, ANNI model in the magnetic field - possible interpretation of the CeSb phase diagram, *Sov. Phys. JETP* **55**, 950–961 (1982).
- [277] T. Tonegawa, K. Takasaki, M. Kaburagi, and J. Kanamori, A method of determining the ground state of the extended range lattice gas model with two kinds of particles, *J. Phys. Soc. Jpn.* **54**, 3362–3375 (1985).
- [278] T. Tonegawa, K. Takasaki, and M. Kaburagi, Exact ground state of the finite-field three-state Potts model on the one-dimensional lattice with first and second neighbor interactions, *J. Phys. Soc. Jpn.* **54**, 4312–4320 (1985).
- [279] M. Kaburagi, Ground state structure of adsorbates on the square lattice net with up to 3rd neighbor interactions, *J. Phys. Soc. Jpn.* **44**, 54–62 (1978).
- [280] J. Kanamori and M. Kaburagi, Exact ground states of the lattice gas and the Ising model on the square lattice, *J. Phys. Soc. Jpn.* **52**, 4184–4191 (1983).



## Bibliography

---

- [281] K. Takasaki, T. Tonegawa, and M. Kaburagi, Exact ground states of the lattice gas model with two kinds of particles and the finite-field three-state Potts model on the square lattice, *J. Phys. Soc. Jpn.* **57**, 570–579 (1988).
- [282] M. Kaburagi, Ground state structures of the face centered rectangular lattice gas model with up to 4th neighbor interactions, *J. Phys. Soc. Jpn.* **44**, 394–401 (1978).
- [283] M. Kaburagi and J. Kanamori, Theoretical analysis of adsorbate structures on metal surface –sodium atoms on tungsten (110) plane–, *J. Phys. Soc. Jpn.* **43**, 1686–1693 (1977).
- [284] Y. Tanaka and N. Uryû, Ground state spin configurations of the triangular Ising net with the nearest and next nearest neighbor interactions, *J. Phys. Soc. Jpn.* **39**, 825–826 (1975).
- [285] Y. I. Dublenych, Ground states of lattice-gas models on the triangular and honeycomb lattices: Devil's step and quasicrystals, *Phys. Rev. E* **80**, 011123 (2009).
- [286] Y. I. Dublenych, Ground states of the lattice-gas model on the triangular lattice with nearest- and next-nearest-neighbor pairwise interactions and with three-particle interaction: Full-dimensional ground states, *Phys. Rev. E* **84**, 011106 (2011).
- [287] Y. I. Dublenych, Ground states of the lattice-gas model on the triangular lattice with nearest- and next-nearest-neighbor pairwise interactions and with three-particle interaction: Ground states at boundaries of full-dimensional regions, *Phys. Rev. E* **84**, 061102 (2011).
- [288] J. Kanamori, Lattice gas model of the  $(7 \times 7)$ ,  $(5 \times 5)$  and  $(2 \times 8)$  structures of Si(111) and Ge(111), *Solid State Commun.* **50**, 363–366 (1984).
- [289] Kanamori, J., Ordering on surfaces, *Ann. Phys. Fr.* **10**, 43–53 (1985).
- [290] J. Kanamori, Lattice gas model analysis of the (111) surface structures of Si, Ge and related systems. II. On the DAS model, *J. Phys. Soc. Jpn.* **55**, 2723–2734 (1986).
- [291] J. Kanamori and M. Okamoto, Lattice gas model analysis of the (111) surface structures of Si, Ge and related systems, *J. Phys. Soc. Jpn.* **54**, 4636–4647 (1985).
- [292] Y. I. Dublenych, Ground states of the Ising model on the Shastry-Sutherland lattice and the origin of the fractional magnetization plateaus in rare-earth-metal tetraborides, *Phys. Rev. Lett.* **109**, 167202 (2012).
- [293] M. D. Lipkin, Ground states of a frustrated Ising model with one-, two- and three-body interactions, *Physica A* **150**, 18–39 (1988).
- [294] O. G. Mouritsen, B. Frank, and D. Mukamel, Cubic Ising lattices with four-spin interactions, *Phys. Rev. B* **27**, 3018–3031 (1983).
- [295] A. Seko, K. Shitara, and I. Tanaka, Efficient determination of alloy ground-state structures, *Phys. Rev. B* **90**, 174104 (2014).



- [296] J. Kanamori and Y. Kakehashi, Conditions for the existence of ordered structure in binary alloy systems, *J. Phys. Colloq. (Paris)* **38**, C7–279 (1977), publisher: EDP Sciences.
- [297] A. Finel and F. Ducastelle, in *Phase transformations in Solids*, edited by T. Tsakalakos (Norrh-Holland, 1984) p. 293.
- [298] A. Narita and S. Katsura, Ground State and the Magnetization Process of the Body-Centered Tetragonal Lattice with Ising Spins, *Prog. Theor. Phys.* **52**, 1448–1462 (1974).
- [299] A. Narita and S. Katsura, Ground State and the Magnetization Process of the Body-Centered Tetragonal Lattice with Ising Spins, *Prog. Theor. Phys.* **53**, 913–913 (1975).
- [300] T. Moriya and H. Ino, Ordered structures of interstitial solutes in BCC lattice, *J. Phys. Soc. Jpn.* **46**, 1776–1784 (1979).
- [301] S. M. Allen and J. W. Cahn, A correction to the ground state of FCC binary ordered alloys with first and second neighbor pairwise interactions, *Scripta Metall.* **7**, 1261–1264 (1973).
- [302] P. Cenedese and J. W. Cahn, Ordering in Close-Packed Structures: A Comparison of HCP and FCC Using CVM, *Prog. Theor. Phys. Suppl.* **115**, 95–113 (1994).
- [303] J. Kanamori, Atomostic approach to ordering, in *Modulated structures - 1979*, AIP Conference Proceedings, edited by J. M. Cowley, J. B. Cohen, M. B. Salomon, and B. J. Wuensch (American Institute of Physics, New York, 1979) p. 117.
- [304] J. W. Cahn and R. Kikuchi, Ground state of f.c.c. alloys with multiatom interactions, *Acta Metall.* **27**, 1329–1336 (1979).
- [305] J. M. Sanchez and D. De Fontaine, Theoretical prediction of ordered superstructures in metallic alloys, in *Structure and Bonding in Crystals*, Industrial Chemistry Library, Vol. 2, edited by M. O’Keeffe and A. Navrotsky (Elsevier, 1981) pp. 117–132, ISSN: 0926-9614.
- [306] C. Wolverton, G. Ceder, D. de Fontaine, and H. Dreyssé, Ab initio determination of structural stability in fcc-based transition-metal alloys, *Phys. Rev. B* **48**, 726–747 (1993).
- [307] P. De Meulenaere, M. Rodewald, and G. Van Tendeloo, Anisotropic cluster model for the short-range order in  $\text{Cu}_{1-x}\text{Pd}_x$ -type alloys, *Phys. Rev. B* **57**, 11132–11140 (1998).
- [308] A. K. Singh and S. Lele, Ordered ground-state structures in binary h.c.p. alloys using the configuration polyhedron method, *Philosophical Magazine B* **65**, 967–987 (1992).
- [309] A. K. Singh and S. Lele, Ordered structures in ternary hcp alloys, *Bull. Mater. Sci.* **14**, 11–33 (1991).
- [310] A. K. Singh, V. Singh, and S. Lele, Ground state structures in ordered binary H.C.P. alloys with pairwise third neighbour interactions, *Acta Metall. Mater.* **39**, 2847–2856 (1991).
- [311] A. K. Singh and S. Lele, The stability of  $\text{A}_{n+3}\text{B}_{n+1}$  long period APB modulated HCP superstructures, *Scripta Metall. Mater.* **27**, 443–447 (1992).

## Bibliography

---

- [312] A. K. Singh and S. Lele, Ordered ground-state structures in binary h.c.p. alloys using the configuration polyhedron method, [Philosophical Magazine B \*\*65\*\*, 967–987 \(1992\)](#).
- [313] R. McCormack, M. Asta, G. Ceder, and D. de Fontaine, Phase Transformations in Hexagonal-Close-Packed Alloys: Analysis with the Cluster Variation Method, [MRS On-line Proceedings Library \*\*291\*\*, 395–400 \(1992\)](#).
- [314] B. N. Sarma, N. Ravisankar, M. Gopal, A. K. Singh, R. Prasad, and S. Lele, Ground state structures in binary h.c.p. alloys using multiatom interactions, [Philosophical Magazine B \*\*70\*\*, 1117–1127 \(1994\)](#).
- [315] I. Ono and T. Oguchi, Magnetization process in spinel lattice, [J. Phys. Soc. Jpn. \*\*25\*\*, 373–378 \(1968\)](#).
- [316] M. Kaburagi, T. Tonegawa, and J. Kanamori, Modulated phases in the simple hexagonal Ising lattice with competing interactions, [J. Phys. Jpn. \*\*53\*\*, 1971–1982 \(1984\)](#).
- [317] D. D. Fontaine, Cluster Approach to Order-Disorder Transformations in Alloys (Academic Press, 1994) pp. 33–176, iSSN: 0081-1947.
- [318] V. M. Parakkat, K. Xie, and K. M. Krishnan, Tunable ground state in heterostructured artificial spin ice with exchange bias, [Phys. Rev. B \*\*99\*\*, 054429 \(2019\)](#).

# Jeanne Colbois

## Curriculum Vitae

Nationality: Swiss  
Date of Birth: May 19, 1994  
Rue de Lausanne 31  
1028 Prévèrèges, Switzerland  
☎ +4179 268 29 33  
✉ [jeanne.colbois@epfl.ch](mailto:jeanne.colbois@epfl.ch)  
🆔 0000-0002-5495-9466



### Education

- Sept. 2017 - **PhD in Physics**, Institute of Physics, Ecole Polytechnique Fédérale de Lausanne.  
now Thesis title: *Tensor network investigation of frustrated Ising models*. PhD advisor: Prof. Frédéric Mila.  
Defence date: March 10, 2022. Provisional public defence date: April 2022
- Sept. 2012 - **BSc and MSc in Physics and Applied Physics**, Ecole Polytechnique Fédérale de Lausanne.  
July 2017 Master thesis title: *Physics of the further-neighbour, kagome lattice Ising antiferromagnet: a dual worm approach*. Supervisor: Prof. Frédéric Mila.
- Sept. 2009 - **High School Certificate**, Lycée Denis-de-Rougemont, Neuchâtel.  
Aug. 2012 Diploma work title: *Discovering a fascinating physics phenomenon: a hundred years of superconductivity*.  
Awards for the best averages in Mathematics; in Physics and Applied Mathematics; and for best GPA.

### Research achievements

- Sept. 2017 - **PhD**, Institute of Physics, Ecole Polytechnique Fédérale de Lausanne.  
now Supervisor: Prof. Frédéric Mila. Provisional public defence date: April 2022.
- Development of contractible tensor networks for classical frustrated Ising models [1].
- Investigation of farther-neighbour, frustrated models on the kagome lattice with Monte Carlo and tensor network methods. Interpretation of experiments on an artificial spin system, in collaboration with the group of Prof. Laura J. Heyderman at the Paul Scherrer Institute [2].
- Study of classical skyrmions on small lattices, as part of a project to characterize the topology of the quantum analog of a classical skyrmion [3].

### Teaching and supervision

- Sept. 2019 - Co-supervising Samuel Nyckees's Master thesis: *Tensor network investigation of the three-state chiral Potts model*. The project later resulted in a publication [4].  
Jan. 2020
- Jan. 2018 - Co-supervising 9 semester projects on applying Tensor Networks (iTEBD, CTMRG, TRG) and  
Dec. 2021 Monte Carlo (single spin flip, loop algorithms) to classical spin systems.
- Sept. 2017 - Teaching assistant for various lectures: quantum physics, advanced solid state physics, statistical  
Jan. 2021 physics, computational physics.

### Experience outside academia

- July 2016 - Internship in the Electro-acoustic design team in Bernafon, Bern, Switzerland: Development of  
Feb. 2017 electromagnetic field simulations of various parts of a hearing aid in audio frequency range; design and execution of the experiments for the validation of these simulations.

### Programming Languages

C++ (Monte Carlo simulations, extension modules for Python); Python; Matlab (tensor networks);  
Mathematica (exact tensor network contractions); Bash (slurm, git).

### Languages

French (native), English (C1, CAE in 2011), German (B2)

## Publications

- <sup>1</sup>B. Vanhecke, J. Colbois, L. Vanderstraeten, F. Verstraete, and F. Mila, "Solving frustrated Ising models using tensor networks", [Phys. Rev. Research 3, 013041 \(2021\)](#).
- <sup>2</sup>J. Colbois, K. Hofhuis, Z. Luo, X. Wang, A. Hrabec, L. J. Heyderman, and F. Mila, "Artificial out-of-plane Ising antiferromagnet on the Kagome lattice with very small farther-neighbor couplings", [Phys. Rev. B 104, 024418 \(2021\)](#).
- <sup>3</sup>O. M. Sotnikov, V. V. Mazurenko, J. Colbois, F. Mila, M. I. Katsnelson, and E. A. Stepanov, "Probing the topology of the quantum analog of a classical skyrmion", [Phys. Rev. B 103, L060404 \(2021\)](#).
- <sup>4</sup>S. Nyckees, J. Colbois, and F. Mila, "Identifying the Huse-Fisher universality class of the three-state chiral Potts model", [Nuclear Physics B 965, 115365 \(2021\)](#).

## Talks and posters

### Invited talks

- Aug. 2021 **Online Artificial Spin Ice Sessions (OASIS) 2021**, *Artificial out-of-plane Ising antiferromagnet on the Kagome lattice with very small farther-neighbor couplings*, (Online talk).

### Seminars

- Jan. 2021 **Max Planck Institute of Quantum Optics, Germany (host: Patrick Emonts, PhD student in Prof. Ignacio Cirac's group)**, *Studying frustrated Ising models using tensor networks*, (Online seminar).
- June 2019 **Ghent University, Belgium (host: Prof. Frank Verstraete)**, *Some ideas and an example for finding lower bounds for the ground state energies of short-range classical Ising models*.

### Contributed talks

- Feb. 2022 **Entanglement in strongly correlated systems 2022, Benasque, Spain**, *Incomplete lifting of degeneracy in the  $J_1 - J_2 - J_3$  Ising antiferromagnet on the Kagome lattice*.
- Jan. 2022 **Magnetism and Magnetic Materials Conference 2022, Online (New Orleans, United States)**, *Artificial out-of-plane Ising antiferromagnet on the Kagome lattice with very small farther-neighbor couplings*, (Online talk).
- Nov. 2020 **Magnetism and Magnetic Materials Conference 2020, Online (Florida, United States)**, *New approaches to the nearest-neighbour (?) Ising antiferromagnet on the Kagome lattice*, (Online talk).
- Aug. 2019 **Annual Meeting of the Swiss Physical Society 2019, Zürich University, Switzerland**, *Progressive lifting of the ground-state degeneracy of the farther neighbour Kagome Ising antiferromagnet*.
- Aug. 2019 **Summer school on Quantum Magnetism, EPFL, Switzerland**, *Farther-neighbour couplings in the Kagome lattice Ising antiferromagnet: A method of inequalities to find exact ground-state energies*.

### Posters

- Feb. 2021 **Entanglement in strongly correlated systems 2021, Online (Benasque, Spain)**, *Solving frustrated Ising models using tensor networks*.  
Joint poster with Bram Vanhecke
- Feb. 2020 **Entanglement in strongly correlated systems 2020, Benasque, Spain**, *Monte Carlo, tensor network and exact methods for the Kagome Ising antiferromagnet with farther-neighbour interactions*.
- Nov. 2019 **European Tensor Network School 2019, San Sebastian, Spain**, *Monte Carlo, tensor network and exact methods for the Kagome Ising antiferromagnet with farther-neighbour interactions*.
- Feb. 2019 **Entanglement in strongly correlated systems 2019, Benasque, Spain**, *Progressive lifting of the ground-state degeneracy of the long-range Kagome Ising antiferromagnet*.

- Aug. 2018 **Swiss Workshop on Materials with Novel Electronic Properties 2018, Les Diablerets, Switzerland**, *Progressive lifting of the ground-state degeneracy of the long-range kagome Ising antiferromagnet.*
- June 2018 **Machine Learning for Quantum Many-body Physics (MLQ 18), Dresden, Germany**, *Progressive lifting of the ground-state degeneracy of the long-range kagome Ising antiferromagnet. Awarded the Nature Reviews Physics Poster Prize*
- June 2018 **Trends in Quantum Magnetism (673. Wilhelm und Else Heraeus-Seminar), Bad Honnef, Germany**, *Progressive lifting of the ground-state degeneracy of the long-range kagome Ising antiferromagnet.*
- [Outreach](#)
- Nov. 2020 **Seminar for the EPFL Physics Students association, Lausanne**, *The simplest model of microscopic magnetism: an informal discussion on 100 years of Ising model (in French).*
- April 2017 **Presentation for high school students, Neuchâtel**, *Physics for helping people with hearing impairments (in French).*

## Miscellaneous

- 2015 - 2020 Saxophonist, pianist (member of musical commissions from 2018 to 2020):  
Concert Band du Littoral Neuchâtelois (2015-2020); EPFL Big Band (2018-2020).
- 2018 - 2021 Jazz/Improvisation piano studies.
- 2001 - 2018 Classical piano studies: Diploma of Amateur studies, with Honours (2016, Conservatoire de Musique Neuchâtelois); Classical saxophone studies (2009-2014).